Design and Synthesis of Novel Columnar Liquid Crystalline Molecules

A Thesis Submitted in Partial Fulfilment of the Requirements for the Degree of Doctor of Philosophy

at

IIT Guwahati

by

Rahul Ahmed

Roll No. 196122023

Department of Chemistry
Indian Institute of Technology Guwahati
Guwahati-781039, Assam
India

June 2025

"Learning gives creativity, creativity leads to thinking, thinking provides knowledge, and knowledge makes you great."

-A.P.J. Abdul Kalam

Dedicated to

All my esteemed teachers.........

DECLARATION

I do hereby declare that the research work embodied in this thesis entitled "***Design and Synthesis of Novel Columnar Liquid Crystalline Molecules***" has been carried out by me under the supervision of **Prof. A. S. Achalkumar** in the Department of Chemistry, Indian Institute of Technology Guwahati, Assam- 781039, Indian.

In keeping with the general practice of reporting scientific observations, due acknowledgments have been made wherever the work described is based on the findings of other investigators.

IIT Guwahati   Rahul Ahmed

June, 2025   Roll No. 196122023

Dr. A. S. Achalkumar, FRSC, FICS
Professor
Department of Chemistry
Indian Institute of Technology Guwahati
Guwahati – 781039, Assam, India
Phone: +91-361-258-2329
Fax: +91-361-258-2349
E-mail: achalkumar@iitg.ac.in

CERTIFICATE

This is to certify that the research work presented in this thesis entitled "***Design and Synthesis of Novel Columnar Liquid Crystalline Molecules***" is an authentic record of the results obtained from the research work carried out by **Mr. Rahul Ahmed (Roll No. 196122023)** under my supervision in the Department of Chemistry, Indian Institute of Technology Guwahati, India. This original work has not been submitted elsewhere for a degree or award.

IIT Guwahati	Dr. A.S. Achalkumar
June 2025	Thesis Supervisor

ACKNOWLEDGEMENTS

The journey to completing my thesis, which embodies the culmination of years of experience and the ideas I have developed, has been one of hard work that ultimately led to success. Throughout my five years in research, I have been fortunate to receive unwavering support from many individuals, for whom I am deeply grateful for their kindness, guidance, encouragement, and assistance.

I extend my deepest gratitude to my supervisor, Prof. A.S. Achalkumar, whose expert guidance, inspiration, and innovative scientific insights have been pivotal in shaping the direction of this thesis. His steadfast support allowed me to explore my scientific ideas and develop research questions that piqued my curiosity. Our countless hours of enriching discussions on science and concepts broadened my understanding and propelled this work forward. Completing this project would have been daunting without his patience and mentorship. Whenever I encountered uncertainty or hesitated to explore new avenues, his unwavering encouragement and scientific enthusiasm motivated me to reach my goals. Undoubtedly, choosing him as my supervisor has been one of the most rewarding decisions of my academic career.

In addition to my supervisor, I would like to express my deepest gratitude and sincere appreciation to my esteemed doctoral committee members, Prof. Tharmalingam Punniyamurthy, Prof. Subhas Chandra Pan, and Prof. Kalyanasis Sahu. Their thoughtful evaluations, invaluable suggestions, consistent support, and encouragement have been instrumental to my academic progress. I am genuinely grateful for their contributions. I also extend my thanks to Prof. Manoj AG Namboothiry, Anjana K N, and Anitha B from IISER Thiruvananthapuram for their assistance with conductivity measurements. Furthermore, I acknowledge Dr. Vinay Sharma and Dr. Shweta Thakar from Gujarat University for their support in my bioimaging study. Lastly, I am grateful to Prof. Sandeep Kumar from Nitte Meenakshi Institute of Technology, Alakananda Patra from Raman Research Institute, and Dr. D.S. Shankar Rao from CeNS, Bangalore for their guidance and assistance with the X-ray Diffraction studies. I sincerely appreciate all for their invaluable contributions and support.

I sincerely thank the Indian Institute of Technology Guwahati for nurturing my research career and providing the facilities and financial support throughout my work. I also wish to acknowledge the Central Instruments Facility and Centre for Nano Technology, IIT Guwahati, for offering the essential analytical facilities required during my research.

I am deeply grateful to my batchmates for their invaluable help and support, without which it would have been impossible to continue my five years of Ph.D. research. I sincerely thank all my lab members, both past and present—Dr. Vinod Kumar Vishwakarma, Dr. Paresh Kumar Behara, Dr. Priyanka Kant, Dr. Rahul Uttam, Mr. Sagar Pal, Mr. E. Santhosh Kumaran, Mr. Mrinmoy Roy, Mr. Nandan Kumar, Ms. Neichoi Lhouvam, Mr. Dharmendra Adak, Mr. Sarwar Parvez, Mr. Praveen Kandpal, Ms. Savita Kumari, Mr. Abhishek Tiwari, and Dr. Vedeshwar Narayan Singh—for their assistance, engaging scientific discussions, and for maintaining a positive and collaborative working environment throughout my Ph.D. journey. I am also thankful to the almighty for blessing me with wonderful senior friends and batchmates who have been by my side since my research career, offering their guidance and support.

Finally, my Ph.D. journey would not have been possible without the unwavering love, care, blessings, support, patience, selfless sacrifices, and encouragement of my parents and family members. They constantly motivated me to observe the world around me and to question how and why things work. Above all, I am deeply grateful to the almighty God, without whose guidance nothing would have been achievable, and I pray for His continued blessings.

Rahul Ahmed

Some of the findings of this thesis have been communicated/published in international journals as given below:

1. **R. Ahmed**, P. K. Behera, K.N. Anjana, B. Anitha, A. Patra, S. Kumar, M. Namboothiry, and A.S. Achalkumar, Novel Class of Ambipolar Columnar Liquid Crystals Based on Cyclic Dipeptide and Isatin Hybrids, *ChemPhysChem*, 2025, **e202400980**.

2. **R. Ahmed**, K.N. Anjana, V. Sharma, S. Thakar, B. Anitha, P. K. Behera, D. Adak, D. S. Rao, M. Namboothiry and A. S. Achalkumar, Phenoxazine-Based Ambipolar Luminescent Room-Temperature Liquid Crystals Capable of Bioimaging Applications, *J. Mater. Chem. B*, 2025, **13**, 6351.

3. **R. Ahmed**, V. Sharma, S. Thakar, P. K. Behera, P. Kandpal, D. S. Rao and A. S. Achalkumar, Indolo [2,3-b]quinoxaline, a core for the stabilization of room temperature liquid crystalline self-assembly, aggregation-induced emission and bioimaging applications. (Accepted in **ACS Applied Bio Materials, 2025**).

Articles that are not included in this thesis:

1. P. S. Shrivastav, N. Talpada, A. S. Sharma, V. S. Sharma, **R. Ahmed**, A. S. Achalkumar, R. S. Varma, Synthesis of Pyrrolo [2,1-a]isoquinolines using Cu NPs decorated microcrystalline cellulose in 2-Methyl-THF: A biodegradable heterogeneous nanocatalyst for the sustainable cascade approach, *Molecular Catalysis*, 2024, **569**, 114569.

2. P. K. Behera, F. Chen, I. Mondal, S. Lenka, P. Gautam, N. Khatiwoda, I. Siddiqui, V.E. Krishnaprasad, **R. Ahmed**, D. S. Shankar Rao, S. P. Senanayake, J.H. Jou, A. S. Achalkumar, Superior electron mobility, red electroluminescence with high quantum efficiency from printable room temperature columnar liquid crystalline perylene bisimide, *Chemical Engineering Journal*, 2024, **488**,150762.

3. N. Talpada, A. S. Sharma, V. S. Sharma, **R. Ahmed**, H. Mali, P. S. Shrivastav, A. S. Achalkumar, R. S. Varma, Visible light mediated synthesis of 3-indolmethyl chromones via the cyclization of o-hydroxyaryl enaminones with 3-indoleacetic acids catalyzed by graphitic carbon nitride adorned with copper nanoparticles, *ChemNanoMat*, **2024**, e202300641.

4. N. Talpada, A. S. Sharma, V. S. Sharma, R. S. Varma, P. S. Shrivastav, **R. Ahmed** and A.S. Achalkumar, Visible light mediated synthesis of 1,3-diarylated imidazo[1,5-a] pyridines via oxidative amination of C–H catalyzed by graphitic carbon nitride, *Org. Biomol. Chem.*, 2023,

21, 9552.

5. Se-annulated Unsymmetrical Perylene Ester Imide exhibiting Room-Temperature Columnar Hexagonal Mesophases, P. K. Behera; A. Patra; M. Roy; **R. Ahmed**; S. Kumar; V. Belyaev; A. Kazak; X. K. Ren; A.S. Achalkumar. (Manuscript is submitted)

Patent files are given below:

1. Patent No: 202521001368

Title: "A Process for The Synthesis of Pyrrolo [2,1-a] isoquinolines Derivatives by using deep eutectic solvents"

Authors: Ms. Sweety Sojitra, Dr. Vinay Sharma**, Mr. Rahul Ahmed**, Dr. Hitendra Mali, Dr. Anuj Sharma, Dr. Achalkumar Ammathnadu Sudhakar, Dr. Mallika Sanyal, Dr. Pranav S. Shrivastav

2. Patent No: 202521001370

Title: "An Improved Process for The Synthesis of Cinnamic Acid Derivatives by Using Green Deep Eutectic Solvent"

Authors: Ms. Sweety Sojitra, Mr. Parth Parmar, Mr. Jaimin Panchal, Dr. Vinay Sharma, **Mr. Rahul Ahmed**, Dr. Anuj Sharma, Dr. Achalkumar Ammathnadu Sudhakar, Dr. Mallika Sanyal, Dr. Pranav S. Shrivastav.

3. Patent No: 202521001745

Title: – "Iron Catalysed Sustainable Synthesis of Substituted Quinazoline Derivatives by Using Biodegradable Deep Eutectic Solvents"

Authors: Ms. Sweety Sojitra, Mr. Parth Parmar, Dr. Vinay Sharma, **Mr. Rahul Ahmed**, Dr. Anuj Sharma, Dr. Achalkumar Ammathnadu Sudhakar, Dr. Mallika Sanyal, Dr. Pranav S. Shrivastav

5. Patent No:202421077038

Title: "Green Process for The Synthesis of Substituted Benzoxazole Derivatives Through Deep Eutectic Solvents"

Authors: Mr. Om Dalal, Mr. Parth Parmar, **Mr. Rahul Ahmed**, Dr. Vinay Sharma, Dr. Achalkuma Ammathnadu Sudhakar, Dr. Mallika Sanyal, Dr. Pranav S. Shrivastav

Papers presented in National/Internal Conferences (Oral/Poster):

1. Poster Presentation at a National Conference: "National Conference on Liquid Crystals" (NCLC), Andhra University, India, 2023.

2. Poster Presentation at an International Conference: "SPSI-MACRO-2023", IIT Guwahati, India, 2023.

3. Oral Presentation at a National Conference: "National Conference on Polymer and Advanced Functional Materials (NCPAFM) held at IASST, Guwahati, India, December 2024.

4. Oral Presentation at an International Conference: "Innovation and Advances in Chemical Sciences (IACS-2025)" held at Cotton State University, India, January 2025 (Best Oral Presentation).

5. Oral Presentation at a National Conference: "National Seminar on Science for Sustainable Development (SSD)-2025" held at B. Borooah College, India, January 2025.

CONTENTS

Chapter 1 Introduction to Liquid Crystals

Chapter 2 Novel Class of Ambipolar Columnar Liquid Crystals Based on Cyclic Dipeptide and Isatin Hybrids

Chapter 3 **Phenoxazine-Based Ambipolar Luminescent Room-Temperature Liquid Crystals Capable of Bioimaging Applications**

Chapter 4 Indolo [2,3-b]quinoxaline, a core for the stabilization of room temperature liquid crystalline self-assembly, aggregation-induced emission bioimaging applications.

List of abbreviations used in the text

anhyd	anhydrous
bs	broad singlet
Cr	crystal
Col	columnar
d	doublet
DCM	dichloromethane
dd	doublet of a doublet
equiv	equivalents
Et	ethyl
Et_3N	triethyl amine
EtOAc	ethyl acetate
g	gram
h	hour
Hz	hertz
I	isotropic
IR	infrared
kJ	kilojoules
J	coupling constant
K	kelvin
LC	liquid crystal
m	multiplet
m	meta
MHz	megahertz
min	minutes
mmol	mili mole (s)
n	normal

N	nematic
NMR	Nuclear magnetic resonance
p	para
q	quartet
R_f	retention factor
rt	room temperature
s	singlet
t	triplet
THF	tetrahydrofuran
TMS	tetramethyl silane
TLC	thin-layer chromatography
UV	ultra violet
XRD	X-ray diffraction

GENERAL REMARKS

All commercially obtained chemicals were used as received, and solvents were dried according to standard protocols. Silica gel or neutral alumina was used as the stationary phase for column chromatography. In contrast, aluminum sheets coated with silica gel were used for thin-layer chromatography (TLC) to monitor reactions and column purifications. Infrared spectra were recorded at room temperature using a Perkin Elmer IR spectrometer (PerkinElmer UATR TWO), with spectral positions reported in wave numbers (cm^{-1}). NMR spectra were acquired on a 400 MHz and 600 MHz Nuclear Magnetic Resonance (NMR) Spectrometer (Bruker, Model: ADVANCE III HD). Chemical shifts in ^{1}H NMR were referenced to TMS as an internal standard and reported in ppm, with coupling constants given in Hz. Mass spectra were obtained using a MALDI-TOF mass spectrometer (BRUKER, Model: AUTOFLEX SPEED), with α-Cyano-4-hydroxycinnamic acid as the matrix. The liquid crystalline behavior of mesogenic compounds, including birefringence and fluidity, was investigated using a polarized optical microscope (Nikon Eclipse LV100POL) equipped with a programmable hot stage (Mettler Toledo FP90), with observations made on clean glass slides and coverslips. Differential scanning calorimetry (DSC) under a nitrogen atmosphere determined transition temperatures and enthalpy changes. A Mettler Toledo DSC1 instrument was employed, and transition temperatures were consistent with those observed under the polarizing microscope. The first heating and cooling cycles were performed at 5°C/min. Variable temperature X-ray diffraction (XRD) studies were carried out using samples in Lindemann capillaries. A high-resolution X-ray powder diffractometer (PANalytical X'Pert PRO) with a fast detector (PIXcel) was used, and the sample temperature was controlled using a Mettler hot stage/programmer (FP82HT/FP90). Thermogravimetric analysis (TGA) was performed using a Mettler Toledo TG/SDTA 851 e under nitrogen flow at a heating rate of 10 °C/min. UV-Vis spectra were recorded using a Perkin Elmer Lambda 750 UV/VIS/NIR spectrometer. Fluorescence emission in solution was investigated using a Horiba Fluoromax-4 fluorescence spectrophotometer or a Perkin Elmer LS 50B spectrometer. Fluorescence and phosphorescence decay lifetimes were measured using an FLS1000 fluorescence spectrometer. For nematode cell imaging, nematodes were cultured on Nematode Growth Medium (NGM) agar plates and stained before examination under a Lynx LM-52-3001 fluorescence microscope equipped with RGB filters, with images captured using Motic Image Plus software. Cyclic Voltammetry (CV) studies were conducted using a Metrohm Autolab PGSTAT204 electrochemical workstation with the assistance of NOVA software. Particle size and polydispersity indices (PDI) were measured using a Malvern DLS CS90.

PREFACE

Liquid crystals (LCs) are distinctive functional soft materials exhibiting order and mobility at molecular, supramolecular, and macroscopic levels. The molecules responsible for this unique behavior, mesogens, are anisotropic in shape. These mesogens can be organic (forming thermotropic and lyotropic phases), inorganic (metal oxides forming lyotropic phases), or organometallic (metallomesogens). Traditionally, the anisometric molecules that stabilize thermotropic LC phases are rod-like (calamitic) or disc-like (discotic). Calamitic LCs form the foundation of the well-established flat-panel display industry. In recent years, discotic LCs have also seen significant progress, both scientifically and in terms of applications, and are gradually gaining traction in organic electronics. It is also recognized that LC behavior can be achieved with molecules that deviate from conventional LC shapes. A common feature of most such materials is the structural contrast within the molecule; these molecules consist of incompatible chemically distinct parts. In these cases, the primary driving force for the self-assembly of these molecules into LC phases is the nano-segregation of chemically or physically different building blocks, which allows for efficient space filling in the condensed state.

This thesis, entitled "*Design and Synthesis of Novel Columnar Liquid Crystalline Molecules*," is organized into four chapters, each reflecting the research findings accumulated during this study. Chapter 1 introduces liquid crystals, focusing mainly on discotic liquid crystals, and explores their wide range of applications in fields such as photovoltaic devices, OLEDs, OFETs, and sensing technologies. Chapter 2 presents the synthesis of a novel cyclic dipeptide-isatin hybrid, crafted through a double Knoevenagel condensation process using 2,5-diketopiperazine and a variety of isatin derivatives. These new compounds, featuring flexible chains and extended aromatic rings, exhibit high solubility and excellent thermal stability, with decomposition temperatures surpassing 370 °C. Notably, their molecular design facilitates efficient space-filling, stabilizing the columnar liquid crystalline phase. The charge carrier mobility of these compounds was assessed using the space charge limited current (SCLC) technique. Chapter 3 introduces a series of phenoxazine (PO) derivatives, where the addition of peripheral alkyl chains stabilizes a room-temperature columnar phase while imparting luminescent properties. One derivative demonstrates phosphorescence, solvatochromism, and ambipolar behavior, with remarkable charge carrier mobilities. Furthermore, it shows excellent cellular permeability and uniform tissue distribution, positioning it as an effective fluorescent probe for bioimaging applications. Chapter 4 delves into the design, synthesis, and exploration of mesomorphic behavior in four indole [2,3-b]quinoxaline-based D-A molecules. These compounds, particularly those with a higher number of alkyl chains and a more aromatic core, stabilize liquid crystalline phases such as columnar hexagonal and oblique phases, each with distinct isotropic points. Density functional theory (DFT) calculations reveal crucial structural and electronic characteristics, while photophysical studies highlight their broad absorption spectra, significant Stokes shifts, and enhanced emission in the solid state. Additionally, AIE experiments confirm the compounds' solid-state emission properties, which, in the aggregate state, are harnessed for bioimaging applications.

Chapter 1

Introduction to Liquid Crystal

1.1. Introduction to liquid crystals

Until 1888, it was believed in the scientific community that matter could only exist in three possible states—solid, liquid, and gas—under appropriate temperature and pressure conditions. However, liquid crystals represent a unique phase between these traditional phases. In crystalline solids, molecules are arranged in a regular lattice, exhibiting both positional and orientational order. In contrast, amorphous solids do not have long-range orientational order. Liquids, on the other hand, lack both types of order, allowing the molecules to move freely and adopt random orientations.[1-4]

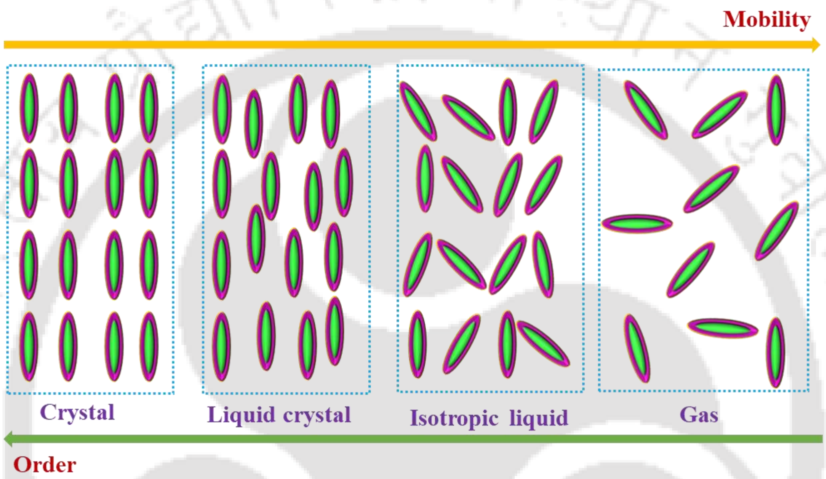

Figure 1.1. Schematic representation of molecular order in the crystal, liquid crystal, liquid, and gaseous states.

When a crystalline solid (Cr) is heated, it melts into a turbid, viscous liquid at temperature T_1 (K). As the temperature increases, the substance transitions into a clear isotopic liquid (I.L) at a higher temperature, T_2 ($> T_1$). Between T_1 and T_2, the liquid exhibits birefringence, an optical anisotropy visible under polarized light, suggesting a crystalline structure while maintaining fluidity. This unique phase, combining crystalline order and liquid-like fluidity, is called a liquid crystal (LC).[5] These intriguing intermediate states of matter form through the self-assembly of shape-anisotropic molecules, known as mesogens. The liquid crystal phase is susceptible to external stimuli such as temperature, pressure, light, and electric and magnetic fields. These phases are positioned thermodynamically between crystalline solids and isotropic liquids called mesomorphic or mesophases.[6-9]

$$\mathbf{Cr} \overset{\mathbf{T_1}}{\rightleftharpoons} \mathbf{LC} \overset{\mathbf{T_2}}{\rightleftharpoons} \mathbf{I.L} \qquad \mathbf{T_1<T_2}$$

1.2. A brief history of liquid crystals

The field of liquid crystals began in 1888 when F. Reinitzer discovered cholesteryl benzoate's (**1.1**) "double melting" behavior. This phenomenon was later studied by German physicist Otto Lehmann, a specialist in polarizing optical microscopy.[10]

In the early 20th century, Ludwig Gattermann observed a liquid crystal phenomenon with p-azoxyanisole compound (**1.2**),[10] and Daniel Vorländer later synthesized around 1100 liquid crystals, proposing that linear molecules, known as calamitic liquid crystals, exhibited the liquid crystal phase.[10] In 1972, G. W. Gray synthesized cyanobiphenyl mesogens, with 5CB (**1.3**) being the most effective, leading to advancements in liquid crystal display (LCD) technology.[11] In 1977, S. Chandrasekhar discovered that disc-shaped (discotic) molecules could also exhibit mesophases (**1.4**), and over 3000 discotic liquid crystals were later documented.[12] In 1996, Niori et al. introduced bent-core (banana-shaped) mesogens (**1.5**), which led to significant research, especially after the discovery of ferroelectricity in non-chiral forms.[13] Liquid crystals have become vital in many applications, including displays, sensors, and more.

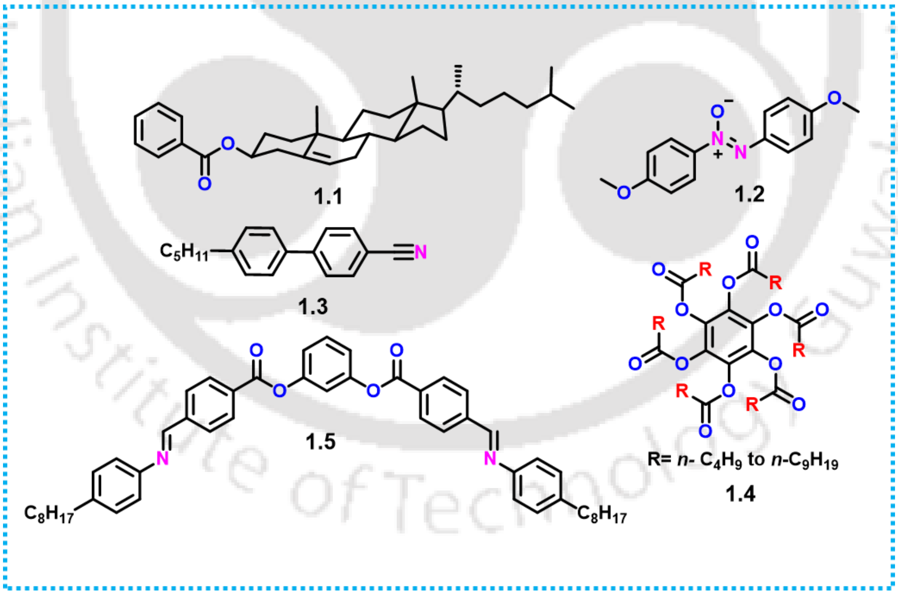

Figure 1.2. Structure of cholesteryl benzoate derivative (**1.1**); para-azoxyanisole derivative (**1.2**); a calamitic (rod-like) LCs 4-alkyl-4’-cyanobiphenyl (**1.3**); discotic (disc-like) LCs benzene-hexa-n-alkanoates (**1.4**) and bent-core (banana-shaped) mesogen (**1.5**).

1.3. Classification

Liquid crystals can be classified in different ways. One approach is based on the molar mass of the constituent molecules, with categories including low molar mass (monomeric, dimeric, and oligomeric) and high molar mass (main, side, and mixed chain polymeric) liquid crystals. Another classification is based on achieving the liquid crystalline phase through temperature changes (thermotropic) or a solvent (lyotropic).[14]

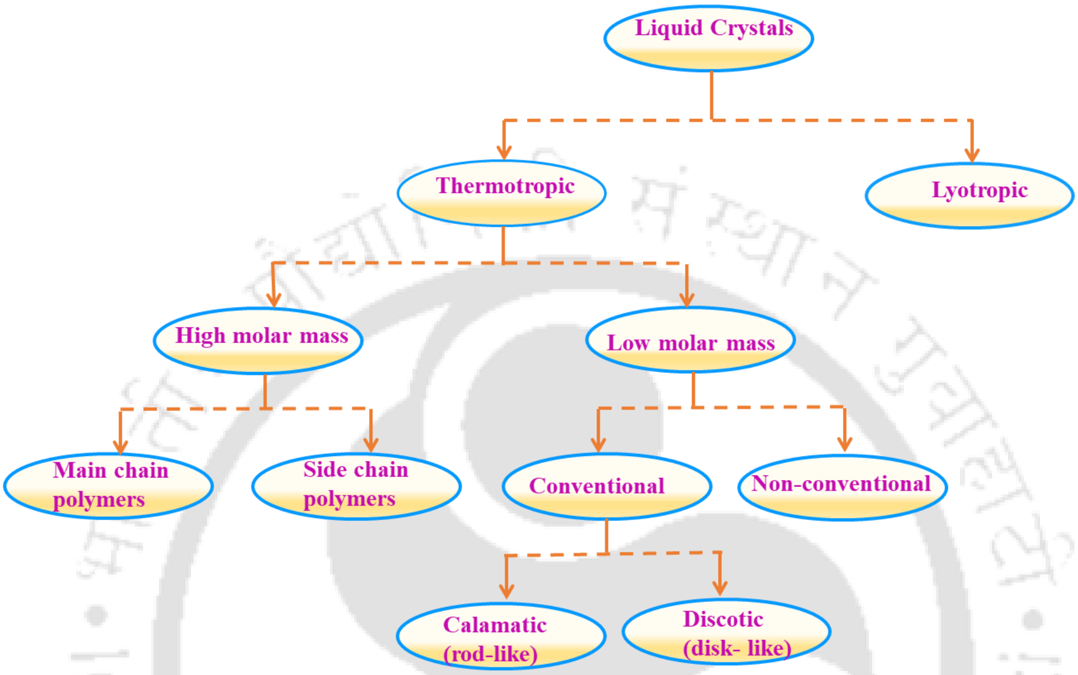

Figure 1.3. Schematic representation of general classification of liquid crystals.

This thesis focuses exclusively on thermotropic liquid crystals (LCs), which are significant for fundamental research and practical applications, such as electro-optic displays and temperature or pressure sensors. In contrast, lyotropic liquid crystals are biologically essential and are believed to play a crucial role in living organisms.

1.4. Thermotropic liquid crystals

When the liquid crystalline phases are obtained by varying the compounds' temperature, they are called thermotropic liquid crystals. [13,15] The mesophase can be obtained by heating a solid or cooling an isotropic liquid. The transition temperature from the crystal to the mesophase is called the *melting point*, while the transition temperature from the mesophase to the isotropic liquid is called the *clearing point*. When thermodynamically stable mesophases are obtained by heating and cooling, the phases are called enantiotropic. If the mesophase is obtained only while cooling the isotropic liquid, it is called the monotropic phase. Thermotropic liquid crystal materials have specific molecular structures, which are composed of two parts: the central core and the side chain. Here, the core part is a rigid body that carries shape anisotropy to the molecule, and the side chain part is a flexible region that provides mobility.

Materials exhibiting thermotropic liquid crystal (LC) properties are primarily organic or metal-containing organic compounds. While countless organic compounds are known, few display this fascinating LC behavior. These compounds typically consist of rigid (hard) and flexible (soft) regions. Aromatic or certain non-aromatic cores often provide the rigidity, while paraffinic chains contribute to the flexibility. The unique combination of these distinct regions is carefully designed to impart a specific anisotropic shape to the molecule. The mobility in such systems arises from the large amplitude motions of the flexible chains, while orientational order is achieved through the parallel alignment of anisotropic molecules. Positional order, on the other hand, primarily results from specific attractive forces and amphilicity. The presence and magnitude of permanent dipole moments and the anisotropy of molecular polarizability are key factors in determining the strength and effectiveness of these molecular interactions. Ultimately, the molecular shape anisotropy plays a crucial role in governing the formation and nature of the liquid crystalline phases.

1.4.1. Conventional liquid crystals

Conventionally, rod-like and disc-shaped mesogens exhibit thermotropic mesomorphism, known as calamitics and discotics.

1.4.1.1. Calamitic liquid crystals

The most common type of molecules that form mesophase is rod-like molecules. These molecules possess an elongated (molecular length is significantly greater than the molecular breadth), as depicted in Figure 1.4.

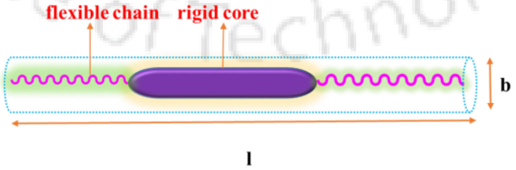

Figure 1.4. The general template for calamitic liquid crystals, where l >> b.

Rod-like or calamitic molecules stabilize nematic (N) and smectic (Sm) mesophases. In the nematic phase (N), the mesogens align to exhibit long-range orientational order, but there is no positional order. This phase represents the least ordered mesophase, closest to the isotropic liquid state, with molecules spontaneously orienting themselves with their long axes approximately parallel to one another, though they lack positional order.

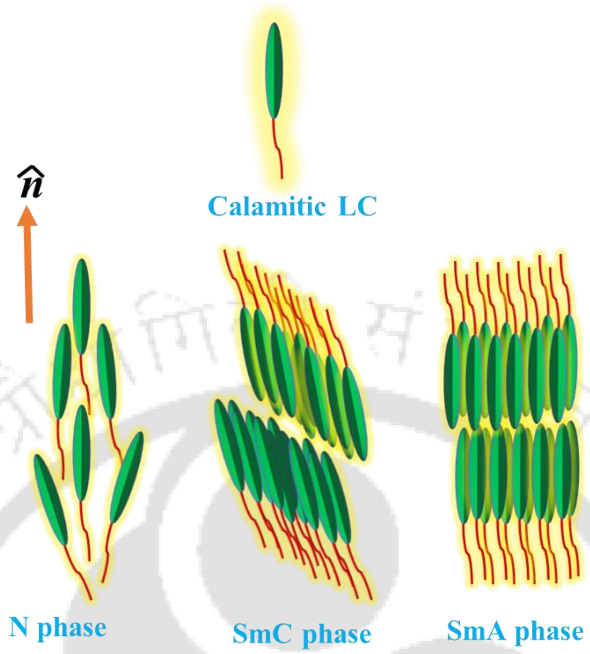

Figure 1.5. Schematic showing the mesophases stabilized by calamitic liquid crystal.

In contrast, smectic (Sm) liquid crystals exhibit orientational and positional order. Smectic phases are divided into subclasses based on each layer's molecular arrangement. While the total number of smectic mesophases is not fixed, several types have been defined, including SmA, SmB, SmC, SmF, and SmI. Among these, the SmA and SmC phases (Figure 1.5) are the least ordered and most common. The SmA phase, characterized by its layered structure and strong aromatic stacking, shows great promise for charge carrier applications. The SmC phase shares the same layered structure as SmA but with molecules tilted relative to the layer plane. In both phases, there is no positional order between molecules within the layers.[16,17] Besides the nematic and smectic mesophases, calamitic liquid crystals display a chiral variant of the nematic mesophase, known as the chiral nematic or cholesteric (N*) phase. This phase arises in systems where the molecules themselves are chiral.[17]

1.4.1.2. Discotic liquid crystals

In 1977, S. Chandrasekhar and co-workers discovered that disk-like molecules, known as discotics, such as benzene hexaalkanotes, could self-assemble into liquid crystal phases.[18] This finding challenged the prevailing belief that only rod-like compounds could exhibit mesomorphism,[19] thus ushering in a new era of liquid crystal research. Over the following four decades, extensive studies have highlighted the importance of discotics in both fundamental science and technological applications. A general structural template (Figure 1.6) illustrates that disc-shaped mesogens typically consist of flat or nearly flat molecules with three-, four-, or six-fold rotational symmetry.[20] These molecules are connected to several alkyl chains of the same or varying lengths through ester, ether, or thioether linkages.

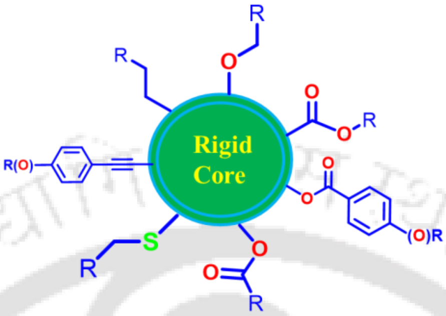

Figure 1.6. The general template of discotic liquid crystals.

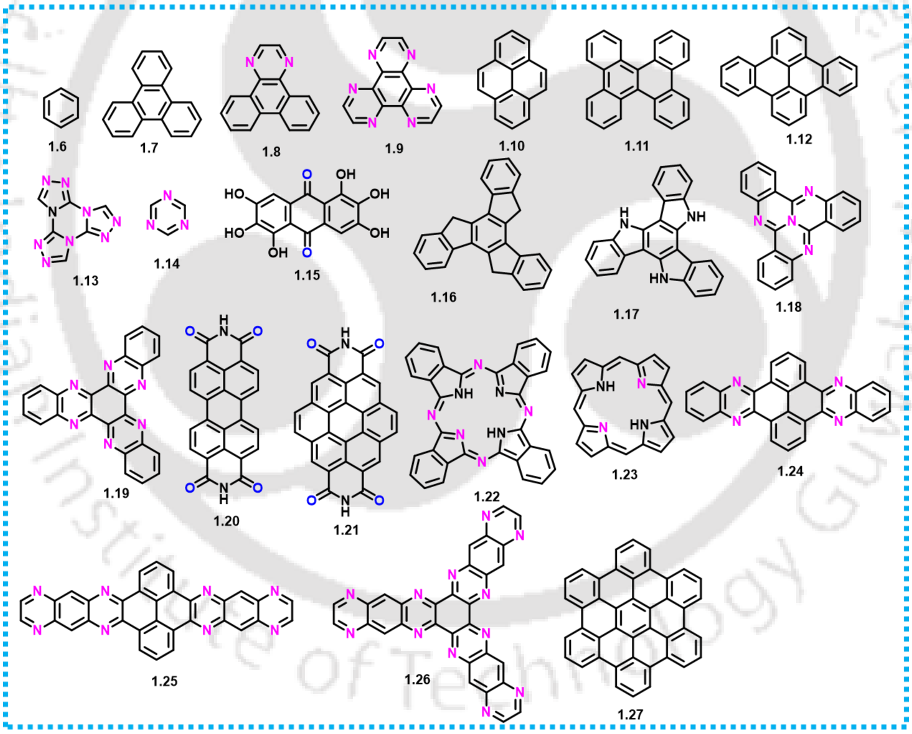

Figure 1.7. Selected aromatic cores used in discotic mesogens (**1.6-1.29**).

Discotic liquid crystals have been reported with a wide range of discotic cores,[20] including benzene (**1.6**), triphenylene (**1.7**), diazatriphenylene (**1.8**), hexatetratriphenylene (**1.9**), pyrene (**1.10**), dibenzo [g, p] chrysene (**1.11**), dibenzonaphthacene (1.12), tristriazootriazine (**1.13**), triazine (**1.14**), rufigallol (**1.15**), truxne (**1.16**), triazatruxene/triindole (**1.17**), tricyacloquinazoline (TCQ, **1.18**), hexaaazatrinaphthylene (HATAN, **1.19**), perylene diimide

(**1.20**), coronene diimide (**1.21**), phathalocyanine (PC, **1.22**), porphyrin (**1.23**), quinoxalinophenenthrophenezine (TQPP, **1.24**), pyrazinopyrazinoquinoxalinophenantthrophenazine (TPPQPP, **1.25**), dodecazatrianthracene (DATAN, **1.26**), and hexa-perrihexabenzocoronene (HBC, **1.27**), as shown in Figure 1.7.

1.4.1.2.1. Discotic mesophase

As is well known, discotic molecules exhibit two types of mesophase, namely, (a) nematic (N) phase and (b) columnar (Col) phase. The salient features of this LC phase are described below.[21]

1.4.1.2.1.1. Nematic (N) phase

The nematic phases of disc-shaped molecules can be categorized into three types: (a) nematic discotic or discotic nematic, (b) chiral nematic, and (c) nematic columnar.

The molecules remain parallel in the nematic discotic phase, exhibiting orientational order without long-range positional order (Figure 1.8a). The discotic nematic phase is the least ordered mesophase. The flat molecules in this phase have complete translational and rotational freedom around their short axes. On average, their long axes (spanning the discotic mesogen's plane) align parallel to a general plane. The nematic phase of disc-shaped molecules is generally immiscible with the nematic phase of rod-shaped molecules, even though both exhibit similar fluid schlieren textures. Unlike typical calamitic nematics, the discotic nematic phase is optically negative, with the director being the preferred axis of orientation for the disc normals (or the short molecular axis). The symbol "N_D" is commonly used to represent the discotic nematic phase. Still, since the symmetry of the nematic phase formed by disc-shaped molecules is the same as that formed by rod-shaped molecules, it has been suggested that the subscript "D" be removed from the "N_D" symbol.[22]

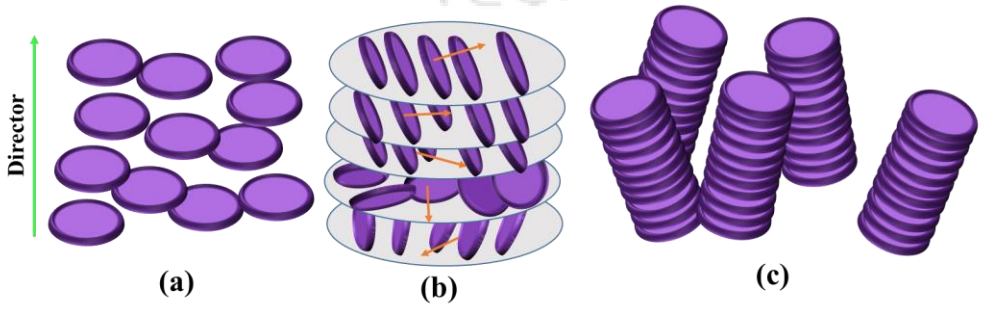

(a) (b) (c)

Figure 1.8. Structure of different nematic phases formed by discotic liquid-crystal compounds: (a) discotic nematic (N_D), (b) chiral discotic nematic (N_D*), (c) columnar nematic (N_{col}).

Like chiral calamitic or cholesteric phases, chiral discotic nematic mesophases N_D* also exit. The mesophase occurs in mixtures of discotic nematic, mesomorphic, or non-mesomorphic chiral dopants and pure chiral discotic molecules. The chiral discotic nematic (N_D*) structure is schematically shown in Figure 1.8b. A columnar stacking of the molecules characterizes the nematic columnar (N_{Col}) phase. However, these columns do not form two-dimensional lattice structures. They display a positional short-range and orientational long-range order (Figure 1.8c). [23,24]

1.4.1.2.1.1.2. Columnar (Col) phase

In the columnar phase of discotic liquid crystals (DLCs), molecules with flexible alkyl chains naturally stack into columns, which then arrange into various two-dimensional lattice structures, such as hexagonal (Col_h), rectangular (Col_r), or oblique (Col_{ob}) phases. The columnar hexagonal mesophase is characterized by a hexagonal packing of the molecular columns, often denoted as Col_h, where "h" stands for hexagonal. The planar space group of the hexagonal columnar mesophase is *P*6/mmm. [25-32]

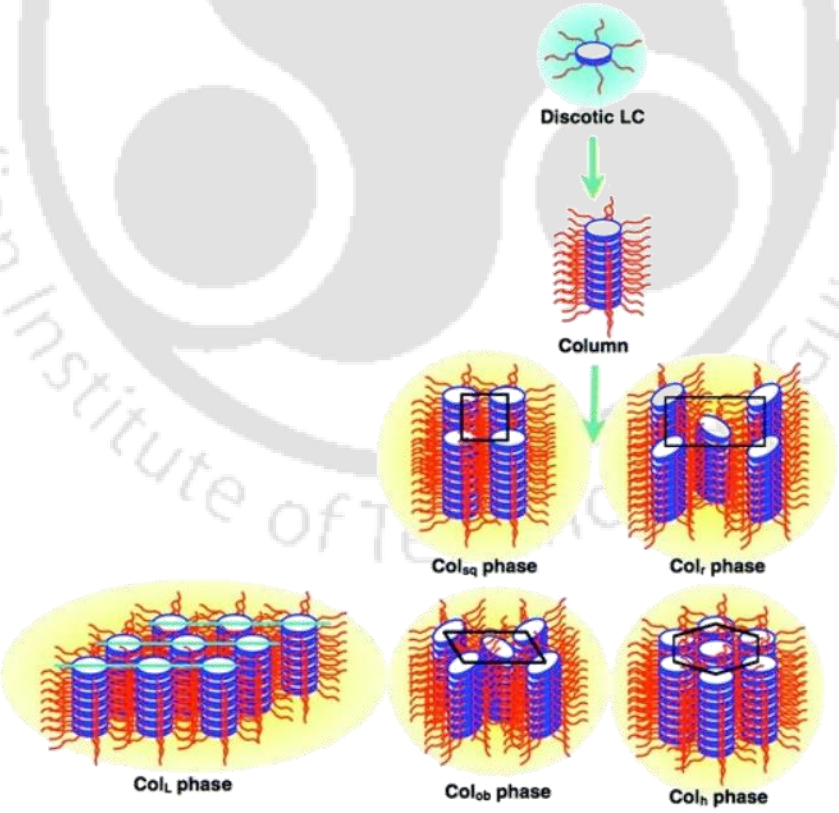

Figure 1.9. Schematic showing the mesophases stabilized by discotic LC phases (adopted from ref. 38).

The columnar rectangular mesophase features aromatic cores of molecules stacked in columns, surrounded by disordered aliphatic chains arranged in a rectangular pattern. The symmetries of the 2D lattices are described by three planar space groups: $P2_1$/a, $P2$/a, and $C2$/m, which belong to a subset of space groups with no transitional periods along the principal symmetry axis, the column direction.[33-35] The arrangement of columns in a columnar oblique mesophase is illustrated in Figure 1.9, with elliptical cross-sections representing the tilted columns. This 2D lattice follows the symmetry of the space group $P_{1.}$[5] Due to the strong core-core interactions, columnar oblique mesophases are rare. A layered structure exists in the mesophases of certain discotic compounds, such as bis(p-*n*-decyl benzoyl), methane copper (II), and some perylene derivatives. This columnar lamellar mesophase, represented by the symbol $\mathrm{Col_L}$, is shown in Figure 1.9.[36-38]

DLCs are characterized by long-range ordering into stacked discs that form columns, causing aromatic cores to overlap while the alkyl chains provide fluidity and liquid crystalline properties.[39-41] These are multifunctional soft materials with many applications, including energy generation and storage, photovoltaics, drug delivery, sensing, and nanomaterials.[42] Additionally, DLCs can be integrated into nanoporous solids and have potential in adaptive photonic metamaterials. DLCs exhibit high anisotropic charge mobilities in the columnar phase, with the greatest mobilities along the column axes. Notably, DLCs can self-heal grain boundaries and other structural defects through thermal annealing followed by cooling from the isotropic state. Although DLCs do not naturally carry charge, external stimuli such as electrical current can induce charge within the system. The alkyl chains maintain the spacing between columns and act as insulating sheaths that prevent lateral charge migration.

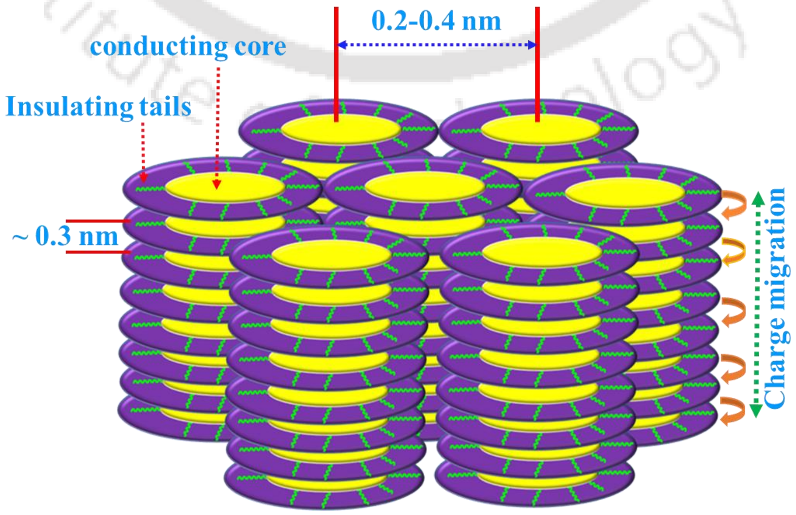

Figure 1.10. One-dimensional charge migration in DLCs.

As a new class of organic semiconductors, DLCs transport charges and excitons more efficiently than traditional conjugated polymers. Ongoing research, including ours, has demonstrated that DLCs with columnar phases can function as 'molecular wires,' making them highly effective for various organic electronic devices.[43-50]

To measure charge-carrier mobility in DLC materials, several techniques and geometries have been used, including pulse radiolysis time-resolved microwave conductivity (PR-TRMC), time-of-flight (TOF), steady-state space charge-limited current (SCLC), and field-effect mobility.[20]

1.4.2. Non-conventional liquid crystals

Driven by curiosity and the pursuit of new mesophases, considerable attention has been given to the design and synthesis of novel molecular architectures where the anisometric shape deviates from the traditional rod or disc form.[51] These compounds are collectively referred to as 'non-conventional liquid crystals.' [51] A key characteristic of most such materials is the structural contrast within the molecule, meaning they consist of chemically distinct molecular parts incompatible with each other. Non-conventional LCs encompass a wide range of anisotropic molecular designs, including oligomeric,[52] phasmidic, polycatenars (dumbbell-shaped or hybrid structures combining rod and disc-like forms),[53] bananas (bent-core molecules),[54] star-shaped molecules,[55] dendrimers,[56] and rod-coil type LCs.[57] The molecular shapes and structures of various non-conventional LCs (**1.28-1.32**) are illustrated in Figure 1.11.

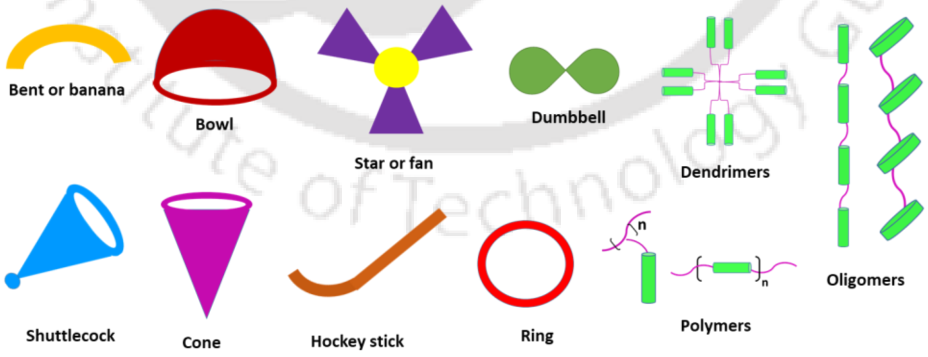

Figure 1.11. Schematic showing the non-conventional molecular shapes used to stabilize LC phases.

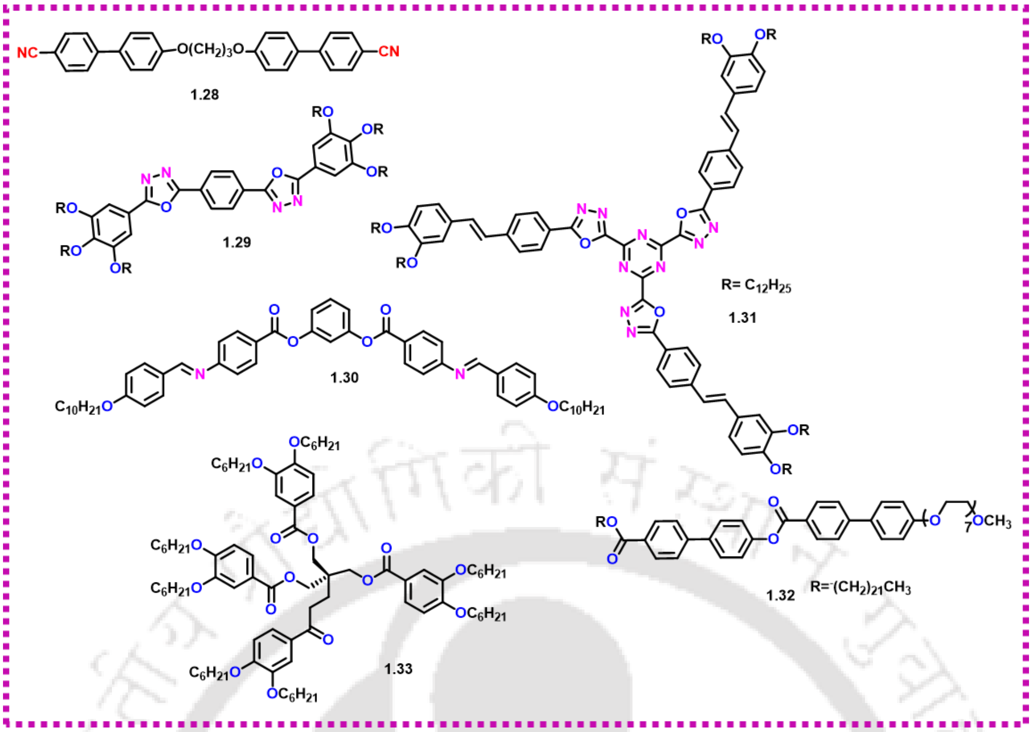

Figure 1.12. Molecular structures of different types of non-conventional LCs (**1.28-1.33**).

1.5. Identification and characterization of mesophase morphology

Three key techniques are essential for identifying and characterizing mesophase morphologies: polarized optical microscopy (POM), differential scanning calorimetry (DSC), and X-ray diffraction (XRD). Employing one or more of these methods provides a reliable means of developing accurate models for the material's mesophase morphology and thermal behavior. [2]

Polarized Optical Microscopy (POM) is a key technique for characterizing the mesomorphism of a compound. In this method, a small sample (less than 1 mg) is placed between a glass slide and cover slip and then positioned on a heated stage under a microscope. The technique relies on the birefringence of the mesophase, where plane-polarized light passes through the sample and a second polarizer, oriented at 90° to the first. This creates characteristic interference patterns due to the interaction of refracted rays. In contrast, when the material is in the isotropic state (in this case, liquid), it appears black between crossed polarizers. This happens because the isotropic nature of the sample does not allow it to split the incident light into ordinary and extraordinary rays. Consequently, the second polarizer blocks the light, resulting in a dark appearance. These textures indicate a particular mesophase and are most distinct when the sample is cooled from the isotropic state (Figure 1.14).[2]

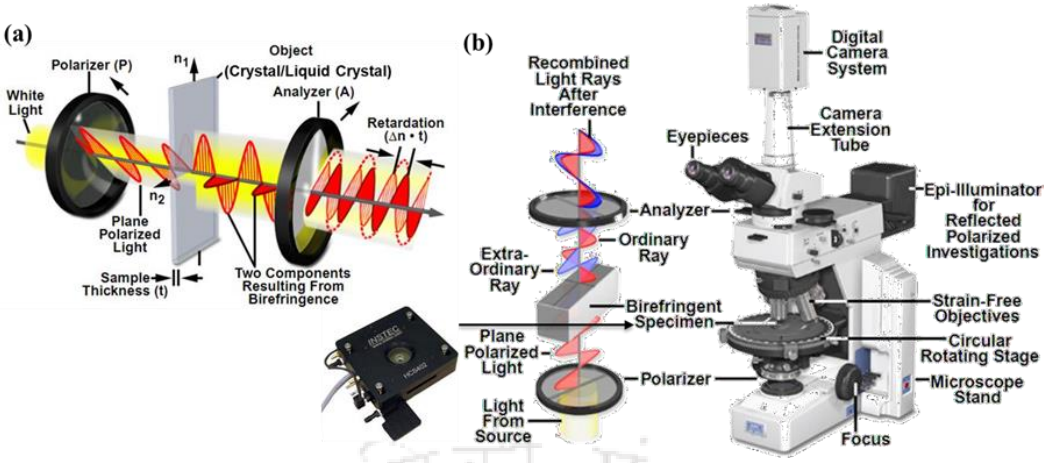

Figure 1.13. (a) Birefringent crystals/liquid crystals between crossed polarizers. (b) The basic configuration of a programmable hot-stage equipped polarizing optical microscope (POM) ©Nikon Corporation (adopted from ref. 58).

Figure 1.14. (a) Different textures of columnar mesophases (a) nematic, (b) smectic, and (c) columnar (adopted from ref. 2)

In a DSC experiment, the enthalpy change accompanying a phase transition of the sample is recorded as a function of temperature. Since thermotropic mesophases can form during heating, cooling, or both, the transitions associated with these phases typically appear as exothermic or endothermic peaks. Thermograms of mesomorphic materials usually show multiple peaks corresponding to different transformations. The enthalpy associated with these thermal events helps correlate phase transitions with the degree of ordering, leading to initial insights into their structural organization. For example, a small enthalpy change during the transition from a liquid crystal (LC) to an isotropic liquid suggests a more disordered mesophase. Therefore, phase transition information can be inferred from the relative magnitudes of the transition enthalpies, with larger values typically observed for crystal-to-mesophase transitions than mesophase-to-mesophase or mesophase-to-isotropic liquid transitions. While this information is valuable, it does not allow for broad generalizations, and the corresponding entropy changes provide more valuable insights (Figure 1.15).[2]

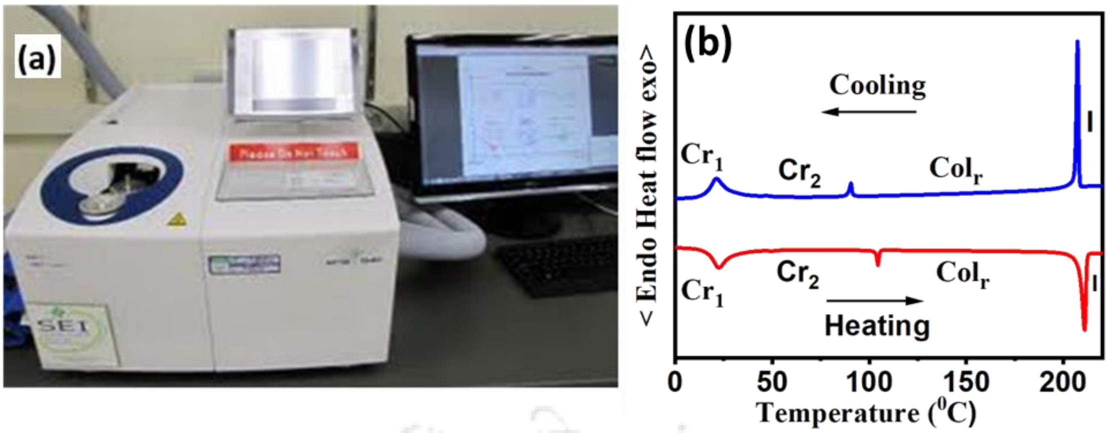

Figure 1.15. a) Differential scanning calorimeter (DSC); (b) DSC thermogram of a mesogenic compound showing columnar phase transitions (adopted from ref. 59).

X-ray diffractometry is a powerful technique for structural analysis, obeyed by Bragg's law ($n\lambda = 2d\sin(\theta)$).[60] Powder X-ray diffractometry can provide some insight into the nature of the phases, but it cannot distinguish between reflections caused by inter-columnar and intra-columnar order. Therefore, macroscopically oriented samples suitable for structural analysis must be extruded. Wide-angle X-ray scattering (WAXS) measurements, taken with the vertical orientation of filaments perpendicular to the incident X-ray beam, generate two-dimensional diffractograms that offer information about the stacking within columns and the two-dimensional packing of those columns, separated along the vertical and horizontal directions, respectively (Figure 1.16). Analysis of the X-ray patterns yields, in addition to structural symmetry information in terms of planar space groups, quantitative data on (i) the ordering of the chains and the cores of the mesogens, (ii) the core-core correlation length along the column axis, and (iii) the spacing between columns.[5,61]

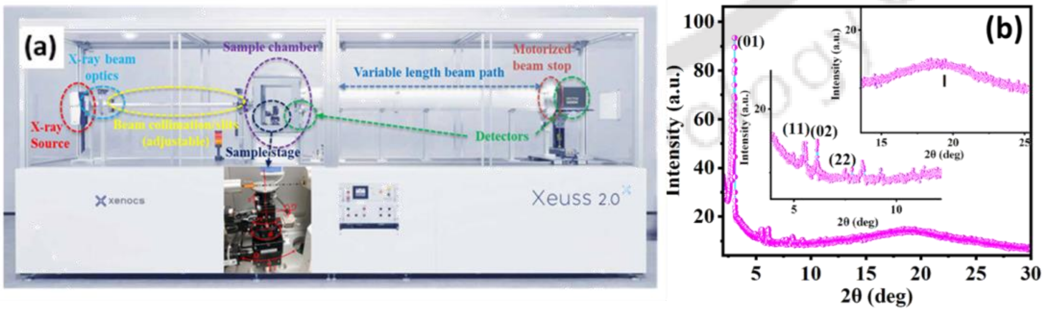

Figure 1.16. (a) The experimental setup for SAXS/WAXS Xenocs Xeuss 2.0 instrument reproduced from ©2019-2020 MGML. (b) The XRD plot of a columnar liquid crystalline compound (intensity *vs* 2θ).

Other experimental techniques, such as electro-optic measurement and nuclear magnetic resonance (NMR) spectroscopy, are also used to characterize mesophases.

1.6. Applications and prospects of liquid crystals

Liquid crystals (LCs) and their associated technologies have become essential in everyday life, with applications ranging from wristwatches and pocket calculators to computers, laptops, and televisions.

1.6.1. Display applications

Twisted and supertwisted nematic displays, which use calamitic liquid crystals (rod-shaped molecules), have been dominant in commercial LCDs. However, they suffer from narrow and non-uniform viewing angles. Recent developments, such as multidomain techniques and optical compensators, have improved viewing angles but require complex processes. Recently, discotic nematic liquid crystals have been used as an alternative to calamitic nematics to address this issue, offering broad and symmetric viewing angles without contrast reversal—however, their high viscosity results in slow devices. To overcome problems like viewing angle, brightness, and contrast, compensation films with negative birefringence, made from discotic liquid crystals, have been introduced. Fuji Photo Films commercialized such films using a triphenylene-based cross-linked polymer, which has become the most successful commercial application of discotic liquid crystals.[62-65]

1.6.2. Thermal Sensors

The chiral nematic phase of cholesteric liquid crystals reflect light at a wavelength proportional to the pitch, which is temperature-dependent. This allows the reflected wavelength to serve as a temperature indicator, enabling temperature measurement by observing the color. By combining different cholesteric liquid crystals, devices can be created to detect a wide range of temperatures. These mixtures are highly sensitive to even small temperature changes, making them useful in various practical applications, such as thermal sensors in medicine, packaging, and electronics.

1.6.3. Columnar fluid phases as a promising media for modern applications

The self-organization of discotic mesogens, driven by π-π interactions between the aromatic cores, forms the columnar mesophase. This columnar (Col) phase is especially notable for its ability to facilitate charge migration along a one-dimensional path. In this phase, the central aromatic core functions as the conductive unit, while the surrounding peripheral chains act as an insulating barrier. This phase's self-assembling and self-healing properties enhance its optical and conductive performance through structured organization. By carefully designing the molecules, these properties can be optimized for organic solar cells (OSCs) (Figure 1.17 a), providing benefits such as excellent processability, high absorption coefficients, and efficient charge carrier mobility, making them cost-effective alternatives to inorganic materials.

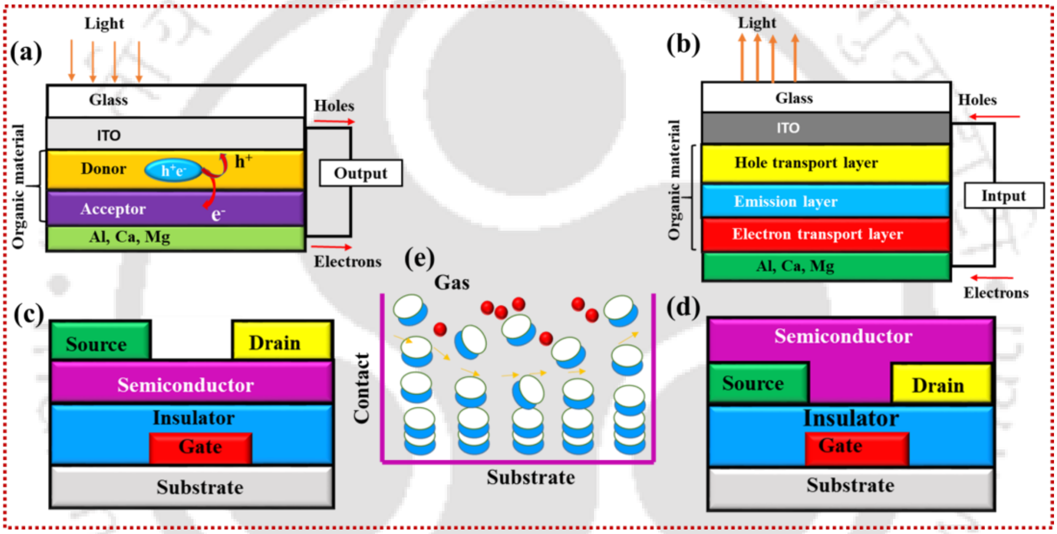

Figure 1.17. (a) Schematic showing the device structure of an organic heterojunction solar cell. (b) Organic light-emitting diode. (c) Schematic of the organic field-effect transistor with a top-contact device, where the source and drain electrodes are deposited on an organic semiconducting layer, (d) a bottom-contact device, where the organic semiconductor is deposited on the prefabricated source and drain electrodes (adopted from ref. 68). (e) Schematic illustration of gas sensor.

Col phases derived from electron-rich and electron-poor discotic liquid crystals (DLCs) show great promise, closely mimicking the behavior of single-crystal organic semiconductors. Additionally, the "edge-on" alignment of Col phases can be integrated into the active layers of organic field-effect transistors (OFETs), crucial components in molecular electronics (Figure 1.17c, d). Recently, Col phases have become essential in developing organic light-emitting diodes (OLEDs), which can act as effective emitting and conductive layers with appropriate structural design. A columnar phase combining hole/electron transport and luminescent properties is ideal for OLED fabrication (Figure 1.17 b).[66-70]

1.6.4. Other applications

Liquid crystals find numerous other applications also. Polymers form an essential subclass of liquid crystal materials and occur in nature as the solution of some biopolymers. They are critical to processing advanced high-modulus engineering materials like Kevlar.[71] Apart from columnar liquid crystals, other forms of liquid crystals like nematic, smectic, cholesteric liquid crystals are utilized in a wide range of modern technologies, including organic solar cells,[72,73] switchable bright windows[74-76] (such as polymer-dispersed liquid crystals (PDLC)), intracellular fluorescent imaging,[77] drug delivery, and liquid crystalline (LC) polymers, elastomers, mechanical actuators, and sensors,[78,79] paints,[80] Biomedical application,[81] among other applications.

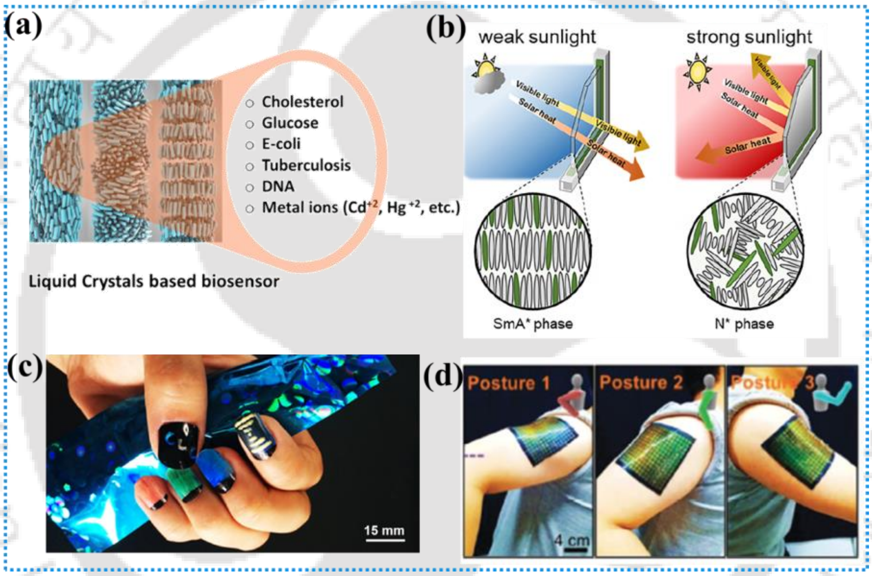

Figure 1.18. (a) Various applications of LC-based biosensors concerning targeted diseases (adopted from ref. 81). (b) Schematic representation of the self-regulating energy-saving window (adopted from ref. 75). (c) Application of the Cholesteric liquid crystal paints as fingernail polish (adopted from ref. 79). (d) Photos of the color variation during arm movement (adopted from ref. 80).

1.7. Thesis layout

This thesis investigates the synthesis and characterization of a new class of organic materials, focusing on structure-property relationships, mesomorphic properties, and photophysical and theoretical analyses. Some of these molecules exhibit both room-temperature and high-temperature discotic columnar liquid crystal behavior, which has been applied in various fields, including mobility studies and bioimaging. A brief overview of the subsequent chapters is provided.

Chapter 2 presents the synthesis and characterization of six new cyclic dipeptide-isatin (CI) hybrid derivatives, modified with peripheral flexible tails of varying lengths. These hybrids were synthesized through a double Knoevenagel condensation of 2,5-diketopiperazine with isatin derivatives that feature flexible chains and aromatic rings. The resulting compounds exhibit high solubility and excellent thermal stability (decomposition temperatures >370°C), and in particular, especially the molecular design with efficient space-filling stabilized columnar liquid crystalline phase. One of the liquid crystalline derivatives' hole and electron carrier mobilities was measured as 9.46×10^{-4} $cm^2V^{-1}s^{-1}$ and 7.88×10^{-4} $cm^2V^{-1}s^{-1}$, respectively, indicating promising ambipolar charge transport properties. The study aims to combine liquid crystal behavior with the unique features of cyclic dipeptides and isatin to create self-assembling organic semiconductors.

Chapter 3 introduces a series of phenoxazine (PO) derivatives, where the addition of peripheral alkyl chains stabilizes a room-temperature columnar phase while imparting luminescent properties. One derivative demonstrates phosphorescence, solvatochromism, and ambipolar behavior, with remarkable hole and electron carrier mobilities measured as 1.92×10^{-4} $cm^2V^{-1}s^{-1}$ and 1.19×10^{-4} $cm^2V^{-1}s^{-1}$, respectively. Furthermore, it shows excellent cellular permeability and uniform tissue distribution, positioning it as an effective fluorescent probe for bioimaging applications.

Chapter 4 focuses on the synthesis of a class of Indolo[2,3-b]quinoxaline (IQ) luminescent liquid crystal molecules obtained by condensing extended *N*-alkylated isatin derivatives with various benzene diamine compounds. These new compounds exhibit high solubility and exceptional thermal stability. Their efficient space-filling interactions stabilize a room-temperature columnar liquid crystalline phase in compounds with two and four peripheral *N*-alkoxy chains. Density functional theory (DFT) calculations provide insights into their structural and electronic properties, while photophysical studies reveal broad absorption spectra, significant Stokes shifts, and enhanced solid-state emission. Additionally, AIE experiments confirm the compounds' solid-state emission properties, which are effectively utilized in bioimaging applications.

1.8. References

1. B. Wunderlich and J. Grebowicz, *Adv. Polym. Sci*., 1984, **2**, 60/61, 1-59.

2. D. Andrienko, Introduction to liquid crystals, *J. Mol. Liq*., 2018, **267**, 520–541.

3. D. Demus, J. Goodby, G. W. Gray, H. W. Spiess, V. Vill, *Wiley-VCH*, Weinheim,1998, **13**.

4. S. Chandrasekhar, Cambridge University Press, Cambridge, 1992.

5. K. Ohta, Physics and Chemistry of Molecular Assemblies, World Scientific, 2020.

6. P. J. Collings, S. J. Patel, Oxford University Press, Oxford, 1997.

7. H. Kelker, W. Hatz, VCH, Deerfield Beach, *FL*, 1980.

8. P. J. Collings, Princeton University Press, 1990.

9. P. G. De Gennes, J. Prost, 2nd ed., Oxford University Press, New York, 1993.

10. M. Mitov, Liquid-Crystal Science from 1888 to 1922: Building a Revolution, *ChemPhysChem*, 2014, **15**, 1245 – 1250.

11. G. W. Gray, K. J. Harrison, J. A. Nash, and E. P. Raynes, *Electron. Lett*., 1973, **9**, 616.

12. S. Chandrasekhar, B. K. Sadashiva and K. A. Suresh, *Pramana*, 1977, **9**, 471-480.

13. T. Niori, T. Sekine, J. Watanabe, T. Furukawa, and H. Takezoeb, Distinct ferroelectric smectic liquid crystals consisting of banana-shaped achiral molecules, *J. Mater. Chem*., 1996, **6**, 1231-1233.

14. J. Guardià, J.A. Reina, M. Giamberini and X. Montané, An Up-to-Date Overview of Liquid Crystals and Liquid Crystal Polymers for Different Applications: *A Rev. Polym*., 2024, **16**, 2293.

15. G. Vertogen, W. H. de Jeu, Thermotropic Liquid Crystals, Fundamentals, Springer Berlin Heidelberg, 1988.

16. C. Tschierske, *Angew. Chem. Int. Ed*., 2013, **52**, 8828-8878

17. (a) Goodby, Mandle, Davis, Zhong and Cowling, *Liq. Cryst.*, 2015, **42**, 593–622; (b) H.S. Kitzerow, C. Bahr, Chirality in liquid crystals, Springer-Verlag, New York, 2001.

18. (a) R.J. Bushby, O. R. Lozman, Discotic liquid crystals 25 years on, *Current opinion in colloidal & Interface Science*, 2002, **7**, 343-354. (b) S. Chandrasekhar, S. K. Prasad, Recent developments in discotic liquid crystals, *Contemporary Physics*, 1999, **40**, 4, 237- 245.

19. S. Laschat, A. Baro, N. Steinke, F. Giesselman, C. Hagele, G. Scalia, R. Judele, E. Kapatsina, S. Sauer, A. Schreivogel, and M. Tosoni, *Angew.Chem. Int. Ed*., 2007, **46**, 4832.

20. B. R. Kaafarani, Discotic Liquid Crystals for Opto-Electronic Applications, *Chem. Mater*., 2011, **23**, 378–396.

21.S. Kumar, Self-organization of disc-like molecules: chemical aspects, *Chem. Soc. Rev*., 2006, **35**, 83–109.

22. C. V. Yelamaggad, V. Prasad, M. Manickam, S. Kumar, C. V. Yelamaggad, V. Prasad, M. Manickam, S. Kumar, *Mol. Cryst. Liq. Cryst*., 1998, **325**, 33.

23. G. Heppke, D. Kruerke, C. Lohning, D. Lotzsch, D. Moro, M. Muller, H. Sawade, New chiral discotic triphenylene derivatives exhibiting a cholesteric blue phase and a ferroelectrically switchable columnar mesophase, *J. Mater. Chem.*, 2000, **10**, 2657.

24. T. Wöhrle, I. Wurzbach, J. Kirres, A. Kostidou, N. Kapernaum, J. Litterscheidt, J. C. Haenle, P. Staffeld, A. Baro, F. Giesselmann and S. Laschat, *Chem Rev*., 2016, **116**, 1139–1241.

25. H. K. Bisoyi, Q. Li, Stimuli directed alignment of self-organized one-dimensional semiconducting columnar liquid crystal nanostructures for organic electronics, *Prog. Mater. Sci*., 2019, **104**, 1.

26. H. K. Bisoyi, Q. Li, Liquid Crystals: Versatile Self-Organized Smart Soft Materials, *Chem. Rev*., 2022, **122**, 4887−4926.

27. R. Termine and A. Golemme, Charge Mobility in Discotic Liquid Crystals, *Int. J. Mol. Sci.*, 2021, **22**, 877.

28. A.E. Murschell, T. C. Sutherland, Anthraquinone-Based Discotic Liquid Crystals, *Langmuir*, 2010, **26**, 12859–12866.

29. X. Zhou, S.W. Kang, S. Kumar, R. R. Kulkarni, S. Z. D. Cheng, and Q. Li, Self-Assembly of Porphyrin and Fullerene Supramolecular Complex into Highly Ordered Nanostructure by Simple Thermal Annealing, *Chem. Mater*., 2008, **20**, 3551–3553.

30. T. Kato, T. Yasuda, Y. Kamikawa and M. Yoshio, Self-assembly of functional columnar liquid crystals, *Chem. Commun*., 2009, **7**, 729–739.

31. R. De, S. K. Pal, Self-assembled discotics as molecular semiconductors, *Chem. Commun*., 2023, **59**, 3050–3066.

32. A. M. Levelut, *J. Chem. Phys*.,1983, **80**, 149.

33. C. Destrade, P. Foucher, H. Gesparoux, H. T. Nguyen, A. M. Levelut, J. Malthete, *Mol. Cryst. Liq. Cryst*., 1984, **106**, 121.

34. J. Billard, J.C. Dubois, C. Vaucher and A.M. Levelut, *Mol. Cryst. Liq. Cryst*., 1981, **66**, 115-122.

35. A. M. Giroud-Godquin, J. Billard, *Mol. Cryst. Liq. Cryst*., 1981, **66**, 147.

36. K. Ohta, H. Muroki, A. Takagi, K. I. Hatada, H. Ema, I. Yamamoto, K. Matsuzaki, *Mol. Cryst. Liq. Cryst*., 1986, **140**, 131.

37. H. Sakashita, A. Nishitani, Y. Sumiya, H. Terauchi, K. Ohta, I. Yamamoto, *Mol. Cryst. Liq. Cryst*., 1988, **163**, 211.

38. V. K. Vishwakarma, A.S. Achalkumar, Structure-property relationships of quinoxaline-based liquid crystals, *Soft Matter,* 2021, **17**, 8221.

39. S. Kumar, The Liquid Crystals book, Chemistry of Discotic Liquid Crystals from Monomers to Polymers, CRC Press, *Taylor & Francis Group*, 2011.

40. M. Baron, Definitions of basic terms relating to low molar mass and polymer liquid crystals, *Pure Appl. Chem*., 2001, **73**, 845.

41. M. Kumar and S. Kumar, Liquid crystals in photovoltaics: a new generation of organic photovoltaics, *Polym. J.*, 2017, **49**, 85–111.

42. P. K. Behera, F. R. Chen, I. Mondal, S. Lenka, P. Gautam, N. Khatiwoda, I. Siddiqui, V. E. Krishnaprasad, R. Ahmed, D. S. Shankar Rao, S. P. Senanayake, J. H. Jou and A. S. Achalkumar, Superior electron mobility, red electroluminescence with high quantum efficiency from printable room temperature columnar liquid crystalline perylene bisimide. *Chem. Eng. J.*, 2024, **488**, 150762.

43. J. De, I. Bala, S. P. Gupta, U. K. Pandey, and S.K. Pal, High Hole Mobility and Efficient Ambipolar Charge Transport in Heterocoronene-Based Ordered Columnar Discotics, *J. Am. Chem. Soc.*, 2019, **141**, 18799−18805.

44. J. Xu, Room-Temperature Columnar Liquid Crystals from Twisted and Macrocyclic 9,9′-Bifluorenylidene Mesogen with Ambipolar Carrier Transport Properties, *ACS Mater. Au*, 2023, **3**, 450−455.

45. D. D. Nguyen, J. Labella, J. L. Martın, C. L. Folcia, J. Ortega, T. Torres, T. Sierra and J. L. Sessler, Columnar liquid crystals based on antiaromatic expanded porphyrins, *Chem. Commun.*, 2024, **60**, 3401–3404.

46. P. K. Behera, K. Yadav, D. S. S. Rao, U. K. Pandey and A. S. Achalkumar, Self-assembled anti-napthalene-3,4:9,10-bis(benzimidazole)s: stabilizing room temperature columnar phase with ambipolar conductivity., *ACS Appl. Electron. Mater.*, 2023, **5**, 5417–5421.

47. J. Hanna, A. Ohno, H. Iino, Charge carrier transport in liquid crystals, *Thin Solid Films*, 2014, **554**, 58–63.

48. P. K. Behera, K. Yadav, D. S. Shankar Rao, U. K. Pandey, and A. A. Sudhakar, Ambipolar columnar self-assembled organic semiconductors based on heteroatom bay-annulated perylene bisimides. *Chem. Asian J.*, 2023, **18**, 202300086.

49. R. Termine, A. Golemme, Charge Mobility in Discotic Liquid Crystals, *Int. J. Mol. Sci.*, 2021, **22**, 877.

50. (a) D. Demus, *Liq. Cryst.*, 1989, **5**, 75; (b) C. Tschierske, *J. Matter. Chem.*, 1988, **8**, 1485; (c) C. Tschierske, *J. Mater. Chem.*, 2001, **11**, 2647.

51. (a) H. Kelker and B. Scheurle, *Angew. Chem.*, 1969, **81**, 903-904; (b) C. T. Imrie and G. R. Luckhurst, in Handbook of liquid crystals, Vol-2B, Eds., D. Demus, J.W. Goodby, G. W. Gray, and H. -W. Spiess, V. Vill, Wiley-VCH, Germany, 1998, part – III, 799; (c) C. T. Imrie and P. A. Henderson, *Curr. Opin. Colloid Interface Sci.*, 2002, **7**, 298-311; (d) C. T. Imrie in Structure and Bonding - Liquid crystals, II, Ed: D. M. P. Mingos, Springer-Verlag, 1999, 149; (e) N. Tamaoki, Adv. Mater., 2001, **13**, 1135-1147; (f) C. V. Yelamaggad, G. Shanker, U. S. Hiremath, and S. K. Prasad, *J. Mater. Chem.*, 2008, **18**, 2927-2949; (g) A. S. Achalkumar, U. S. Hiremath, D. S. Shankar Rao and C. V. Yelamaggad, *Liq. Cryst.*, 2011, **38**, 1563-1589,

52. (a) J. Tang, R. Huang, H. Gao, X. Cheng, M. Prehm, and C. Tschierske, *RSC Adv*., 2012, **2**, 2842-2847; (b) X. Yang, H. Dai, Q. He, J. Tang, X. Cheng, M. Prehm, and C. Tschierske, *Liq. Cryst*., 2013, **40**, 8, 1028-1034; (c) J. Malthete, A. M. Levulut and N. H. Tinh, *J. Phys. Lett.*, 1985, **46**, 875-880; (d) J. Malthete, H. T. Nguyen and C. Destrade, *Liq. Cryst*., 1993, **13**, 171-187.

53. (a) T. Niori, T. Sekine, J. Watanabe, T. Furukawa and H. Takezoe, *J. Mater. Chem*., 1996, **6**, 1231-1233; (b) R. A. Reddy and C. Tschierske, *J. Mater. Chem*., 2006, **16**, 907-961; (c) H. Takezoe and Y. Takanishi, *Jpn. J. of App. Phys*., 2006, **45**, 597-625; (d) G. Pelzi, S. Diele and W. Weissflog, *Adv. Mater.*, 1999, **11**, 707-724; (e) M. B. Ros, J. L. Serrano, M. R. de la Fuente, C. L. Folcia, *J. Mater. Chem*., 2005, **15**, 5093-5098.

54. (a) A. Pegenau, P. Goring and C. Tschierske, *Chem. Commun*., 1996, 2563-2564; (b) M. Lehmann, R. I. Gearba, M. H. J. Koch, and D. A. Ivanov, *Chem. Mater*., 2004, **16**, 374-376; (c) M. Lehmann and M. Jahr, *Chem. Mater*., 2008, **20**, 5453-5456; (d) H. Detert, M. Lehmann and H. Meier, *Materials*, 2010, **3**, 3218–3330; (e) M. Lehmann, *Chem. Eur. J*., 2009, **15**, 3638–3651; (f) S. Varghese, N. S. S. Kumar, A. Krishna, D. S. S. Rao, S. K. Prasad and S. Das, *Adv. Funct. Mater*., 2009, **19**, 2064-2073.

55. (a) J. H. Cameron, A. Facher, G. Lattermann and S. Diele, *Adv. Mater*., 1997, **9**, 398-403; (b) A. Pegenau, T. Hegmann, C. Tschierske and S. Diele, *Chem. Eur. J*., 1999, **5**, 1643-1660; (c) S. I. Stupp, M. Keser and G. N. Tew, *Polymer*, 1998, **39**, 4505-4508; (d) H. Meier, M. Lehmann, and U. Kolb, *Chem. Eur. J*., 2000, **6**, 2462- 2469.

56. M. Lee, D. -W. Lee and B. -K. Cho, *J. Am. Chem. Soc*., 1998, **120**, 13258-13259.

57. 27. (a) P. C. D. Robinson and M. W. Davidson, Nikon, Florida, USA., 2000-2013; (b) D. B. Murphy, K. R. Spring and M. W. Davidson, Nikon, Florida, USA, 2000- 2013; (c) D. B. Murphy, K. R. Spring T. J. Fellers and M. W. Davidson, Nikon, Florida, USA, 2000-2013.

58. R. Ahmed, P. K. Behera, K.N. Anjana, B. Anitha, A. Patra, S. Kumar, M. Namboothiry, and A.S. Achalkumar, Novel Class of Ambipolar Columnar Liquid Crystals Based on Cyclic Dipeptide and Isatin Hybrids, *ChemPhysChem*, 2025, e202400980.

59. A. F. M. Santos, J. L. Figueirinhas, M. Dionísio, M.H. Godinho and L. C. Branco, Ionic Liquid Crystals as Chromogenic Materials, *Materials*, 2024, **17**, 4563.

60. S.K. Prasad, D. S. Shankar Rao, S. Chandrasekhar & Sandeep Kumar, X-RAY Studies on the Columnar Structures of Discotic Liquid Crystals, *Mol. Cryst. Liq. Cryst.*, 2003, **396**, 121–139.

61. T. Sugiyama, T. Hashimoto, K. Katoh, Y. Iimura, S. Kobayashi, Analytical Simulation of Electrooptical Performance of Multidomain Twisted Nematic Liquid Crystal Displays, *Jpn. J. Appl. Phys.*,1995, **4**, 2396.

62. H. Mori, Novel Optical Compensators of Negative Birefringence for Wide-Viewing-Angle Twisted Nematic Liquid-Crystal Displays, *Jpn. J. Appl. Phys.*, 1997, **36**, 1068.

63. M. Oh-e, M. Yoneya, K. Kondo, Switching of negative and positive dielectric-anisotropic liquid crystals by in-plane electric fields, *J. Appl. Phys.*, 1997, **82**, 528.

64. Y. Toko, T. Sugiyama, K. Katoh, Y. Iimura, S. Kobayashi, Amorphous twisted nematic–liquid-crystal displays fabricated by nonrubbing showing wide and uniform viewing-angle characteristics accompanying excellent voltage holding ratios, *J. Appl. Phys.*,1993, **74**, 2071.

65. (a) C. D. Simpson, J. Wu, M. D. Watson and K. Mullen, J. Mater. Chem., 2004, **14**, 494-504; (b) S. Laschat, A. Baro, N. Steinke, F. Giesselmann, C. Hägele, G. Scalia, R. Judele, E. Kapatsina, S. Sauer, A. Schreivogel and M. Tosoni, *Angew. Chem.Int. Ed.*, 2007, **46**, 4832-4887.

66. N. Boden, R. Bissel, J. Clements and B. Movaghar, *Current Science*, 1996, **71**, 599- 601.

67. T. Christ, B. Glusen, A. Greiner, A. Kettner, R. Sander, V. Stumpflen, V. Tsukruk and J. H. Wendorff, *Adv. Mater.*,1997, **9**, 48-52.

68. R. K. Gupta and A. S. Achalkumar, Perylene-Based Liquid Crystals as Materials for Organic Electronics Applications, *Langmuir*, 2019, **35**, 2455−2479.

69. M. Neill and M. Kelly, Liquid Crystals for Charge Transport, Luminescence, and Photonics, *Adv. Mater.*, 2003, **15**, 14.

70. Kwolek, S.L., Du Ont, 1971, US Patent 3600350.

71. R. Nandi and S. K. Pal, Liquid crystal based sensing device using a smartphone, *Analyst*, 2018, **143**, 1046.

72. J. Wen, H. Lin, X. Yu, M. Li, X. Du, J. Luo, G. Yang, C. Zheng, and S. Tao, Efficient and Stable Ternary Organic Solar Cells Using Liquid Crystal Small Molecules with Multiple Synergies, *ACS Appl. Energ Mater*., 2022, **5**, 12809−12816.

73. W. Shen and G. Li, Recent Progress in Liquid Crystal-Based Smart Windows: Materials, Structures, and Design, *Laser Photonics Rev*., 2023, **17**, 2200207.

74. T. Ube, M. Yoshida, S. Kurihara, and T. Ikeda, Sunlight-Driven Smart Windows with a Wide Temperature Range of Optical Switching Based on Chiral Nematic Liquid Crystals, *ACS Appl. Mater. Interfaces*, 2024, **16**, 28638−28644.

75. C. H. Han, J. Lee, C. H. An, S.W. Oh, a liquid crystal bright window for energy saving and harvesting, *Appl. Mater. Today*, 2023, **35**, 101923.

76. J. De, A. Haseeb, R. A. K. Yadav, S. P. Gupta, I. Bala, P. Chawla, K. K. Kesavan, J.H. Jou and S. K. Pal, AIE-active mechanoluminescent discotic liquid crystals for applications in OLEDs and bio-imaging., *Chem. Commun*., 2020, **56**, 14279.

77.S. A. Oladepo, Development and Application of Liquid Crystals as Stimuli-Responsive Sensors, *Molecules*, 2022, **27**, 1453.

78. I. Kim, W. Sik Kim, K. Kim, M. A. Ansari, M. Q. Mehmood, T. Badloe, Y. Kim, J. Gwak, H. Lee, Y.K. Kim, J. Rho, Holographic metasurface gas sensors for instantaneous visual alarms, *Sci. Adv*., 2021, **7**.

79. D. Y. Kim, K. M. Lee, T. J. White, and K. Jeong, Cholesteric liquid crystal paints: in situ photopolymerization of helicoidally stacked multilayer nanostructures for flexible broadband mirrors, *NPG Asia Mater*., 2018, **10**, 1061–1068.

80. Z. Zhang, X. Yang, Y. Zhao, F. Ye, and L. Shang, Liquid Crystal Materials for Biomedical Applications, *Adv. Mater*., 2023, **35**, 2300220.

81. J. Prakash, A. Parveen, Y. K. Mishra, A. Kaushik, Nanotechnology-assisted liquid crystals-based biosensors: Towards fundamental to advanced applications, *Biosens. Bioelectron.*, 2020, **168**, 112562.

Chapter 2

Novel Class of Ambipolar Columnar Liquid Crystals Based on Cyclic Dipeptide and Isatin Hybrids

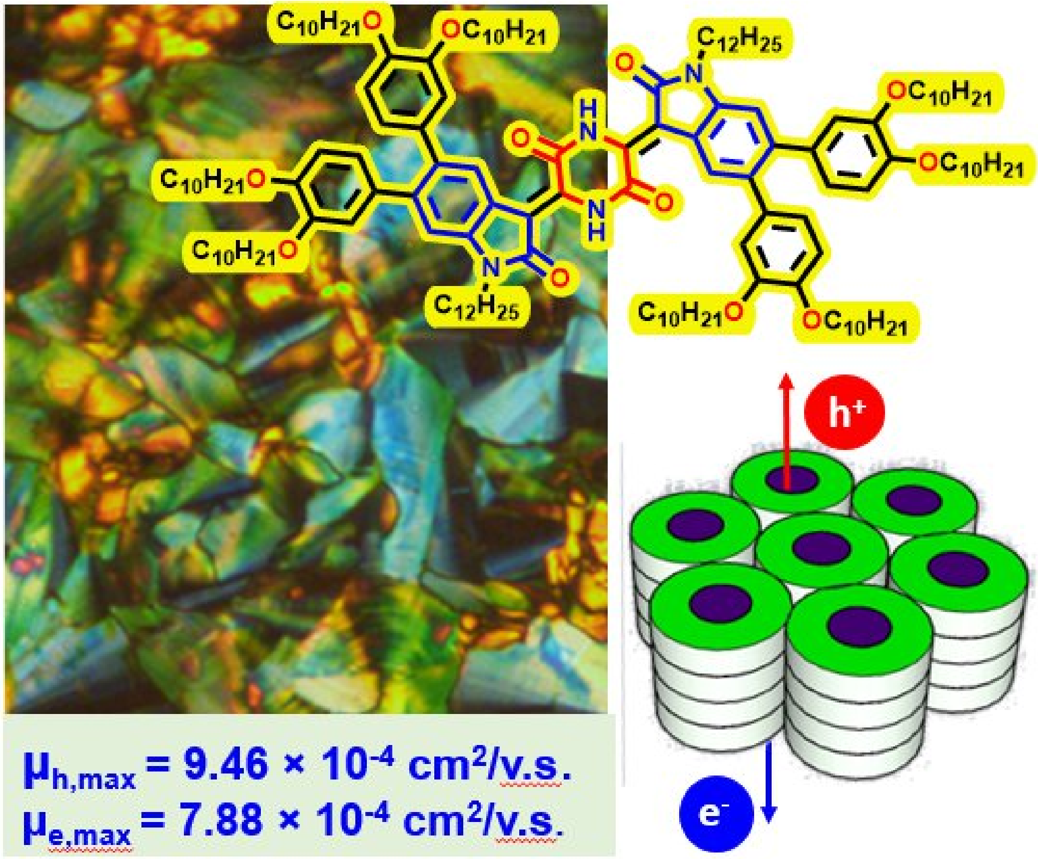

2.1. Introduction

Cyclic dipeptides, consisting of two amino acids joined in a cyclic structure by an amide bond, are abundant in nature and can be synthesized using various chemical and enzymatic methods.[1] These compounds exhibit a broad range of biological activities and have been extensively researched for their potential in pharmaceuticals and medicine. The self-assembly of cyclic dipeptides is primarily driven by non-covalent interactions such as hydrogen bonding, hydrophobic interactions, van der Waals, and electrostatic forces.[2] The exceptional hydrogen-bonding capability of cyclic dipeptides is critical, providing the foundational intermolecular interactions necessary for their self-assembly.[3]

Other non-covalent interactions like π-π stacking and hydrophobic interactions can also contribute to the self-assembly process, depending on the specific amino acid composition or chemical modifications of the cyclic dipeptide molecules.[4] The cyclic dipeptide (CDP) is a versatile and modular unit in molecular architecture, contributing to the creation of various innovative materials.[5-8] These include 1D and 2D biomimetic materials, low molecular weight gelators (**2.1**),[9] detection of phenolic nitro compound (**2.2**),[10] photoluminescent gels (**2.3**),[11] quantum-confined nanostructure (**2.4**),[11] modifiers for chirality in noncovalent molecular assemblies and supramolecular polymers, ambidextrous super gelators (**2.5**),[12] high-strength organic crystals, controlled drug delivery systems, anticancer agents, and agents for DNA delivery (**2.6**).[12]

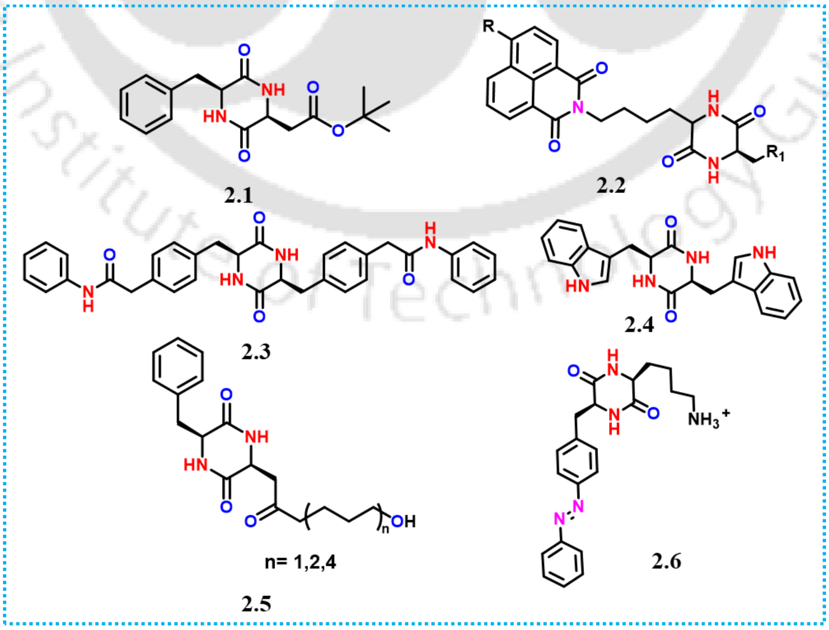

Figure 2.1. Structures of different cyclic dipeptide (CDP) based compounds used for various applications (**2.1-2.6**).

Isatin, a component of the indoline-2,3-dione group, shown in Figure 2.3, is widely distributed in nature, and its derivatives display a wide range of pharmacological activities, including anticancer,[13] antibacterial,[14] antimalarial,[15,16] antituberculosis,[17,18] anti-convulsant,[19] and antiviral properties. The structure of isatin facilitates functionalization and modification, making it a versatile starting material in organic synthesis. Its derivatives can be customized to enhance specific properties or target biological pathways such as SHP1 inhibitors (**2.7**), broadening their potential applications. Isatin-based molecules can be integrated into polymers [20] or nanomaterials to confer desired biological activities or enhance material characteristics.[21] Their ability to undergo diverse chemical reactions enables the creation of hybrid materials or functional surfaces with tailored properties. Several studies highlight the importance of these molecules in developing compounds with promising optoelectronic properties [21] and third-order nonlinear (NLO) optical properties (**2.8-2.10**) [22-24] relevant to optical communication, information storage, and sensing (**2.11**).[25] Isatin crystals are particularly significant in advancing OLEDs (**2.12**), facilitating efficient emission of red light for enhanced power efficiency and favorable external quantum yield.[26]

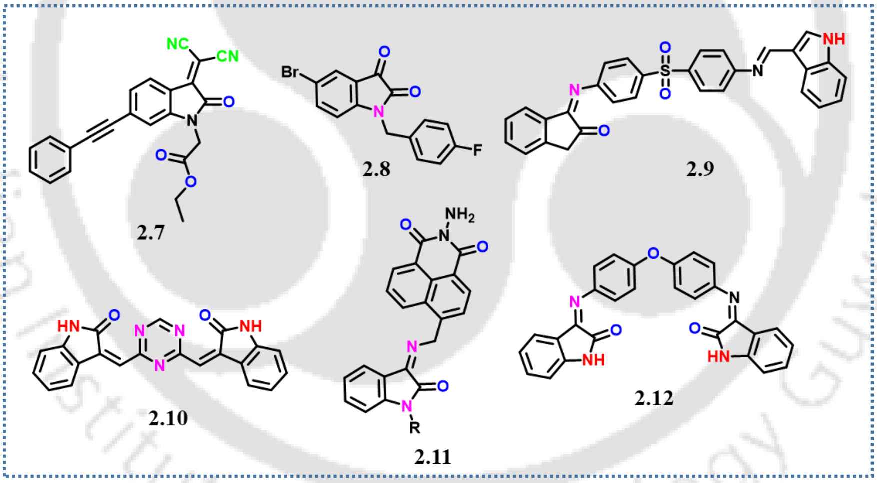

Figure 2.2. Structures of different isatin-based compounds used for various applications (**2.7-2.12**).

Discotic liquid crystals (DLCs) are advanced organic semiconductors known for their superior charge and exciton transport due to self-assembly driven by π-π interactions. These materials spontaneously form columnar structures that organize into two-dimensional mesophases, ideal for energy, sensing, and organic electronics applications. Their cost-effective synthesis and potential as 'molecular wires' make them promising for a wide range of cutting-edge technologies.[27-37]

We envisaged that the amalgamation of liquid crystal behavior to the unique properties of cyclic dipeptides and isatin moiety could open up the self-assembly of functionalized cyclic dipeptide-isatin hybrid (**CI**) to form columnar phases, which is unknown. There is a single report on cyclic dipeptide-based compound stabilizing layered mesophases.[4] At the same time, there are no reports on CDP-isatin hybrids stabilizing columnar LCs to the best of our knowledge. In our pursuit of achieving liquid crystallinity in a novel CDP-isatin-based hybrid molecules (**CI**) class, the central core was designed by combining a CDP moiety and two moieties of isatin. Further variation was conducted by introducing flexible chains on the aromatic unit and isatin nitrogen. Initially, *N*-alkylated bromoisatin with straight or branched chains was condensed with 1,4-diacetylpiperazine-2,5-dione. The molecular structure was conceptualized to combine electron-rich and poor moieties in a single molecular platform to realize an ambipolar self-assembling organic semiconductor.[38-41] Such materials simplify the device structure in organic electronic devices and make them more economically viable.[42] The resultant products were crystalline, even with the CDP-isatin hybrids bearing dendrons on isatin nitrogen (**CI3** and **CI4**). This motivated us to increase the number of peripheral alkyl chains around the central aromatic core by connecting through the phenyl groups, represented by molecules **CI5** and **CI6**. The **CI5** and **CI6** exhibited a columnar rectangular phase over a long thermal range. One of these liquid crystalline CDP-isatin-hybrids (**CI5**) investigated exhibited hole and electron carrier mobility of 9.46×10^{-4} $cm^2V^{-1}s^{-1}$ and 7.88×10^{-4} $cm^2V^{-1}s^{-1}$, respectively, as evidenced by the space charge limited current (SCLC) technique.

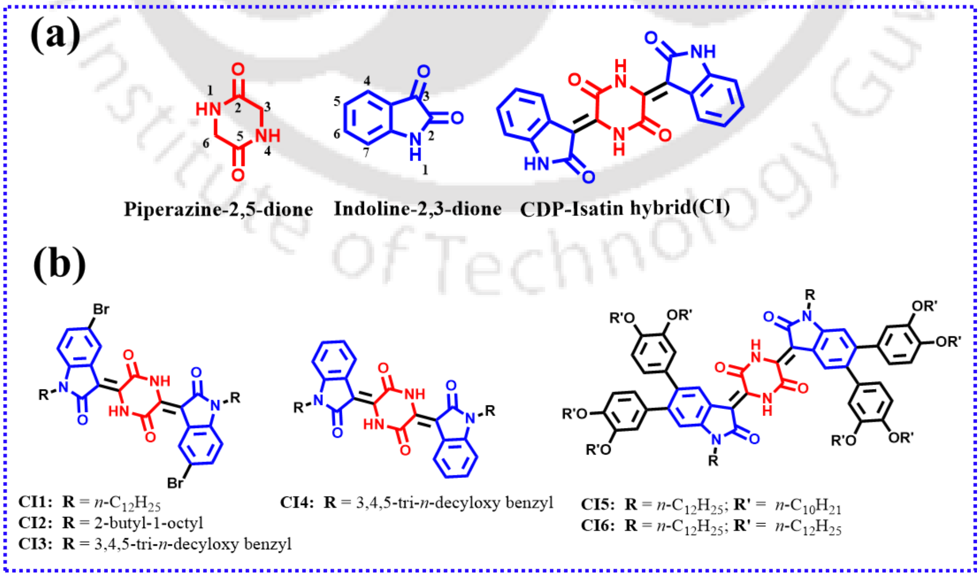

Figure 2.3. Schematic diagram of (a) Cyclic dipeptide (piperazine-2,5-dione), Isatin (indoline-2,3-dione), CDP-isatin hybrid (**CI**). (b) Structures of **CI**s (**CI1-6**) studied in this work.

2.2 Result and Discussion

2.2.1 Synthesis and molecular structural characterization

The synthetic approach utilized to prepare target **CI**s is outlined in scheme 2.1.

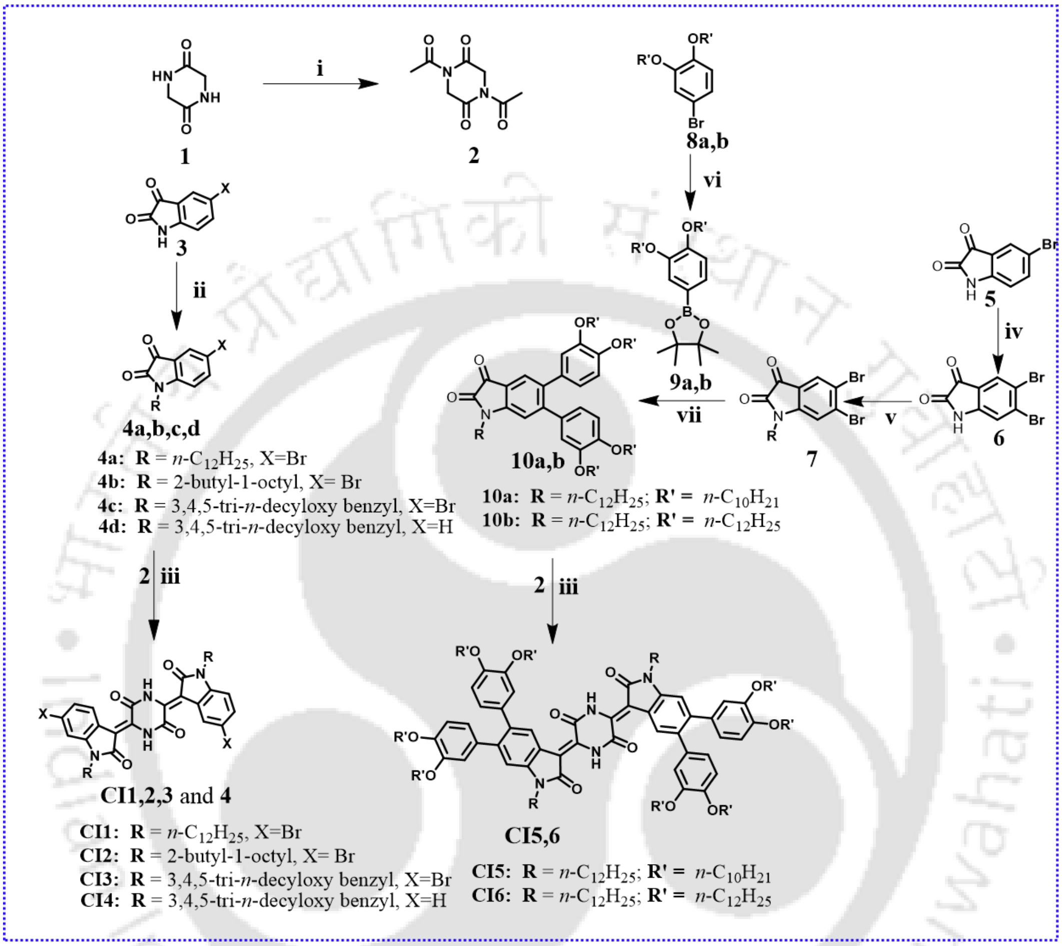

Scheme 2.1. Synthesis of target cyclic dipeptide-isatin hybrid (**CI**); Reagents and Conditions: (i) Acetic anhydride, 130 °C, 24 h, reflux, 55%; (ii) RBr, anhydrous K_2CO_3, DMF, 80 °C, 24 h, 65-70 %; (iii) Et_3N, DMF, 40 °C, 24 h, 60-66%; (iv) NBS, DMF, N_2, 25 °C, 12 h, 40%; (v) RBr, anhydrous K_2CO_3, DMF, 80 °C, N_2 atm, 24 h, 66%; (vi) 1,3,5-Tris(4,4,5,5-tetramethyl-1,3,2-dioxaborolan-2-yl) benzene, $Pd(PPh_3)Cl_2$, KOAc, Toluene ,110 °C, N_2 atm, 24 h, 70-76%; (vii) anhydrous K_2CO_3, Toluene: water, $Pd(PPh_3)_4$, reflux, 18 h, 76-78%.

The target **CI**s (**CI 1-6**) were prepared following a straightforward synthetic pathway (Scheme 2.1). In the first step, 2,5-diketopiperazine was acylated in the presence of acetic anhydride to prepare 1,4-diacetylpiperazine-2,5-dione.[43,44] The *N*-alkylation of compound **3** was carried out via the nucleophilic substitution reaction with different alkyl and benzyl halides in the presence of anhydrous K_2CO_3. Compound **6** was achieved through the Suzuki coupling reaction using the dioxaborolane derivative, $Pd(PPh_3)_4$, as a catalyst in the presence of K_2CO_3 as a base.[45] Finally, the **CI** derivatives were synthesized by a double Knoevenagel condensation reaction of *N*-alkylated isatin derivatives and 1,4-diacetylpiperazine-2,5-dione. The recrystallization of the product using a dichloromethane-methanol mixture yielded a sticky solid with a good yield. All compounds were characterized using standard analytical techniques, including MALDI-TOF mass spectrometry, ^{1}H NMR, ^{13}C NMR, and IR spectroscopy.

2.2.2. Thermal Behavior

The determination of mesomorphism involved complementary techniques. Initially, polarized optical microscopy (POM) with a programmable hot stage was employed to observe optical textures. This method allowed the visualization of linear defects that emerged from the homeotropic domain on cooling from the isotropic state. These structures were then transformed into a mosaic pattern of the columnar rectangular (Col$_r$) phase (Figures 2.5 and 2.6 c). Further, differential scanning calorimetry (DSC) confirmed the transition temperatures and quantified the associated enthalpy changes (Figure 2.5 and Figure A14). Thermogravimetric analysis (TGA) was conducted to assess the thermal stability of **CI**s, which revealed a decomposition onset temperature of 370-390 °C, corresponding to 5 wt.% decomposition (Table 2.1 and Figure 2.4 a).

Furthermore, powder X-ray diffraction (XRD) analyses were conducted to unequivocally assign the symmetry of the columnar phase observed at high and low temperatures. A summarized overview of phase transition temperatures and enthalpy values for all compounds investigated are provided in Table 2.1, Figure 2.5, and Figure A14. The enhanced attractive interactions by extending the aromatic core and the increased fluidity induced by alkyl chains in compounds **CI5** and **CI6** were suggested as contributing factors that realized the liquid crystalline nature compared to compounds **CI1-CI4**.

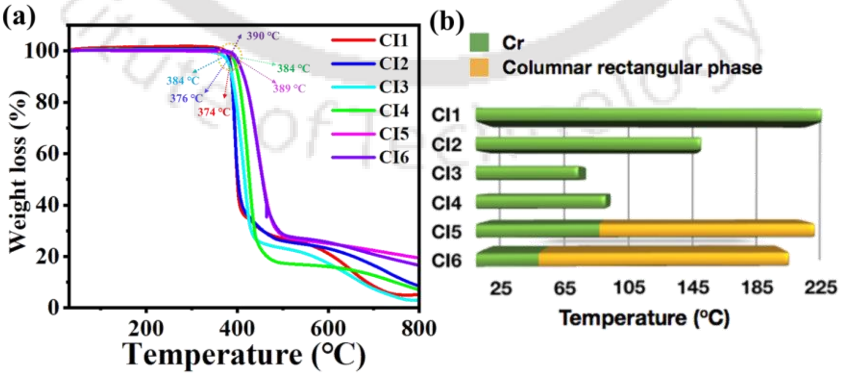

Figure 2.4. (a) TGA plots of compound (heating rate of 10 °C/min, Nitrogen atmosphere). (b) Bargraph representing the mesomorphic behaviors (Considered the first cooling scan of DSC) of **CI** compounds.

Compared to earlier reports, the POM images observed for both compounds at high temperatures showed characteristic textures for columnar phases. However, fluidity was noted with the application of mechanical shear on the samples in the mesophase range.

Table 2.1. Phase transition temperatures (°C), corresponding enthalpies (kJmol^{-1}), and decomposition temperatures were obtained from DSC^{a} and TGA^{b}.

Entry	Phase sequence (kJ/mol)^{a}		T_5^{b} (°C)
	Second Heating	First Cooling	
CI1	Cr 221.2 (32.91) I	I 210.7 (34.97) Cr	374
CI2	Cr 166.2 (45.66) I	I 145.5 (10.35) Cr_2 115.4 (15.21) Cr_1	376
CI3	Cr_1 91.6 (46.81) Cr_2 107.3 (25.43) I	I 79.7 (8.06) Cr	376
CI4	Cr 117.9 (20.95) I	I 94.3 (16.93) Cr	384
CI5	Cr_1 22.7 (10.66) Cr_2 104.8 (3.69) Col_r 211.1 (35.32) I	I 207.1 (39.03) Col_r 90.7 (3.94) Cr_2 21.6 (20.39) Cr_1	389
CI6	Cr_1 37.7 (10.23) Cr_2 71.1 (1.41) Col_r 198 (22.31) I	I 193.1 (22.98) Col_r 58.29 (0.544) Cr_2 23.2 (8.20) Cr_1	390

[a] Peak temperatures in the DSC thermograms obtained during the second heating and first cooling cycles at 5 °C min^{-1}. Col_r = Columnar rectangular phase; I = Isotropic phase. b = Temperature at which 5 wt% decomposition occurred (°C).

During heating and cooling cycles, the DSC thermogram profiles exhibited prominent peaks corresponding to the phase transitions from crystal to columnar phase and columnar to isotropic phase. For example, in the case of compound **CI5**, there is an endothermal transition from one crystalline (Cr_1) phase to another crystalline (Cr_2) phase at ≈ 23 °C (ΔH = 10.6 kJ/mol), followed by another endothermal transition to a mesophase (Col_r) at ≈ 105 °C (ΔH = 3.7 kJ/mol) in the DSC curves (Figure 2.5). During the second heating cycle, a transition from mesophase (Col_r) to isotropic liquid was seen at ≈ 211 °C (ΔH = 35.3 kJ/mol). Upon cooling, exothermic peaks are observed at ≈ 207 °C (ΔH = 39 kJ/mol) and ≈ 91 °C (ΔH = 3.9 kJ/mol), corresponding to transitions from isotropic liquid to mesophase (Col_r) and from mesophase (Col_r) to crystalline phase (Cr_2), respectively. A transition from crystal phase (Cr_2) to crystal phase (Cr_1) is detected at ≈ 21 °C (ΔH = 20.4 kJ/mol). Similar behavior was noticed in the case of **CI6**, containing all dodecyl alkyl chains but with a reduced clearing point due to increased chain length.

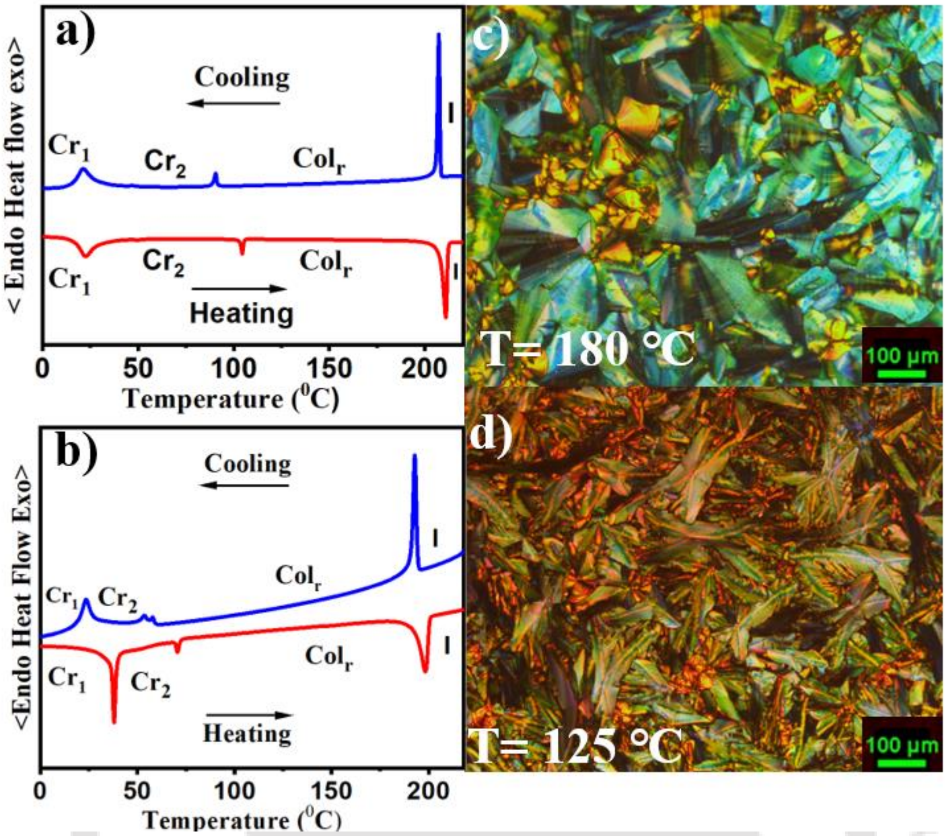

Figure 2.5. DSC thermograms were obtained for (a) **CI5** and (b) **CI6** (blue trace, first cooling scan; red trace, second heating scan). POM images were obtained for the Col$_r$ phase (c) **CI5** at 180 °C, (d) **CI6** at 125°C (scale bar corresponds to 100 µm).

X-ray diffraction studies for compound **CI5** conducted at 180 °C showed several peaks at small angle regions with the *d*-spacings corresponding to the Miller indices (20), (01), (31), (40), (02), (51), (42), (60), (13), (33), (71) and (80), which could be indexed to a columnar rectangular phase with lattice parameters a = 57.4 Å and b = 26.6 Å. (Figure 2.6 a, c, and Table A2.1). In the wide-angle region, a broad halo was observed at 4.54 Å owing to the packing of alkyl and alkoxy chains surrounding the central aromatic core (h_a). A diffused peak with a *d*-spacing of 3.44 Å was observed, corresponding to the core-core interaction (h_c), confirming the close packing of disc-like units of **CI5** in the columnar structure. A similar diffraction pattern was seen at a lower temperature (*i.e.*, at 150 °C), which again could be indexed to a Col$_r$ phase (Figure A15, Table A2.1), similar to the one observed at a higher temperature, with a unit rectangular cell comprising of a single molecule ($Z \approx 1$).[46,47] A model depicting a rectangular columnar arrangement of compound **CI5** at 180 °C is shown in Figure 2.6 c.

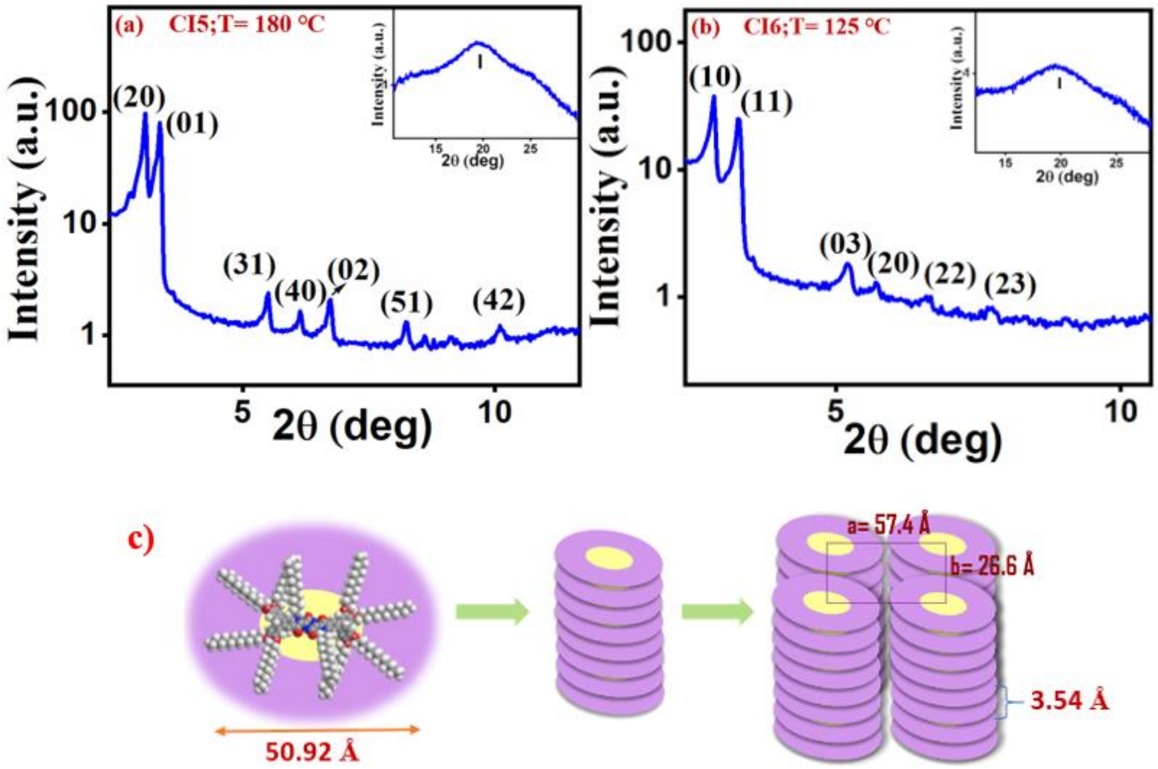

Figure 2.6. X-ray diffractograms for the Col$_r$ phases of (a) **CI5** at 180 °C, (b) **CI6** at 125 °C (insets show the images of the wide-angle region), and (c) the schematic depicting the self-assembly of **CI5** into the Col$_r$ phase at 180 °C.

A similar diffraction pattern was noted in the XRD plots of compound **CI6**; the intensity of core-core peaks was relatively low (Figure 2.6 b). This could result from out-of-plane aromatic rings and overcrowding of the alkyl chains, which is quite commonly found in literature.[48] The XRD patterns obtained at 125 °C and 160 °C suggested stabilizing the Col$_r$ phase in the case of **CI6** (Table A2.1, Figure 2.6 b, Figure A15). The number of molecules forming a disc in a unit rectangular cell at both temperatures was calculated and found to be one ($Z \approx 1$).

2.2.3. Photophysical properties

The absorption and fluorescence characteristics of **CIs** were studied in solution and spin-coated thin films. We have tried to dissolve the compounds in various solvents at a concentration of 1 wt%/vol. Compounds showed good solubility in polar aprotic solvents like chloroform, THF, cyclohexane, and toluene, except ethanol and DMF, where the compounds precipitated. In DMSO, the compounds were insoluble, and precipitation was observed in apolar solvents like hexane, decane, and dodecane. Photophysical studies in solution were carried out with 20 μM chloroform solutions, while 1 wt%/vol. The solution in toluene was used to prepare the thin film. Table 2.2 summarizes the results, while Figures 2.7 and A16–A18 illustrate them. In solution, **CI**s, particularly **CI5** and **CI6**, displayed two distinct absorption features: a prominent band at 464 nm and a shoulder band at 485 nm. The absorption spectra of **CI**s **5** and **6** were consistent with those of other **CI**s, showing a broad absorption band around 485 nm in the more extended wavelength region. This indicates effective charge transfer from electron-donating alkoxy groups to electron-withdrawing imide units, suggesting minimal variation in electronic structure due to substituent differences at the imide nitrogen. Conversely, **CI**s **1-4** showed absorption maxima at 423, 425, and 426 nm, each with a shoulder band at 443, 444, and 446 nm, respectively. The primary peak in the 423-464 nm range is characteristic of the CDP-isatin hybrid core. All **CI**s exhibited high molar extinction coefficients at their absorption peaks (ε: 18,900 to 21,900 $\mathrm{Lmol^{-1}cm^{-1}}$).

The optical band gap for these **CI**s ranged from 2.21 to 2.41 eV, as determined from the red edge of the absorption spectra. The emission spectra were not prominent, likely due to reabsorption by the molecules. The emission spectra of **CI5** showed a single maximum and a shoulder peak at 531 and 581 nm, respectively, with lower intensity, similar to other derivatives with slight positional variations (Figures A17, Table 2.2).

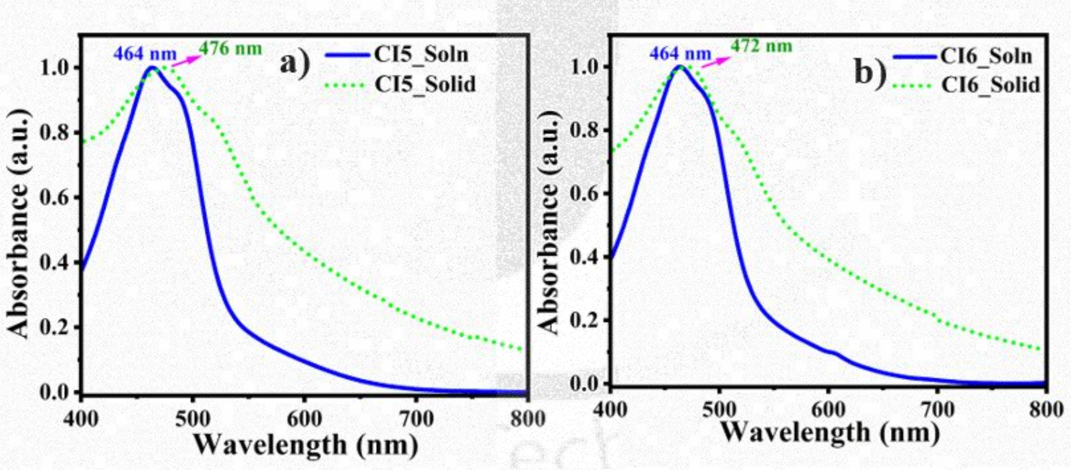

Figure 2.7. Absorption spectra of (a) **CI5** and (b) **CI6** in both solution and thin film states.

CIs generally exhibited low fluorescence in solution, which was further quenched in thin film states (Figure A18). This fluorescence quenching in thin films may be attributed to aggregation-caused quenching (ACQ), typical in organic molecules, due to their planar structure and efficient π-π interactions.[36] Broad absorption bands observed in thin films indicated the formation of excimers (Figure 2.7) [35,36] with a slightly bathochromic shift, suggesting *J*-type or head-to-tail aggregates. Additionally, a red-shifted shoulder peak in the absorption spectra of **CI**s in the thin film could be explained by short-distance charge transfer interactions that facilitate coupling among the π-conjugated aromatic core, enhancing wave function overlap.[49,50]

Table 2.2. Photophysical properties of **CI**s in solution state

Entry	Absorption [nm]	Emission [nm]	Stokes Shift (cm^{-1})	Molar extinction coefficient (ε) ($L\ mol^{-1}\ cm^{-1}$)	$\Delta E_{g,\ opt}$ [eV]
CI1	423, 443	468,531	2273	21625	2.41
CI2	423, 444	469,532	2318	18125	2.40
CI3	425, 446	466,524	2070	18900	2.39
CI4	426, 444	467,534	2061	22450	2.45
CI5	463, 486	531,581	2765	21350	2.32
CI6	464, 487	533,575	2790	21900	2.21

2.2.4. Electrochemical properties

The energy and electron transfer processes, as well as the reversibility of redox reactions, are strongly influenced by the electronic energy levels, particularly the frontier molecular orbitals (HOMO and LUMO levels) of organic semiconductors. These characteristics were examined using cyclic voltammetry (CV) in 0.5 mM solutions of **CI** in anhydrous dichloromethane, with 0.1 M tetrabutylammonium perchlorate (TBAP) as the supporting electrolyte, and a scan rate of 100 mV/s. The results of the electrochemical studies are summarized in Table 2.3. Compounds **CI1**, **CI3**, and **CI5** displayed an irreversible first reduction at -0.95, -1.02, and -1.33 V, respectively. Consequently, the lowest occupied molecular orbital (LUMO) levels of **CI1**, **CI3**, and **CI5** were estimated to be approximately -3.34, -3.28, and -2.97 eV, respectively. Respective highest occupied molecular orbital (HOMO) levels, derived from their optical band gaps ($E_{g,\ opt}$) of 2.41, 2.39, and 2.32 eV, were found to be around -5.75, -5.67, and -5.29 eV, respectively (Table 2.3, Figure 2.8 and Figure A19). In general, this shows that the introduction of more aromatic units in the periphery, as in **CI5**, leads to an increase of HOMO and LUMO levels with a concurrent decrease in the energy gap between the two.

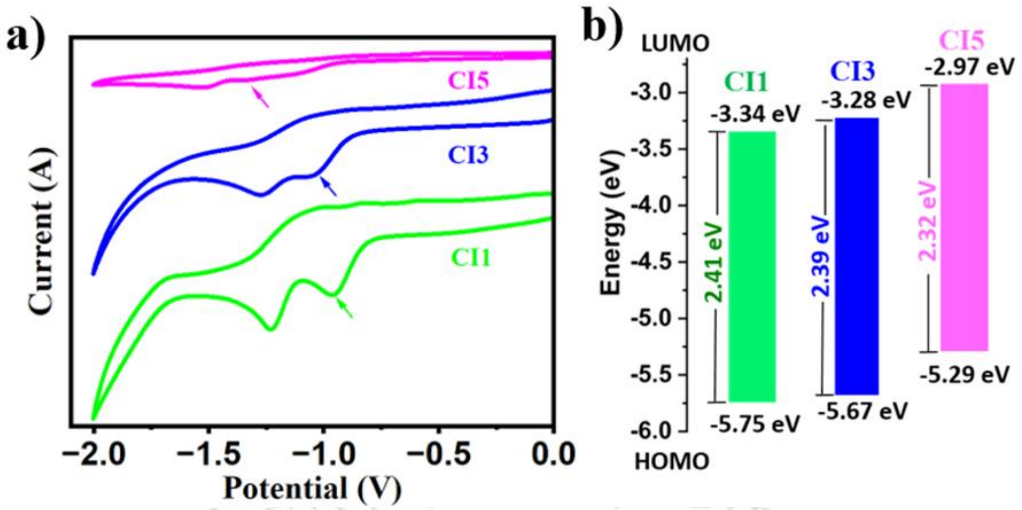

Figure 2.8. (a) Overlay of cyclic voltammograms of **CI** derivatives. (b) Energy band level diagram showing experimental HOMO and LUMO energy levels of **CI** derivatives.

Table 2.3. Electrochemical [a, b] data and data obtained from DFT[h] calculations for compounds **CI1, CI3, CI5**

Electrochemical data					Data from DFT calculation		
Entry	$E_{1st\ red}$[c]	E_{LUMO} [d,e]	E_{HOMO} [d,f]	$\Delta E_{g,\ (opt)}$ [d,g]	E_{LUMO} [d,h]	E_{HOMO} [d,h]	ΔE_g[d,h]
CI1	-0.95	-3.34	-5.75	2.41	-3.29	-5.87	2.57
CI3	-1.02	-3.28	-5.67	2.39	-3.27	-5.81	2.54
CI5	-1.33	-2.97	-5.29	2.32	-2.87	-5.22	2.35

[a] 0.5mM Dichloromethane solutions; [b]experimental conditions: Ag/$AgNO_3$ as reference electrode, glassy carbon working electrode, platinum wire counter electrode, TBAP (0.1M) as a supporting electrolyte, room temperature; [c] in volts (V); [d] in eV; [e] estimated from the formula by using E_{LUMO}= -(4.8 - $E_{1/2,\ Fc/Fc+}$ + $E_{red,\ onset}$) eV; [f] estimated from the formula $E_{HOMO} = E_{LUMO} – E_{(g,\ opt)}$ eV; [g]calculated from the red edge of the absorption band of each compound.$E_{1/2,\ Fc/Fc^+}$ = 0.50 V.[h] Obtained from DFT calculations by employing the combination of Becke3-Lee-Yang-Parr (B3LYP) hybrid functional and 6-31G (d, p) basis set using the Gaussian 09 package.

2.2.5. DFT Studies

Computational studies were carried out in the B3LYP/6-31g (d, p) method using the Gaussian 09 program package to understand the electronic properties and frontier molecular orbital energy level of compound **CI**s. The absence of imaginary frequency ensured the energy-minimized structure of all the compounds.

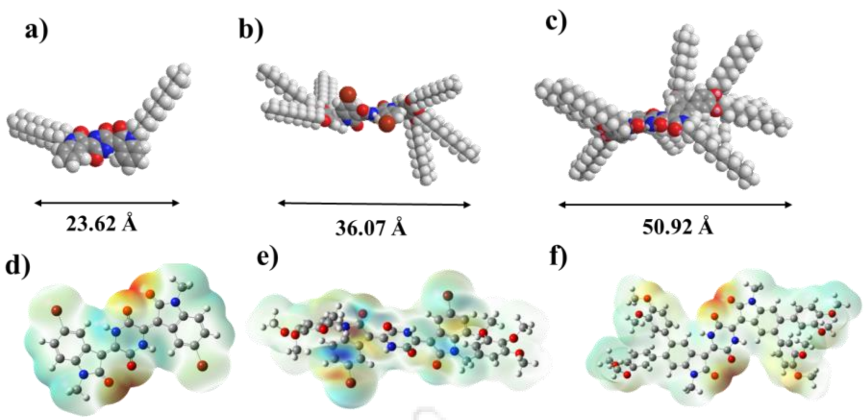

Figure 2.9. Energy minimized molecular model of **CIs** (obtained from Chem3D Ultra) (a) **CI1** (b) **CI3** (c) **CI5**; 3D molecular electrostatic potential contour map of the optimized structure of (d) **CI1**, (e) **CI3**, and (f) **CI5** (In the mapped electro-static potential surface, the red and blue colors refer to the electron-rich and electron-poor regions, respectively, whereas the green color signifies the zero electrostatic potential, chain length is limited to methyl for the sake of computational time).

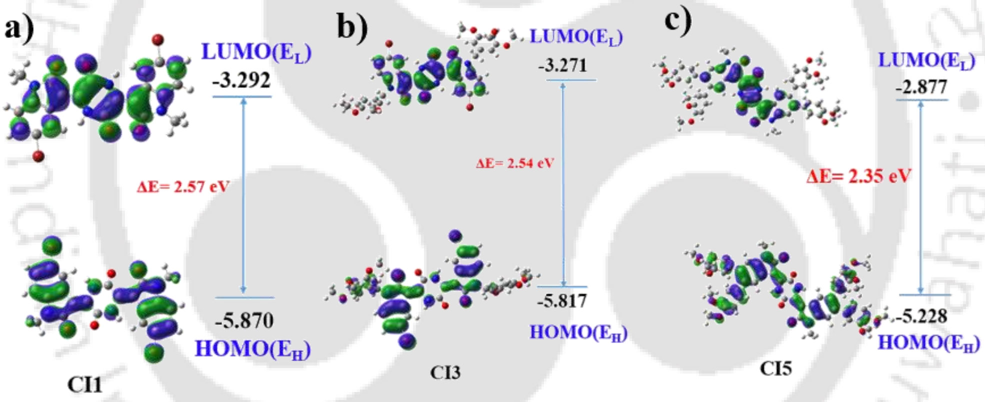

Figure 2.10. Frontier molecular orbitals of compounds (a) **CI1**, (b) **CI2**, and (c) **CI3** obtained from DFT calculations at the B3LYP/6-31G (dp) level; E_H and E_L denote energies of the highest occupied molecular orbital (HOMO) and the lowest unoccupied molecular orbital (LUMO) respectively (Chain length is limited to methyl for the sake of computational time).

In comparison, introducing a tri-*n*-alkoxy benzyl unit at the imide nitrogen in **CI3** decreased the HOMO energy by 0.053 eV, thereby slightly narrowing the HOMO–LUMO gap. However, in **CI5**, due to extended conjugation, the band gap decreased by 0.19 eV compared to **CI3**. As a result, **CI5** exhibits the narrowest HOMO–LUMO gap (2.32 eV) among the three hybrids. These theoretical calculations concord with the experimental data, demonstrating that the band gap decreases by incorporating the aromatic rings decorated with peripheral side chains in the order **CI1** > **CI3** > **CI5**. The optimized molecular diameters of **CI1**, **CI3**, and **CI5** were approximately 23.62 Å, 36.07 Å, and 50.92 Å, respectively, as shown in Figure 2.9. The 3D molecular electrostatic potential (MEP) contour maps display red and blue colors representing negative and positive electrostatic potentials, respectively, with green indicating zero potential. The MEP surfaces highlight electron density concentration around the oxygen atoms of the **CI**, while the central core appears electron deficient (Figures 2.9 and 2.10). Theoretical band gaps for **CI** ranged from 2.57 to 2.35 eV, slightly larger than the optical band gaps but following the same trend as presented in Table 2.3.

2.2.6. Morphology studies

The morphology of the **CI5** compound spin-coated onto ITO-coated glass substrates was analyzed using atomic force microscopy (AFM) and field-emission scanning electron microscopy (FESEM). AFM images indicated a smooth surface with a roughness of 1.362 nm (Figure 2.11 a), while FESEM images showed a uniform surface for **CI5** (Figure 2.11 b). This smooth film formation of **CI5** is a requirement to achieve consistent and reliable results in organic electronic devices.

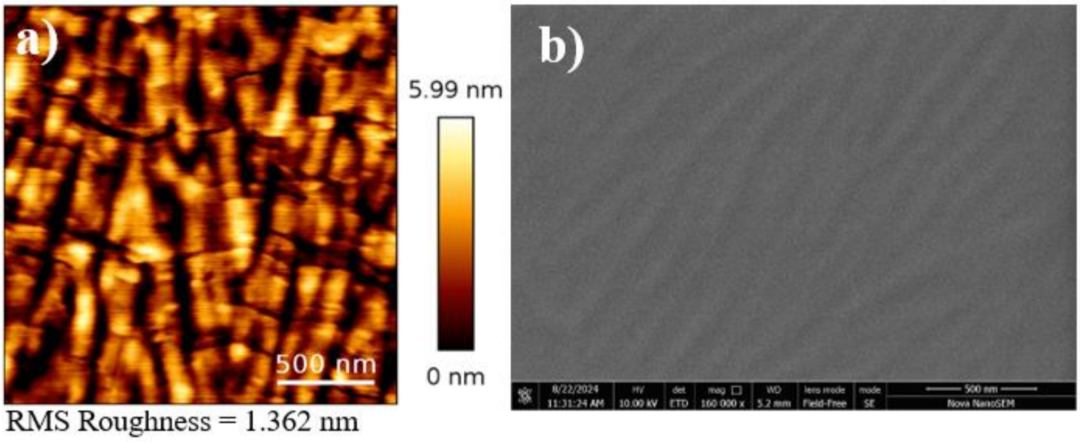

Figure 2.11. (a) The AFM and (b) SEM images of compound **CI5** solution in chlorobenzene were spin-coated on ITO-coated glass substrate, respectively.

2.3. Charge carrier mobility studies

To determine the charge-carrier mobilities of the liquid crystal **CI5**, current density-voltage (J–V) characteristics of the material sandwiched between two electrodes were measured, and the space-charge-limited currents (SCLC) were fitted according to the Mott–Gurney equation (Eq.2.1).

$$J = \frac{9}{8}\varepsilon_0\varepsilon_r\mu\frac{V^2}{L^3} \tag{2.1}$$

where J is the current density, ε_r is the dielectric constant of the compound, ε_0 is the permittivity of free space, μ is the charge carrier mobility, L is the thickness of the compound, and V is the voltage drop across the device. This method estimates the material's charge-carrier mobility in the bulk.

Two distinct SCLC cells, one for measuring hole mobility and another for electron mobility, were fabricated to understand the ambipolar charge transport of the material. Hole-only devices (HOD) were fabricated with an ITO/PEDOT: PSS bottom layer and MoO_3/Ag top layer. In contrast, electron-only devices (EOD) were fabricated with an ITO/ZnO bottom layer and PDINN/Ag top layer. The liquid crystal layer thicknesses of the single-carrier devices were around 130 nm, and the material's dielectric constant calculated from the capacitance–frequency measurement was 5.025. The SCLC data and the corresponding fits according to Equation 2.1 are shown in Figures 2.12 (a) and 2.12 (b), and the device structure is given in Figures 2.12 c & d. The carrier mobility obtained using equation (2.1) is 9.46 $\times 10^{-4}$ $cm^2V^{-1}s^{-1}$ for the hole-only device and 7.88 $\times$ 10^{-4} $cm^2V^{-1}s^{-1}$ for the electron-only device, indicating the ambipolar nature of the material.

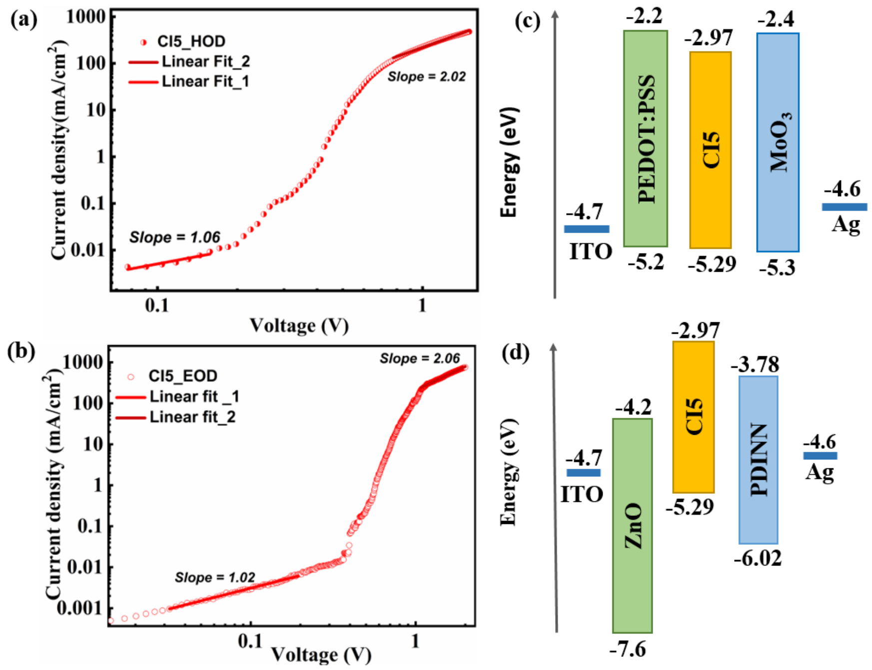

Figure 2.12. J-V characteristics of the (a) hole-only device, (b) electron-only device in the dark. Energy level diagram for the (c) hole-only device, (d) electron-only device.

2.4. Conclusions

In summary, we successfully synthesized six molecular hybrids featuring cyclic dipeptide and isatin moieties and characterized them. Among these molecules, two compounds with more peripheral chains stabilized the liquid crystalline behavior, marking the first such examples in this class of molecules. Further structural aspects of these compounds related to the molecular orientation, frontier molecular orbitals, band gap, and electron density distribution were also analyzed through DFT calculations. All derivatives exhibited high thermal stability and excellent solubility in common organic solvents. Among the six compounds, **CI5** and **CI6** stabilized columnar rectangular liquid-crystalline phase, while the others exhibited crystalline behavior. Photophysical investigations revealed broad absorption spectra with band gap values ranging from approximately 2.21 to 2.41 eV, accompanied by significant Stokes shifts and high molar extinction coefficients. One of these liquid crystalline CDP-isatin-hybrids (**CI5**), investigated with the help of the space charge limited current (SCLC) technique, exhibited hole and electron carrier mobility of 9.46×10^{-4} $cm^2V^{-1}s^{-1}$ and 7.88×10^{-4} $cm^2V^{-1}s^{-1}$ respectively, making it the first example of ambipolar columnar LC in this class of molecules. These findings underscore the potential of this class of solution-processable, self-assembling molecules as ambipolar materials in organic electronic devices.

2.5. Experimental section

This section presents the detailed synthesis procedure and the molecular structural characterization data for the intermediates (2, 8) and target compounds mentioned in the scheme.[43,44,52]

Procedure for synthesis of 4a, b [51]

5-bromoindoline-2,3-dione (0.5 g, 2.1 mmol), 1-bromododecane and or 2-butyl-1-octyl-bromide (0.828 mL, 3.31 mmol), and potassium carbonate (0.917 g, 6.63 mmol) were taken in 50 mL of *N*, *N*-dimethylformamide. This mixture was heated at 80 °C with stirring for 24 h. The reaction mixture was extracted with ethyl acetate (3 × 30 mL), and subsequently, the organic layer was washed with water (twice) and brine. Then, the organic extract was dried over anhydrous Na_2SO_4, and the obtained residue was purified by column chromatography (silica gel, ethyl acetate-hexane 1:9).

4a: R_f = 0.6 (10% EtOAc-Hexane); orange solid, yield: 70 %; IR: ν_{max} in cm^{-1}: 2921, 2856, 1735, 1602, 1464, 1441, 1325, 1259, 1120, 1054, 832, 711. ^1H NMR (600 MHz, $CDCl_3$, ppm):

δ 7.69 (d, *J* = 7.8 Hz, 1H, H_{Ar}), 7.68 (s, 1H, H_{Ar}), 6.81 (d, *J* = 9 Hz, 1H, H_{Ar}), 3.70 (t, *J* = 7.2 Hz, 2H, - NCH_2), 1.67 (m, 2H, -CH_2), 1.33 (bm, 18H, 9×-CH_2), 0.87 (t, *J* = 7.2 Hz, 3H, CH_3). ^{13}C NMR (150 MHz, $CDCl_3$, ppm): δ 182.53, 157.41, 149.78, 140.52, 128.24, 118.76, 116.43, 11.88,40.44, 31.92, 29.61, 29.53, 29.46, 29.35, 29.21, 27,17, 26.87, 22.70, 14.15. MALDI-TOF mass calculated for $C_{20}H_{28}BrNO_2$ (M^+): 393.13, found: 393.421

4b: R_f = 0.5 (10% EtOAc-Hexane); red-orange solid, yield: 75%; IR: ν_{max} in cm^{-1}: 2917, 2849, 1729, 1598, 1466, 1433, 1289, 1121, 841, 707; ^{1}H NMR (600 MHz, $CDCl_3$, ppm): δ 7.66 (d, *J* = 8.4 Hz, 1H, H_{Ar}), 7.62 (s, 1H, H_{Ar}), 6.78 (d, *J* = 8.4 Hz, 1H, H_{Ar}), 3.55 (d, *J* = 7.2 Hz, 2H, -NCH_2), 1.79 (m, 1H, -CH), 1.25 (bm, 16H, 8×-CH_2), 0.84 (m, 6H, 2×-CH_3); ^{13}C NMR (150 MHz, $CDCl_3$, ppm): δ 182.42, 157.71, 150.14, 140.52, 128.03, 118.68, 116.35, 112.17, 44.81, 35.89, 31.74, 31.42, 31.11, 29.59, 28.50, 26.30, 22.99, 22.61, 14.08. MALDI-TOF mass calculated for $C_{20}H_{28}BrNO_2$ (M^+): 393.13, found: 393.421.

Procedure for synthesis of 4c, d [51]

5-bromoindoline-2,3-dione and or indoline-2,3-dione (0.1g, 4.42 mmol), 5-(chloromethyl)-1,2,3-tris(dodecloxy)benzene (0.45g, 6.63 mmol), and potassium carbonate (0.183g, 13.26 mmol) were taken in 30 mL of *N, N*-dimethylformamide. This mixture was heated at 80 °C with stirring for 24 h. The resulting compound was extracted with ethyl acetate (3×30 mL), and subsequently, the organic solution was washed with water (twice) and brine. The organic solutions were dried over anhydrous Na_2SO_4, and the obtained residue was then purified by column chromatography (silica gel, ethyl acetate-hexane 1:9).

4c: R_f = 0.6 (10% EtOAc-Hexane); orange solid, yield: 65%; IR: ν_{max} in cm^{-1}: 2917, 2851,1730,1591,1437,1228, 993, 721; ^{1}H NMR (600 MHz, $CDCl_3$, 25 °C): δ 7.71 (s, 1H, H_{Ar}), 7.59 (d, *J* = 8.4 Hz, 1H, H_{Ar}), 6.7 (d, *J* = 8.4 Hz,1H, H_{Ar}), 6.46 (s, 2H, H_{Ar}), 4.79 (s, 2H, -NCH_2), 3.91 (t, *J* = 6Hz, 6H, 3×-OCH_2) 1.76 (m, 6H, 3×-CH_2), 1.44 (m, 6H, 3×-CH_2), 1.29 (bm, 48H, 24×-CH_2), 0.88 (t, *J* = 9 Hz, 9H, 3×-CH_3).

^{13}C NMR (150 MHz, $CDCl_3$, ppm): δ 183.17, 182.2, 181.13, 156.5, 152.60, 149.80, 148.5, 139.46, 137.20, 128.4, 127.9, 127.08, 124.3, 122.82, 117.7, 115.7, 111.8, 110.1, 105.0, 72.4, 68.30, 43.5, 30.89, 29.26, 28.60, 28.34, 25.0, 21.66,13.09. MALDI-TOF mass calculated for $C_{51}H_{82}BrNO_5$ (M^+): 867.54, found: 867.058.

4d: R_f = 0.67 (10% EtOAc-Hexane); orange solid, yield: 60%; IR: ν_{max} in cm^{-1}: 2917,2851,1730,1591,1437,1337, 1228, 993,721,^{1}H NMR (600 MHz, $CDCl_3$, ppm): δ 7.61 (d, *J* = 6Hz, 1H, H_{Ar}), 7.49 (t, *J* = 7.8 Hz, 1H, H_{Ar}), 7.1 (t, *J* = 7.8 Hz,1H, H_{Ar}), 6.80 (d, *J* = 7.8 Hz, 1H, H_{Ar}), 6.49 (s, 2H, H_{Ar}), 4.8 (s, 2H, $-NCH_2$), 3.92 (t, *J* = 6.6 Hz, 6H, 3×$-OCH_2$), 1.77 (m, 6H,-3×$-CH_2$), 1.44 (m, 6H, 3×CH_2), 1.25 (bm, 48H, 24×$-CH_2$), 0.88 (t, *J* = 9 Hz, 9H, 3×$-CH_3$). ^{13}C NMR (150 MHz, $CDCl_3$, ppm): δ 182.4, 157.37, 152.3, 149.91, 135.13, 128.5, 124.4, 122.9, 116.7, 110.2, 104.3, 72.0, 68.30, 64.7, 43.4, 31.01, 29.3, 28.7, 28.4, 25.1, 21.7,13.20. MALDI-TOF mass calculated for $C_{51}H_{83}NO_5$ (M^+): 789.63, found: 789.621.

Procedure for synthesis of 9a, b [53]

A mixture of compound 8 (1.06 mmol, 1 eq.), bis(pinacolato) diboran (2.12 mmol, 2 eq.), KOAc (12.77 mmol, 12 eq.) and Pd $(PPh_3)Cl_2$ (0.10 mmol, 1 eq.) in toluene (40 mL) was degassed by gently bubbling N_2 for 20 min. The mixture was heated at 110 °C for 36 h. After cooling, it was extracted with Ethyl Acetate (100 mL × 3). The combined organic layer was washed with water (100 mL) and brine solution (100 mL). The combined organic extracts were dried over anhydrous Na_2SO_4, and the obtained residue was then purified by column chromatography (silica gel, ethyl acetate-hexane 2:8).

9a: R_f = 0.6 (10% EtOAc-Hexane); white solid, yield: 70%; IR: ν_{max} in cm^{-1}: 2918, 2851, 1601, 1511, 1350, 1136, 964, 688; ^{1}H NMR (600 MHz, $CDCl_3$, ppm): δ 7.40 (d, *J* = 7.8, 1H, H_{Ar}), 7.31 (s, 1H, H_{Ar}), 6.8 (d, *J* = 6 Hz,1H, H_{Ar}), 4.04 (m, 4H, 2×$-OCH_2$) 1.83 (m, 4H, 2×$-CH_2$), 1.47 (m, 4H, 2×$-CH_2$), 1.36 (bm, 36H, 12×$-CH_2$, 4×$-CH_3$), 0.90 (t, *J* = 6 Hz, 6H, 2×$-CH_3$).^{13}C NMR (150 MHz, $CDCl_3$, ppm): δ 150.93, 147.40, 133.70, 127.60, 126.64, 118.40, 111.69, 82.50, 68.21, 67.84, 30.89, 28.62, 28.59, 28.57, 28.55, 28.42, 28.39, 28.33, 28.32, 28.17, 25.04, 24.98, 23.82, 21.66, 13.07.MALDI-TOF mass calculated for $C_{32}H_{57}BO_4$ $(M+H)^+$: 517.44, found: 517.813.

9b: R_f = 0.67 (10% EtOAc-Hexane); white solid, yield: 76%; IR: ν_{max} in cm^{-1}: 2919, 2850, 1608, 1515, 1350, 1156, 964, 688; ^{1}H NMR (600 MHz, $CDCl_3$, ppm): δ 7.39 (d, *J* = 7.8, 1H, H_{Ar}), 7.30 (s, 1H, H_{Ar}), 6.88 (d, *J* = 7.8 Hz,1H, H_{Ar}), 4.04 (m, 4H, 2×$-OCH_2$), 1.83 (m, 4H, 2×$-CH_2$), 1.47 (m, 4H, 2×$-CH_2$), 1.30 (bm, 44H, 16×$-CH_2$, 4×$-CH_3$), 0.90 (t, *J* = 6 Hz, 6H, 2×$-CH_3$).^{13}C NMR (150 MHz, $CDCl_3$, ppm): δ 152.16, 148.71, 128.85, 119.62, 112.89, 83.76, 69.07, 32.16, 29.88, 29.85, 29.68, 29.64, 29.60, 29.41, 26.29, 26.23, 25.06, 22.92, 14.34.MALDI-TOF mass calculated for $C_{36}H_{65}BO_4Na$ $(M+Na)^+$: 595.49, found: 595.742.

Procedure for synthesis of 6 [54]

Compound 5 (4.3 mmol,1 eq.) in *N*, *N*-dimethylformamide (10 mL), and NBS (6.45 mmol, 1.5 eq.) were added to a solution of the compound. The resulting reaction mixture was stirred at 25 °C for 12 h. After the reaction, the mixture was diluted with water (20 mL), the resultant precipitate was filtered, and the precipitate was dried in vacuo. The crude product was directly used for the next step.

Procedure for synthesis of 7 [54]

5,6-bromoindoline-2,3-dione (6), (0.5 g, 1.64 mmol), 1-bromododecane (0.6 mL, 2.46 mmol), and anhydrous potassium carbonate (0.681 g, 4.92 mmol) were taken in 10 mL of *N*, *N*-dimethylformamide. This mixture was heated at 80 °C with stirring for 24 h. The reaction mixture was extracted with ethyl acetate (3×30 mL), and subsequently, the organic layer was washed with water (twice) and brine. Then, the organic extract was dried over anhydrous Na_2SO_4, and the obtained residue was purified by column chromatography (silica gel, ethyl acetate-hexane 1:9).

7: R_f = 0.65 (10% EtOAc-Hexane); red-orange solid, yield: 66%; IR: ν_{max} in cm^{-1}: 2925, 2859, 1734, 1608, 1545, 1468, 1441, 1320, 1259, 1120, 1057, 832, 708; ^{1}H NMR (600 MHz, $CDCl_3$, ppm): δ 7.85(s, 1H, H_{Ar}), 7.66 (s, 1H, H_{Ar}), 4.10 (t, *J* = 7.8 Hz, 2H, -NCH_2), 1.71 (m, 2H, -CH_2), 1.36 (bm, 18H, 9×-CH_2), 0.88 (t, *J* = 7.2 Hz, 3H, CH_3). ^{13}C NMR (150 MHz, $CDCl_3$, ppm): δ 180.4, 156.58, 145.62, 143.85, 126.13, 120.03, 115.42, 103.4, 40.27, 30.58, 28.29, 25.14, 21.37, 12.81. MALDI-TOF mass calculated for $C_{20}H_{27}Br_2NO_2$ (M^+): 471.04, found: 471.040.

Procedure for synthesis of 10a, b [45]

A mixture of compound **9a** and or **9b** (0.34 mmol, 2 eq.), 5,6-dibromo-1-dodecylindoline-2,3-dione (0.158 mmol, 1 eq.), 2M K_2CO_3 (aq.) (10.5 ml, 6.33 mmol), and $Pd(PPh_3)_4$ (0.006 mmol, 0.042 eq.) in toluene (52.5 mL) was degassed by gently bubbling N_2 for 30 min. The mixture was heated at 110 °C for 24 h. The reaction mixture was extracted with ethyl acetate (3×30 mL), and subsequently, the organic layer was washed with water (twice) and brine. Then, the organic extract was dried over anhydrous Na_2SO_4, and the obtained residue was purified by column chromatography (silica gel, ethyl acetate-hexane 1:9).

10a: R_f = 0.65 (10% EtOAc-Hexane); reddish brown color color solid, yield: 78 %; IR: ν_{max} in cm^{-1}: 2919, 2851, 1721, 1594, 1513, 1463, 1248, 1136, 1069, 850, 722, 655; ^{1}H NMR (600 MHz, $CDCl_3$, ppm): δ 7.80 (d, *J* = 3Hz, 1H, H_{Ar}), 7.56 (d, *J* = 3Hz, 1H, H_{Ar}), 7.07 (m, 2H, H_{Ar}), 6.93 (m, 4H, H_{Ar}), 4.06 (m, 8H, 4×-OCH_2) 3.4 (m, 2H, -NCH_2), 1.87 (m, 8H, 4×-CH_2) 1.53 (m, 8H, 4×-CH_2) 1.35 (bm, 68 H, 34×-CH_2), 0.88 (m, 15H, 5×-CH_3). ^{13}C NMR (150 MHz, $CDCl_3$, ppm): δ 184.35, 149.60, 149.43, 148.8, 146.0,139.5, 136.4, 131.42, 129.83, 127.67, 122.41, 121.9, 119.53, 119.08, 115.09, 114.04, 133.28, 112.27, 69.59, 69.51, 69.36, 41.96, 41.36, 36.08, 34.67, 34.53, 31.92, 31.60, 29.67, 29.64, 29.59, 29.44, 29.36, 29.31, 26.05, 25.28, 22.70, 22.66, 22.62, 20.70, 20.45, 18.76, 14.32, 14.11,11.43. MALDI-TOF mass calculated for $C_{72}H_{117}NO_6Na$ (M^+): 1091.89, found: 1091.041.

10b: R_f = 0.66 (10% EtOAc-Hexane); reddish brown color solid, yield: 76 %; IR: ν_{max} in cm^{-1}: 2920, 2852, 1734, 1594, 1464, 1349, 1139, 1066, 796, 722, 457; ^{1}H NMR (600 MHz, $CDCl_3$, ppm): δ 7.79 (d, *J* = 2Hz, 1H, H_{Ar}), 7.57 (d, *J* = 2Hz, 1H, H_{Ar}), 7.04 (m, 2H, H_{Ar}), 6.90 (m, 4H, H_{Ar}), 4.04 (m, 8H, 4×-OCH_2) 3.45 (m, 2H, -NCH_2), 1.85 (m, 8H, 4×-CH_2) 1.49 (m, 8H, 4×-CH_2) 1.3 (bm, 84 H, 42×-CH_2), 0.88 (m, 15H, 5×-CH_3). ^{13}C NMR (150 MHz, $CDCl_3$, ppm): δ 184.3, 159.65, 149.55, 148.79, 146.04, 139.52, 136.43, 131.3, 129.8, 127.6, 122.3, 121.9, 119.5, 119.04, 115.0, 113.9, 113.19, 112.16, 111.91, 110.88, 68.02, 40.18, 30.68, 28.42, 28.12, 26.76, 25.29, 24.79, 21.44,12.87. MALDI-TOF mass calculated for $C_{80}H_{133}NO_6$ (M^+): 1204.21, found: 1204.651.l,

General procedures for the synthesis of CIs [44]

1,4-diacetylpiperazine-2,5-dione (1eq.), compound 4a-d, and 10a, b (2.2 eq.), and triethyl amine (0.404 mmol, 4 eq.) were taken in a round bottom flask. The mixture was heated at 40 °C for 24 h. After cooling, the reaction mixture was filtered. The precipitate was washed with EtOH, and further purification was done by recrystallization from dichloromethane-methanol.

CI1: R_f = 0.5 (10% EtOAc-Hexane); dark purple color solid, yield: 65 %; IR: ν_{max} in cm^{-1}: 3126, 2917, 2849, 1704, 1654, 1614, 1465, 1428, 1320, 805, 676; ^{1}H NMR (600 MHz, $CDCl_3$, ppm): δ 13.42 (s, 2H, -NH_{CDP}), 9.06 (s, 2H, H_{Ar}), 7.43 (d, 9.6 Hz, 2H, H_{Ar}) 6.75 (d, *J* = 9.6 Hz, 2H, H_{Ar}), 3.80 (t, *J* = 8.4 Hz, 4H, -NCH_2);1.68 (m, 4H, -CH_2), 1.33 (bm, 36H, 18 × -CH_2), 0.88 (t, *J* = 6Hz, 6H, 2×-CH_3).^{13}C(150MHz, $CDCl_3$, 25 °C): δ 169.04, 155.89, 141.06, 132.85, 121.76, 115.78, 109.77, 40.19, 31.92, 29.62, 29.56, 29.48, 29.35,29.24, 27.45,26.91, 22.69, 14.12. MALDI-TOF mass calculated for $C_{44}H_{58}Br_2N_4O_4$ (M^+): 864.28, found: 864.699.

CI2: R_f = 0.5 (10% EtOAc-Hexane); dark purple color solid, yield: 63 %; IR: ν_{max} in cm^{-1}: 3122, 2956, 2921, 2854, 1707, 1648, 1454, 1430, 1316,800, 677; ^{1}H NMR (600 MHz, $CDCl_3$, 25 °C): δ 13.46 (s, 2H, $-NH_{CDP}$), 9.07 (s, 2H, H_{Ar}), 7.44 (m, 2H, H_{Ar}), 6.73 (d, *J* = 8.4Hz, 2H, H_{Ar}), 3.68 (d, *J* = 7.2Hz, 4H, $-NCH_2$); 1.86 (s, 2H, -CH), 1.35 (bm, 32H, 16×$-CH_2$), 0.89 (m, 12H, 4×$-CH_3$). ^{13}C NMR (150 MHz, $CDCl_3$, ppm): δ 168.37, 154.8, 140.44, 132.37, 131.77,130.36 ,120.70, 114.73, 108.91, 43.59, 35.26, 30.76, 30.54, 30.21, 28.61, 27.57, 25.39, 22.0, 21.6, 13.04. MALDI-TOF mass calculated for $C_{44}H_{58}Br_2N_4O_4$ (M^+): 864.28, found: 864.087.

CI3: R_f = 0.5 (10% EtOAc-Hexane); dark brown color solid, yield: 66 %; IR: ν_{max} in cm^{-1}: 3126, 2918, 2850, 1701, 1652, 1466, 1433, 1329, 804, 678; ^{1}H NMR (600 MHz, $CDCl_3$, ppm): δ 13.45 (s, 2H, $-NH_{CDP}$), 9.10 (s, 2H, H_{Ar}), 7.38 (d, *J* = 7.2 Hz, 2H, H_{Ar}), 6.71 (d, *J* = 8.4 Hz, 2H, H_{Ar}), 6.44 (s, 4H, H_{Ar}) 4.90 (s, 4H, 2×- NCH_2), 3.90 (m, 12H, 6×$-OCH_2$); 1.77 (m, 12H, 6×$-CH_2$), 1.43 (m, 12H, 6×$-CH_2$), 1.28 (bm, 96H, 48×$-CH_2$) 0.88 (t, *J* = 6Hz, 18H, 6×$-CH_3$). ^{13}C (150MHz, $CDCl_3$, 25 °C): δ 169.31, 156.20, 153.94, 141.04, 138.29, 13.49, 132.99, 131.40, 129.37, 121.74, 116.24, 110.73, 109.58, 106.17, 73.10, 69.19, 44.19, 32.0, 30.32, 29.75, 29.38, 26.08, 22.75, 14.12. MALDI-TOF mass calculated for $C_{106}H_{166}Br_2N_4O_{10}Na$ $(M+Na)^+$: 1836.09, found: 1836.267.

CI4: R_f = 0.49 (10% EtOAc-Hexane); dark brown color solid, yield: 68 %; IR: ν_{max} in cm^{-1}: 3121, 2917, 2849, 1696,1647, 1613, 1467, 1440, 1382,843, 689: ^{1}H NMR (600 MHz, $CDCl_3$, ppm): δ 13.45 (s, 2H, $-NH_{CDP}$), 8.94 (d, *J* = 7.8 Hz, 2H, H_{Ar}), 7.13 (t, *J* = 7.2 Hz, 3H, H_{Ar}), 6.85 (d, *J* = 7.8 Hz, 3H, H_{Ar}), 6.48 (s, 4H, H_{Ar}) 4.92 (s, 4H, 2×- NCH_2), 3.90 (m, 12H, 6×-OCH_2); 2.17 (s, 6H, 3×$-CH_2$), 1.73 (m,12H, 6×$-CH_2$), 1.42 (m,12H, 6×$-CH_2$), 1.28 (bm, 90H, 45×$-CH_2$) 0.87 (t, *J* = 7.2 Hz, 18H, 6×$-CH_3$).^{13}C(150MHz, $CDCl_3$, 25 °C): δ 168.78, 155.22, 152.52, 141.11, 137.05, 131.98, 129.45,129.31,127.88, 122.28, 119.15, 109.73, 108.29, 105.10, 72.48, 68.32, 43.07, 30.97, 2879, 28.69, 28.65,28.50, 28.44, 28.42, 25.15, 21.74, 13.16. MALDI-TOF mass calculated for $C_{106}H_{168}N_4O_{10}$ (M^+): 1657.28, found: 1657.111.

CI5: R_f = 0.5 (10% EtOAc-Hexane); dark brown color solid, yield: 62 %; IR: ν_{max} in cm^{-1}: 2919, 2851, 1694, 1642, 1606, 1464, 1312, 839, 714; ^{1}H NMR (600 MHz, $CDCl_3$, ppm): δ 13.64 (s, 2H, 2×- NH_{CDP}), 9.31 (s, 2H, H_{Ar}), 7.34 (s, 2H, H_{Ar}), 7.18 (m, 4H, H_{Ar}), 6.93 (d, *J* = 8.4 Hz, 8H, H_{Ar}), 4.0 (m, 16 H, 8 ×$-OCH_2$), 3.49 (m, 4H, 2×- NCH_2), 1.87 (m, 16H, 8×$-CH_2$), 1.59 (s, 8H, 4×$-CH_2$), 1.50 (m, 16H, 8×$-CH_2$), 1.27 (bm, 128H, 64 ×$-CH_2$), 0.87 (m, 30H, 10×-CH_3). ^{13}C (150MHz, $CDCl_3$, 25 °C): δ 169.66, 155.20, 148.39, 147.90, 147.90, 147.63, 136.65, 133.84, 132.33, 133.02, 130.89, 130.51, 124.88, 124.47, 121.11, 120.87, 118.14, 114.41, 113.23, 112.26, 114. 42, 109. 68, 68.50, 68.37, 40.91, 30.92, 28.71, 28.67, 28.62, 28.57, 28.49, 28.46, 28.41, 28.36, 25.08, 25.06, 21.28, 13.10. MALDI-TOF mass calculated for $C_{148}H_{236}N_{4}O_{12}$ (M^{+}): 2261.80, found: 2261.408.

CI6: R_{f} = 0.56 (10% EtOAc-Hexane); dark brown color solid, yield: 64 %; IR: ν_{max} in cm^{-1}: 2918, 2850, 1694, 1601, 1642, 1465, 1313, 840, 714; ^{1}H NMR (600 MHz, $CDCl_{3}$, ppm): δ 13.65 (s, 2H, 2×- NH_{CDP}), 9.31 (s, 2H, H_{Ar}), 7.34 (s, 2H, H_{Ar}), 7.19 (d, J = 12 Hz, 4H, H_{Ar}), 6.94 (d, J = 9Hz, 8H, H_{Ar}), 4.07 (m, 16 H, 8 ×-OCH_{2}), 3.47 (d, J = 4Hz, 4H, 2×- NCH_{2}), 1.84 (m, 16H, 8×-CH_{2}), 1.55 (m, 16H, 8×-CH_{2}), 1.27 (bm, 168H, 84×-CH_{2}), 0.88 (m, 30H, 10×-CH_{3}). ^{13}C (150MHz, $CDCl_{3}$, 25 °C): δ 170.68, 156.24, 149.40, 148.91, 148.65, 137.68, 134.88, 133.35, 133.35, 133.05, 131.93, 131.52, 125.92, 125.50, 122.13, 110.72, 69.52, 69.39, 41.94, 31.96, 31.95, 29.76, 29.70, 29.69, 29.54, 29.43, 29.41, 22.72, 14.4. MALDI-TOF mass calculated for $C_{164}H_{268}N_{4}O_{12}Na$ ($M+Na$)$^{+}$: 2509.04, found: 2509.940.

2.6. Appendix

2.6.1. NMR Spectra

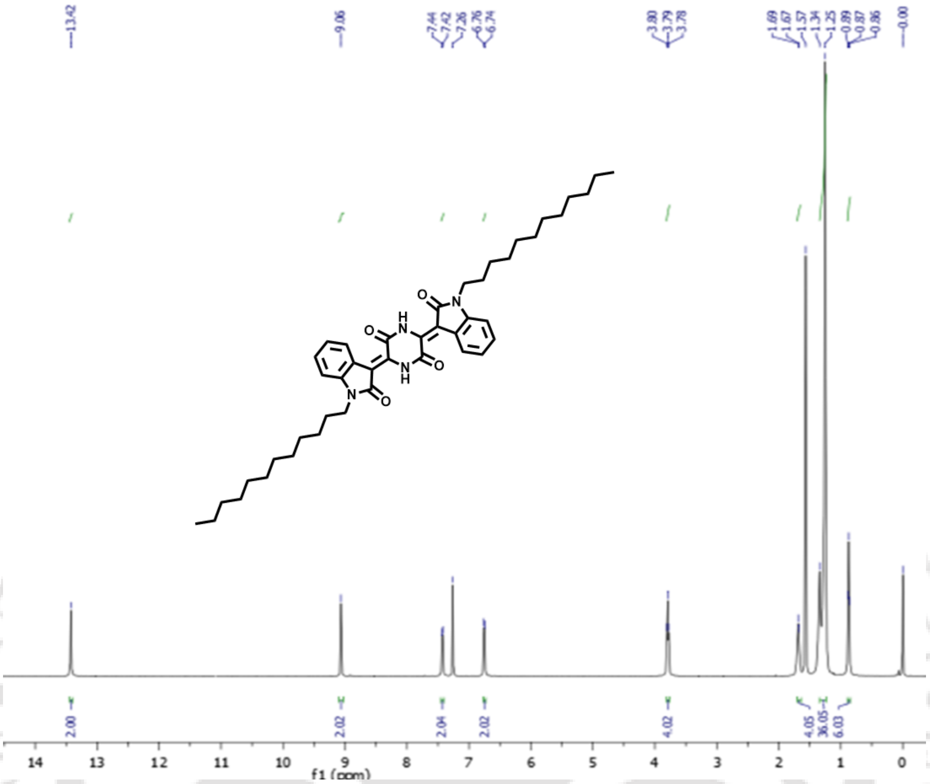

Figure A1. ^{1}H NMR (600 MHz) spectra of **CI1** in $CDCl_3$.

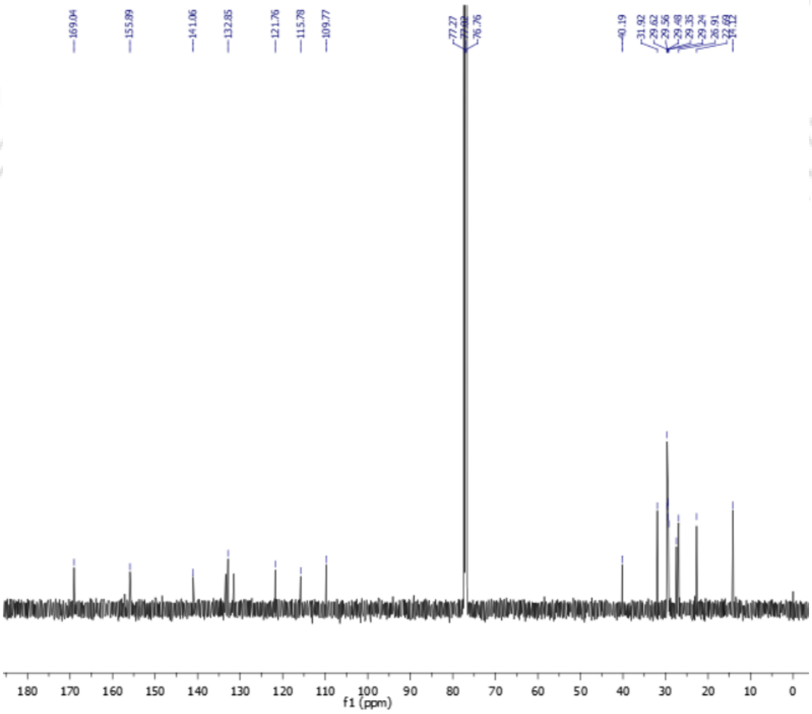

Figure A2. ^{13}C NMR (150 MHz) spectra of **CI1** in $CDCl_3$.

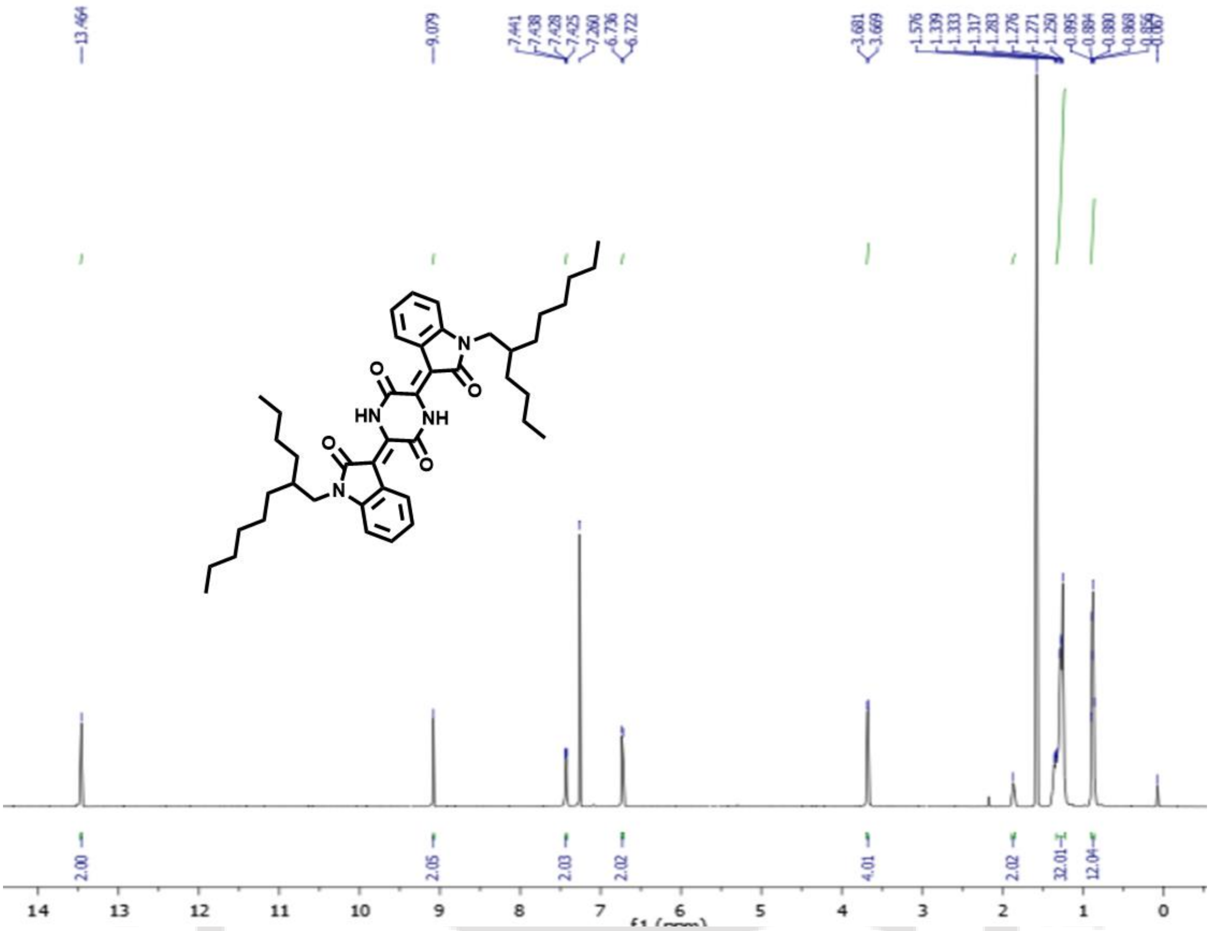

Figure A3. ^{1}H NMR (600 MHz) spectra of **CI2** in $CDCl_3$.

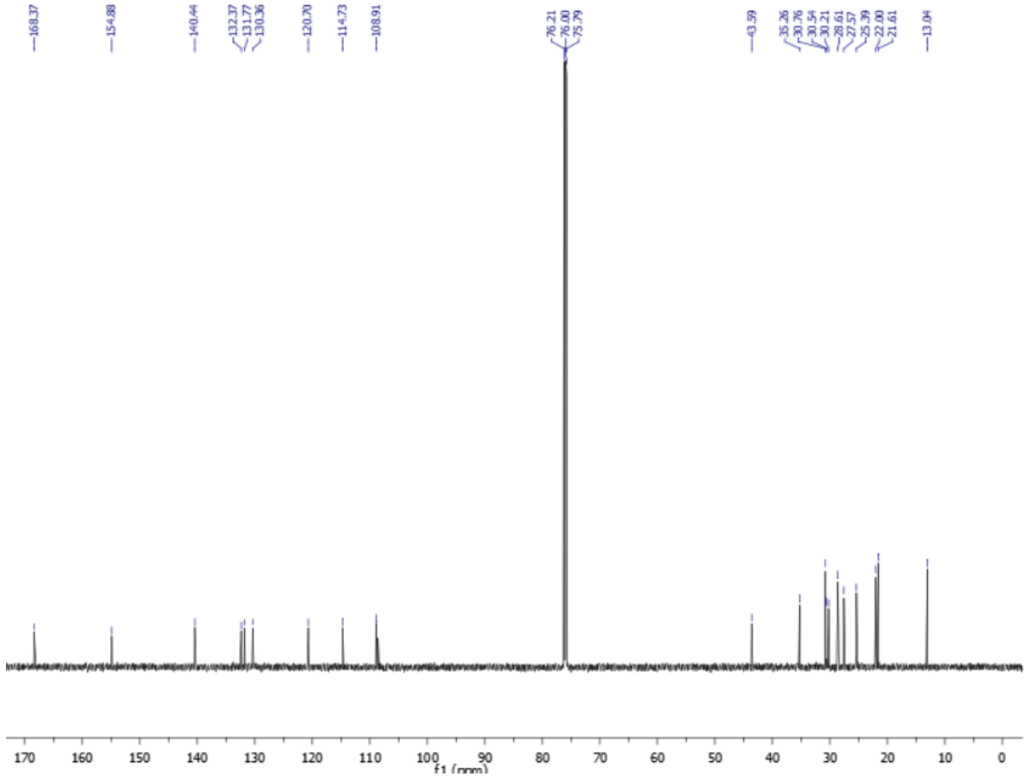

Figure A4. ^{13}C NMR (150 MHz) spectra of **CI2** in $CDCl_3$.

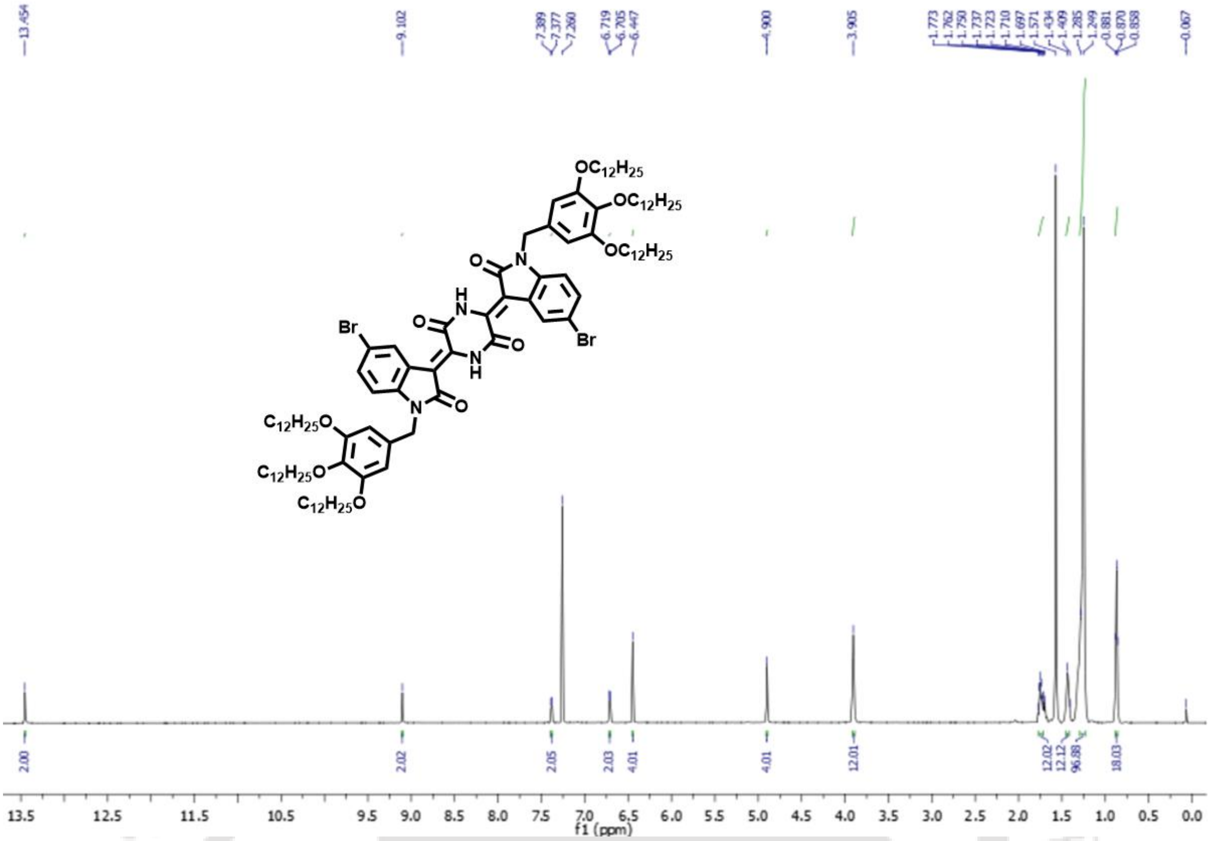

Figure A5. ^{1}H NMR (600 MHz) spectra of **CI3** in CDCl$_3$.

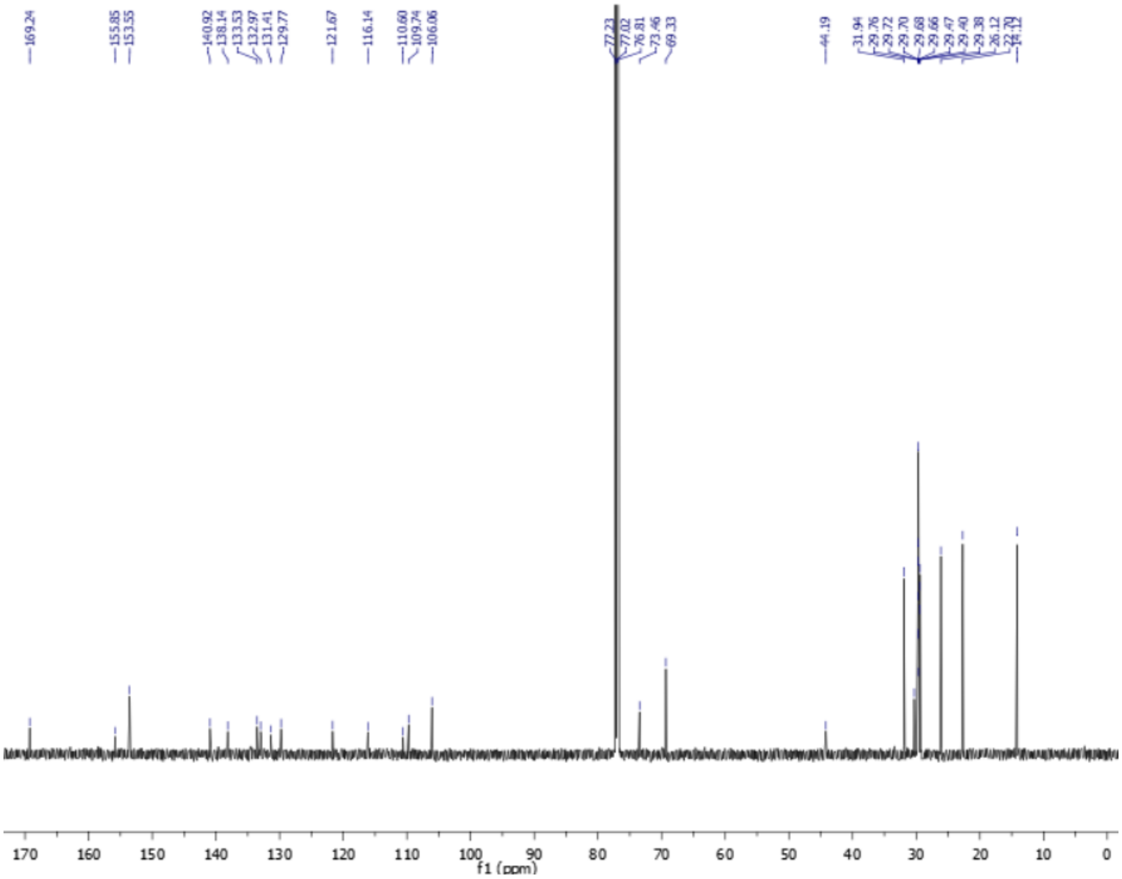

Figure A6. ^{13}C NMR (150 MHz) spectra of **CI3** in CDCl$_3$.

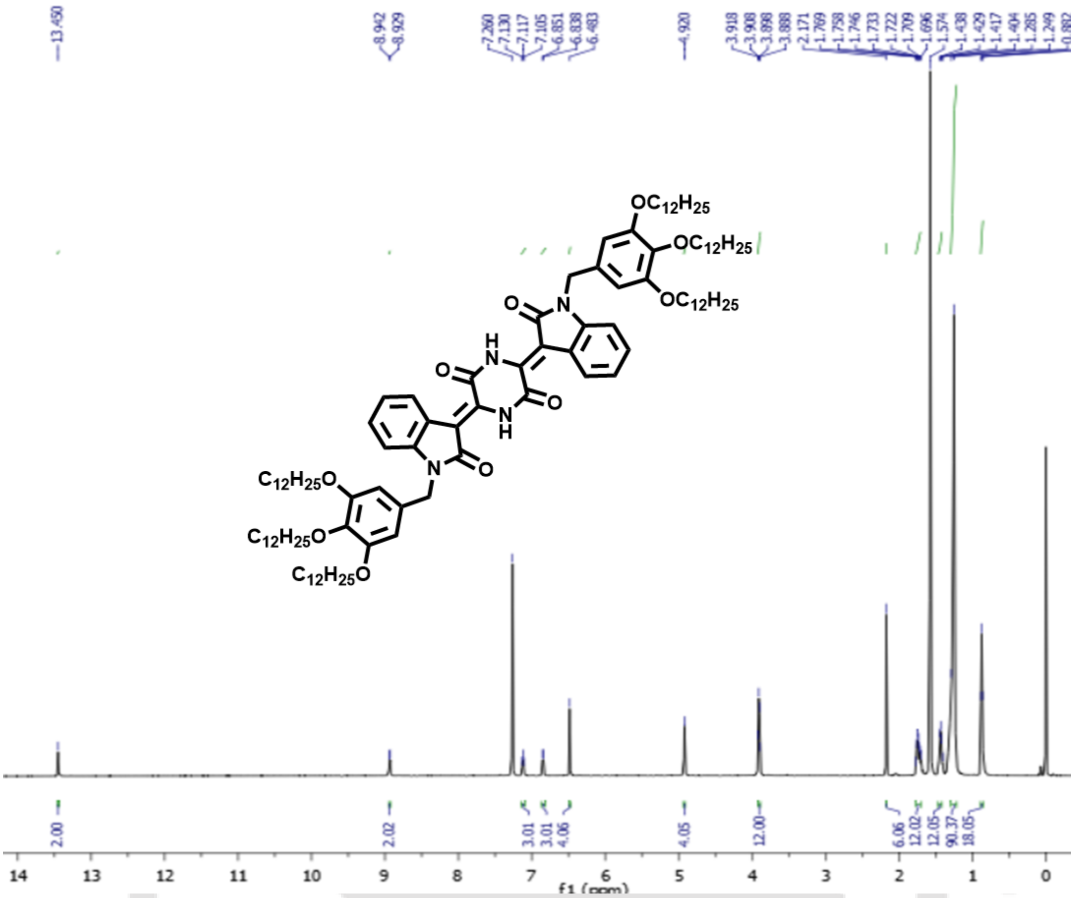

Figure A7. ^{1}H NMR (600 MHz) spectra of **CI4** in CDCl$_3$.

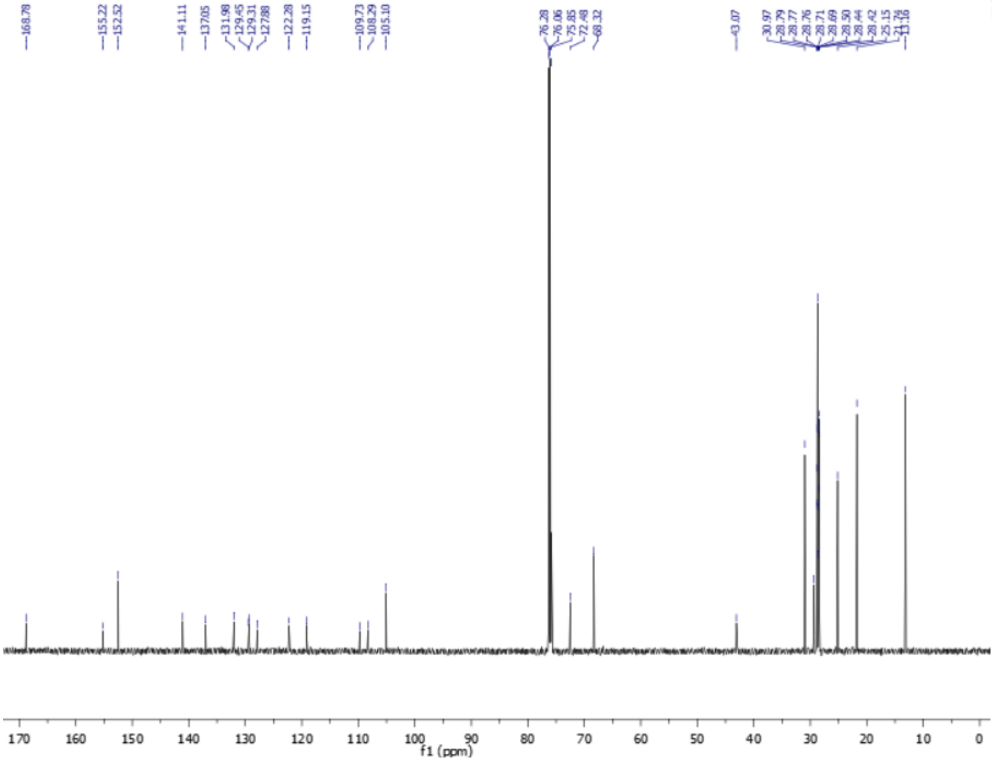

Figure A8. ^{13}C NMR (150 MHz) spectra of **CI4** in CDCl$_3$.

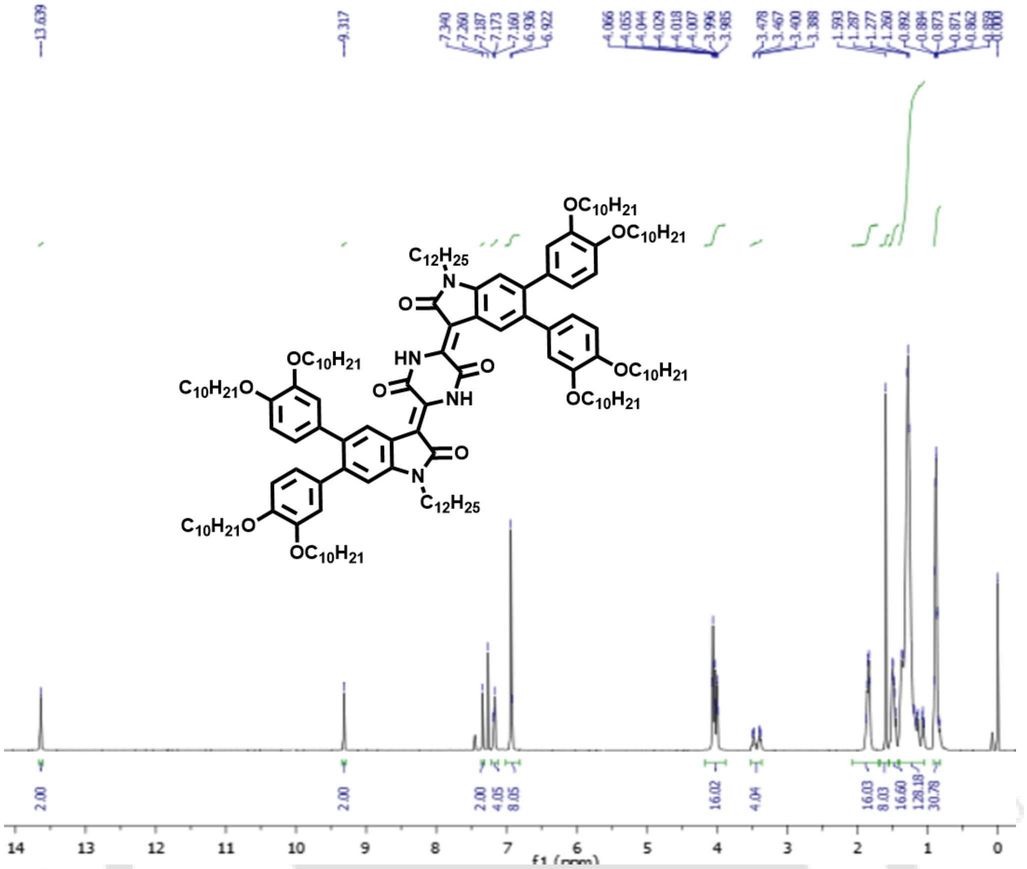

Figure A9. ^{1}H NMR (600 MHz) spectra of **CI5** in $CDCl_3$.

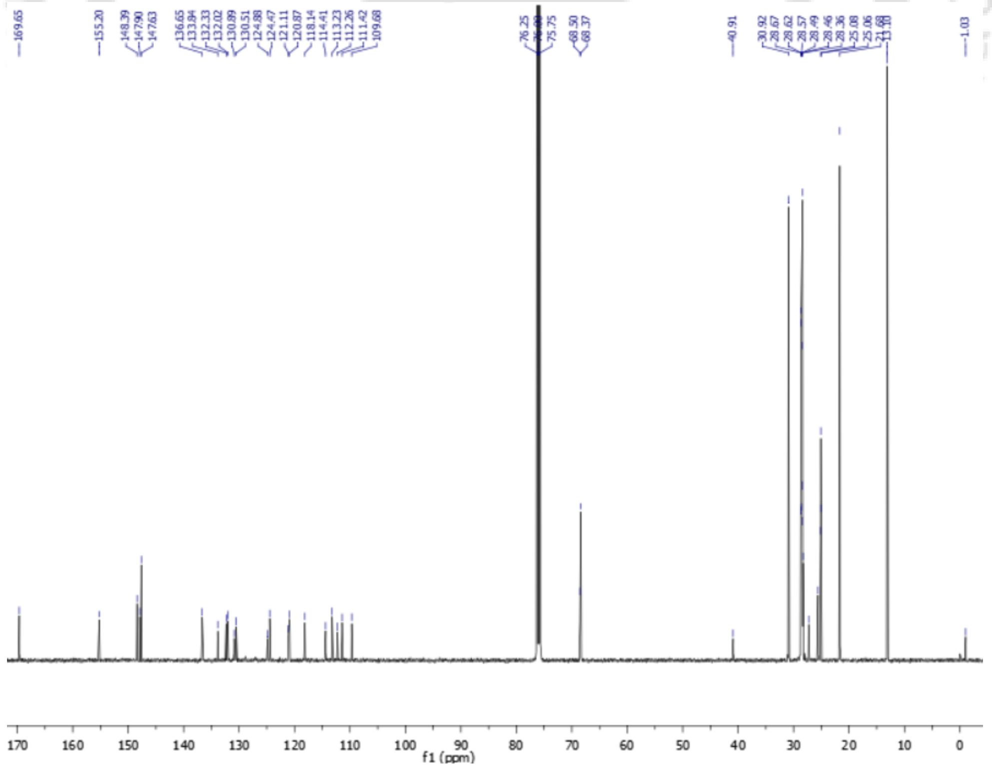

Figure A10. ^{13}C NMR (150 MHz) spectra of **CI5** in $CDCl_3$.

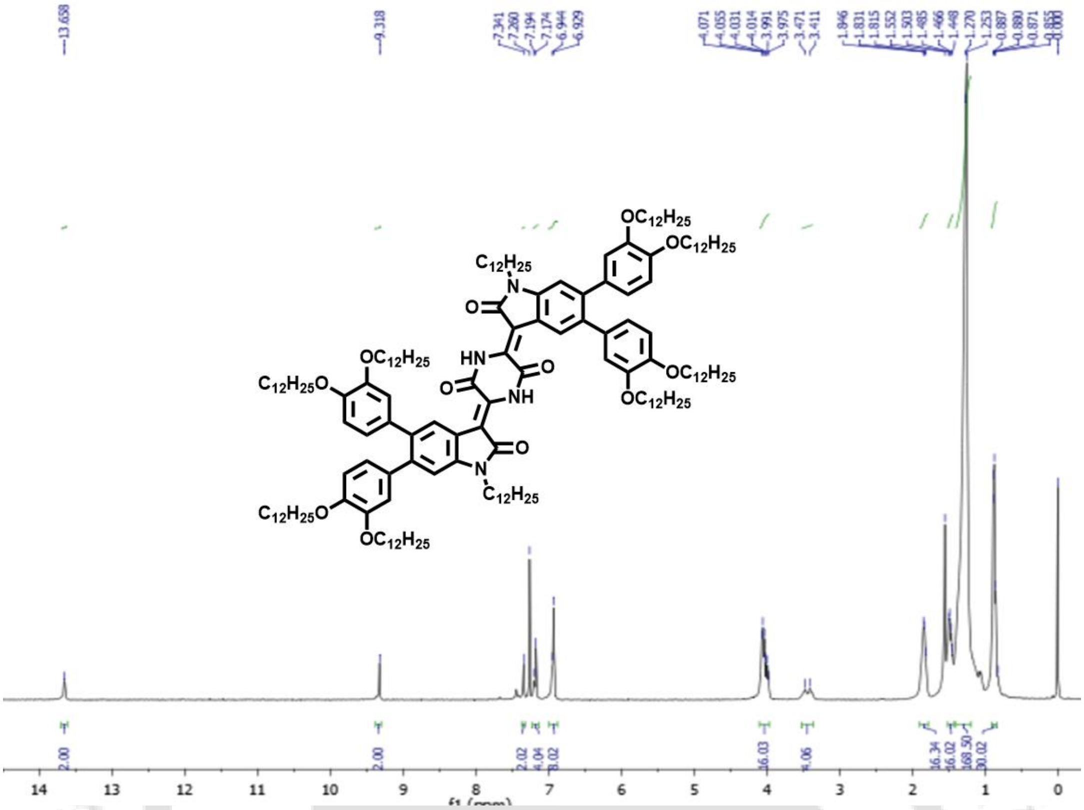

Figure A11. ^{1}H NMR (600 MHz) spectra of **CI6** in $CDCl_3$.

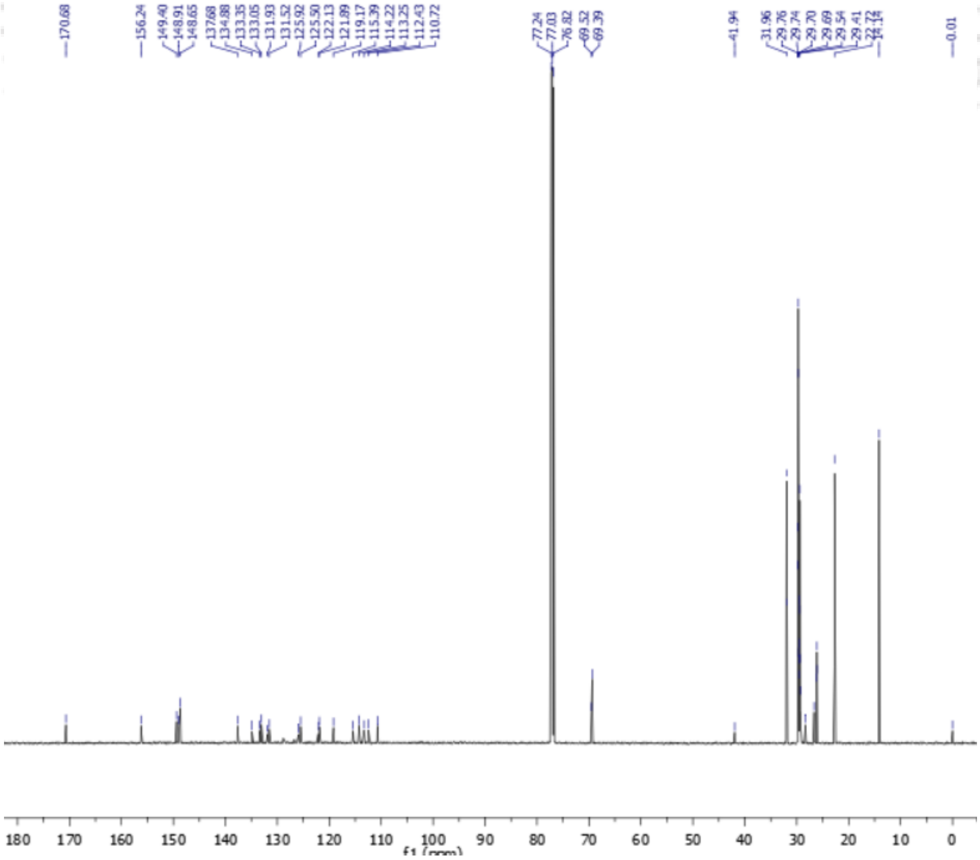

Figure A12. ^{13}C NMR (150 MHz) spectra of **CI6** in $CDCl_3$.

2.6.2. Polarizing optical microscopy (POM)

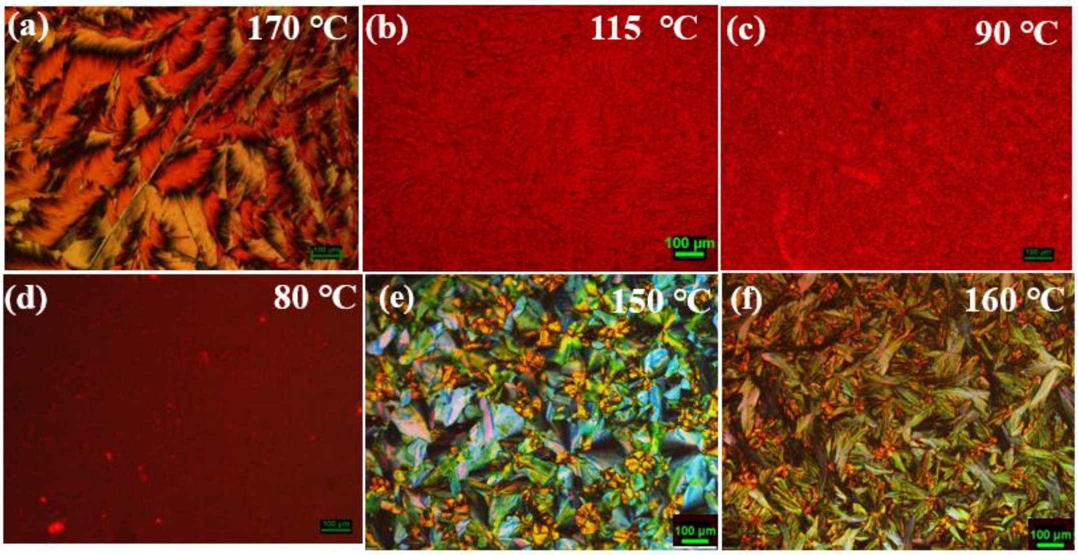

Figure A13. POM images were obtained for a) **CI1**, b) **CI2**, c) **CI3**, d) **CI4**, e) **CI5**, and f) **CI6** on a cooling process from isotropic melt at different temperatures (scale bar 100 μm).

2.6.3 Differential Scanning calorimetry (DSC)

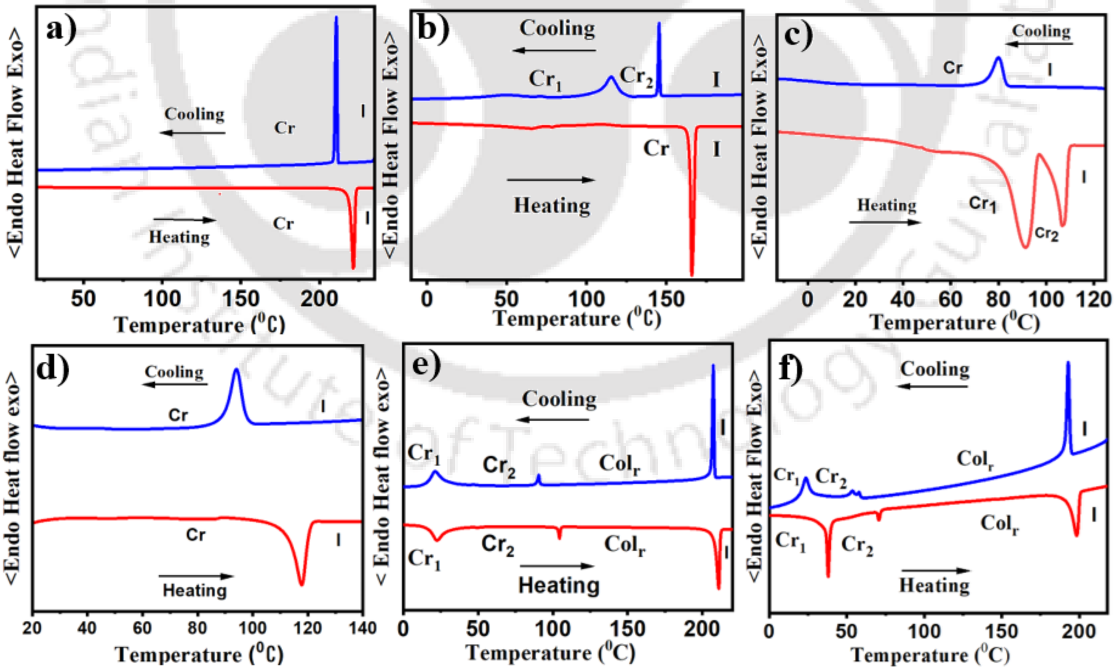

Figure A14. DSC thermograms were obtained for a) **CI1**, b) **CI2**, c) **CI3**, d) **CI4**, e) **CI5**, and f) **CI6** for the first cooling (blue trace) and second heating (red trace) taken at 5 °C/min.

2.6.4 X-Ray Diffraction (XRD) Studies

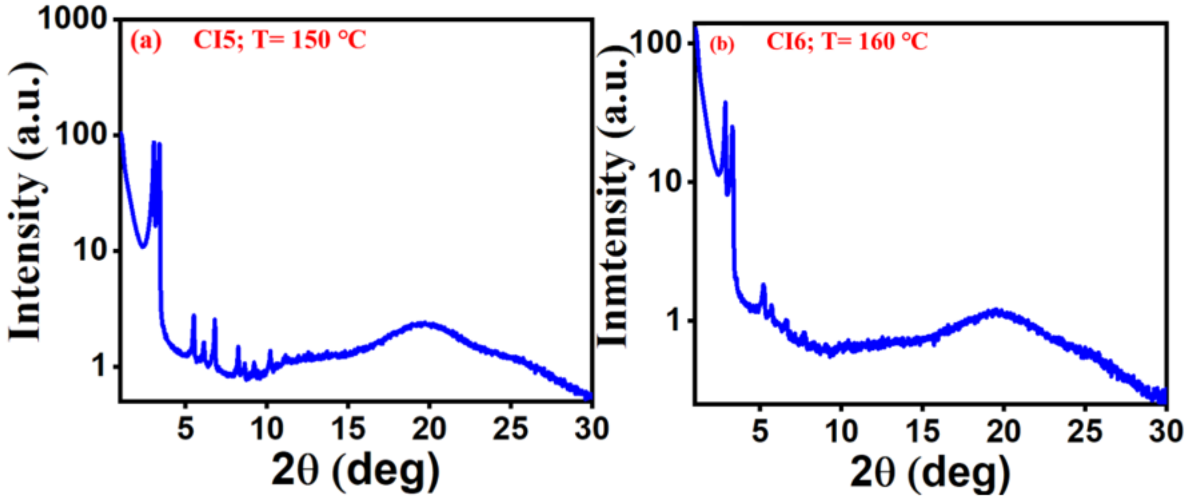

Figure A15. X-ray diffractograms for the Col$_r$ phases of (a) **CI5** at 150°C, (b) **CI6** at 160°C.

Table A2.1. Results of (*hkl*) indexation of XRD profiles of **CIs** at a given temperature (T) of mesophase.

Compounds (D/Å)	Phase (T/$_o$C)	d-spacing		Miller Index (*hk*)	Lattice parameters (Å), Lattice area S (Å^2), Molecular volume (Å^3)
		d$_{obs}$ (Å)	d$_{cal}$(Å)		
CI5 (50.92) MW: 2263.53	Col$_r$ (180 °C)	28.69	28.69	20	*a* = 57.38
		26.64	26.64	01	*b* = 26.64
		15.83	15.54	31	A = 1528.60
		14.27	14.34	40	V = 5258.39
		13.24	13.32	02	Z ≈ 1
		10.57	10.54	51	
		9.78	9.76	42	
		9.50	9.56	60	
		8.79	8.77	13	
		7.99	8.05	33	
		7.87	7.83	71	
		7.18	7.17	80	
		4.54 (h_a)			
		3.44 (h_c)			
	Col$_r$ (150°C)	28.84	28.84	20	*a* = 57.68
		26.03	26.03	01	*b* = 26.03
		15.83	15.47	31	A = 1501.41
		14.42	14.42	40	V = 5119.81
		12.98	13.01	02	Z ≈ 1

		10.77 10.32 9.58 8.65 4.51(h_a) 3.41 (h_c)	10.77 10.54 9.61 8.63	32 51 60 52	
CI6 (55.61) MW: 2487.96	Col$_r$ (160 °C)	30.44 27.59 17.24 15.22 13.73 11.19 10.74 10.15 9.21 7.77 4.59(h_a) 3.47(h_c)	30.44 27.59 17.32 15.22 13.79 11.13 10.56 10.15 9.19 7.71	11 02 21 22 04 32 15 33 06 17	a = 36.49 b = 55.18 A = 2013.52 V = 6986.91 Z ≈ 1
	Col$_r$ (125 °C)	31.13 26.73 17.29 15.51 13.32 11.51 10.43 10.32 9.74 8.59 7.59 7.09 4.52 (h_a) 3.35 (h_c)	31.13 26.73 17.38 15.56 13.36 11.59 10.38 10.43 9.88 8.66 7.59 7.10	10 11 03 20 22 23 30 05 15 25 26 43	a = 31.13 b = 52.15 A = 1623.43 V = 5438.49 Z ≈ 1

The diameter (D) of the disk (estimated from Chem 3D Pro 8.0 molecular model software from Cambridge Soft). d_{obs}: spacing observed; d_{cal}: spacing calculated (deduced from the lattice parameters; a,b for Col$_r$ phase). The spacings marked h_a and h_c correspond to diffuse reflections in the wide-angle region arising from correlations between the alkyl chains and core regions. Z indicates the number of molecules per columnar slice of thickness h_c, estimated from the lattice area S and the volume V.

2.6.5. Photo physical studies

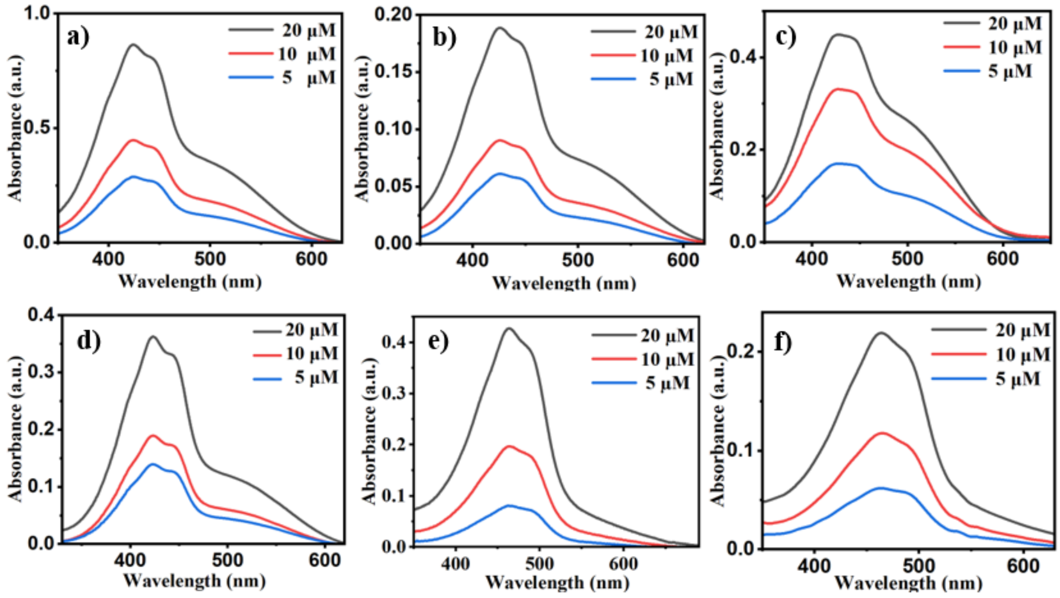

Figure A16. Absorption spectra of compounds a) **CI1**, b) **CI2**, c) **CI3**, d) **CI4**, e) **CI5**, and f) **CI6** in micromolar chloroform solutions as a function of concentration.

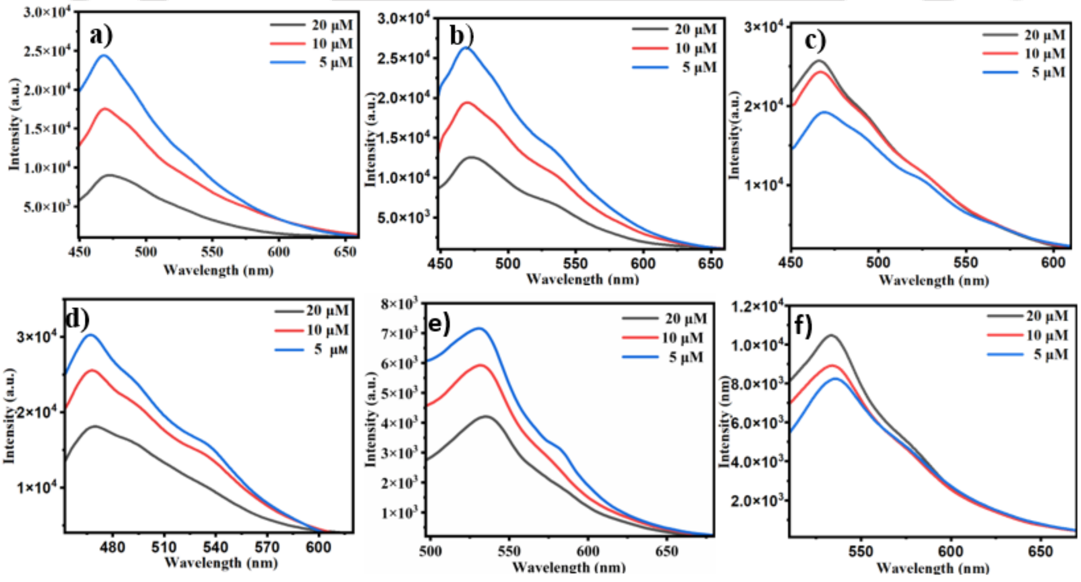

Figure A17. Emission spectra of compounds a) **CI1**, b) **CI2**, c) **CI3**, d) **CI4**, e) **CI5**, and f) **CI6** in micromolar chloroform solutions.

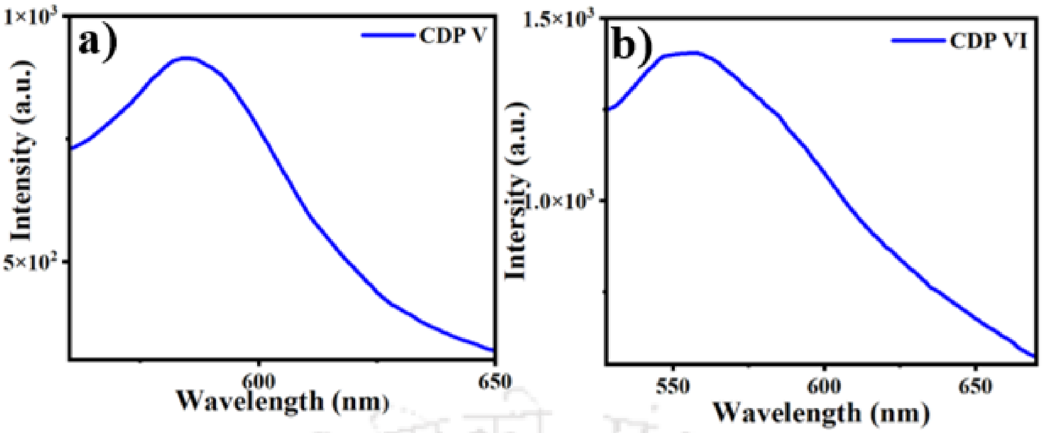

Figure A18. Emission spectra of compounds a) **CI5**, b) **CI6** in thin film state.

2.6.6. Electrochemical Studies

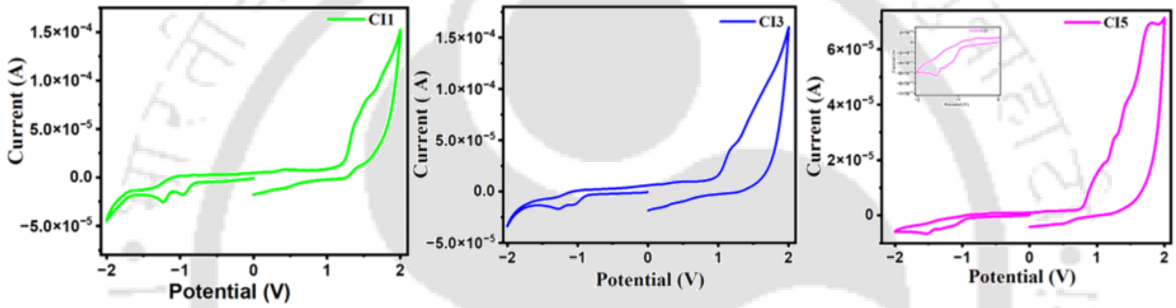

Figure A19. Cyclic voltammograms of **CI**s **(CI1, CI3, CI5)** (insets show the reduction half of **CI5**) in micromolar dichloromethane solutions in scan rate 100 mv/s.

2.6.7. Device fabrication

To initiate the process, glass/ITO substrates were cleaned in an ultrasonic water bath with a diluted detergent solution, deionized water, acetone, and isopropanol successively. The cleaned ITO substrates were then treated with UV-ozone for 30 minutes. For the fabrication of hole only device, PEDOT: PSS solution was spin-coated onto the ITO substrates at 3000 rpm for 40 seconds, followed by annealing at 150 °C for 10 minutes. On top of the PEDOT: PSS layer, a solution of **CI5** in chlorobenzene (35 mg/ml) was spin-coated at 1500 rpm for 60 seconds. Finally, 10 nm of MoO_3 and 100 nm of silver were deposited sequentially on the **CI5** layer via thermal evaporation. For the fabrication of an electron-only device, a ZnO solution prepared by the sol-gel method was spin-coated onto the ITO substrate at 4000 rpm for 50 seconds and annealed at 210°C for 15 minutes. The **CI5** solution was then spin-coated at 1500 rpm for 60 seconds. A PDINN solution in methanol was subsequently spin-coated to form a thin layer (less than 5 nm), followed by a 100 nm thick silver layer deposition via thermal evaporation.

2.6.6. Dielectric constant calculation

To determine the dielectric constant of the material, capacitance-frequency (C-F) measurements were carried out. For C-F measurements, a 200 nm thick layer of **CI5** was spin-coated on top of UV-Ozone treated ITO, and 100 nm Au was thermally evaporated. The material's dielectric constant was calculated from the flat region, corresponding to the geometric capacitance of the C-F curve (Figure A20).

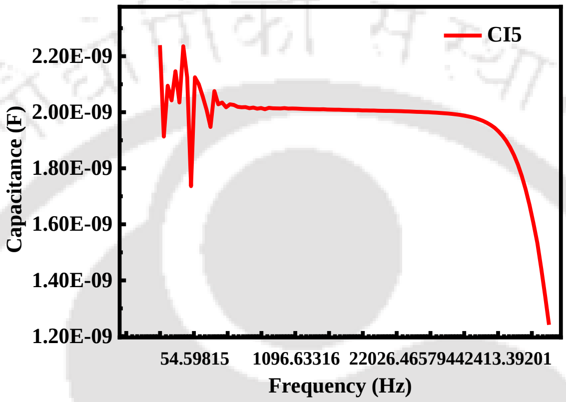

Figure A20. Capacitance- frequency measurement of the device fabricated with **CI5.**

2.7. References

1. M. Amorín, A. Pérez, J. Barberá, H. L. Ozores, J. L. Serrano, J. R. Granja and T. Sierra, *Chem. Commun.*, 2014, **50,** 688-690.

2. T. Govindaraju, M. Pandeeswar, K. Jayaramulu, G. Jaipuria and H. S. Atreya, *Supramol. Chem.*, 2011, **23**, 487-492.

3. A. S. Safiullina, S. A. Ziganshina, N. M. Lyadov, A. E. Klimovitskii, M. A. Ziganshin, and V. V. Gorbatchuk, *Soft Matter*, 2019, **15**, 3595–3606.

4. S. Manchineella and T. Govindaraju, *Chempluschem*, 2017, **82**, 88–106.

5. B. Roy and T. Govindaraju, *Bull Chem Soc Jpn*, 2019, **92**, 1883–1901.

6. M. A. Ziganshin, A. S. Safiullina, A. V. Gerasimov, S. A. Ziganshina, A. E. Klimovitskii, K. R. Khayarov and V. V. Gorbatchuk, *J. Phys. Chem. B*, 2017, **121**, 8603–8610.

7. S. Manchineella and T. Govindaraju, *RSC Adv.*, 2012, ***2*** (13), 5539-5542.

8. M. L. Bolognesi, H. N. A. Tran, M. Staderini, A. Monaco, A. López-Cobẽas, S. Bongarzone, X. Biarnés, P. López-Alvarado, N. Cabezas, M. Caramelli, P. Carloni, J. C. Menéndez and G. Legname, *ChemMedChem*., 2010, ***5***, 1324-1334.

9. (a) A. J. Kleinsmann and B. J. Nachtsheim, *Chemical Communications*, 2013, **49**, 7818–7820; (b) S. Manchineella, N.A. Murugan, T. Govindaraju, Cyclic dipeptide-based ambidextrous supergelators: Minimalistic rational design, structure-gelation studies, and in situ hydrogelation., *Biomacromolecules*, 2017, **18**, 3581-3590.

10. C. Balachandra and T. Govindaraju, *J. Org. Chem.*, 2020, ***85***, 1525-1536.

11. (a) N. Shimosaraya, T. Sotani, Y. Miyagi, E. A. Q. Mondarte, K. Suthiwanich, T. Hayashi, Y. Nagata, H. Sogawa and F. Sanda, *Soft Matter*, 2022, **18**, 137–145; (b) K. Tao, Z. Fan, L.Sun, P. Makam, Z. Tian, M. Ruegsegger, S. S. Niv, D. Hansford, R. Aizen, Z. Pan, S. Galster, J. Ma, F. Yuan, Quantum confined peptide assemblies with tunable visible to near-infrared spectral range, *Nat*. Comun. 2018, **9**, 3217.

12. (a) H. Hoshizawa, Y. Minemura, K. Yoshikawa, M. Suzuki, K. Hanabusa, Thixotropic hydrogelators based on a cyclo(dipeptide) derivative, *Langmuir*, 2013, **29**, 14666-14673; (b) Z. L. Pianowski, J. Karcher and K. Schneider, Photoresponsive self-healing supramolecular hydrogels for light-induced release of DNA and doxorubicin, *Chem. Commun.*, 2016, ***52***, 3143.

13. Y. Dong, L. Gao, Q. Cao, Z. Cao, S. Gan, J. Li, Y. Zhu, Y. Zhou, C. Zhang, and W. Wang., Synthesis, Fluorescence, and Bioactivity of Novel Isatin Derivatives, *J. Phys. Chem. B.* 2024, **128**, 6123−6133.

14. H. Guo, Isatin Derivatives and Their Anti-bacterial Activities., Eur. *J. Med. Chem.* 2019, **164**, 678−688.

15. Chiyanzu, I.; Clarkson, C.; Smith, P. J.; Lehman, J.; Gut, J.; Rosenthal, P. J.; Chibale, K. D. Synthesis and Anti-plasmodial Evaluation in Vitro of New 4-aminoquinoline Isatin Derivatives.; *Bioorg. Med. Chem.* 2005, **13**, 3249−3261.

16. Thakur, R. K.; Joshi, P.; Baranwal, P.; Sharma, G.; Shukla, S. K.; Tripathi, R.; Tripathi, R. P. Synthesis and Antiplasmodial Activity of Glyco-conjugate Hybrids of Phenylhydrazono-indolinones andGlycosylated 1,2,3-triazolyl-methyl-indoline-2,3-diones.; *Eur. J. Med.Chem.* 2018, **155**, 764−771.

17. Aboul-Fadl, T.; Abdel-Aziz, H. A.; Abdel-Hamid, M. K.; Elsaman, T.; Thanassi, J.; Pucci, M. J. Schiff Bases of Indoline-2,3-dione: Potential Novel Inhibitors of Mycobacterium Tuberculosis (Mtb) DNA gyrase., *Molecules.*, 2011, **16**, 7864−7879.

18. Osman, H. M.; Elsaman, T.; Yousef, B. A.; Elhadi, E.; Ahmed, A. A. E.; Eltayib, E. M.; Mohamed, M. S.; Mohamed, M. A.; Mancini, P. M. Schiff Bases of Isatin and Adamantane-1-carbohydrazide: Synthesis, Characterization and Anticonvulsant Activity. *J. Chem.* 2021, **2021**, 6659156.

19. Kakkar, R.; Isatin and its derivatives: a survey of recent syntheses, reactions, and applications. *Med. Chem. Comm.* 2019, **10**, 351-368.

20. B. Kasi, V. Murugesan, N. Kaliaperumal, Super acid-catalyzed polymerization of phenothiazine and modified isatin, *Appl. Petrochem. Res.*, 2019, **9**, 91–100

21. Thirumalaiselvam, B.; Kanagadurai, R.; Jayaraman, D.; Natarajan, V.; Growth and characterization of third order nonlinear optical material: isatin., *Phys. B Condens. Matter.*, 2013, **427**, 91-96.

22. Nuyken, O.; Jungermann, S.; Wiederhirn, V.; Bacher, E.; Meerholz, K. Modern trends in organic light-emitting devices (OLEDs).; *Monatsh. Chem./Chem. Mon.* 2006, **137**, 811–824.

23. B. Thirumalaiselvama, R. Kanagadurai, D. Jayaraman, V. Natarajan, Growth and characterization of third order nonlinear optical material: Isatin, *Physica B*, 2013, **427**, 91–96.

24. Z Ghufran Salih Yaqoob, Qusay M.A. Hassan, Ahmed Majeed Jassem, H.A. Sultan, Adil Muala Dhumad, C.A. Emshary, Isatin-indole hybrid molecule: A simple synthesis to design an efficient NLO material, *Opt. Mater.*, 2024, **149**, 149, 114983.

25. P. Tisovský, M. Horváth, K. Csicsai, J. Donovalová, J. Filo, M. Cigá ˇn, R. Sokolík, G. Addová and A. Gáplovský, Isatin-1,8-Naphthalimide Hydrazones: A Study of Their Sensor and ON/OFF Functionality, *Molecules*, 2019, **24**, 397.

26. Sharbati, M. T.; Rad, M. N.; Soltani, S.; Behrouz, F.; Emami, F.; Nekoei, A.-R. Fabrication and electrical characterization of red organic light emitting diode using an isatin derivative as an organic chromophore. *Opt. Eng.*, 2011, **50**, 044002.

27. X. Zhou, S.W. Kang, S. Kumar, R. R. Kulkarni, S. Z. D. Cheng, and Q. Li, Self-Assembly of Porphyrin and Fullerene Supramolecular Complex into Highly Ordered Nanostructure by Simple Thermal Annealing, *Chem. Mater.*, 2008, **20**, 3551–3553.

28. H. K. Bisoyi, Q. Li, Liquid Crystals: Versatile Self-Organized Smart Soft Materials, *Chem. Rev.*, 2022, **122**, 4887−4926.

29. H. K. Bisoyi, Q. Li, Stimuli directed alignment of self-organized one-dimensional semiconducting columnar liquid crystal nanostructures for organic electronics, *Prog. Mater. Sci.*, 2019, **104**, 1.

30. S. Kumar, Chemistry of Discotic Liquid Crystals from Monomers to Polymers, *CRC Press*, 2011.

31. T. Wöhrle, I. Wurzbach, J. Kirres, A. Kostidou, N. Kapernaum, J. Litterscheidt, J. C. Haenle, P. Staffeld, A. Baro, F. Giesselmann and S. Laschat, *Chem Rev*, 2016, **116**, 1139–1241.

32. S. Kumar, Self-organization of disc-like molecules: chemical aspects, *Chem. Soc. Rev.*, 2006, **35**, 83–109.

33. P. K. Behera, M. R. Nagar, R. K. Gupta, S. Pradhan, D. S. S. Rao, S. K. Prasad, L. The, A. Choudhury, J. H. Jou, and A. S. Achalkumar, highly stable deep red-to-NIR OLEDs with an external quantum efficiency of 4.9% from room temperature nanostructured columnar fluids based on hetero atom bay-annulated perylene bisimides. *J. Mater. Chem. C.*,2022, **10**, 18351.

34. S. K. Pal, S. Setia, B.S. Avinash and S. Kumarb, Triphenylene-based discotic liquid crystals: recent advances, *Liquid Crystals*, 2013, **40**, 12, 1769–1816,

35. J. Eccher, G. C. Faria, H. Bock, H. v. Seggern, and I. H. Bechtold, Order Induced Charge Carrier Mobility Enhancement in Columnar Liquid Crystal Diodes, *ACS Appl. Mater. Interfaces*, 2013, **5**, 11935−11943.

36. M. Kumar and S. Kumar, Liquid crystals in photovoltaics: a new generation of organic photovoltaics, *Polym. J.*, 2017, **49**, 85–111.

37. P. K. Behera, F. R. Chen, I. Mondal, S. Lenka, P. Gautam, N. Khatiwoda, I. Siddiqui, V. E. Krishnaprasad, R. Ahmed, D. S. Shankar Rao, S. P. Senanayake, J. H. Jou and A. S. Achalkumar, Superior electron mobility, red electroluminescence with high quantum efficiency from printable room temperature columnar liquid crystalline perylene bisimide. *Chem. Eng. J.*, 2024, **488**, 150762.

38. J. De, I. Bala, S. P. Gupta, U. K. Pandey, and S.K. Pal, High Hole Mobility and Efficient Ambipolar Charge Transport in Heterocoronene-Based Ordered Columnar Discotics, *J. Am. Chem. Soc.*, 2019, **141**, 18799−18805

39. J. Xu, Room-Temperature Columnar Liquid Crystals from Twisted and Macrocyclic 9,9′-Bifluorenylidene Mesogen with Ambipolar Carrier Transport Properties, *ACS Mater. Au.*, 2023, **3**, 450−455.

40. P. K. Behera, K. Yadav, D. S. S. Rao, U. K. Pandey and A. S. Achalkumar, Self-assembled anti-napthalene-3,4:9,10-bis(benzimidazole)s: stabilizing room temperature columnar phase with ambipolar conductivity. *ACS Appl Electron Mater*, 2023, **5**, 5417–5421

41. P. K. Behera, K. Yadav, D. S. Shankar Rao, U. K. Pandey, and A. A. Sudhakar, Ambipolar columnar self-assembled organic semiconductors based on heteroatom bay-annulated perylene bisimides. *Chem. Asian J.*, 2023, **18**, e202300086.

42. P. Singh, M. Ghadiyali, S. Chacko, R.M. Kamble, D-A- D based pyrido-pyrazino[2,3-b]indole amines as blue-red fluorescent dyes: Photophysical, aggregation-induced emission, electrochemical and theoretical studies, *J. Lumin.*, 2022, **242**,118568.

43. W.-R. Li, K.-C. Kao, Y.-C. Yo and C. K. Lai, Liquid-crystalline properties of unsaturated piperazine-2,5-dione derivatives. *Helv. Chim. Acta.*, 1999, **82**, 1400.

44. A. R. Katritzky, W. Q. Fan, Conjugated systems derived from piperazine-2,5-dione, *J. Heterocycl. Chem.*, 1988, **25**, 821.

45. S. Boonnab, C. Chaiwai, P. Nalaoh, T. Manyum, S. Namuangruk, C. Chitpakdee, T. Sudyoadsuk and V. Promarak, Synthesis, characterization, and physical properties of pyrene-naphthalimide derivatives as emissive materials for electroluminescent devices. *Eur. J. Org. Chem.*, 2021, **2021**, 2402-2410.

46. S. Sauer, N. Steinke, A. Baro, S. Laschat, F. Giesselmann, W. Kantlehner, Guanidinium Chlorides with Triphenylene Moieties Displaying Columnar Mesophases. *Chem. Mater.*, 2008, **20**, 1909–1915.

47. M. Lehmann, C. Ko¨hn, H. Meier, S. Renker and A. Oehlhof, Supramolecular order of stilbenoid dendrons: importance of weak interactions, *J. Mater. Chem*., 2006, **16**, 441–451.

48. C. Krause, R. Zorn, F. Emmerling, J. Falkenhagen, B. Frick, P. Huber and A. Schönhals, Vibrational density of states of triphenylene-based discotic liquid crystals: dependence on the length of the alkyl chain. *Phys. Chem. Chem. Phys.*, 2014, **16**, 7324.

49. J. H. Kim, T. Schembri, D. Bialas, M. Stolte and F. Würthner, F. Slip-stacked J-aggregate materials for organic solar cells and photodetectors. *Adv. Mater*., 2022, **34**, 2104678.

50. N. J. Hestand and F. C. Spano. Expanded *H*- and *J*-molecular aggregates theory: the effects of vibronic coupling and intermolecular charge transfer, *Chem. Rev*., 2018, **118**, 7069.

51. S. K. Pathak, R. K. Gupta, S. Nath, D. S. Shankar Rao, S. K. Prasad, A.S. Achalkumar, Columnar Self-Assembly of Star-Shaped Luminescent Oxadiazole and Thiadiazole Derivatives., *J. Mater. Chem. C.*, 2015, **3**, 2940-2952.

52. S.K. Pathak, B. Pradhan, M. Gupta, S. K. Pal, and A.S. Achalkumar, Liquid-Crystalline Star-Shaped Supergelator Exhibiting Aggregation-Induced Blue Light Emission., *Langmuir* 2016, **32**, 9301−9312.

53. Q. Zhang, H. Peng, G. Zhang, Q. Lu, J. Chang, Y. Dong, X. Shi, and J. Wei, Facile Bottom-Up Synthesis of Coronene-based 3-Fold Symmetrical and Highly Substituted Nanographenes from Simple Aromatics., *J. Am. Chem. Soc.* 2014, **136**, 5057–5064.

54. Y. Ding, L. Zhao, Y. Fu, L. Hao, Y. Fu, Y. Yuan, P. Yu, Y. Teng, Synthesis and Antiproliferative Activities Evaluation of Multi-Substituted Isatin Derivatives. *Molecules*, 2021, **26**, 176.

Chapter 3

Phenoxazine-Based Ambipolar Luminescent Room-Temperature Liquid Crystals Capable of Bioimaging Applications

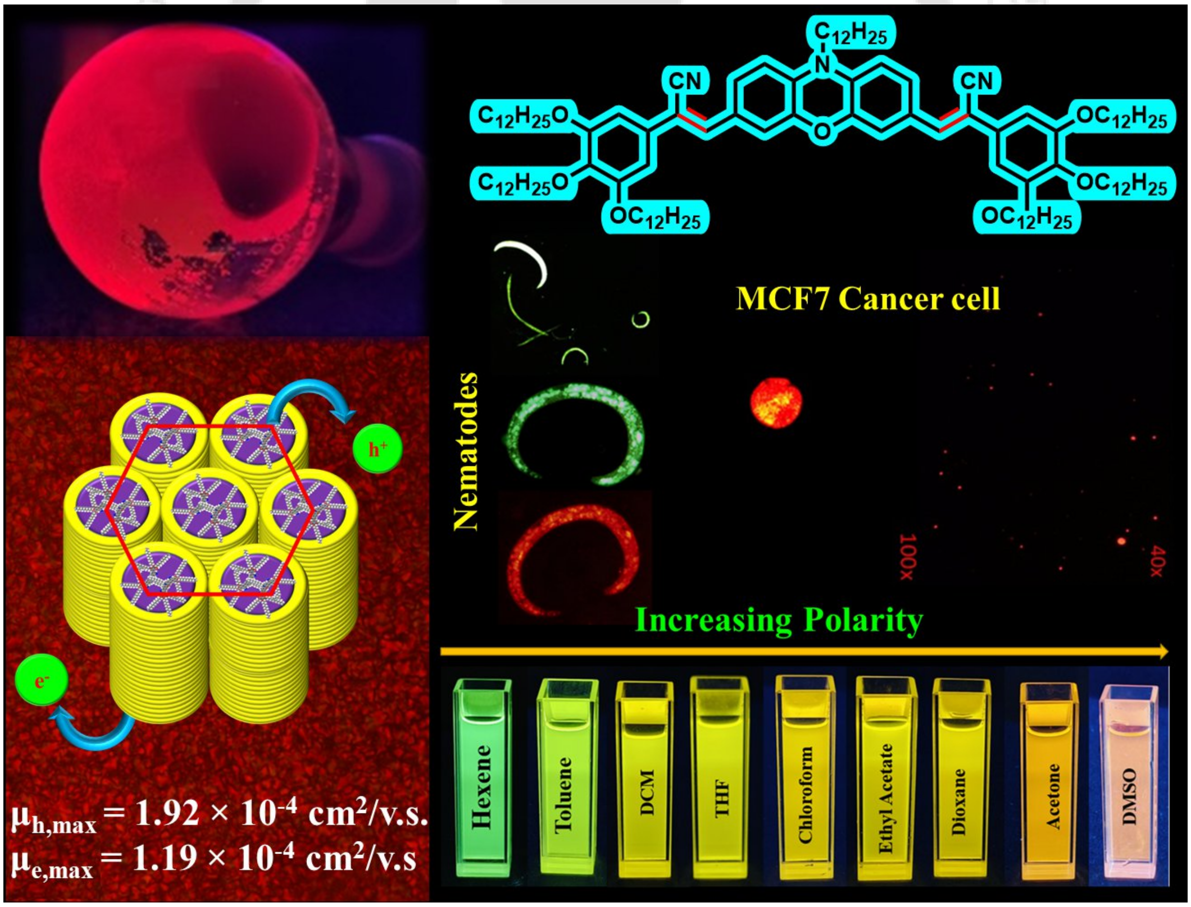

3.1. Introduction

Phenoxazine, an intriguing heterocyclic compound with a fused tricyclic structure and a distinctive butterfly-shaped conformation resulting from the folding of its two benzene rings around the O–N axis, is gaining attention as a promising candidate for electronic and optoelectronic applications. Its unique structure enhances its electron-donating properties, as evidenced by its ionization potential, 0.7 eV lower than carbazole's, making its radical cations more stable.[1-3] Heterocycles like phenoxazine have long been incorporated into organic semiconducting materials, where their presence improves thermal, chemical, thermo-oxidative, and photochemical stabilities and fluorescence quantum yields.[4] Despite the extensive research on carbazole-based emissive molecules, phenoxazine has been less explored as a building block for OLEDs (**3.2, 3.3**),[2] OFETs, and bio-imaging materials (**3.8, 3.9**).[5-9] Notably, phenoxazine has been employed in dye-sensitized solar cells (DSSCs) as an electron donor (**3.1**), where its strong electron-donating ability has led to higher conversion efficiencies compared to similar sensitizers like triphenylamine and phenothiazine.[10-12] Before its role in perovskite solar cells (PSCs, **3.4**), phenoxazine was widely used in designing light harvesters for bulk heterojunction organic solar cells (**3.5**) due to its ease of modification and powerful electron-donating properties.[14-16] The presence of an oxygen atom in its structure slightly diminishes the overall aromaticity of the ring system,[1,] while the dipole moment (μ = 1.93 D) suggests a non-planar configuration.[17] The proton or substituent on the nitrogen atom can adopt positions between and outside the planes of the lateral rings, adding to the compound's versatility. While most phenoxazine derivatives exhibit melting points below 200 °C and are generally stable, those substituted with hydroxy or amino groups at the para position relative to the bridging nitrogen are more prone to oxidation. Furthermore, phenoxazine has become a key component in monochromic luminescence (**3.7**)[18], and the design of thermally activated delayed fluorescence (TADF, 3.6) molecules [19,20] plays an essential role as an electron donor.[21] By understanding the relationship between the stacking modes of phenoxazine derivatives and their luminescent properties, researchers can better design and synthesize organic compounds with phenoxazine substructures, ultimately enhancing the performance of optoelectronic devices.

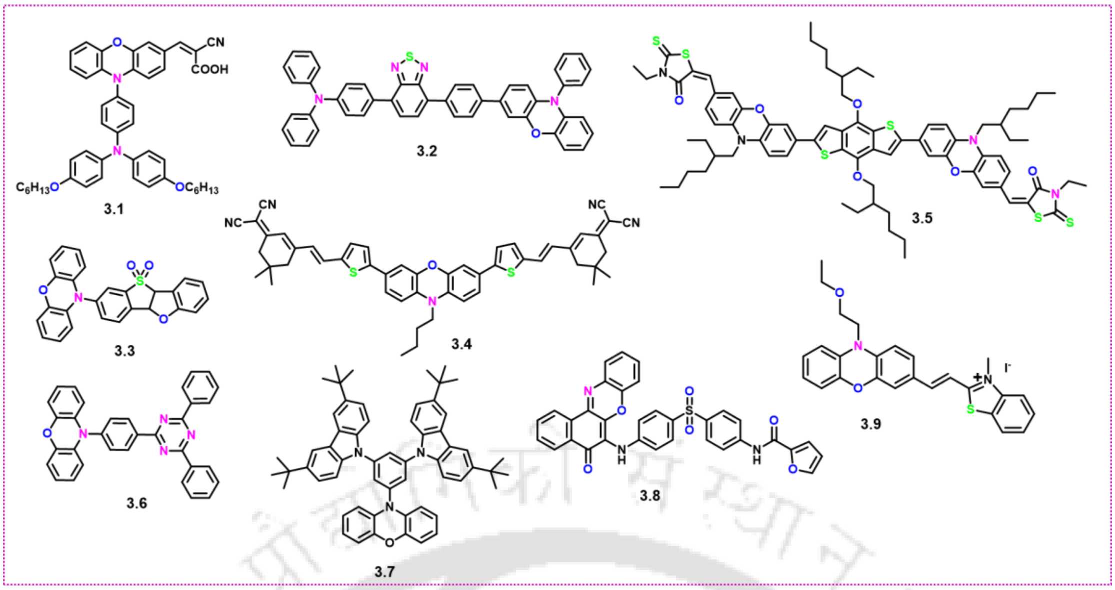

Figure 3.1. Structures of Phenoxazine-based compounds are used in various applications (**3.1-3.9**).

Recently, luminescent liquid crystals (LLCs) have garnered increasing interest due to their fundamental phenomenological significance and appealing technological applications, including anisotropic light-emitting diodes, polarized organic lasers, light-emitting liquid crystal displays (LCDs), information storage, sensors, and one-dimensional semiconductors. The intrinsic light-emitting properties and unique self-organizing features give LLCs several novel advantages. For instance, LLCs can create various stimuli-responsive luminescent materials because liquid crystals are highly sensitive to external stimuli of mechanical, electrical, thermal, and magnetic origin.[22,23]

Traditional fluorescent stains have issues like limited tissue penetration, photobleaching, high background noise, stability concerns, cell toxicity, staining anomalies, and reduced specificity that can impact these dyes' effectiveness in various applications.[24] Using phenoxazine as a biological stain offers numerous advantages, including high photostability, strong fluorescence, application versatility, biocompatibility, and potential therapeutic benefits. These compounds exhibit strong fluorescence, enhancing stained structures' visibility under microscopy.[25] Their high quantum yields contribute to transparent and bright images of cellular components, facilitating detailed analysis of biological samples. Many phenoxazine derivatives exhibit low cytotoxicity, making them suitable for live cell staining without adversely affecting cellular viability.

Despite the exciting potential of LLCs, preserving light-emitting properties remains a significant challenge due to aggregation-caused emission quenching (ACQ) in traditional organic luminophores. [26-28] Thus, preventing quenching in the aggregated state of liquid crystal materials becomes a key concern while preserving the liquid crystalline self-assembly.[29-31] A comprehensive literature review revealed a striking scarcity of research on phenoxazine-based bioimaging derivatives, with little to no exploration in this area. Moreover, to our knowledge, phenoxazine-based room-temperature luminescent liquid crystals (LLCs) have yet to be synthesized or studied. This gap in the literature presented a unique challenge and an exciting opportunity to design and synthesize novel phenoxazine-based liquid crystals. To our surprise, the field of phenoxazine-based luminescent liquid crystal compounds remains notably underexplored. Driven by this void, we have successfully synthesized a new class of room-temperature LLCs. These materials consist of two alkoxy phenyl groups, connected via a cyano-vinylene bond to an *N*-alkylated phenoxazine, resulting in a bent-shaped molecular structure. The non-planar nature of phenoxazine[17] and the cyano-phenylvinylene fluorophore groups lend themselves to strong fluorescence in both solution and solid states.[32] Furthermore, the photophysical properties of cyano-phenylvinylenes can be finely tuned by external factors such as temperature, pressure, solvents, pH, and light.[32]

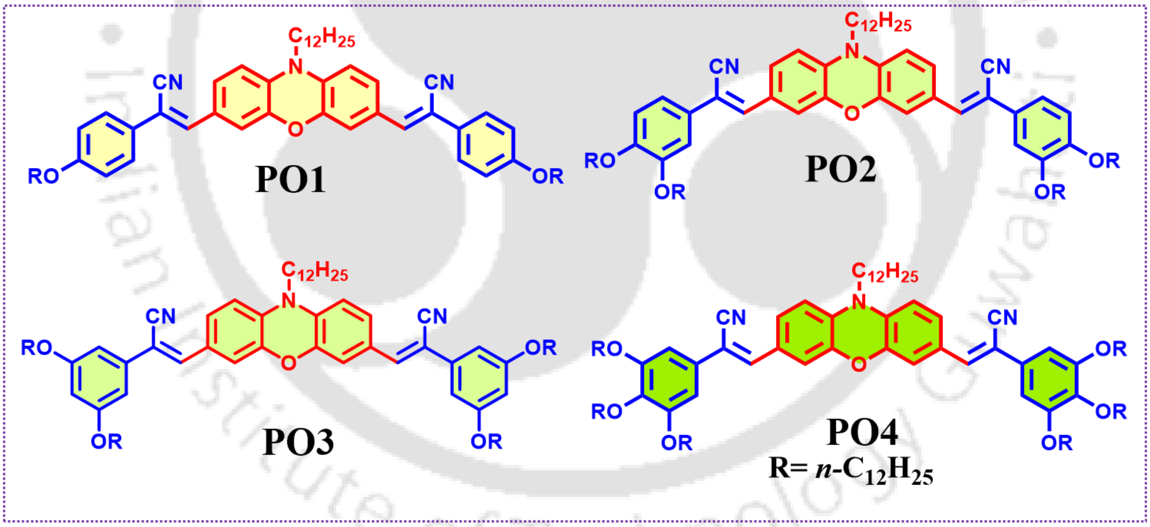

Figure 3.2. Structures of **PO** are studied in this work.

Our synthesis journey began with the reaction of a mono-alkoxy benzyl acetonitrile derivative with an *N*-alkylated phenoxazine dialdehyde, resulting in a crystalline material (**PO1**, with two alkoxy chains). To explore further, the number of peripheral alkoxy chains was increased to four, while varying the substitution positions (**PO2** and **PO3**) still resulted in crystalline materials. Interestingly, the tri-*n*-alkoxy derivative (**PO4**, with six alkoxy chains) maintained a stable room-temperature columnar hexagonal phase over a wide thermal range without compromising its luminescent properties in the solid state. The molecular design combines electron donor and acceptor components in a single structure, imparting ambipolar charge transport characteristics in the columnar phase. These materials' excellent solubility and stability also facilitated the visualization of nematodes and MCF7 human breast cancer cells under fluorescence microscopy.

3.2. Result and Discussion

3.2.1. Synthesis and molecular structural characterization

The synthetic approach utilized to prepare target **PO**s is outlined in schemes 3.1 and 3.2

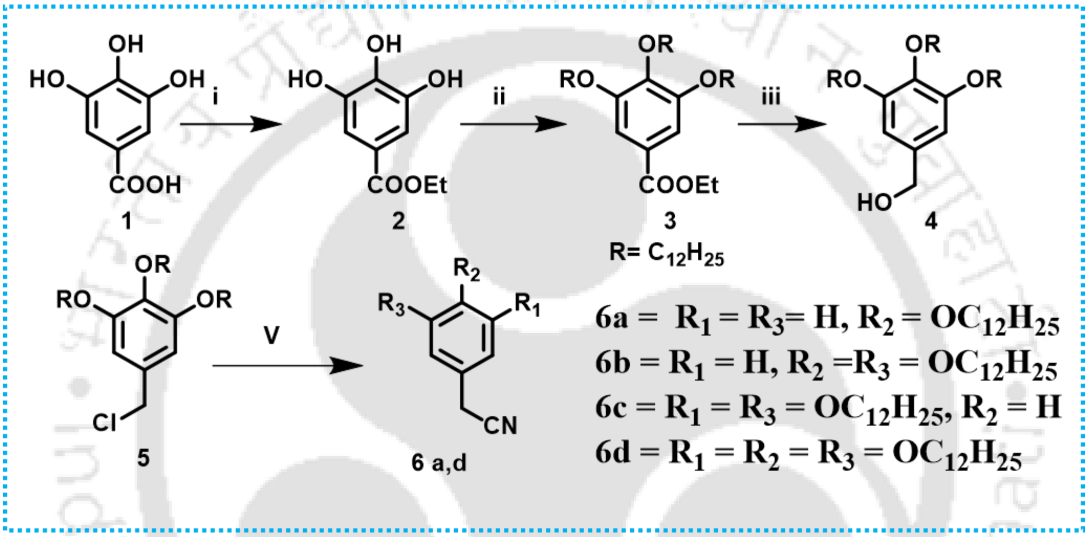

Scheme 3.1. Synthesis of phenyl acetonitrile derivatives **6**; Reagents and Conditions: (i) C_2H_5OH, conc. H_2SO_4, 80 °C, 24 h, 86%; (ii) $C_{12}H_{25}Br$, 80 °C, N_2 atm, 90%, 24 h; (iii) LAH, THF, 0 °C -rt, 12 h, 80%; (iv) $SOCl_2$, dry DCM, N_2 atm, 0 °C -rt, 2 h, 97%; (v) NaCN, DMF, 100 °C, 18 h, 65-70%.

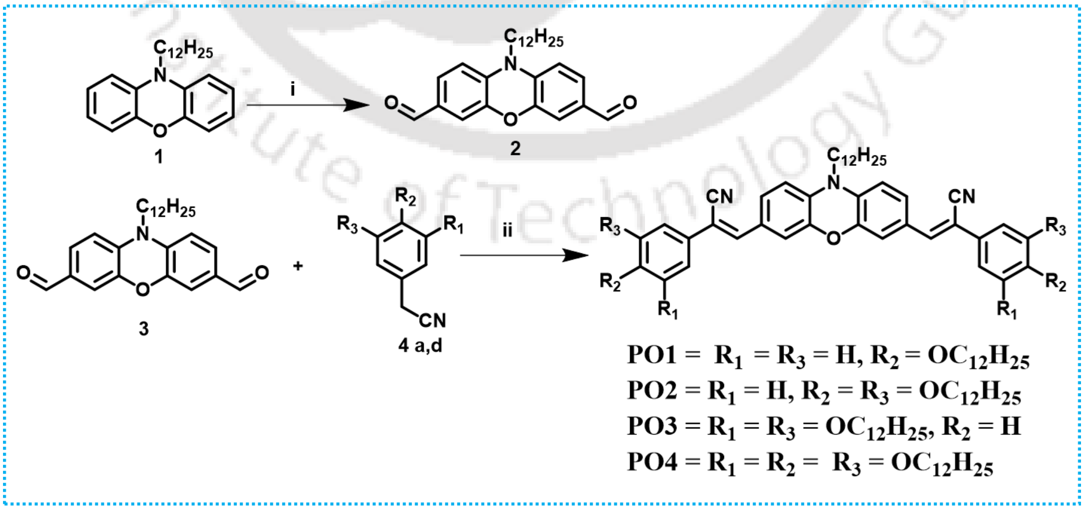

Scheme 3.2. Synthesis of target Phenoxazine derivatives (**POs**); Reagents and Conditions: (i) $POCl_3$, DMF, 0 °C-80 °C, 24 h, 75%; (ii) KOt-Bu, *tert*-BuOH, 2 h, 50 °C, 60-72%.

The target **PO**s were prepared following a straightforward synthetic pathway (Scheme 3.1 and 3.2). In the first step, *N*-alkylated phenoxazine dialdehyde **2** is prepared using $POCl_3$ and DMF by a well-known Vilsmeier–Hack reaction.[33,34] Finally, the **PO** derivatives were synthesized by a double Knoevenagel condensation reaction of phenyl acetonitrile derivatives (**4a,d**) and *N*-alkylated phenoxazine dialdehyde (**2**) using potassium *tert*-butoxide as a base and *tert*-butanol as a solvent in mild temperature.[35] The column purification of all the products using a hexane-ethyl acetate mixture yielded a sticky solid with a good yield. All compounds were characterized using standard analytical techniques, including MALDI-TOF mass spectrometry, ^{1}H NMR, ^{13}C NMR, and IR spectroscopy. Thermogravimetric analysis (TGA) was performed to evaluate the thermal stability of the compounds, revealing a decomposition onset temperature of 249-397 °C for 5 wt% decomposition (Table 3.1, Figure 3.3).

3.2.2. Thermal Behaviour

The mesomorphism was initially explored with polarized optical microscopy (POM) with a controllable hot stage to observe optical textures. This method allowed the visualization of the fluidity (in response to mechanical shear) and birefringent patterns by heating the sample at room temperature and cooling it from the isotropic state. While the compounds **PO1-PO3** did not show any such changes, they transformed into isotropic liquid. In contrast, the compound **PO4**, which was a sticky gummy solid, showed birefringence coupled with the fluidity on heating, while cooling from the isotropic liquid showed the formation of a mosaic pattern that is usually observed for columnar phases (Figure 3.3b and Figure 3.4a).[36]

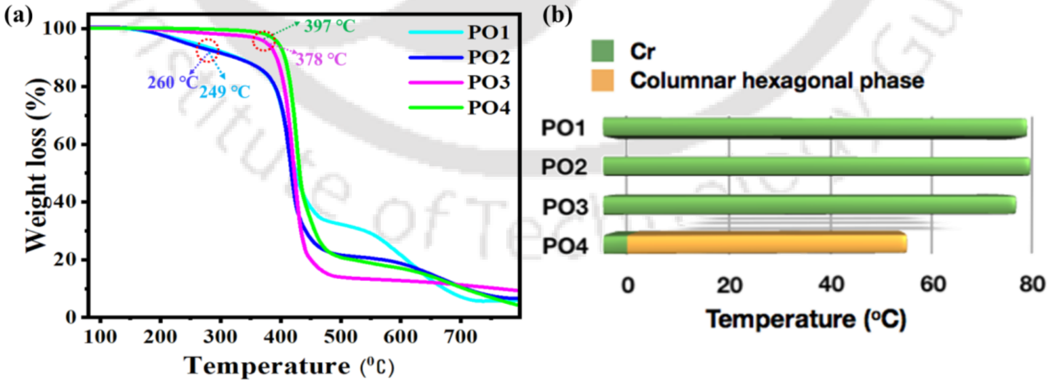

Figure 3.3. (a) TGA plots of compound (heating rate of 10 °C/min, Nitrogen atmosphere). (b) Bargraph representing the mesomorphic behaviors (Considered the first cooling scan of DSC) of **PO** compounds.

The isotropic point of the compound **PO4** was first determined using polarized optical microscopy. The DSC thermograms revealed two distinct transitions upon heating: crystal to mesophase and mesophase to isotropic state, concurrent with the POM observations (Figure

3.4b, Table 3.1, Figure A10). After cooling the isotropic state, two transitions were noticed again, i.e. isotropic to mesophase and mesophase to crystal. Notably, the crystal-to-mesophase transition occurred well below room temperature (at approximately 4 °C, ΔH = 15.8 kJ/mol), confirming the compound's liquid crystalline nature at room temperature. The relatively low clearing point ≈ 53°C (ΔH = 2.0 kJ/mol, Figure 3.4b), makes this compound particularly suitable for device applications.

Table 3.1. Phase transition temperatures (°C), corresponding enthalpies ($kJmol^{-1}$), and decomposition temperatures were obtained from DSC[a] and TGA[b]

Entry	Phase sequence (kJ/mol)[a]		T_5[b] (°C)
	Second Heating	First Cooling	
PO1	Cr 73.9 (41.3) I	G[c]	249
PO2	Cr 74.5 (16.0) I	I 37.8 (11.0) Cr	378
PO3	Cr 72.0 (0.04) I	G[c]	260
PO4	Cr 4.07 (15.8) Col$_h$ 52.7 (2.0) I	I 47.6 (13.8) Col$_h$5.8 (17.6) Cr	397

[a] Peak temperatures in the DSC thermograms obtained during the second heating and first cooling cycles at 5 °C min^{-1}; Col$_h$ = Columnar hexagonal phase; I = Isotropic phase; b = Temperature at which 5 wt% decomposition occurred (°C); c = crystallization is not detected, the compound remains liquid and slowly freezes to a glassy state.

Furthermore, the Powder X-ray diffraction analyses were conducted to unequivocally assign the symmetry of the columnar phases observed at high and low temperatures. A summarized overview of phase transition temperatures and enthalpy values for all compounds investigated is provided in Table 3.1 and Figure A10. The enhanced attractive interactions of the aromatic core complemented with the increased fluidity/nanophase segregation offered by the alkyl chains in compound **PO4** were suggested as contributing factors that realized the liquid crystalline behavior compared to other compounds **PO1-PO3**.

The symmetry of the Col phase exhibited by **PO4** was investigated using powder X-ray diffraction studies at 50 °C and room temperatures. Both the XRD patterns were almost similar. The XRD pattern of **PO4** at 50 °C revealed one distinct Bragg peak in the small-angle region at 30.96 Å, corresponding to the Miller indices (10) (Figure 3.4c; Table 3.2). Though the single peak can not confirm any particular mesophase, in literature, there are many references where such a single peak is assigned to the columnar phase with a hexagonal lattice,[37] with a lattice parameter of a ≈ 35.75 Å. In the wide-angle regime, a d-spacing of 4.71 Å was observed, indicative of the fluid-like packing of alkyl chains. The intracolumnar distance, *i.e.*, the distance between the discs within a column, was 4.19 Å. Thus, the mesophase was confirmed to be a columnar hexagonal phase. The lattice parameters remained almost unchanged over the entire mesophase temperature range (28 °C to 50 °C). The molecular organization within the Col phase was further examined, revealing that approximately two molecules formed a unit cell (Z ≈ 2). A schematic representation (Figure 3.4 d) illustrates the self-assembly of **PO4** molecules into columns, which subsequently organize into a columnar hexagonal lattice. This analysis underscores the unique ability of **PO4** to maintain a stable room temperature Col$_h$ phase (Figure A11), distinguishing it from other phenoxazine derivatives under similar conditions. Thus, the **PO** unit bearing only six peripheral chains exhibits a liquid crystalline phase, while the same bearing lesser chains did not stabilize the liquid crystalline phase; in other words, compound **PO1-PO3** do not efficiently fill the space, while the two molecules **PO4** efficiently fill the space to form a disc-like structure, which then self-assemble to form columnar structures.

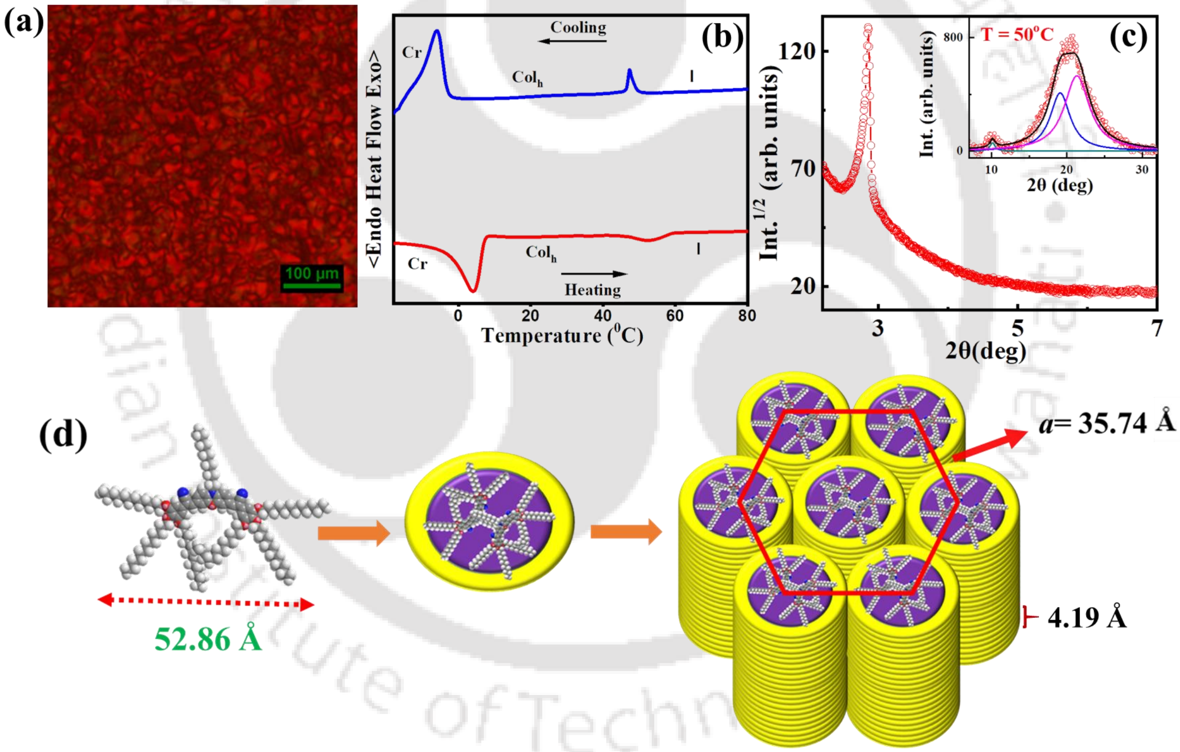

Figure 3.4. (a) POM image obtained for the Col$_h$ phase **PO4** at 50 °C (scale bar corresponds to 100 μm). (b) DSC thermogram was obtained for **PO4** (blue trace, first cooling scan; red trace, second heating scan). (c) X-ray diffractograms for the Col$_h$ phases of **PO4** at 50 °C (insets show the images of the wide-angle region) and (d) the schematic diagram depicting the self-assembly of **PO4** into the Col$_h$ phase at 50 °C.

Table 3.2. Results of (*hkl*) indexation of XRD profiles of **PO**s at a given temperature (T) of mesophase

Compounds (D/Å)	**Phase (T/°C)**	d_{obs} **(Å)**	d_{cal} **(Å)**	**Miller indices *hkl***	**Lattice parameters (Å), Lattice area S (Å^2), Molecular volume (Å^3)**
PO4 (52.68 Å) **MW:** 1711.76	Col$_h$ (50)	30.96 8.74 (d) 4.71(h$_a$) 4.19 (h$_c$)	30.96	10 22	a = 35.75 S = 1106.80 V = 5213.03 Z ≈ 2
	Col$_h$ (28)	31.68 8.70 (d) 4.69 (h$_a$) 4.19 (h$_c$)	31.68	10 22	a = 36.58 S = 1158.79 V = 5434.73 Z ≈ 2

[a]The diameter (D) of the disk (estimated from Chem 3D Pro 8.0 molecular model software from Cambridge Soft). d_{obs}: spacing observed; d_{cal}: spacing calculated (deduced from the lattice parameters; a for Col$_h$ phase; c is the height of the unit cell). The spacings marked h_a and h_c correspond to diffuse reflections in the wide-angle region arising from correlations between the alkyl chains and core regions, d = diffuse peak.

3.2.3. Photophysical properties

The photophysical properties of the four compounds (**PO1, PO2, PO3,** and **PO4**) were studied in both solution and thin film states, with the thin films spin-coated on a quartz substrate. The compounds exhibited good solubility in various solvents of varying polarity like chloroform, THF, cyclohexane, and toluene at a concentration of 1 wt%/vol. Photophysical measurements in solution were conducted using 20 μM chloroform solutions, while 1 wt%/vol. toluene solutions were used to prepare the thin films. The absorption spectra of the **PO** derivatives in micromolar solutions displayed broad absorption bands around 480-485 nm in the more extended wavelength region, indicating effective intramolecular charge transfer (**ICT**) from the electron-donating phenoxazine moiety to the electron-withdrawing cyano vinylene units. The results are summarized in Table 3.3, with Figures 3.5 and A12 illustrating the data. Corresponding emission spectra revealed emission maxima in the 537−545 nm range (Figures 3.5 and A13), with significant Stokes shifts ranging from 2082−2269 cm^{-1} (Table 3.3). These compounds also exhibited high molar extinction coefficients ranging from 15395−27880 L mol^{-1} cm^{-1} (Table 3.3). The optical energy gap, estimated from the absorption onset, was 2.30 eV.

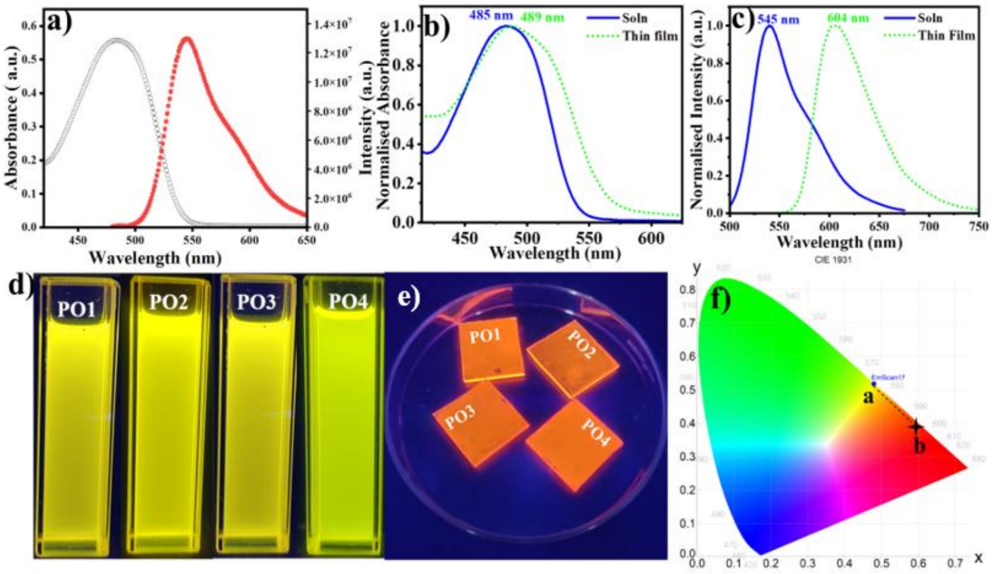

Figure 3.5. (a) Absorption spectra (black) & emission spectra (red) of compound **PO4** solution states. (b) Absorption spectra & (c) emission spectra of compound **PO4** solution and thin film states. (d) Photographs of micromolar solutions of compounds **PO1**− **PO4** in chloroform; (e) spin-coated thin films on quartz plates under UV light of long wavelength (λ = 365 nm). (f) CIE coordinate of emission of **PO4** compound.

Thin films of the compounds on quartz plates displayed broad, red-shifted absorption and emission bands, with the Stokes shift increasing to 3658 cm^{-1}-3851 cm^{-1} compared to the solution state (Figure 3.5 & A14, Table 3.3). The compounds emitted bright yellow fluorescence in the solution, which shifted to orange-red fluorescence in the solid state, as shown by the CIE coordinates, and the position changed from a to b (Figure 3.5c-f).

Table 3.3. Photophysical properties of **PO**s in solution and thin film state

Compd.	Solution State^a						Thin film State^b			
	Absorption [nm]	Emission [nm]	Stokes Shift (cm^{-1})	ε (L mol^{-1} cm^{-1})	ΔE g, opt [eV]	Abs. Q.Y	Abs. [nm]	Emission [nm]	Stokes Shift (cm^{-1})	Abs. Q.Y
PO1	483	537	2082	15395	2.32	36.64	493	602	3672	1.79
PO2	483	540	2185	15395	2.29	42.80	492	600	3658	2.79
PO3	484	542	2210	15095	2.30	24.73	492	606	3823	2.62
PO4	485	545	2269	27880	2.30	25.75	490	604	3851	2.21

This shift in fluorescence emission in longer wavelengths in thin films may be attributed to the non-planarity of the phenoxazine molecule, which reduces nonradiative decay by restricting torsional motion and with further enhancements by appropriate intermolecular arrangements (e.g., *J*-aggregation).[38] The broad absorption bands observed in thin films suggest the formation of excimers (Figures 3.5 b, A14), with a slight bathochromic shift indicative of *J*-type or head-to-tail aggregates. Additionally, a red-shifted λ_{max} peak in the absorption spectra of the **PO**s in the thin film, as shown in Figure 3.5 b, could be explained by short-distance charge transfer interactions that promote coupling among the π-conjugated aromatic cores, enhancing wave function overlap.[39] The fluorescence efficiency of the compounds was assessed by measuring their absolute quantum yields, which ranged from 24% to 43% (Table 3.3, Figures A15). Time-resolved photoluminescence measurements in both solution and thin film states (Figures 3.6 and 3.7) showed that among all the derivatives, **PO4** exhibited the highest lifetime of 2.78 ns in the thin film state (Table 3.4).

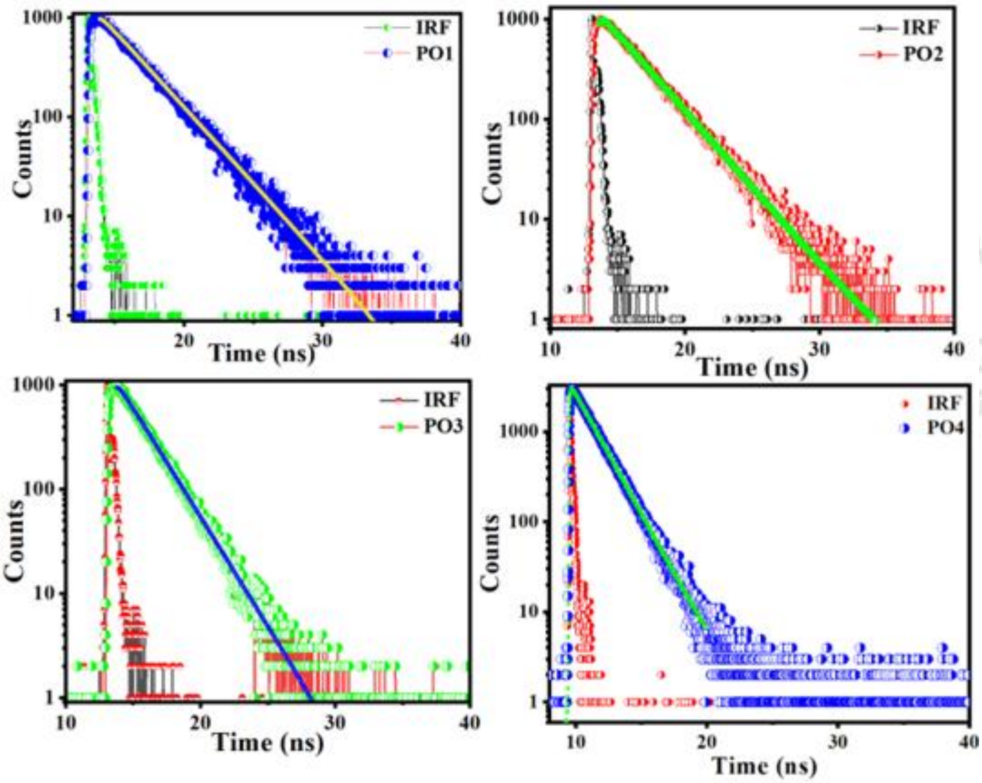

Figure 3.6. Time-resolved PL decay curves of **PO** (**PO1-PO4**) in solutions state.

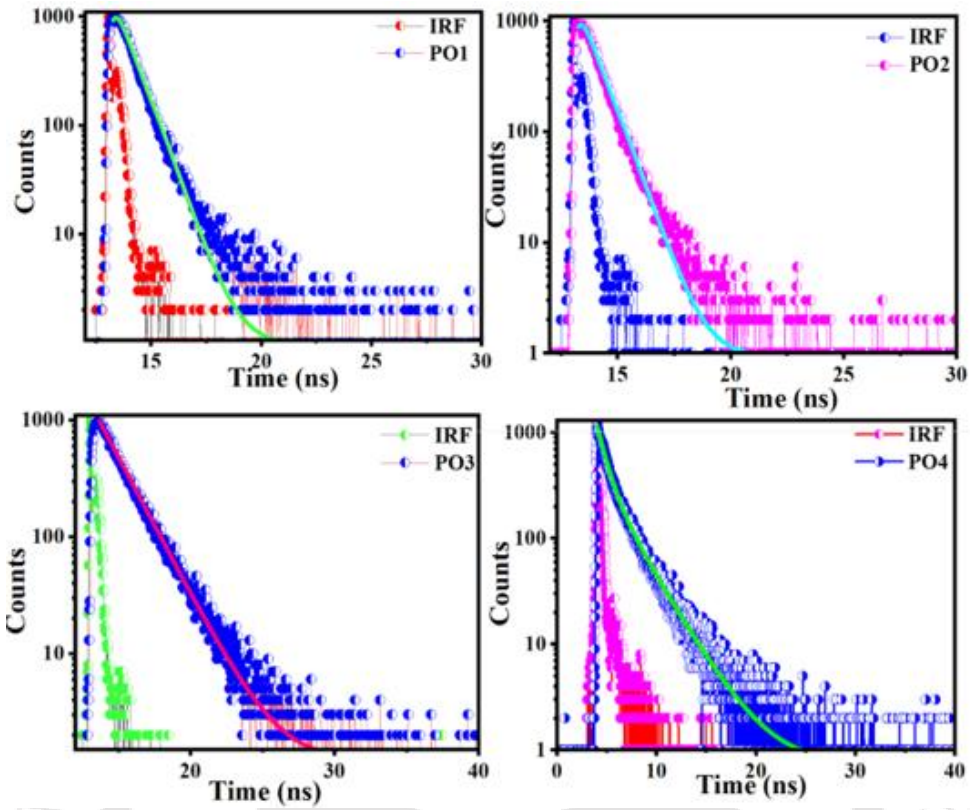

Figure 3.7. Time-resolved PL decay curves of **PO** (**PO1-PO4**) in a thin film state.

Table 3.4. The fluorescence lifetime of **PO**s in solution and thin film state and phosphorescence lifetime in solution

Entry	Fluorescence Lifetime (ns)		Phosphorescence Lifetime (ms)	
	Solution[a]	Thin film[b]	Solutions	
			RT	77K
PO1	2.84	0.76	---	--
PO2	2.82	0.75	---	---
PO3	2.07	1.85	---	---
PO4	2.35	2.78	0.067	2.7

The phosphorescence behavior of the **PO4** compound was investigated at room temperature (RT) and 77 K in THF, as shown in Figure 3.8. Upon irradiation at 485 nm, **PO4** displayed dual emission, consisting of fluorescence and phosphorescence at RT. The phosphorescence peak at 654 nm exhibited a typical emission lifetime of 0.067 ms. At 77 K (Table 3.4), two prominent phosphorescence peaks were observed at 598 and 645 nm, with a phosphorescence decay lifetime of 2.7 ms. The fine vibrational structure observed in the phosphorescence is likely associated with the locally excited (LE) state. Thus, compound **PO4** exhibits weak room-temperature phosphorescence, which increases at 77 K due to the reduced flexibility of the luminescent species, leading to the radiative relaxation processes.[40-43.] From the time-dependent-density functional theory (TD-DFT) calculations, the S_1 and T_1 levels of **PO4** were 2.32 eV and 1.53 eV, with a ΔE_{ST} of 0.79 eV.

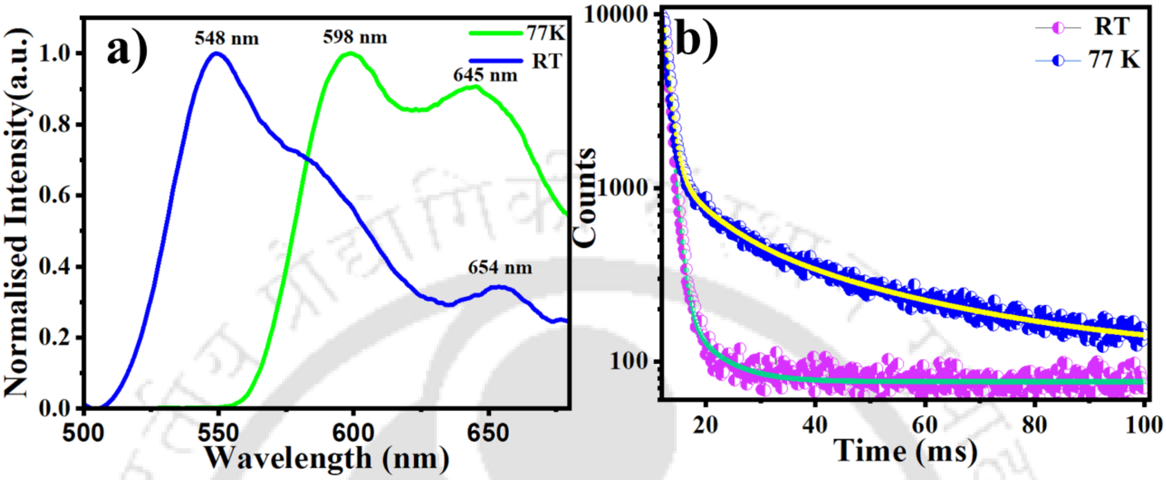

Figure 3.8. (a) Steady-state PL spectra (blue trace) at RT and 77K (green trace) (delay100 µs & 0.1 gatting) of **PO4** and (b) decay lifetime.

3.2.3.1. Solvatochromic effect

To further investigate the nature of the excited state in **PO4**, we examined the solvatochromic behavior by analyzing its absorption and emission spectra in various solvents, ranging from non-polar solvents like hexane to highly polar solvents such as DMSO (Figure 3.9b & 3.9c). **PO4** exhibited a significant positive solvatochromic shift, as shown in Figure 3.9a. The compound displayed greenish fluorescence in the non-polar solvent hexane (f = 0.0012), with absorption and emission maxima at 420 nm and 507 nm, respectively. As the solvent polarity increased, from toluene to chloroform to DMSO (f = 0.313), the emission color progressively shifted from greenish-yellow to yellow and eventually to orange-red (Figure 3.9). This color change was accompanied by a substantial bathochromic shift of 85 nm in the emission spectra of **PO4**. This shift can be attributed to changes in the absorption maximum, which arise from differences in solvation energy between the ground and excited states in various solvents. The red shifted emission in more polar solvents, such as acetone and DMSO, suggests that the excited state, which is more polar than the ground state, becomes more stable, requiring less excitation energy. This results in a bathochromic shift in comparison to non-polar solvents like hexane. This red shift in emission with increasing solvent polarity by stabilization of the excited state is known as positive solvatochromism.[44]

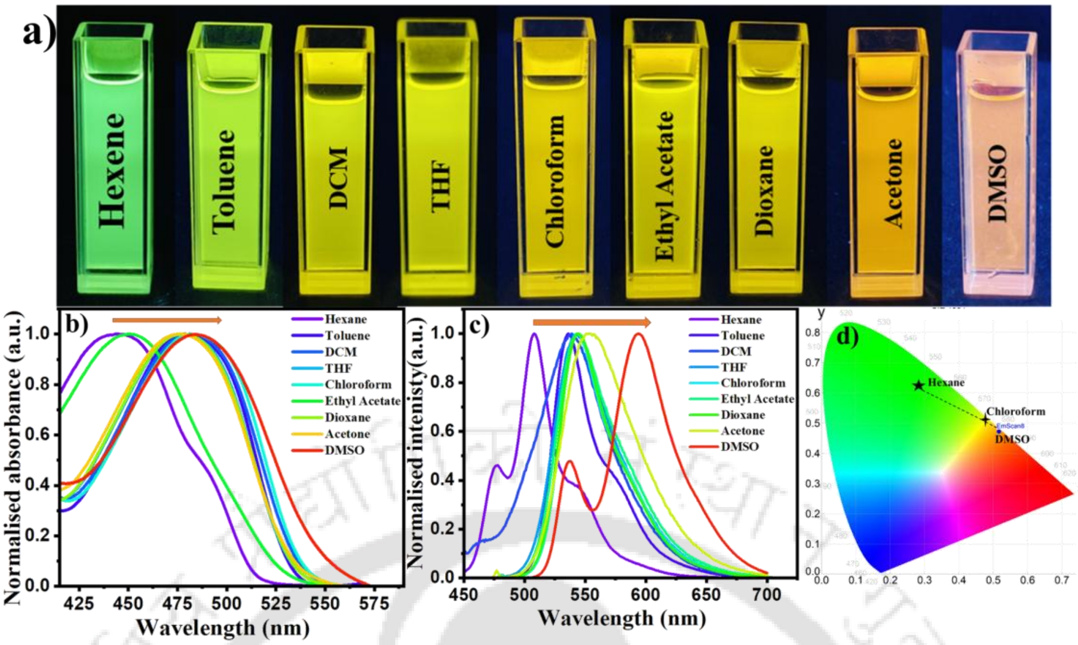

Figure 3.9. (a) A photograph depicting solvatochromism under 365 nm UV irradiation. (b) Absorption & (c) emission spectra (20 µM) in different solvents, and (d) CIE coordinate of showing different colors in different solvents of **PO4** compound.

In a donor-acceptor (D–A) molecule, the low-lying excited state (S_1) can be categorized into three types: a localized π–π* state (LE), a delocalized charge-transfer (CT) state, and a hybridized π–π* and CT state (HLCT).[45] To understand this solvatochromic effect of the low-lying excited state (S_1) of **PO4**, the relationship between the Stokes shift (υ_a - υ_f) and solvent polarity is explored using the Lippert-Mataga plot (Figure 3.10, formula A1, Table A1). As depicted in Figure 3.10, the slope of the plot, which correlates the Stokes shift (υ_a - υ_f) with the solvent polarizability (f (ε, n)), shows a variation between low- and high-polarity solvents. This non-linear behavior suggests that the excited-state S_1 of **PO4** displays a hybridized character, combining both locally excited (LE) and charge transfer (CT) states, *i.e.*, hybridized local and charge-transfer (HLCT) excited states. The nature of the excited state changes with the solvent: in low-polarity solvents such as hexane, the excited state is primarily LE, while in highly polar solvents like DMSO, the excited state is dominated by CT character. In solvents of intermediate polarity, such as dichloromethane and THF, the excited state exhibits a hybrid of both LE and CT characteristics.[46-48]

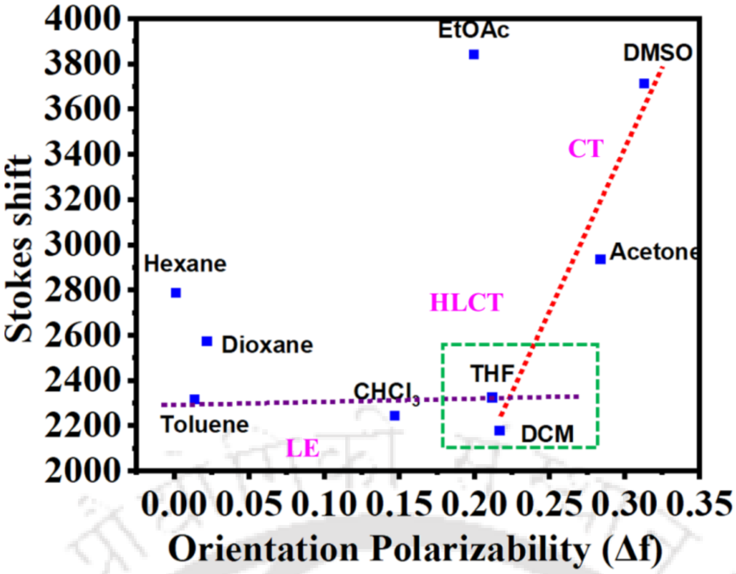

Figure 3.10 Lippert-Mataga plot of compound **PO4** obtained in a diverse range of solvents.

3.2.4. Electrochemical properties

The energy and electron transfer processes, as well as the reversibility of redox reactions, are significantly influenced by the electronic energy levels, particularly the frontier molecular orbitals (HOMO and LUMO levels) of organic semiconductors.

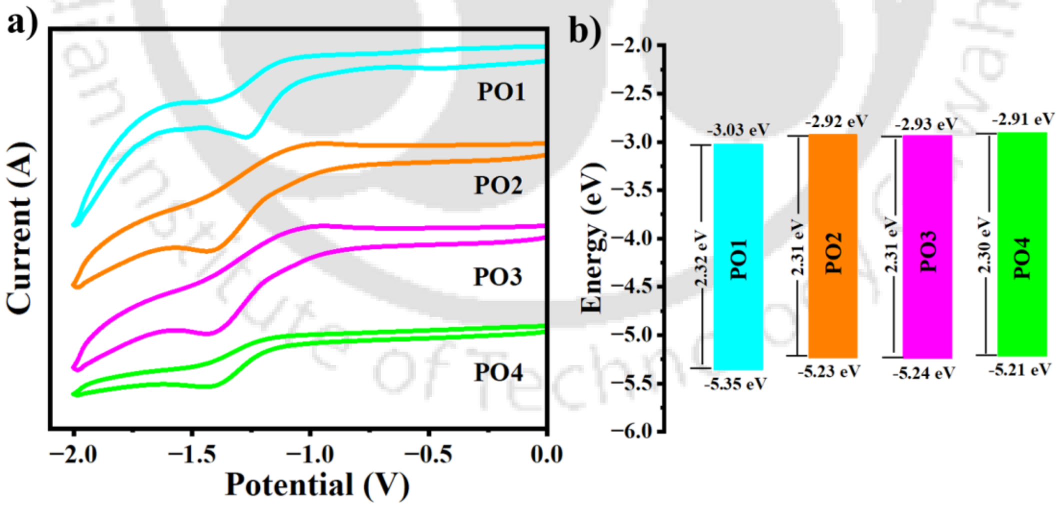

Figure 3.11. (a) Overlay of Cyclic voltammogram of **POs**. (b) Energy band level diagram showing experimental HOMO and LUMO energy levels of **POs**.

These characteristics were investigated through cyclic voltammetry (CV) in 0.5 mM solutions of **PO**s in anhydrous dichloromethane, with 0.1 M tetrabutylammonium perchlorate (TBAP) as the supporting electrolyte and at a scan rate of 100 mV/s. The electrochemical results summarized in Table 3.5, Figures 3.11 and A17, show that compounds **PO1**, **PO2**, **PO3**, and

PO4 exhibited an irreversible first reduction at -1.27, -1.37, -1.36, and -1.38 V, respectively. From these values, the estimated lowest occupied molecular orbital (LUMO) levels of **POs** were found to be -3.03, -2.92, -2.93, and -2.91 eV, respectively. The corresponding highest occupied molecular orbital (HOMO) levels, derived from their optical band gaps ($E_{g,\ opt}$) of 2.32, 2.31, 2.31, and 2.30 eV, were found to be around -5.35, -5.23, -5.24, and -5.21 eV, respectively (see Table 3.5, Figure 3.11). Overall, these results indicate that the number of alkoxy chains has minimal effect on the electrochemical properties of these compounds.

Table 3.5. Electrochemical[a,b] data, and the data obtained from DFT[h] calculations for **POs**

	Electrochemical data				Data from DFT calculation		
Entry	$E_{1st\ red}$ [c]	E_{LUMO} [d,e]	E_{HOMO} [d,f]	$\Delta E_{g,\ (opt)}$ [d,g]	E_{LUMO} [dh]	E_{HOMO} [dh]	ΔE_g [d,h]
PO1	-1.27	-3.03	-5.35	2.32	-2.03	-4.99	2.96
PO2	-1.37	-2.92	-5.23	2.31	-2.06	-4.98	2.92
PO3	-1.36	-2.93	-5.24	2.31	-1.98	-4.90	2.92
PO4	-1.38	-2.91	-5.21	2.30	-2.02	-4.93	2.91

[a] 0.5mM Dichloromethane solutions; [b]experimental conditions: Ag/AgNO3 as reference electrode, glassy carbon working electrode, platinum wire counter electrode, TBAP (0.1M) as a supporting electrolyte, room temperature; [c] in volts (V); [d] in eV; [e] estimated from the formula by using $E_{LUMO} = -(4.8 - E_{1/2}, Fc/Fc^+ + E_{red}, onset)$ eV; [f] estimated from the formula $E_{HOMO} = E_{LUMO}$ - Eg, opt) eV; [g]calculated from the red edge of the absorption band of each compound.$E_{1/2},\ ^{Fc/Fc+}$ = 0.50.[h] Obtained from DFT calculations by employing the combination of Becke3-Lee-Yang-Parr (B3LYP) hybrid functional and 6-31G(d, p) basis set using the Gaussian 09 package.

3.2.5. DFT studies

To investigate the geometry, electronic structure, molecular conformation, and frontier molecular orbitals (FMOs: HOMO and LUMO) of **PO**s, we conducted density functional theory (DFT) calculations using the B3LYP/6-31G (d, p) method. Analysis of the HOMO and LUMO distributions revealed that the energy levels are mainly localized around the central aromatic ring and the phenyl acetonitrile group, as shown in Figure 3.12, A19 and A20. For **PO1**, the calculated HOMO and LUMO energy levels were -4.99 eV and -2.03 eV, respectively, yielding a HOMO–LUMO gap of 2.96 eV. In contrast, the introduction of a tri-*n*-alkoxy chain in the phenyl acetonitrile unit of **PO4** lowered the HOMO energy by 0.04 eV, slightly reducing the HOMO–LUMO gap. However, in **PO2** and **PO3**, the band gap remained nearly the same as in **PO4**. These theoretical results are consistent with the experimental data, confirming the slight decrease in the band gap with the increase in peripheral side chains. The optimized molecular diameters of the **PO**s were approximately 53 Å, as shown in Figure A19 a. The 3D molecular electrostatic potential (MEP) maps reveal electron density concentration around the oxygen atom and CN units of the POs, while the central core remains electron-deficient (Figure 3.12 d). The theoretical band gaps for the **PO**s ranged from 2.96 to 2.91 eV, slightly larger than the optical band gaps, but showed the same trend as presented in Table 3.5.

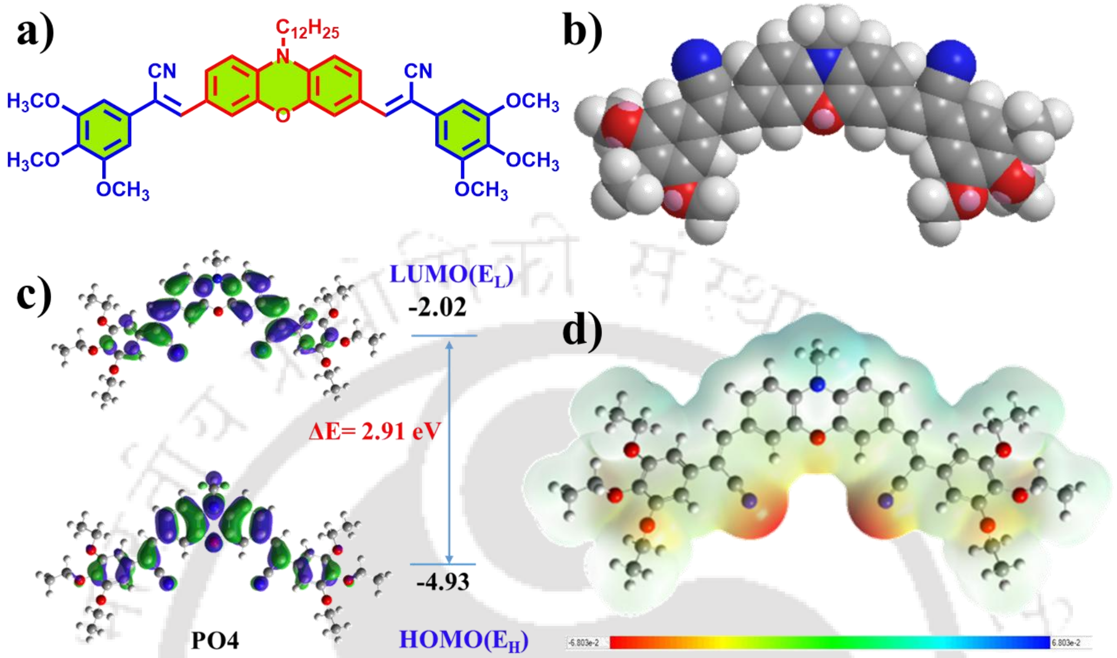

Figure 3.12. Schematic representation of (a) the structure of **PO4,** (b) molecular models, (c) frontier molecular orbitals of **PO4** obtained from DFT calculations at the B3LYP/6-31G (d, p) level, and (d) 3D molecular electrostatic potential contour maps. (E_H and E_L denote the energies of the HOMO and LUMO, respectively (chain length is limited to methyl for the sake of computational time)).

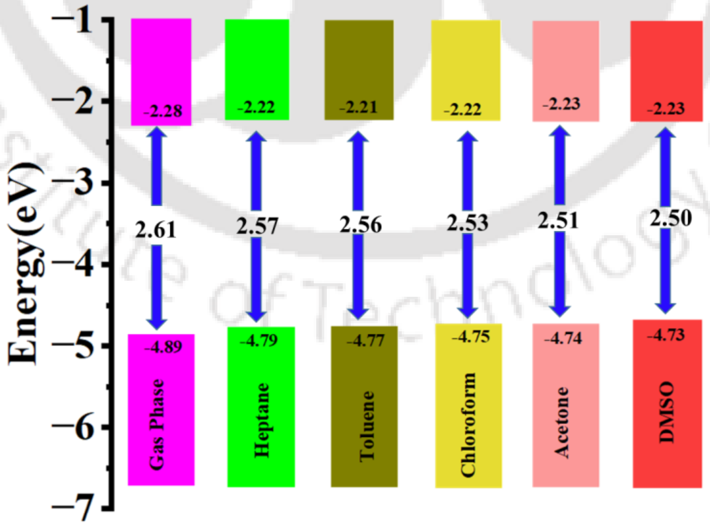

Figure 3.13. Schematic diagram showing the HOMO-LUMO level and energy band-gap performed of compound **PO4** in the gaseous phase, heptane, toluene, chloroform, acetone, and DMSO solvents (TD-DFT studies were calculated at B3LYP/6-31G (d, p), PCM model).

To investigate the HLCT characteristics in the excited state, time-dependent density functional theory (TD-DFT) calculations using the CAM-B3LYP/6-31G (d, p) level of theory were performed to explore the excited-state properties of the first 10 singlets (S_0 to S_{10}) and triplets (T_1 to T_{10}) states (Table A2). The energy difference between the high-lying singlet state S_1 and the triplet state T_3 was 0.31 eV, while the difference between S_2 and T_4 was 0.24 eV. These relatively large ΔE_{ST} values (S_1-T_3 and S_2-T_4) suggest that reverse intersystem crossing (RISC) is unlikely to occur between these states.[53,54] Therefore, RISC is expected to proceed from the triplet state closest to the HLCT singlet state via the hot exciton channel. Due to the narrow energy gaps, hot exciton RISC can occur from T_7 to S_3, with a $\Delta E_{(S3–T7)}$ of 0.03 eV (Figure A21and Table A2).[52,55] Analysis of the natural transition orbitals (NTOs) revealed that some excited states are dominated by local excitation (LE), confirming the presence of LE states (e.g., S_3, S_4, S_5, S_6, S_8, S_9, S_{10}, T_1, T_4, T_5, T_6, T_7 and T_8), where the hole and particle are located in the same fragment. Additionally, states where the hole and particle are located in different fragments indicate charge transfer (CT) excited states dominance (e.g., S_1, S_2, S_7, T_2, T_3, T_9, and T_{10}). As a result, the excited states of **PO4** exhibited HLCT characteristics, showing a combination of both LE and CT states (Figure 3.14, Table A2).[55-65] Fluorescent molecules with HLCT characteristics exhibit higher external quantum efficiency (EQE) above the theoretical limit of 5% in OLED devices, highlighting the potential of **PO4** as an emissive layer in OLEDs.

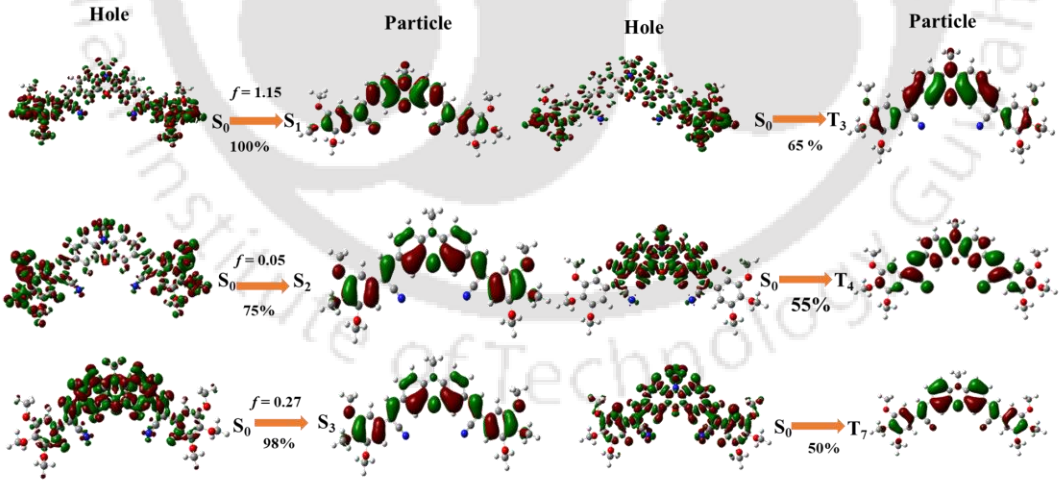

Figure 3.14. Natural transition orbitals (NTOs) of S_1/S_2/S_3/T_3/ T_4/ T_7 (f: oscillator strength).

The TD-DFT study of **PO4** in the gaseous state and different solvents further supports the bathochromic shift from nonpolar to polar solvents, as shown in Figure 3.13. With increasing solvent polarity from heptane to DMSO, the HOMO-LUMO gap decreases from 2.57 eV to 2.50 eV, and the ΔE_{ST} value decreases from 0.79 eV to 0.60 eV (Table 3.6).

Table 3.6. Theoretical TD-DFT calculations of **PO4**.

TD-DFT analysis						
PO4 (Phase/ solvent)	S_1	T_1	ΔE_{ST} (eV)	HOMO (eV)	LUMO (eV)	ΔE_g (eV)
Gas phase	2.32	1.53	0.79	-4.89	-2.28	2.61
Heptane	2.20	1.52	0.68	-4.79	-2.22	2.57
Toluene	2.18	1.52	0.66	-4.77	-2.21	2.56
Chloroform	2.16	1.51	0.65	-4.75	-2.22	1.15
Acetone	2.15	1.50	0.65	-4.74	-2.23	2.51
DMSO	2.14	1.50	0.64	-4.73	-2.23	2.50

3.2.6. Morphology studies

The morphology of the **PO4** compound spin-coated onto ITO-coated glass substrates was analyzed using atomic force microscopy (AFM) and field-emission scanning electron microscopy (FESEM). AFM images indicated a smooth surface with a roughness of 2.7 nm (Figure 3.15 b), while FESEM images showed a uniform surface for **PO4** (Figure 3.15 a). This smooth film formation of **PO4** is a requirement to achieve consistent and reliable results in organic electronic devices. The AFM and FESEM images of the drop cast of all **PO**s are shown in Figure A18.

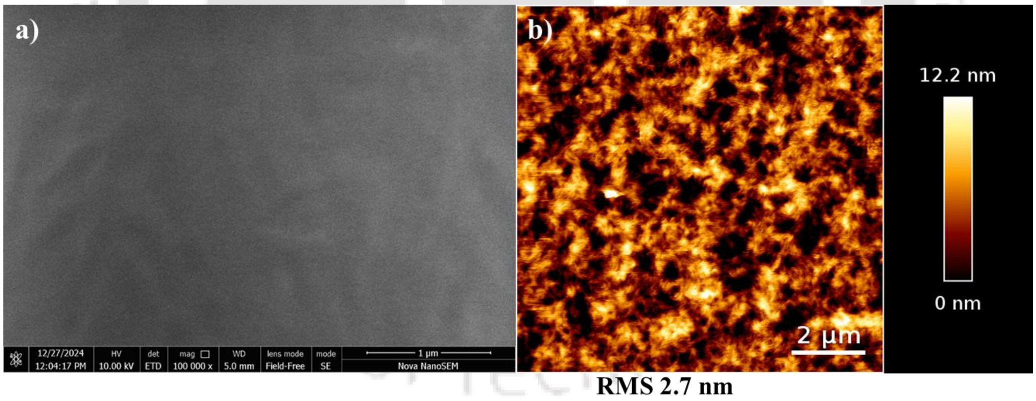

Figure 3.15. (a) The SEM image and (b) AFM image of compound **PO4** solution in chlorobenzene were spin-coated on ITO-coated glass substrate, respectively.

3.3. Charge carrier mobility studies

The charge-carrier mobilities of the liquid crystal **PO4** were determined by measuring its current density-voltage (J–V) characteristics in a device configuration where the material was

(3.1)

sandwiched between two electrodes. The space-charge-limited currents (SCLC) were analyzed using the Mott–Gurney equation (Eq. 3.1):

$$J = \frac{9}{8}\varepsilon_0\varepsilon_r\mu\frac{V^2}{L^3} \tag{3.1}$$

Where J is the current density, ε_r is the dielectric constant of the **PO4**, $\varepsilon_0$is the permittivity of free space, μ is the charge carrier mobility, L is the thickness of the **PO4** layer, and V is the voltage drop across the device. This method provides an estimate of the material's bulk charge-carrier mobility.

Two distinct SCLC cells were fabricated to investigate the ambipolar charge transport properties of the material: one for hole mobility and the other for electron mobility. Hole-only devices (HODs) consisted of an ITO/PEDOT: PSS bottom layer and a MoO_3/Ag top layer, while electron-only devices (EODs) employed an ITO/ZnO bottom layer and a PDINN/Ag top layer. The liquid crystal layer thickness in both single-carrier devices was approximately 100 nm, and the dielectric constant, calculated from capacitance-frequency measurements, was 3.95 nF (Figure A22). The SCLC data and the corresponding fits according to Equation 3.1 are shown in Figures 3.16(a) and 3.16(b), with the device structure depicted in the inset. The charge-carrier mobility, calculated using Equation (3.1), is 1.92×10^{-4} $cm^2V^{-1}s^{-1}$ for the hole-only device and 1.19×10^{-4} $cm^2V^{-1}s^{-1}$ for the electron-only device, confirming the ambipolar nature of the material. The charge carrier mobilities are comparable to other organic semiconductors with similar structures (Table A3).[62-70]

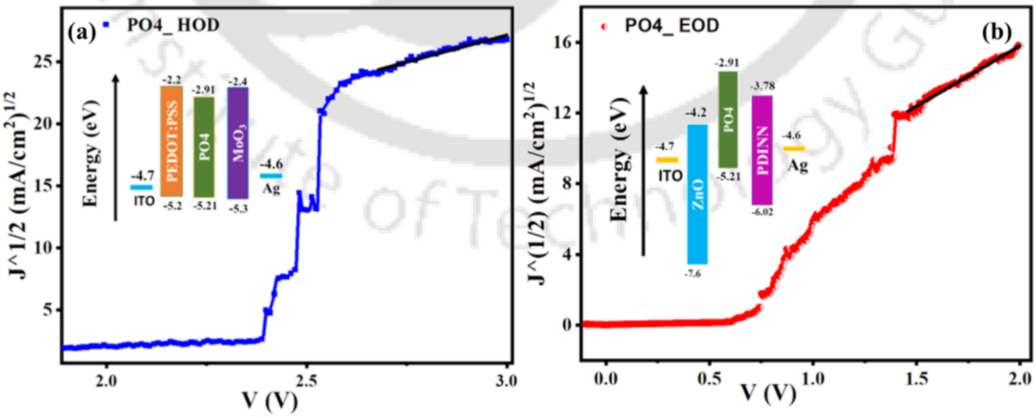

Figure 3.16. J-V characteristics of (a) the hole-only device and (b) electron-only device in the dark (inset: device structures).

3.4. Bioimaging studies

Fluorescent compounds continue to drive significant advancements in the field of bioimaging. The compound **PO4** exhibited exceptional fluorescence properties and a high quantum yield, highlighting its potential as an effective agent for nematode cell imaging studies. Its low crystallization tendency and robust fluorescence characteristics made it well-suited for such applications. Nematodes are commonly used as model organisms in scientific research due to their simple anatomy, well-understood biology, and adaptability across various experimental setups. Their unsegmented, cylindrical body, short lifecycle, and straightforward anatomical structure make them ideal for studying biological processes and disease mechanisms. Furthermore, their ease of cultivation and minimal maintenance contribute to their widespread laboratory use. Numerous studies have established nematodes as a reliable model for toxicological evaluations, particularly in assessing the effects of chemical probes.[71,72]

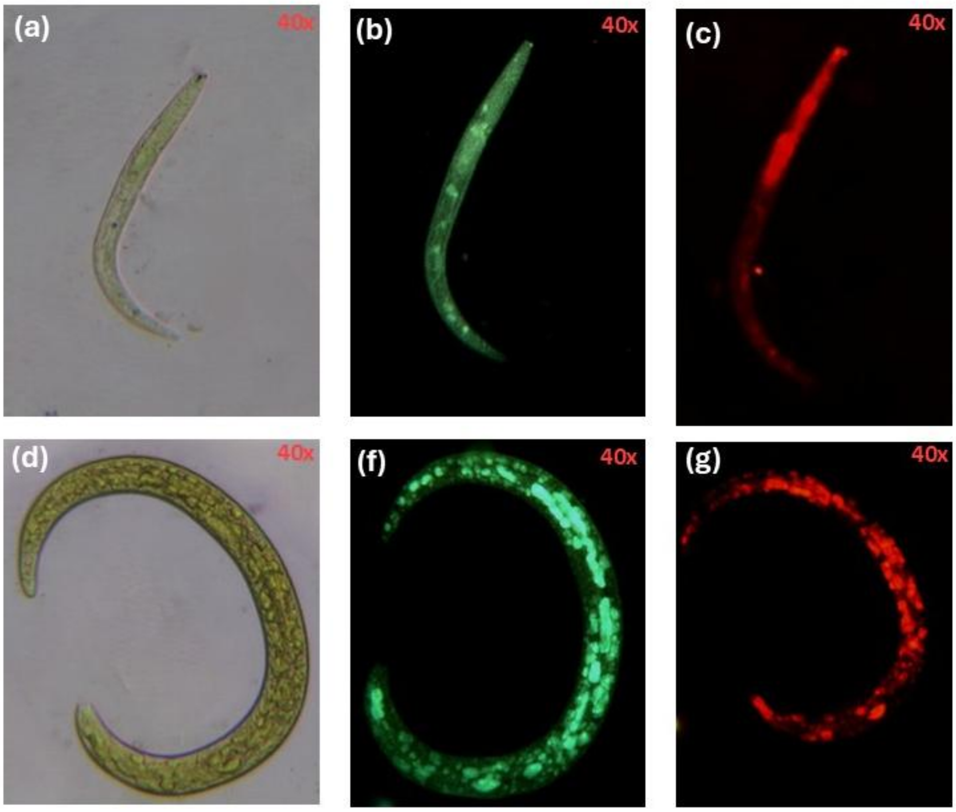

Figure 3.17. Exposure of nematodes to compound **PO4** in THF (10 µM) under different filters (a, d) white light; (b, f) with blue filter and (c, g) with green filter.

A solution of compound **PO4** was prepared in THF solvent and introduced to nematodes for imaging (Figure 3.17). Although the compound exhibited aggregation-caused quenching (ACQ) in aqueous media, it showed excellent imaging results when dissolved in THF due to its enhanced fluorescence, particularly when viewed under green and blue filters in fluorescence microscopy. The compound stained the entire body of the nematode, allowing for detailed visualization of its anatomical and cellular structures. This uniform staining highlights its potential as a reliable tool for advanced imaging in biological research. Notably, no crystallization was observed at room temperature, ensuring the compound's even dispersion within the nematodes. This consistent distribution allowed for thorough and effective staining of the entire organism, providing precise and reliable insights into the nematode's anatomy and internal structures.

The fluorescence observed in the nematodes indicated that the compound could permeate the organism effectively. Notably, no visible damage was detected, demonstrating the biocompatibility of the phenoxazine-based fluorescent luminophore for biological applications. To further evaluate its effectiveness, the luminophore solution was diluted to 10 μM and introduced to multiple nematodes (Figure 3.18). Fluorescence microscopy revealed that all the nematodes absorbed the solution, resulting in uniform staining of their internal and external surfaces. Observations were made using simple light microscopy and blue and green fluorescence filters. At lower concentrations, the luminophore showed reduced crystallization tendencies and moderate fluorescence permeability, suggesting that imaging selectivity could be finely tuned by adjusting the compound concentration. In the early stages, the motility of the nematodes was tracked, demonstrating the utility of this method for real-time monitoring of their movement. This approach allows for direct visualization of nematode locomotion, offering valuable insights into their dynamics, responses to external stimuli, and environmental interactions. These capabilities are beneficial for studying nematode biology and have potential applications in parasitology, toxicology, and ecological research. The findings also highlight the broader applicability of phenoxazine-based luminophores for cellular imaging beyond nematodes. In addition, freely moving nematodes during imaging suggest the absence of acute toxic effects, further supporting the non-toxic nature of **PO4** in a living system. No signs of cellular damage were observed in our biological studies, providing initial evidence of biocompatibility.

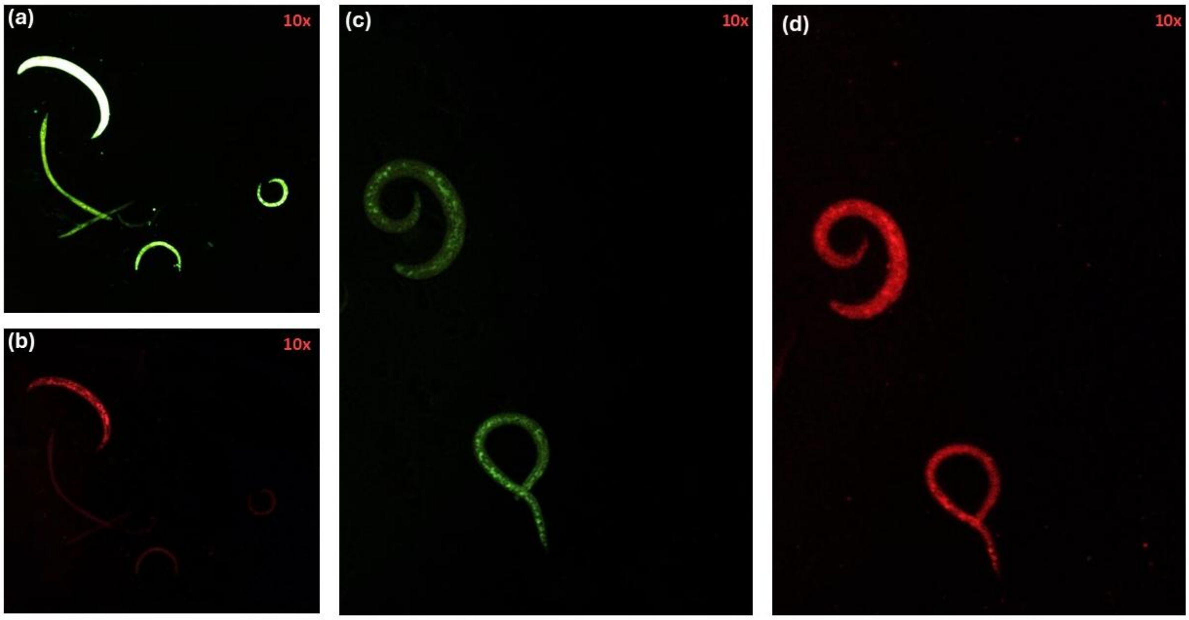

Figure 3.18. Exposure of multiple nematodes to a solution of compound **PO4** in THF (10 μM) was observed under different filters (a–f).

Light-emitting compounds in imaging have become a cornerstone in cancer diagnostics and treatment, greatly enhancing the contrast between well-perfused and poorly perfused regions within cancer cells. Inspired by the promising performance of the phenoxazine-functionalized compound **PO4** in nematode cell imaging, we are excited to explore its potential in advancing bioimaging applications, particularly for targeting the MCF7 human breast cancer cell line. Using fluorescence microscopy, we captured detailed images of **PO4**-stained cancer cells, enabling a thorough examination of cellular morphology and histology. This high-resolution technique revealed even the most minor clusters of cells, which traditional imaging methods might miss, and holds promise for adapting to a wide range of cancers, potentially integrating with other imaging modalities to enhance diagnostic precision.[73] Investigating changes in cell morphology is vital in cancer research, as these alterations can profoundly impact cell growth, gene expression, and overall behavior. Our observations of **PO4**-stained cells show a remarkable improvement in cellular visibility compared to unstained cells, with even minor, previously indiscernible cells detected through fluorescence imaging. These compounds enable efficient and precise staining of cancer cells with minimal spectral overlap, significantly reducing background interference and enhancing imaging clarity.[74] Recent strides in cancer research have highlighted the value of single-cell analysis, providing a clear, temporal, and spatial understanding of apoptosis—the process of programmed cell death.[75]This approach allows researchers to individually track the events leading to cell death, revealing insights often hidden in bulk-cell analyses. Studying a single cell also eliminates distractions from neighboring cells, offering a focused investigation of the unique or pathological features specific to cancer cells.[76]

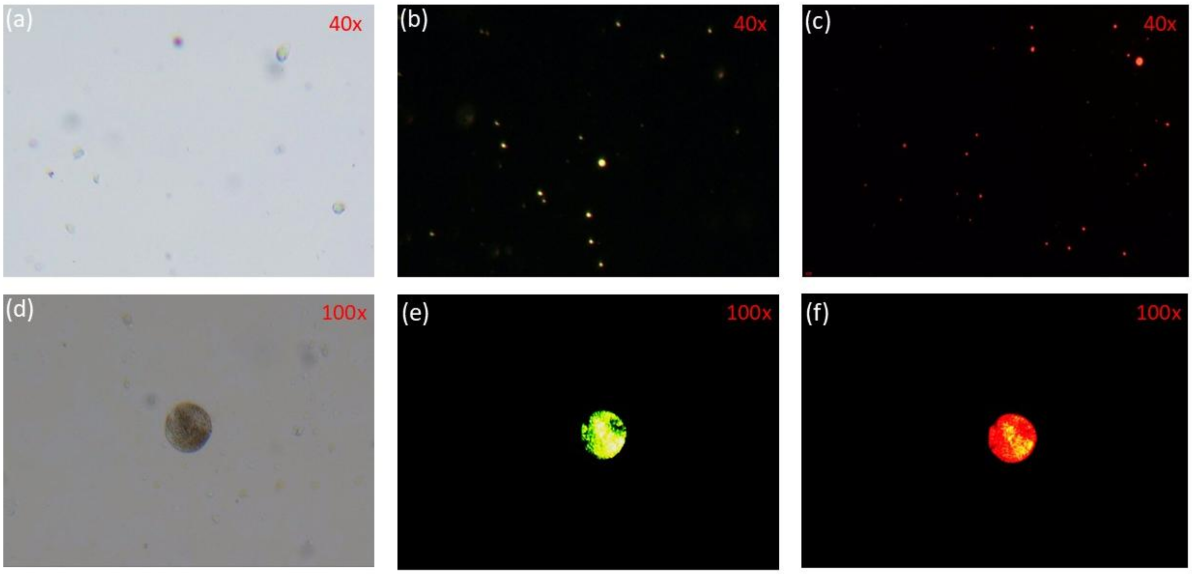

Figure 3.19. Fluorescent staining of MCF7 cancer cells using compound **PO4**. Panels (a) and (d) show unstained normal cells as controls. Panels (b) and (e) display stained cells observed under a blue filter, while panels (c) and (f) display the same under a green filter.

The uptake of compound **PO4** into MCF7 cells was examined using fluorescence microscopy with various RGB filters. The results revealed that the probe efficiently penetrated the plasma membrane, resulting in distinct and compelling staining of the cancer cells, highlighting its potential for bioimaging applications. In cancer research assays, DMSO is commonly used as a solvent to facilitate the uptake of staining compounds, and this approach was also applied to compound **PO4**. Intense fluorescence staining was observed under different filters, suggesting a strong affinity due to π-π stacking interactions from the compound's rigid aromatic structure, which enhances its specificity and binding efficiency in cellular environments.[77] When the stained cells were viewed through a green filter, they emitted bright red fluorescence (Figure 3.18 c, f), which became even more intense at higher resolutions. At lower resolutions, even smaller cells were visible. In contrast, blue filters produced green images (Figure 3.19 b, e) with relatively lower fluorescence intensity, providing more apparent cell outlines and transparent visualizations. Higher magnification imaging was employed to capture clear, localized fluorescence signals, allowing for accurate visualization of intracellular changes that might not be evident at lower magnifications. This strategy minimizes the risk of misinterpretation and enhances data reliability. Both lower and higher magnifications were used to ensure an unbiased and precise analysis of **PO4**-stained cells. Additionally, regions with a dense cell population were prioritized (Figure 3.19 d, f) to optimize imaging conditions, reduce background noise in high-magnification images, and improve clarity and fluorescence specificity. Combining these techniques achieved more detailed morphological observations essential for diagnostic purposes. Notably, the intense staining did not cause any visible changes in cell morphology, indicating that the compound does not induce membrane disruption or cell death. Furthermore, it produced rapid effects without requiring intricate procedures during staining, making it a user-friendly technique. These findings suggest that the compound selectively interacts with cellular structures while enhancing imaging clarity. The compound maintained its functional state throughout the staining process, with no solidification or precipitation occurring at room temperature. This stability is attributed to functionalizing a central hydrophobic aromatic phenoxazine core with terminally substituted aliphatic alkyl groups, reducing the compound's crystallinity. This structural design promotes efficient cell membrane penetration while maintaining interactions with intracellular targets and active sites. The results highlight the compound's potential as a reliable fluorescent probe for imaging breast cancer cells. It provides vigorous fluorescence intensity without compromising cell integrity, reduces background noise, and ensures consistent and uniform staining.[78] To accurately quantify fluorescence intensity, as raw intensity measurements could underestimate staining in flattened cells compared to rounded ones, we calculated corrected total cell fluorescence (CTCF) using Image J 1.54f software. This analysis confirmed that the green and blue filters consistently produced the most potent signals (Figure A23).

In the literature, Ma et al. and Palanisamy et al. reported that phenoxazine-based probes had detection limits ranging from 0.11 μM to 0.60 μM for bioimaging in live cells and zebrafish.[6,7] In contrast, **PO4** exhibited exceptional fluorescence imaging capabilities at an ultra-low concentration of 0.0004 μM, orders of magnitude lower than previously reported probes. This remarkable sensitivity highlights **PO4**'s superior imaging potential without direct quantitative fluorescence intensity comparisons. Our study, **PO4,** demonstrated high quantum yields (24–43%) and significant Stokes shifts (2082−2269 cm^{-1} in solution and 3658−3851 cm^{-1} in thin films), contributing to enhanced imaging contrast. Additionally, PO4 exhibited excellent photostability, retaining its fluorescence intensity during extended imaging sessions without significant photobleaching or signal loss. Unlike conventional fluorescent stains, which often suffer from high background noise and stability concerns, **PO4** showed strong fluorescence in both solution and solid states, facilitating uniform and high contrast staining in MCF7 cancer cells and nematodes. Furthermore, the hybridized localized and charge-transfer (HLCT) behavior in **PO4** enhances emission efficiency, balancing brightness and stability.

Techniques such as Forster Resonance Energy Transfer (FRET) could be employed to study molecular interactions. At the same time, super-resolution microscopy (e.g., STORM and PALM) could provide nanoscale imaging of cancer structures.[79] Additionally, approaches like Multiphoton Microscopy (MPM) and Fluorescence Lifetime Imaging Microscopy (FLIM) offer deep tissue penetration and metabolic insights, respectively, which could further expand the applicability of **PO** molecules in biomedical imaging (Provenzano et al., 2009).[80] Future studies can explore these integrations to maximize PO molecules' diagnostic and analytical potential in future cancer research.

3.5. Conclusions

In conclusion, we have developed and characterized a new series of phenoxazine (**PO**) derivatives. One of these derivatives stabilizes a room-temperature columnar hexagonal phase while retaining its luminescent properties in the solid state. All the compounds showed high absorption coefficients and significant Stokes shifts. In solution, they emitted in the yellow region, but in the solid state, their fluorescence shifted to the orange-red region due to *J*-aggregation. Notably, the **PO4** derivative exhibited phosphorescence at 77 K and displayed positive solvatochromism with hybrid localized and charge-transfer (HLCT) characteristics. **PO4** demonstrated ambipolar behavior, with hole and electron mobilities of 1.92×10^{-4} $cm^2V^{-1}s^{-1}$ and 1.19×10^{-4} $cm^2V^{-1}s^{-1}$, respectively. Additionally, **PO4** showed excellent permeability in nematodes, efficiently crossing cellular membranes and distributing uniformly across tissues. Imaging studies at room temperature revealed its remarkable permeability, high intensity, and resistance to crystallization interference. Overall, the distinctive structural and photophysical properties of **PO4** position it as a reliable and efficient fluorescent probe for imaging MCF7 cancer cells. Its intense fluorescence, minimal background interference, and compatibility with standard imaging techniques make it a promising tool for advancing cancer diagnostics and research.

3.6. Experimental section

This section presents the detailed synthesis procedure and the molecular structural characterization data for the intermediates and target compounds mentioned in the scheme. [81,82]

Procedure for the synthesis of ethyl 3,4,5-tri(dodecyloxy) benzoate (3) [81,82]

A mixture of ethyl gallate (15.1 mmol, 1equiv.), anhydrous K_2CO_3 (99.7 mmol, 6.6 equiv.), and *n*-bromododecane (50.5 mmol, 3.3 equiv.) were taken in dry DMF (40 mL) and heated at 80 °C for 24 h under a nitrogen atmosphere. Then, the reaction mixture was poured into ice water and extracted with ethyl acetate. The combined extract was washed with water and brine, later dried over anhydrous Na_2SO_4, and concentrated. The crude product was purified by column chromatography on silica (100-200). Elution with hexanes followed by 5-10% ethylacetate-hexanes yielded the desired product.

R_f = 0.61(10% EtOAc-hexanes); white solid; yield: 90%; IR: ν_{max} in cm^{-1} 2924, 2853, 1716, 1590, 1504, 1465, 1432, 1333, 1222, 1119; ^1H NMR (600 MHz, $CDCl_3$, ppm): δ 7.25 (s, 2H, H_{Ar}), 4.37 (q, *J* = 6 Hz, 2H, OCH_2), 4.02 (t, *J* = 6 Hz, 6H, 3×-OCH_2), 1.83 (m, 4H, 2×-CH_2), 1.76 (m, 2H, CH_2), 1.49 (m, 6H, 3×-CH_2), 1.39 (t, *J* = 6 Hz, 3H, CH_3), 1.26 (bm, 48H, 24×-CH_2), 0.88 (t, *J* = 6 Hz, 9H, 3×-CH_3). ^{13}C NMR (150 MHz, $CDCl_3$, ppm): δ 166.45, 152.81,142.35, 125.05, 108.02, 73.47, 69.18, 64.10, 60.92, 31.96, 31.64, 29.77, 29.75, 29.74, 29.71, 29.68,29.65, 29.41, 29.38, 29.34, 26.10,22.70, 14.40,14.10. MALDI-TOF mass calculated for $C_{45}H_{82}O_5$ $(M+ Na)^+$: 725.62, found: 725.623

Procedure for the synthesis of 3,4,5- tridodecyloxy benzyl alcohols (4) [82]

To a stirred suspension of lithium aluminum hydride (LAH) (4.26 mmol, 1.5 equiv.) in dry THF (20 mL) under a nitrogen atmosphere, added the solution of ethyl 3,4,5-tri(dodecyloxy) benzoate (2.84 mmol, 1 equiv.) in dry THF dropwise at 0 °C. Then, the reaction mixture was allowed to reach room temperature and stirred for 2 h. The addition of moist sodium sulfate quenched the excess LAH present. The reaction mixture was extracted with EtOAc (6 × 30 mL). The combined extracts were washed with water, dried over anhydrous Na_2SO_4, and concentrated in a vacuum. Purification was done by column chromatography over silica gel (60-120) with 10% EtOAc-hexanes as eluent.

R_f = 0.15 (10% EtOAc-hexanes), white solid, yield: 80%; IR: ν_{max} in cm^{-1} 3417, 2922, 2852.51, 1590, 1467, 1438, 1334, 1231, 1124, 806, 722, 466; ^1H NMR (600 MHz, $CDCl_3$, ppm): δ 6.55 (s, 2H, H_{Ar}), 4.59 (s, 2 H, CH_2), 3.98 (t, *J* = 6Hz, 4H, 2×-OCH_2), 3.93 (t, *J* = 6Hz, 2H, -OCH_2), 1.80 (m, 6H, 3×-CH_2), 1.47 (m, 6 H, 3×-CH_2), 1.33 (bm, 48 H, 24×CH_2), 0.88 (t, *J* = 6 Hz, 9H, 3×-CH_3); ^{13}C NMR (150 MHz, $CDCl_3$, ppm): δ 153.29, 137.61, 136.04, 105.37, 73.45, 69.13, 65.09, 31.96, 31.94, 30.34, 29.77, 29.75, 29.72, 29.67, 29.64, 29.44, 29.41, 29.38, 26.16, 26.12,22.71, 14.12, MALDI-TOF mass calculated for $C_{43}H_{80}O_4$ $(M+ Na)^+$: 683.61, found: 683.613

Procedure for the synthesis of 3,4,5- tridodecyloxy benzyl chloride (5) [82]

3,4,5- tridodecyloxy benzyl alcohol (1.78 mmol, 1equiv.) was dissolved in Dry DCM (20 mL) with stirring and cooled to 0 °C under Ar atmosphere. $SOCl_2$ (3.18 equiv.) was added to the above reaction mixture and stirred at room temperature for 2 h. The reaction mixture was slowly quenched with saturated $NaHCO_3$. The reaction mixture was extracted with methylene chloride, and the organic layer was washed with saturated brine solution and dried over anhydrous Na_2SO_4. A light yellowish-white solid was obtained after the removal of the solvent and used without further purification for the next step of the reaction.

Procedure for the synthesis of 2-(4-(dodecyloxy) phenyl) acetonitrile (6a) [81]

1-(chloromethyl)-4-(dodecyloxy) benzene (4.03 mmol, 1equiv.), and Sodium cyanide (20.19 mmol, 5 equiv.) was dissolved in DMF (20 mL). The mixture was stirred at 100 °C for 18 h. The reaction mixture was poured into water and extracted with DCM. The combined organic layers were washed with water and brine, and anhydrous Na_2SO_4 was dried and concentrated in vacuo. The crude product was purified by column chromatography using a 5-10% ethyl acetate-hexane system to get the pure product as a white solid.

R_f = 0.50 (10% EtOAc-hexanes), white solid, yield: 70%; IR: ν_{max} in cm^{-1} 2960, 2932, 2847, 2288, 1588, 1509, 1469, 1449, 1393, 1330, 1250, 1239, 1124, 820, 723; ^1H NMR (600 MHz, $CDCl_3$, ppm): δ 7.22 (d, J = 9 Hz, 2H, H_{Ar}), 6.89 (d, J = 9 Hz, 2H, H_{Ar}), 3.94 (t, J = 6.6 Hz, 2H, OCH_2), 3.67 (s, 2H, CH_2), 1.79 (m, 2H, CH_2) 1.45 (m, 2H, CH_2), 1.30 (bm, 16 H, 8×-CH_2), 0.88 (t, J = 6.6 Hz, 3H, CH_3).^{13}C(150MHz, $CDCl_3$, 25 °C): δ 158.94, 129.04, 121.53, 118.25, 115.10, 68.16, 31.93, 31.44, 30.20, 29.67, 29.65, 29.61, 29.58, 29.40, 29.36, 29.22, 26.03, 22.832, 22.70, 14.13. MALDI-TOF mass calculated for $C_{20}H_{31}NO$ $(M+Na)^+$: 324.24, found: 324.192.

Procedure for the synthesis of 2-(3,4-bis(dodecyloxy)phenyl) acetonitrile (6b) [81]

4-(chloromethyl)-1,2-bis(dodecyloxy)benzene (5.72 mmol, 1equiv.), and Sodium cyanide (28.62 mmol, 5 equiv.) was dissolved in DMF (20 mL). The mixture was stirred at 100 °C for 18 h. The reaction mixture was poured into water and extracted with DCM. The combined organic layers were washed with water and brine, and anhydrous Na_2SO_4 was dried and concentrated in vacuo. The crude product was purified by column chromatography using a 5-10% ethyl acetate-hexane system to get the pure product as a white solid.

R_f = 0.52 (10% EtOAc-hexanes), white solid, yield: 68%; IR: ν_{max} in cm^{-1} 2955, 2921, 2855, 2247, 1595, 1506, 1469, 1443, 1393, 1337, 1250, 1236, 1124, 820, 728; ^{1}H NMR (600 MHz, $CDCl_3$, ppm): δ 6.85 (d, J = 10.2 Hz, 2H, H_{Ar}), 6.81 (s, 1H, H_{Ar}), 3.98 (m, 4H, 2×-OCH_2), 3.64 (s, 2H, CH_2), 1.81 (m, 4H, 2×-CH_2) 1.41 (m, 4H, 2×-CH_2), 1.26 (bm, 32 H, 16×-CH_2), 0.88 (t, J = 7.8 Hz, 6H, 2×-CH_3).^{13}C (150MHz, $CDCl_3$, 25 °C): δ 149.62, 148.97, 122.17, 120.33, 118.22, 114.10, 113.45, 69.40, 63.10, 32.82, 31.94, 29.71, 29.67, 29.64, 29.43, 29.38, 29.26, 26.03, 23.18,22.70, 14.12. MALDI-TOF mass calculated for $C_{32}H_{55}NO_2$ (M+Na)$^+$: 508.42, found: 508.451.

Procedure for the synthesis of 2-(3,5-bis(dodecyloxy)phenyl) acetonitrile (6c) [81]

1-(chloromethyl)-1,3-bis(dodecyloxy)benzene (4.03 mmol, 1equiv.), and Sodium cyanide (20.19 mmol, 5 equiv.) was dissolved in DMF (20 mL). The mixture was stirred at 100 °C for 18 h. The reaction mixture was poured into water and extracted with DCM. The combined organic layers were washed with water and brine, and anhydrous Na_2SO_4 was dried and concentrated in vacuo. The crude product was purified by column chromatography using a 5-10% ethyl acetate-hexane system to get the pure product as a white solid.

R_f = 0.52 (10% EtOAc-hexanes), white solid, yield: 66%; IR: ν_{max} in cm^{-1} 2954, 2918, 2850, 2246, 1595, 1509, 1469, 1443, 1399, 1337, 1259, 1238, 1124, 820, 729; ^{1}H NMR (600 MHz, $CDCl_3$, ppm): δ 6.49 (s, 2H, H_{Ar}), 6.37 (s, 1H, H_{Ar}), 4.62 (d, J = 6 Hz, 2H, CH_2), 3.94 (t, J = 6.6 Hz, 4H, 2×-OCH_2), 1.75 (m, 4H, 2×-CH_2) 1.42 (m, 4H, 2×-CH_2), 1.30 (bm, 32 H, 16×-CH_2), 0.87 (t, J = 6.6 Hz, 6H, 2×-CH_3).^{13}C (150MHz, $CDCl_3$, 25 °C): δ 160.53, 143.22, 118.89, 105.06, 200.55, 68.08, 65.46, 311.94, 29.69, 29.66, 29.63, 29.61, 29.42, 29.37, 29.28, 29.07, 22.71, 14.13. MALDI-TOF mass calculated for $C_{32}H_{55}NO_2$ (M+Na)$^+$: 508.42, found: 508.585.

Procedure for the synthesis of 2-(3,4,5-tris(dodecyloxy)phenyl) acetonitrile (6d) [81]

3,4,5-tridodecyloxy benzyl chloride (0.73 mmol, 1equiv.) and Sodium cyanide (3.67 mmol, 5 equiv.) were dissolved in DMF (10 mL). The mixture was stirred at 100 °C for 18 h. The reaction mixture was poured into water and extracted with DCM. The combined organic layers were washed with water and brine, and anhydrous Na_2SO_4 was dried and concentrated in vacuo. The crude product was purified by column chromatography using a 5-10% ethyl acetate-hexane system to get the pure product as a white solid.

R_f = 0.53 (10% EtOAc-hexanes), white solid, yield: 65%; IR: ν_{max} in cm^{-1} 2954, 2920, 2850, 2249, 1595, 1506, 1467, 1443, 1393, 1337, 1250, 1236, 1124, 816, 722; ^{1}H NMR (600 MHz, $CDCl_3$, ppm): δ 6.47 (s, 2H, H_{Ar}), 3.96 (t, J = 6 Hz, 4H, 2×OCH_2), 3.93 (t, J = 6 Hz, 2H, OCH_2), 3.65 (s, 2H, CH_2), 1.80 (m, 6H, 3×-CH_2) 1.46 (m, 6H, 3×-CH_2), 1.26 (bm, 48 H, 24×-CH_2), 0.88 (t, J = 6Hz, 9H, 3×-CH_3).^{13}C(150MHz, $CDCl_3$, 25 °C): δ 153.58, 137.84, 124.67, 118.01, 106.36, 73.49, 69.25, 31.95, 31.94, 30.31, 29.76, 29.74, 29.71, 29.67, 29.65, 29.61, 29.41, 29.38, 29.36, 26.12, 26.08, 23.77, 22.70, 14.13. MALDI-TOF mass calculated for $C_{44}H_{79}NO_3$ $(M+Na)^+$: 692.61, found: 692.497.

Procedure for the synthesis of 10-dodecyl-10H-phenoxazine-3,7-dicarbaldehyde (8) [81]

In 100 mL Rbf containing N_2 atm, filled with 14 mL of $POCl_3$ and 12 mL DMF at 0 °C. The solution was allowed to warm to room temperature. After 15 min., compound 7 (5.06 mmol, 1 eq. in 10 mL DCM) is added to the reaction mixture dropwise. Then, the resultant reaction mixture was heated to 90 °C for 24 h. After completion of the reaction, it cooled to room temperature and poured into crushed ice. Then, it was neutralized with aqueous NaOH solution and worked up with dichloromethane. The organic layer was washed with water, and the solvent was removed and dried. Then, it is purified by column chromatography using a 5-10% chloroform-hexane system to get the pure product as a yellow solid.

R_f = 0.33 (10% EtOAc-hexanes), yellow solid, yield: 75%; IR: ν_{max} in cm^{-1} 2915, 2848, 2726, 1687, 1627, 1499, 1389, 1312, 1134.70, 793, 650, 410; ^{1}H NMR (600 MHz, $CDCl_3$, ppm): δ 9.70 (s, 2H, H_{CHO}), 7.35 (d, J = 8.4 Hz, 2H, H_{Ar}), 7.11 (s, 2H, H_{Ar}), 6.60 (d, J = 8.4 Hz, 2H, H_{Ar}), 3.58 (t, J = 7.8 Hz, 2H, -NCH_2), 1.70 (m, 2H, CH_2) 1.45 (m, 4H, 2×-CH_2), 1.28 (bm, 14 H, 7×-CH_2), 0.89 (t, J = 6.6Hz, 3H, CH_3).^{13}C (150MHz, $CDCl_3$, 25 °C): δ 189.63, 144.97, 157.46, 131.22, 128.32, 114.86, 111.59, 44.74, 31.92, 29.62, 29.57, 29.54, 29.34, 29.32, 26.80, 25.08, 22.69, 14.13. MALDI-TOF mass calculated for $C_{26}H_{33}NO_3$ (M^+): 407.25, found: 407.553.

General procedures for the synthesis of POs [83]

The mixture of compound 8 (0.24 mmol, 1eq.) and compound 6a, d (0.51mmol, 2.1 eq.) in *tert*-butylalcohol (10 mL) was stirred at 50 °C. Potassium *tert*-butoxide (0.51mmol, 2.1 eq.) was added to the mixture and stirred for 2 h. The resulting precipitate was filtered and purified by column chromatography using a 2% ethyl acetate-hexane system to get the pure product as a reddish-orange solid.

PO1: R_f = 0.67 (10% EtOAc-hexanes); redish-orange solid; yield: 69%; IR: v_{max} in cm^{-1}: 2920, 2849, 2204, 1607, 1494, 1358, 1183, 1025, 967, 826, 652; ^{1}H NMR (400 MHz, CDCl$_3$, ppm): δ 7.55 (d, J = 8 Hz, 4H, H_{Ar}), 7.41 (d, J = 8Hz, 2H, H_{Ar}), 7.17 (s, 2H, H_{Ar}), 7.14 (s, 2H, H_{vinyl}), 6.93 (d, J = 8 Hz, 4H, H_{Ar}), 6.53 (d, J = 8 Hz, 2H, H_{Ar}), 4.0 (t, J = 6.8 Hz, 4H, 2×-OCH$_2$), 3.55 (t, J = 7.6 Hz, 2H, -NCH$_2$), 1.81 (m, 6H, 3×-CH$_2$), 1.27 (bm, 54H, 17×-CH$_2$), 0.88 (t, J = 6.4 Hz, 9H, 3×-CH$_3$). ^{13}C (150MHz, CDCl$_3$, 25 °C) δ: 158.73, 143.57, 137.51, 132.96, 126.69, 126.07, 126.03, 124.94, 117.73, 114.65, 113.94, 110.52, 106.94, 67.25, 43.28, 30.98, 30.49, 29.23, 28.76, 28.73, 28.70, 28.67, 28.64, 28.46, 28.42, 28.25, 25.95, 25.07, 24.24, 21.76, 13.20. MALDI-TOF mass calculated for $C_{66}H_{91}N_3O_3$ (M$^+$): 973.71, found: 973.383

PO2: R_f = 0.68 (10% EtOAc-hexanes); redish-orange solid; yield: 67%; IR: v_{max} in cm^{-1} 2918, 2849, 2209,1578, 1498, 1466, 1388, 1119, 1068, 824, 627; ^{1}H NMR (400 MHz, CDCl$_3$, ppm): δ 7.40 (d, J = 6.6 Hz, 2H, H_{Ar}), 7.16 (s, 4H, 2×H_{Ar}, 2×H_{vinyl}), 7.13 (d, J = 8Hz, 4H, H_{Ar}), 6.89 (d, J = 6.8, 2H, H_{Ar}), 4.03 (m, 8H, 4×-OCH$_2$), 3.52 (t, J = 6 Hz, 2H, -NCH$_2$), 1.84 (m, 8H, 4×-CH$_2$), 1.49 (m, 8H, 4×-CH$_2$), 1.29 (bm, 86H, 43×-CH$_2$), 0.88 (t, J = 6 Hz,15H, 5×-CH$_3$). ^{13}C (150MHz, CDCl$_3$, 25 °C) δ: 148.98, 148.34, 143.52, 137.70, 132.93, 126.62, 126.58, 124.89, 117.81, 117.63, 114.64, 112.55, 110.47, 110.27, 107.15, 68.54, 68.26, 43.23, 30.91, 30.48, 29.12, 28.69, 28.65, 28.62, 28.44, 28.41, 28.36, 28.32, 28.31,28.21, 25.87,2503, 25.01, 21.67, 13.09. MALDI-TOF mass calculated for $C_{90}H_{139}N_3O_5$ (M$^+$): 1342.07, found: 1342.899.

PO3: R_f = 0.67 (10% EtOAc-hexanes); redish-orange solid; yield: 69%; IR: v_{max} in cm^{-1}: 2918, 2850, 2209,1589, 1498, 1499, 1466,1386, 1298, 1169, 1058, 826, 651; ^{1}H NMR (600 MHz, CDCl$_3$, ppm): δ 7.31 (d, J = 6.6 Hz, 2H, H_{Ar}), 7.13 (s, 2H, 2×H_{vinyl}), 7.12 (s, 2H, H_{Ar}), 6.68 (s, 4H, H_{Ar}), 6.41 (d, J = 9Hz, 2H, H_{Ar}), 6.37 (s, 2H, H_{Ar}), 3.92 (t, J = 6Hz, 8H, 4×-OCH$_2$), 3.39 (m, 2H, -NCH$_2$), 1.77 (m, 8H, 4×-CH$_2$), 1.45 (m, 8H, 4×-CH$_2$), 1.28 (bm, 84H, 42×-CH$_2$), 0.89 (t, J= 6 Hz,15H, 5×-CH$_3$). ^{13}C (150MHz, CDCl$_3$, 25 °C) δ: 159.30, 143.02, 139.03, 135.08, 132.66, 125.92, 125.36, 117.23, 114.29, 110.11, 106.32, 102.92, 100.04, 66.88, 43.00, 30.68, 28.45, 28.42, 28.41, 28.38, 28.23, 28.13, 28.06, 25.62, 24.83, 24.77, 23.89, 21.45, 21.40, 12.87. MALDI-TOF mass calculated for $C_{90}H_{139}N_3O_5$ (M+ H)$^{+:}$ 1343.07, found: 1343.336.

PO4: R_f = 0.70 (10% EtOAc-hexanes); reddish-orange sticky solid; yield: 60%; IR: v_{max} in cm^{-1} 2918, 2851, 2202, 1580, 1501, 1389, 1116, 1067, 899, 798, 720, 613; ^{1}H NMR (600 MHz, CDCl$_3$, ppm): δ 7.42 (d, J = 8.4 Hz, 2H, H_{Ar}), 7.18 (s, 2H, 2×H_{vinyl}), 7.16 (s, 2H, H_{Ar}), 6.79 (s, 4H, H_{Ar}), 6.55 (d, J = 9Hz, 2H, H_{Ar}), 4.02 (t, J =6.6 Hz, 8H, 4×-OCH$_2$), 3.98 (t, J =6.6 Hz, 4H, 2×-OCH$_2$), 3.54 (t, J =7.2 Hz, 2H, -NCH$_2$), 1.82 (m, 8H, 4×-CH$_2$), 1.74 (m, 6H, 3×CH$_2$), 1.48 (m, 14H, 7×-CH_2), 1.26 (bm, 112H, 56×-CH_2), 0.88 (t, *J* = 6 Hz, 21H, 7×-CH_3). ^{13}C (150MHz, $CDCl_3$, 25 °C) δ: 153.45, 144.57, 139.77, 139.08, 134.13, 129.94, 127.50, 126.10, 118.58, 115.77, 111.54, 108.49, 104.60, 73.61, 69.38, 44.28, 31.94, 29.77, 29.75, 29.73, 29.68, 29.66, 29.63, 29.44, 29.42, 29.39, 26.12, 22.71, 14.13. MALDI-TOF mass calculated for $C_{114}H_{187}N_3O_7$ $(M+ H)^+$: 1711.44, found: 1711.388.

3.7 Appendix

3.7.1 NMR Spectra

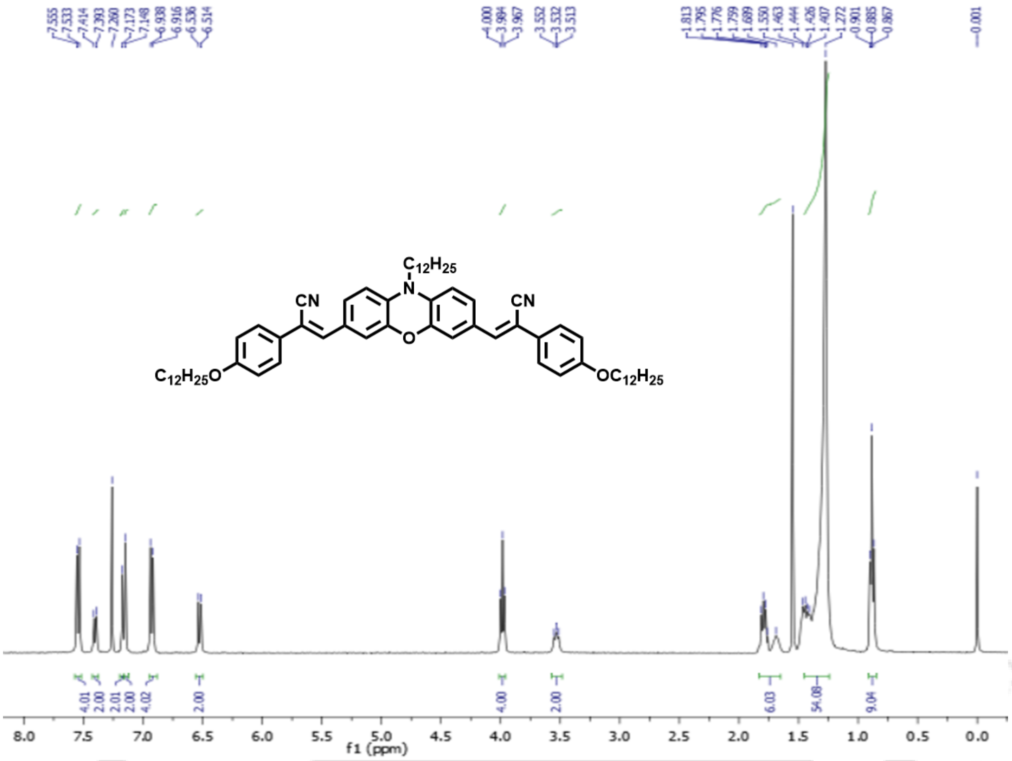

Figure **A1.** ^{1}H NMR (600 MHz) spectra of **PO1** in $CDCl_3$.

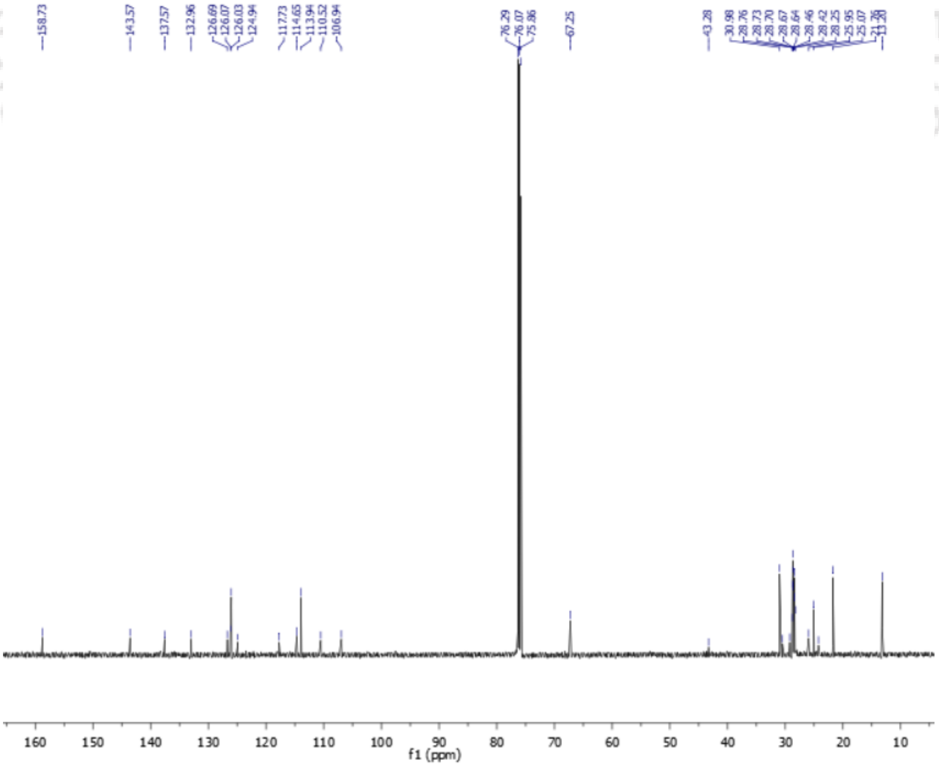

Figure A2. ^{13}C NMR (150 MHz) spectra of **PO1** in $CDCl_3$.

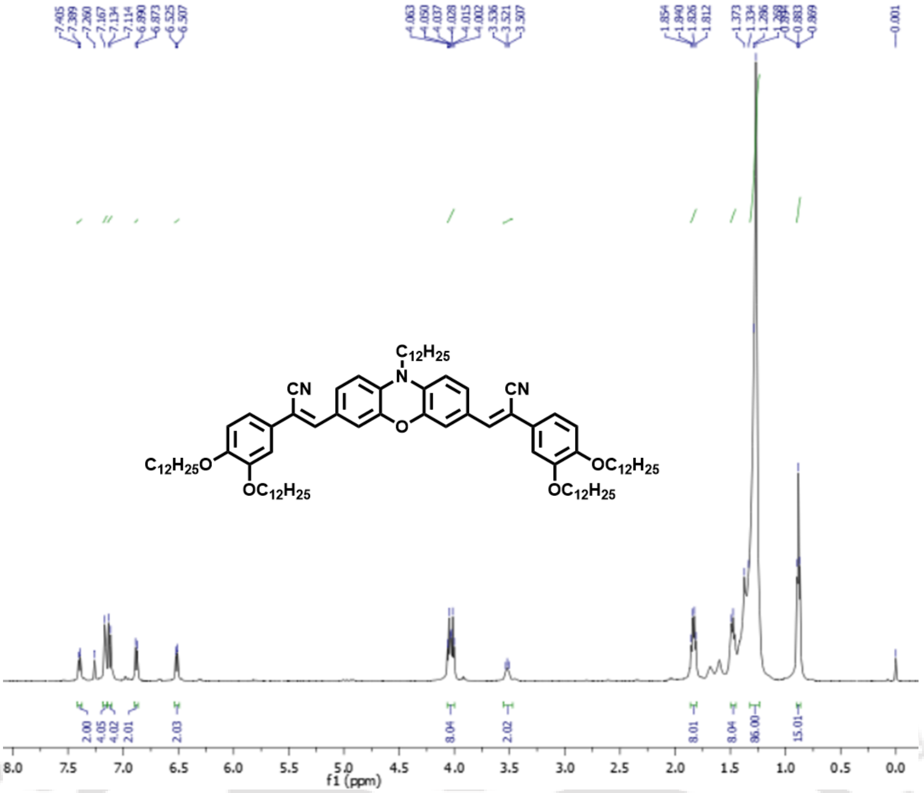

Figure A3. ^{1}H NMR (600 MHz) spectra of **PO2** in $CDCl_3$.

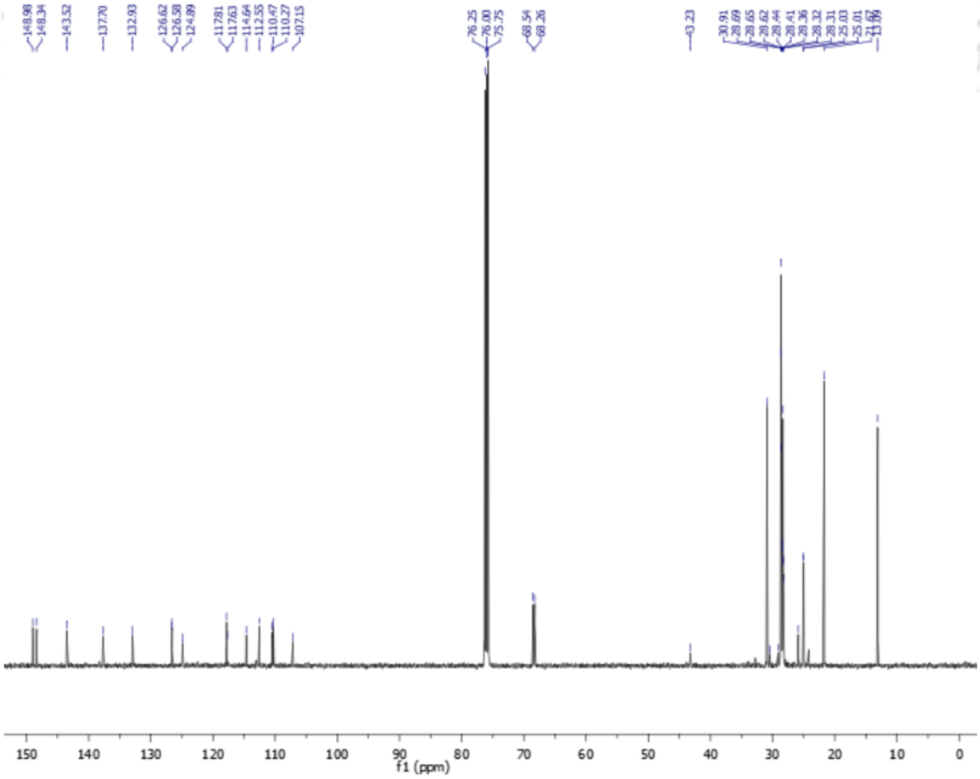

Figure A4. ^{13}C NMR (150 MHz) spectra of **PO2** in $CDCl_3$.

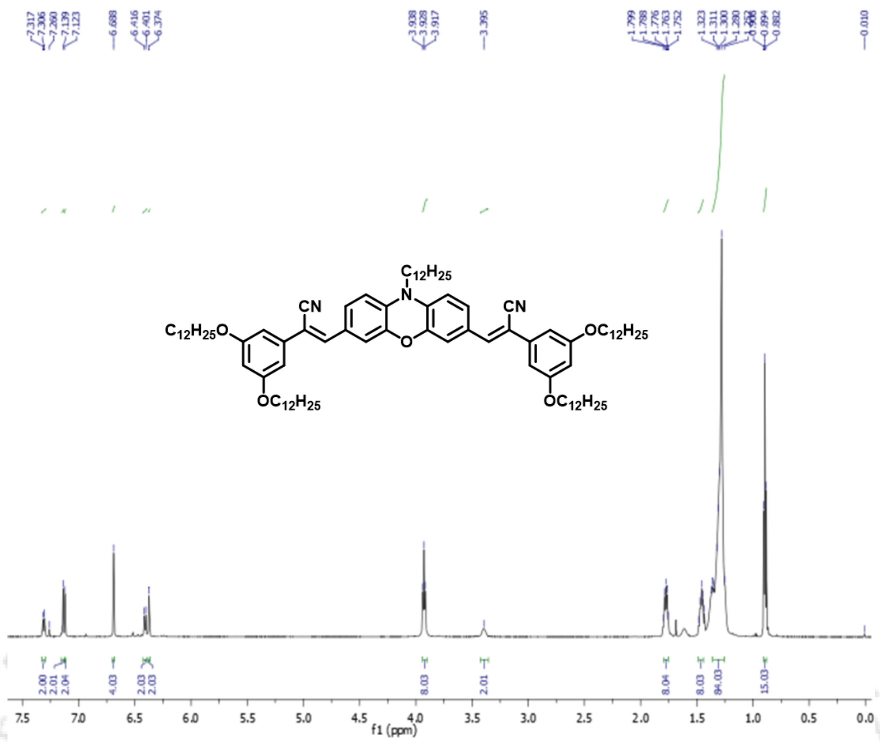

Figure A5. ^1H NMR (600 MHz) spectra of **PO3** in $CDCl_3$.

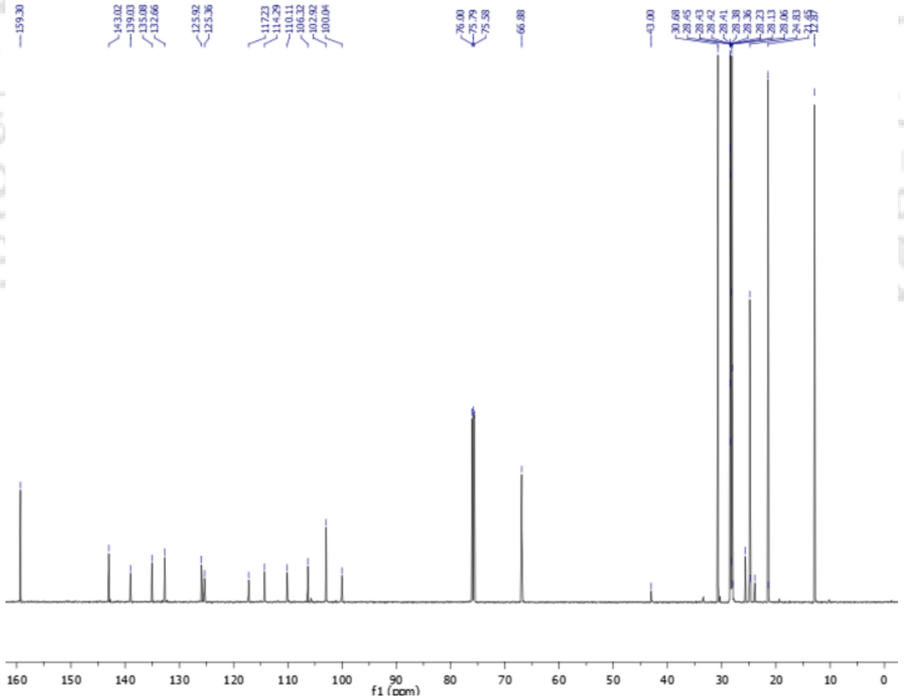

Figure A6. ^{13}C NMR (150 MHz) spectra of **PO3** in $CDCl_3$.

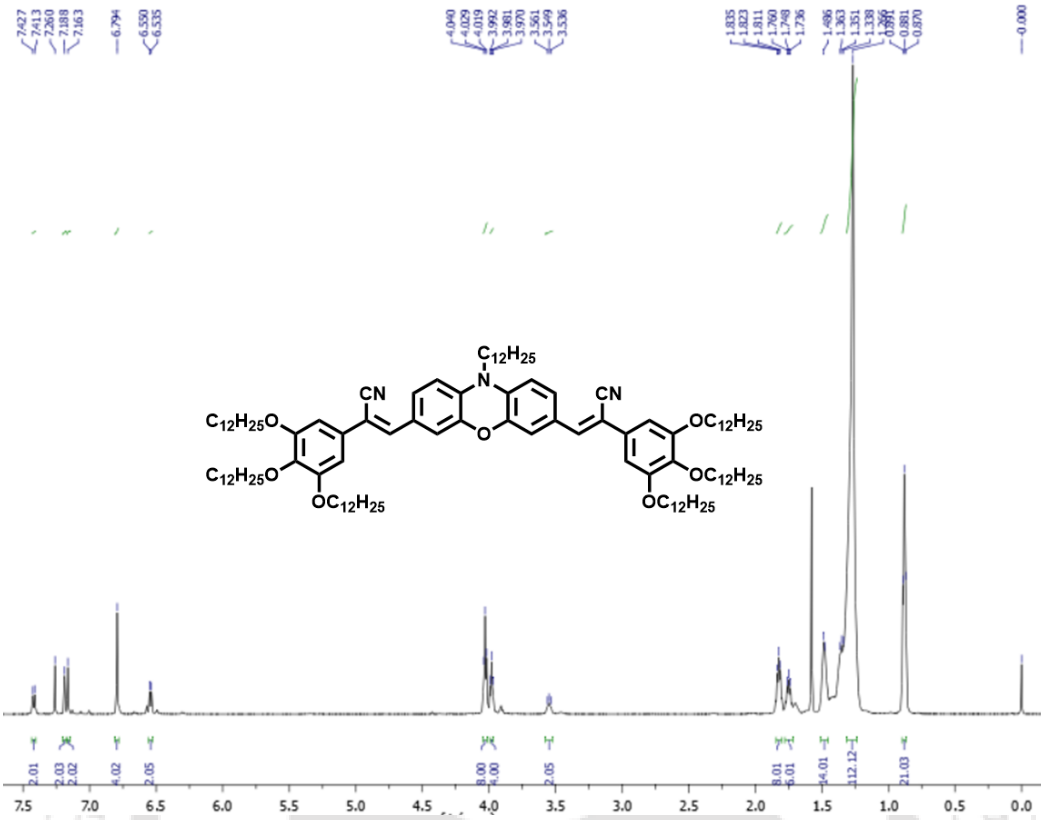

Figure A7. ^{1}H NMR (600 MHz) spectra of **PO4** in $CDCl_3$.

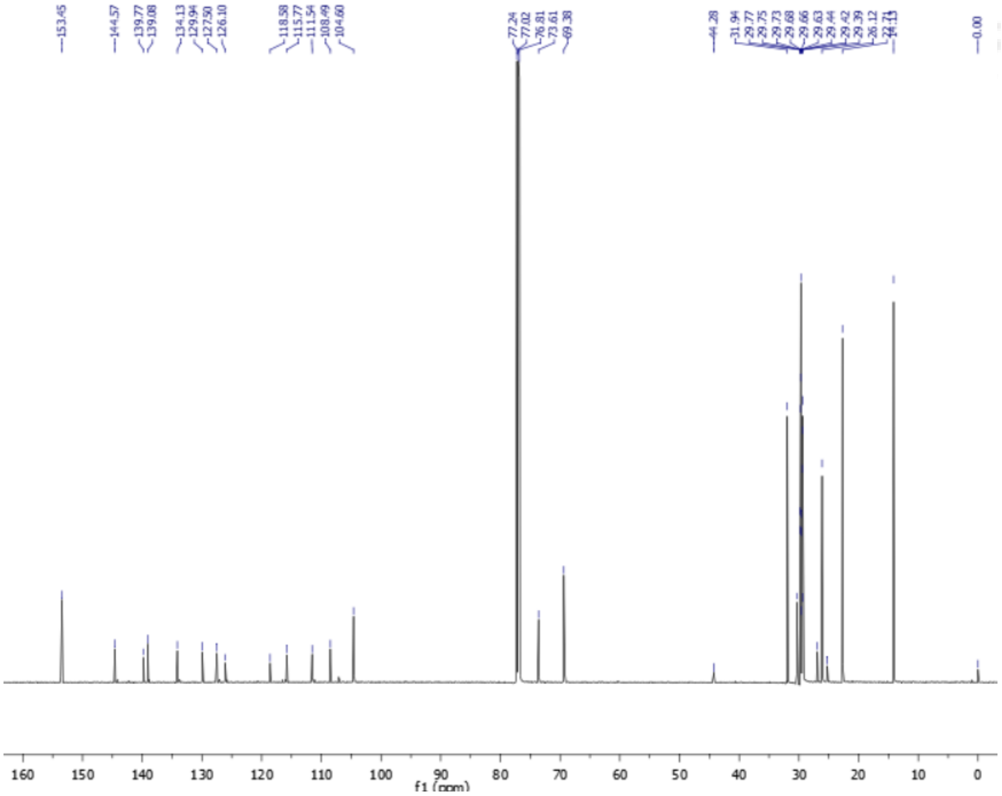

Figure A8. ^{13}C NMR (150 MHz) spectra of **PO4** in $CDCl_3$.

3.7.2. Polarizing optical microscopy (POM)

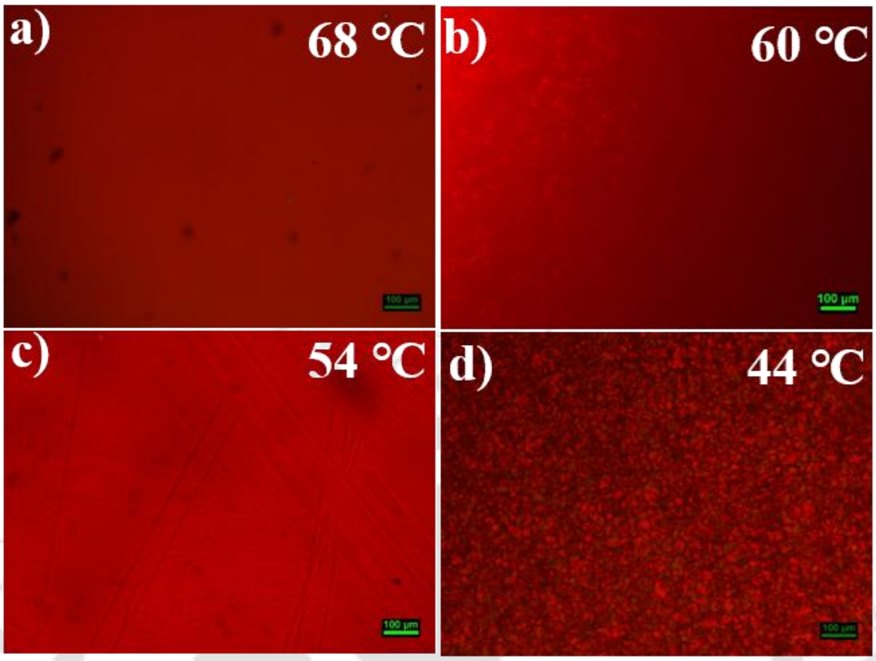

Figure A9. POM images of a) **PO1**, b) **PO2**, c) **PO3**, and d) **PO4** on a cooling process from isotropic melt.

3.7.3. Differential Scanning calorimetry (DSC)

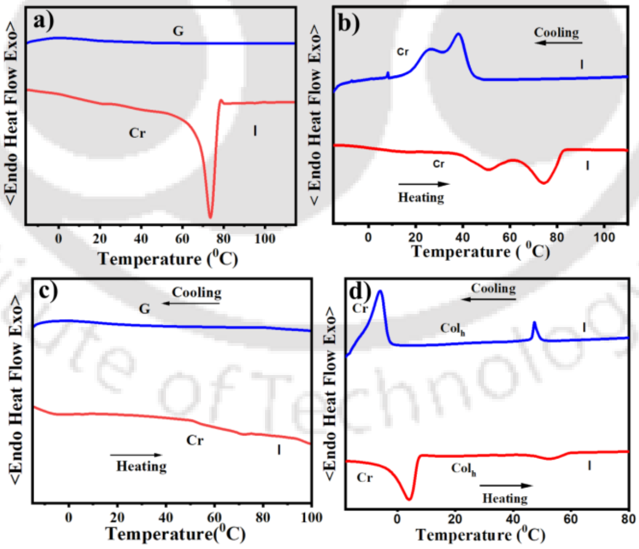

Figure A10. DSC thermograms were obtained for a) **PO1**, b) **PO2**, c) **PO3**, and d) **PO4** for the first cooling (blue trace) and second heating(red trace) taken at 5 °C/min.

3.7.4. X-Ray Diffraction (XRD) Studies

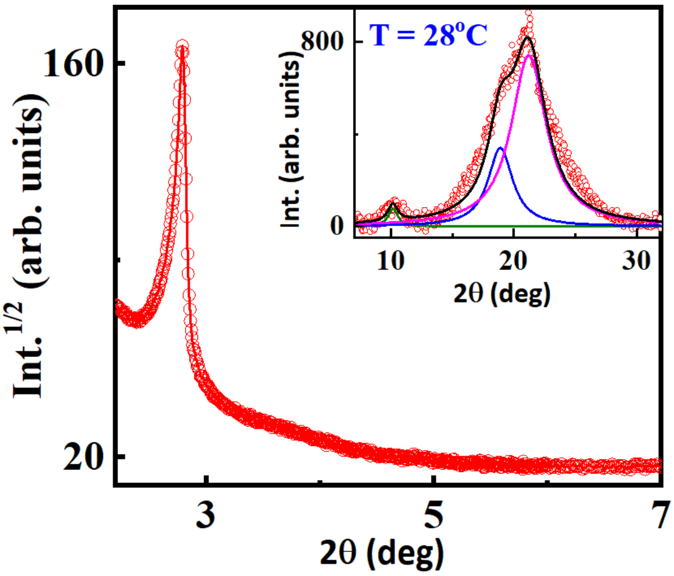

Figure A11. X-ray diffractograms for the Col$_h$ phases of **PO4** at 28 °C (insets show the images of the wide-angle region)

3.7.5. Photophysical studies

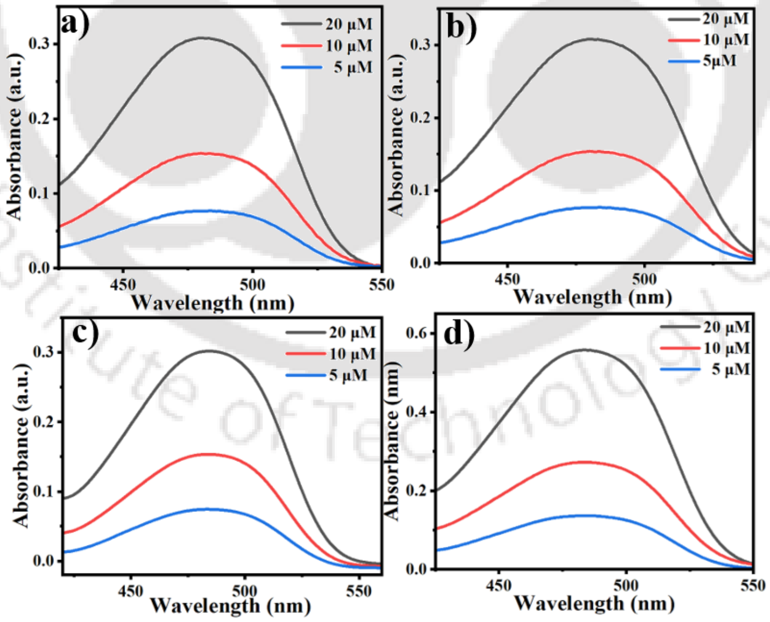

Figure A12. Absorption spectra of compounds a) **PO1**, b) **PO2**, c) **PO3**, and d) **PO4** in micromolar chloroform solutions.

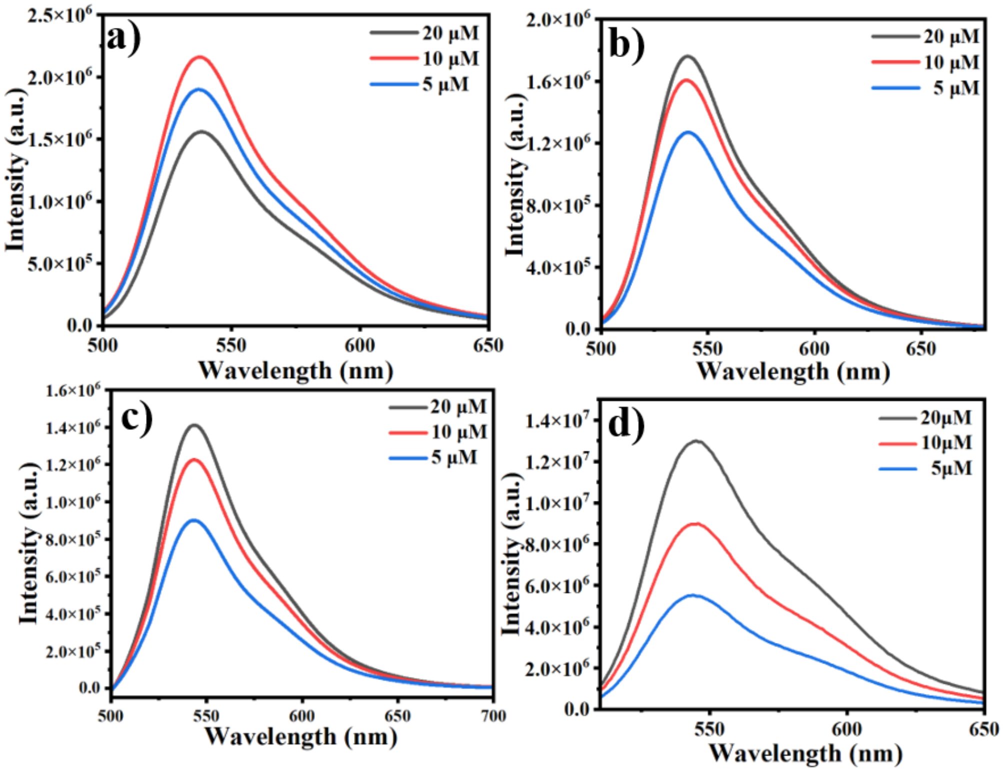

Figure A13. Emission spectra of compounds a) **PO1**, b) **PO2**, c) **PO3**, and d) **PO4** in micromolar chloroform solutions.

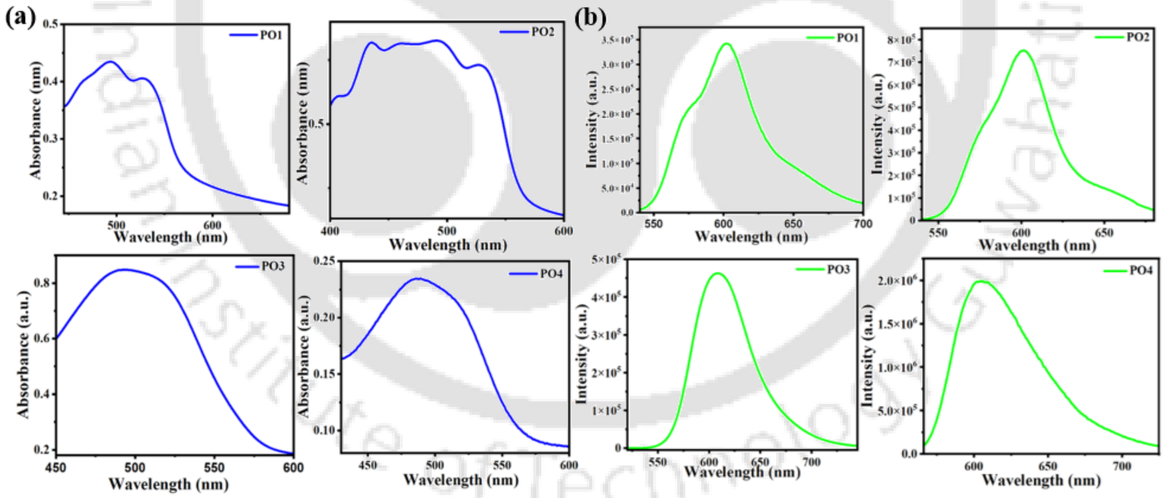

Figure A14. (a) Absorption spectra (blue inline); (b) emission spectra (in green line) of **PO**s (**PO1-PO4**) in the thin film respectively.

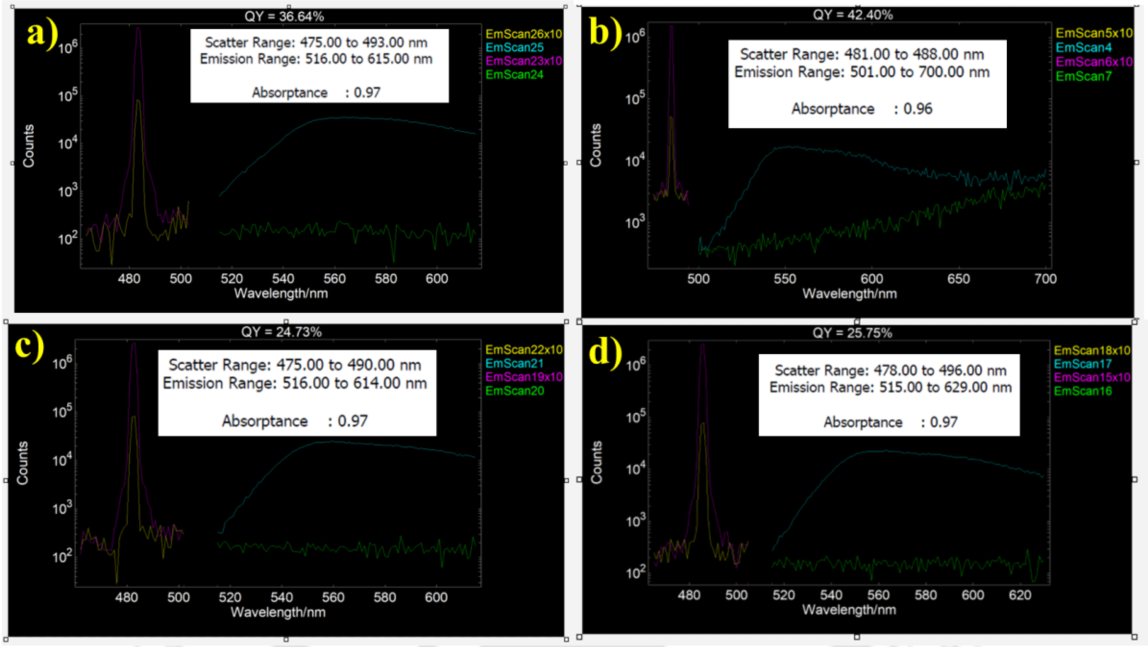

Figure A15. Graphical representations of quantum yield data were obtained using the FLS1000 Fluorescence Spectrometer for (a) **PO1**, b) **PO2**, (c) **PO3**, and (d) **PO4** in the solution.

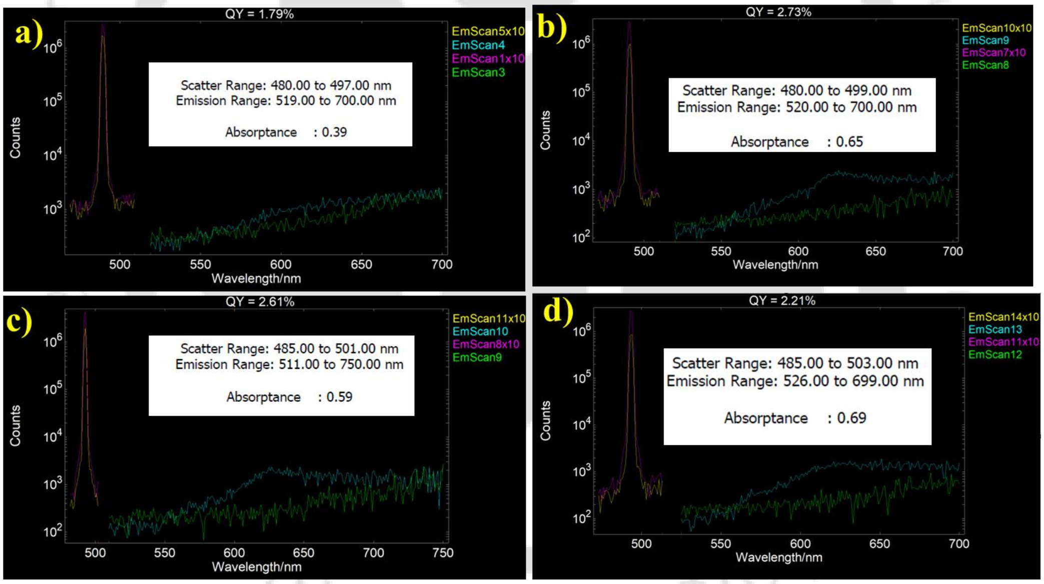

Figure A16. Graphical representations of quantum yield data were obtained using the FLS1000 Fluorescence Spectrometer for (a) **PO1**, b) **PO2**, (c) **PO3**, and (d) **PO4** in the solid.

3.7.6. Solvatochromic effect

The influence of the solvent environment on the optical property of the compound **PO4** can be understood using the Lippert-Mataga equation. This model describes the interactions between the solvent and the dipole moment of solute:

$$hc\ (\upsilon_a - \upsilon_f) = hc\ (\upsilon^0_a - \upsilon^0_f) + 2\ (\mu_e - \mu_g)^2/a^3\ f\,(\varepsilon, n) \text{----------- formula A1}$$

Where f is the orientation polarizability of solvents, μ_e is the excited–state dipole moment,

μ_g is the ground-state dipole moment; a is the solvent cavity (Onasagar) radius, derived from the Avogadro number (N), molecular weight (M), and density (d = 1.0 g/cm^3); ε and n are the solvent dielectric and the solvent refractive index, respectively; f (ε, n) and a can be calculated respectively as follows:

$$f(\varepsilon, n) = (\varepsilon\text{-}1/\ 2\varepsilon+1)\text{-}\ (n^2\text{-}1/2n^2+1),\ a= (3M/4\ N\pi d)^{1/3}$$

Table A1. Photophysical properties of **PO4** in a diverse range of solvents vary with polarity.

Solvent	Polarity	Absorption (nm)	Emission (nm)	Stokes Shift (cm^{-1})	Orientation Polarizability (Δf)
Hexane	0.1	445	508	2786	0.0012
Toluene	2.4	476	535	2316	0.014
Dichloromethane	3.1	480	536	2176	0.217
Tetrahydrofuran	4.0	479	539	2323	0.212
Chloroform	4.1	484	543	2244	0.147
Ethyl Acetate	4.4	450	544	3839	0.200
1,4-Dioxane	4.8	478	545	2571	0.022
Acetone	5.1	475	552	2936	0.284
Dimethyl Sulfoxide	7.2	486	593	3712	0.313

3.7.5. Electrochemical studies

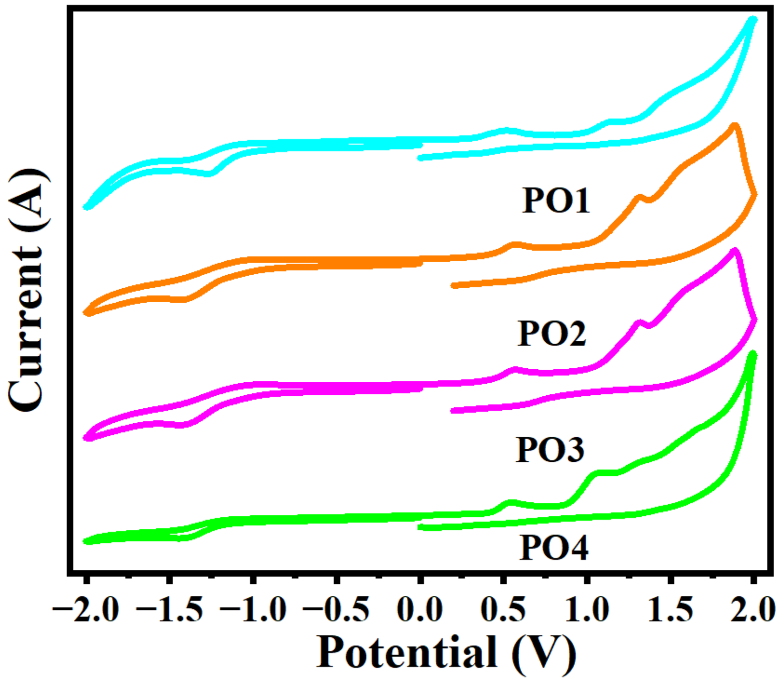

Figure A17. Cyclic voltammograms of **PO**s in micromolar dichloromethane solutions in scan rate 100mv/s.

3.7.7. Morphology studies

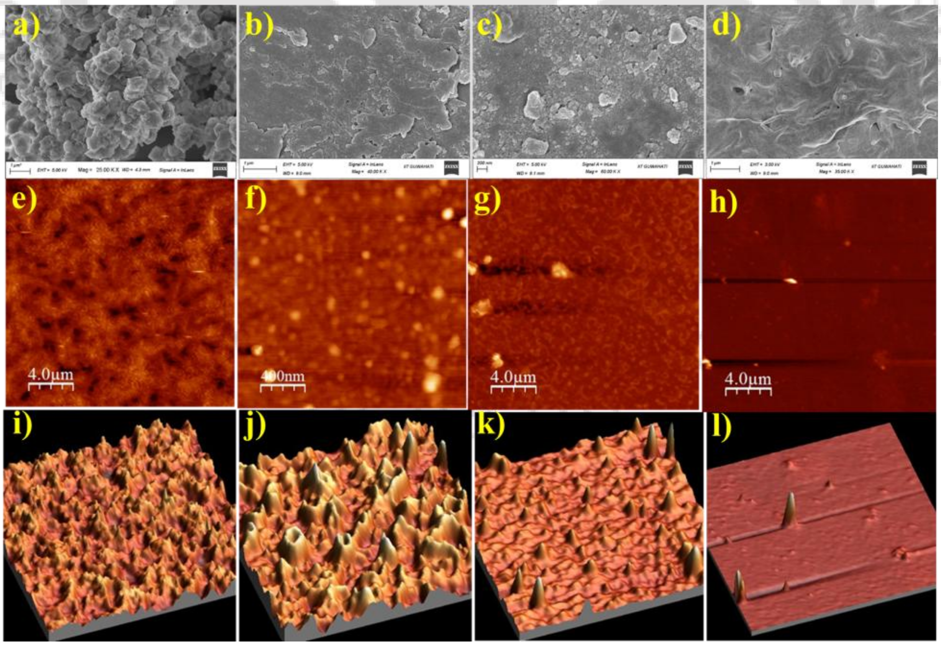

Figure A18. The SEM images (a, b, c, d); AFM images (e, f, g, h), and 3D view of AFM images (i, j, k & l) of **PO1**, **PO2**, **PO3**, and **PO4** compounds drop cast respectively.

3.7.8. DFT Studies

Computational studies were carried out in the B3LYP/6-31g (d, p) method using the Gaussian 09 program package to understand the electronic properties and frontier molecular orbital energy level of compound **PO**s. The absence of imaginary frequency ensured the energy-minimized structure of all the compounds.

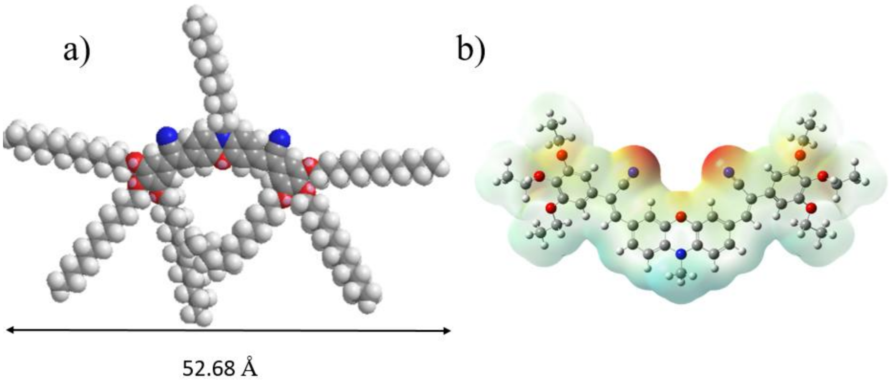

Figure A19. (a) Energy minimized molecular model of **PO4 (**obtained from Chem3D Ultra). (b) The 3D molecular electrostatic potential (MEP) contour maps (chain length is limited to methyl for the sake of computational time).

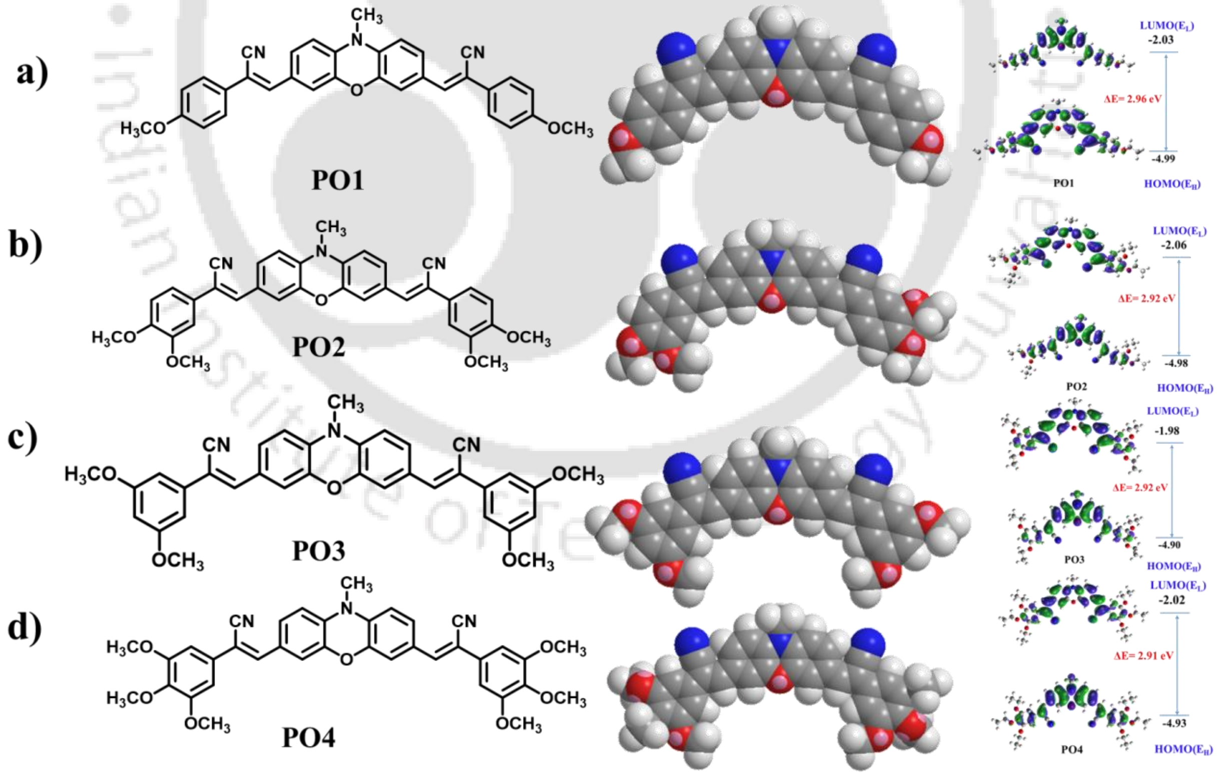

Figure A20. Molecular models and frontier molecular orbitals of **PO**s obtained from DFT calculations at the B3LYP/ 6-31G (d, p) level (E_H and E_L denote energies of the HOMO and LUMO, respectively (chain length is limited to methyl for the sake of computational time)).

Table A2. Calculated natural transition orbitals (NTO) of singlet and triplet excited states.

Excited states (Energies)	**Hole**	**Contributon**	**Particle**	**Contribution**
S_1 (2.324)	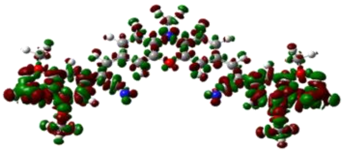	**1.00**	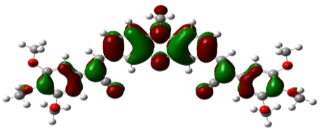	**1.00**
S_2 (2.892)	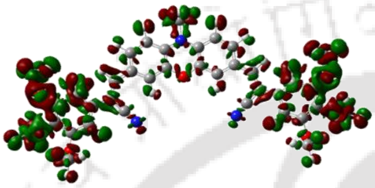	**0.75**	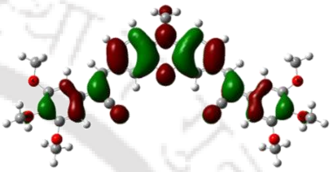	**0.75**
S_3 (3.355)	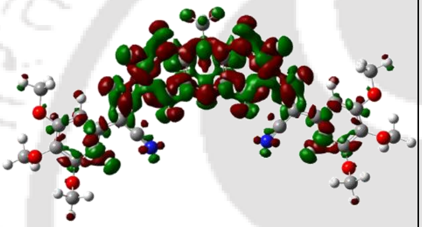	**0.98**	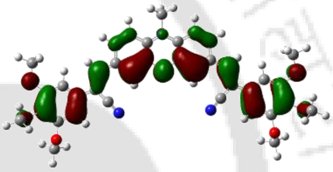	**0.98**
S_4 (3.397)	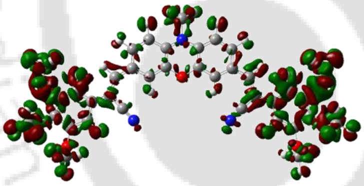	**0.79**	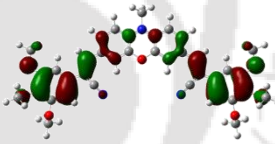	**0.79**
S_5 (3.572)	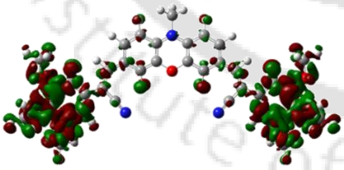	**0.89**	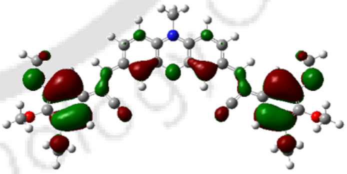	**0.89**
S_6 (3.603)	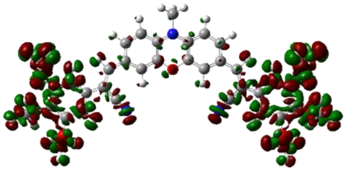	**0.88**	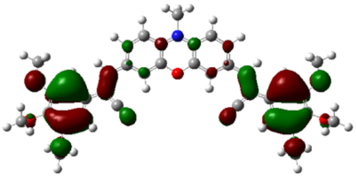	**0.88**

S$_7$ **(3.722)**	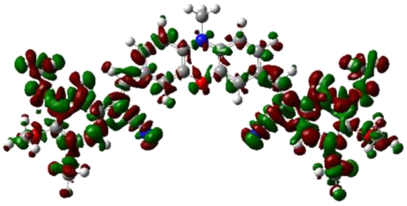	**0.92**	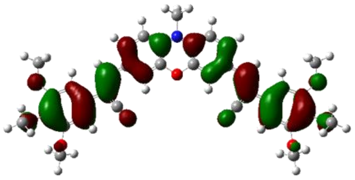	**0.92**
S$_8$ **(3.936)**		**0.96**	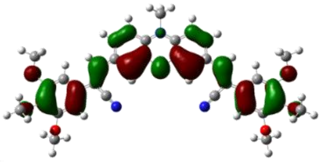	**0.96**
S$_9$ **(3.976)**	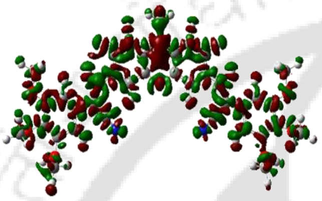	**0.72**	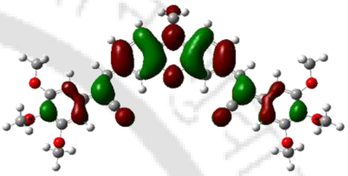	**0.72**
S$_{10}$ **(4.197)**	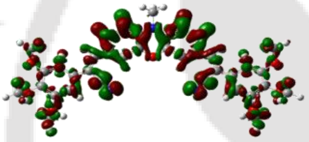	**0.89**	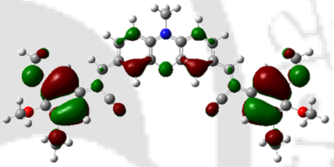	**0.89**
Excited states (Energies)	**Hole**	**Contribution**	**Particle**	**Contribution**
T$_1$ **(1.537)**	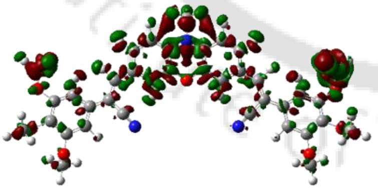	**0.90**	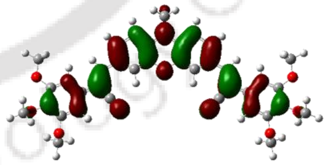	**0.90**
T$_2$ **(1.895)**	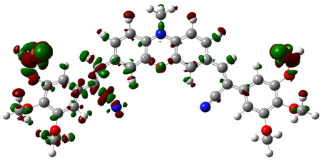	**0.59**	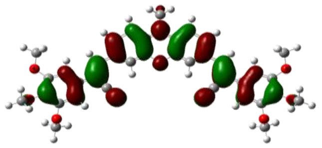	**0.59**

	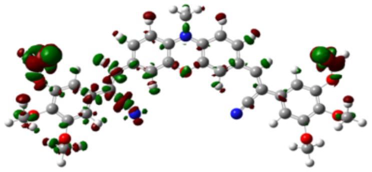	**0.40**	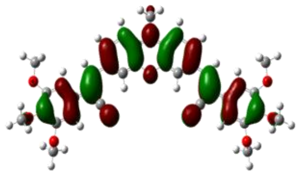	**0.40**
T_3 **(2.637)**	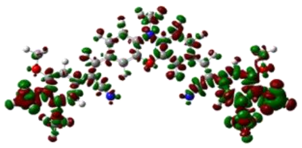	**0.65**	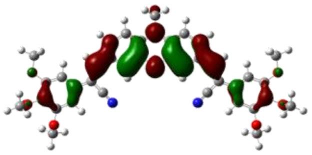	**0.65**
	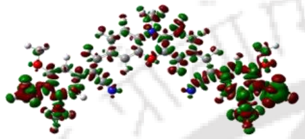	**0.32**	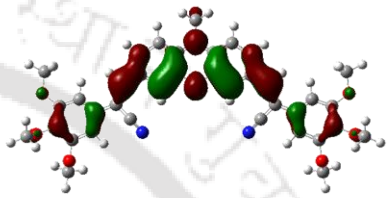	**0.32**
T_4 **(2.651)**	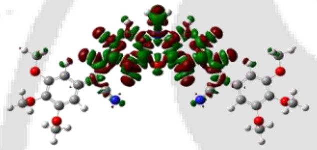	**0.55**	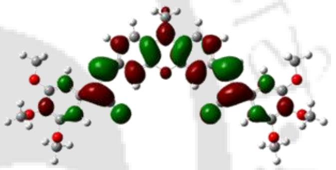	**0.55**
	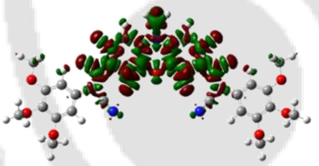	**0.43**	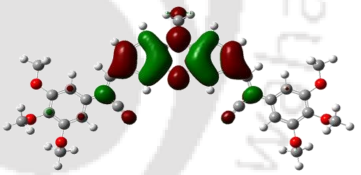	**0.43**
T_5 **(3.234)**	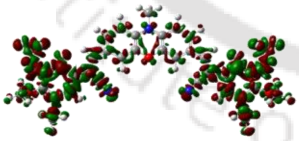	**0.78**	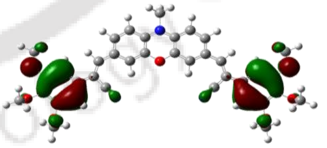	**0.78**
T_6 **(3.243)**	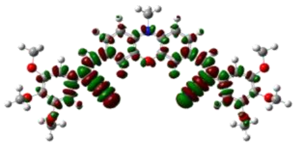	**0.78**	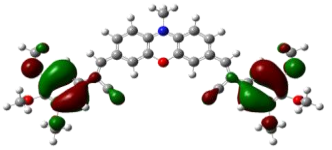	**0.78**

T_7 (3.386)	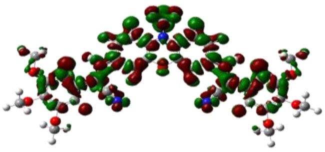	0.50	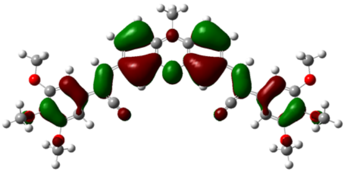	0.50
	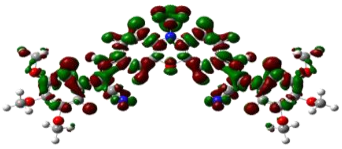	0.47	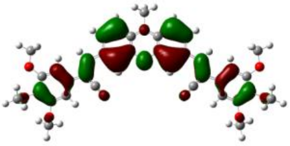	0.47
T_8 (3.504)	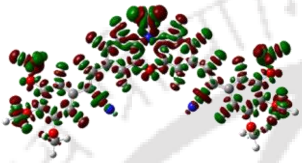	0.91	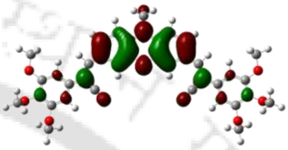	0.91
T_9 (3.540)	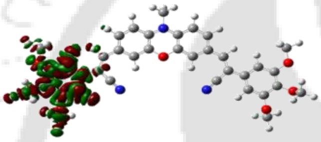	0.74	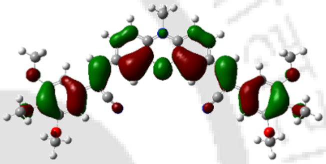	0.74
T_{10} (3.722)	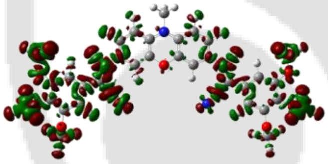	0.66	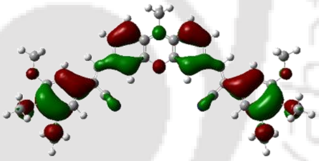	0.66

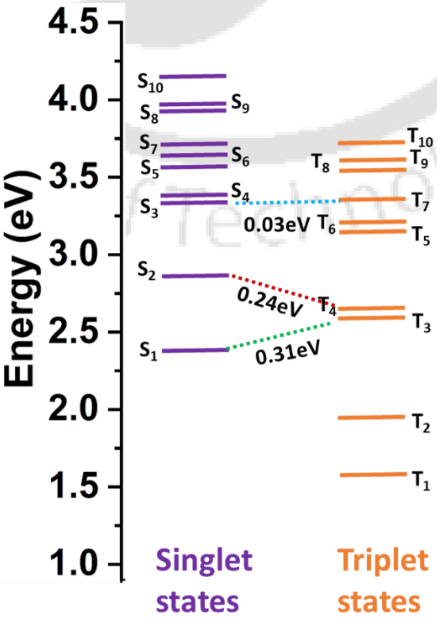

Figure A21. Energy level diagram of theoretically calculated singlet and triplet.

3.7.9. Device fabrication

The process was initiated by cleaning glass/ITO substrates in an ultrasonic water bath using a sequential treatment with diluted detergent solution, deionized water, acetone, and isopropanol. After washing, the ITO substrates were treated with UV-ozone for 30 minutes. For the hole-only device (HOD), a PEDOT: PSS solution was spin-coated onto the ITO substrates at 3000 rpm for 40 seconds and then annealed at 150 °C for 10 minutes. The **PO4** solution in chlorobenzene (35 mg/ml) was subsequently spin-coated onto the PEDOT: PSS layer at 1000 rpm for 60 seconds. Finally, 10 nm of MoO_3 and 100 nm of silver were deposited sequentially on the PO4 layer using thermal evaporation. For the electron-only device (EOD), the ZnO solution prepared via the sol-gel method was spin-coated onto the ITO substrates at 4000 rpm for 50 seconds and annealed at 210°C for 15 minutes. The **PO4** solution was then spin-coated onto the ZnO layer at 1500 rpm for 60 seconds. A thin *N*, *N*'-bis{3-[3-(dimethylamino)propylamino]propyl}perylene-3,4,9,10-tetracarboxylic iimide (PDINN) PDINN layer (less than 5 nm), prepared in methanol, was spin-coated on the top, followed by deposition of a 100 nm thick silver electrode through thermal evaporation.

3.7.10. Dielectric constant calculation

To determine the dielectric constant of the material, capacitance-frequency (C-F) measurements were carried out. For C-F measurements, 180 nm thick layer of **PO4** was used. Capacitance of the **PO4** layer was determined to be 1.70 nF and from that the dielectic constant is calculated as 3.95.

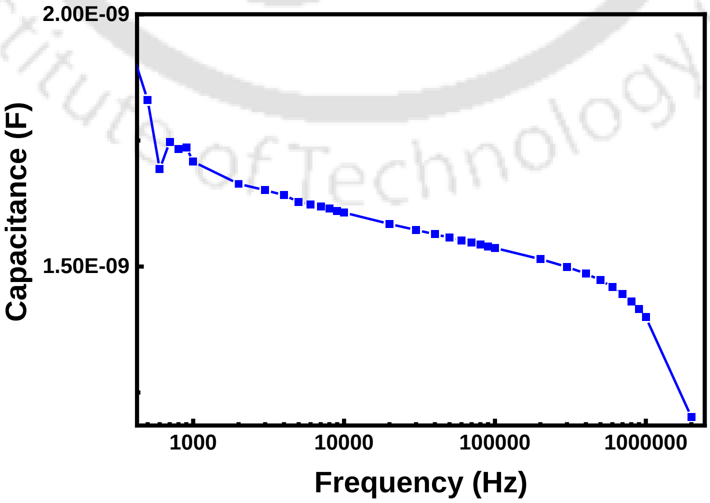

Figure A22. Capacitance- frequency measurement of the device fabricated with **PO4**.

Table A3. Charge carrier mobility is measured in organic molecules using different methods.

Sl.No.	Structure of the Molecule	Mobility (cm^2/V.s)	Measurement Method	Reference
1a	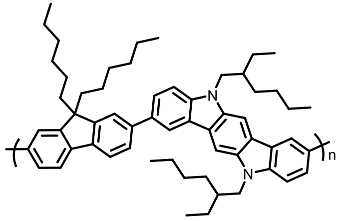 PF-m-In	$\mu_h = 6.73\times 10^{-5}$	OFET	62
1b	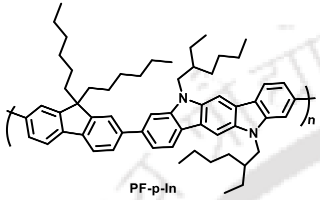 PF-p-In	$\mu_h = 1.50\times 10^{-4}$	OFET	62
2	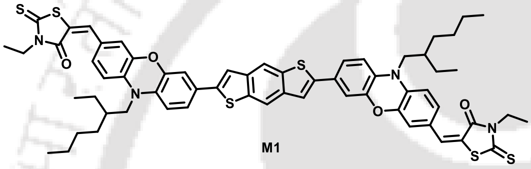 M1	$\mu_h = 2\times 10^{-6}$	OFET	63
3a	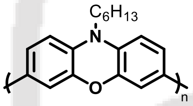 PO6	$\mu_h = 0.6\times 10^{-6}$	OFET	64
3b	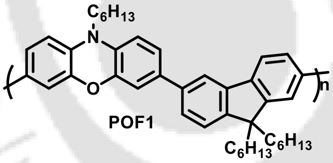 POF1	$\mu_h = 3\times 10^{-5}$	OFET	64
3c	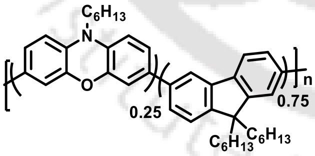 POF2	$\mu_h = 2\times 10^{-5}$	OFET	64
3d	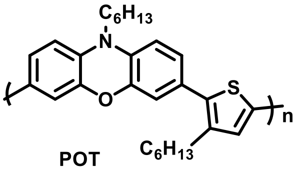 POT	$\mu_h = 8\times 10^{-5}$	OFET	64

4a	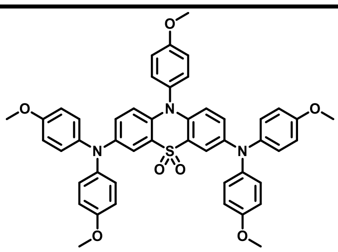 PDO1	$\mu_h = 1.76\times 10^{-4}$	SCLC	65
4b	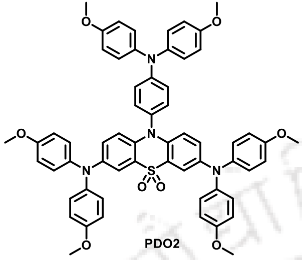 PDO2	$\mu_h = 5.93\times 10^{-4}$	SCLC	65
5	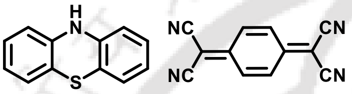 PTZ−TCNQ co-crystal	$\mu_h = 3\times 10^{-4}$	OFET	66
6a	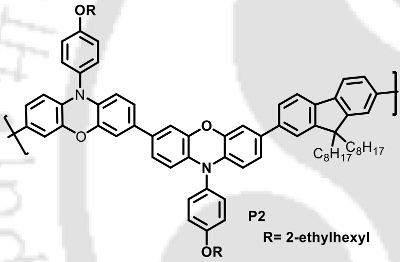 P2 R= 2-ethylhexyl	$\mu_h = 1.4\times 10^{-4}$	OFET	67
6b	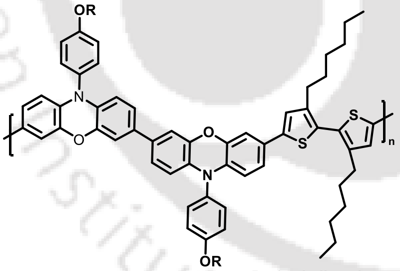 P3 R= 2-ethylhexyl	$\mu_h = 9\times 10^{-5}$	OFET	67
7a	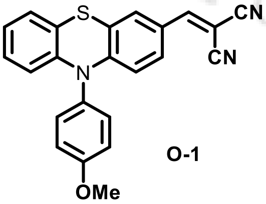 O-1	$\mu_h = 1\times 10^{-3}$	Impedance spectroscopy	68
7b	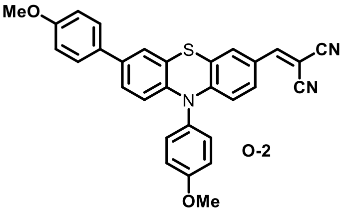 O-2	$\mu_h = 1\times 10^{-6}$	Impedance spectroscopy	68

7c	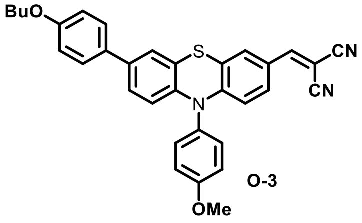	$\mu_h = 1\times 10^{-6}$	Impedance spectroscopy	68
8a	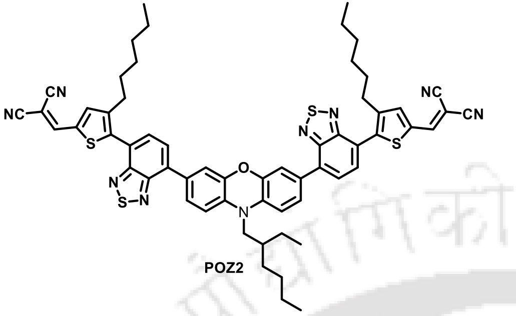	$\mu_h = 5.98\times 10^{-4}$	SCLC	69
8b	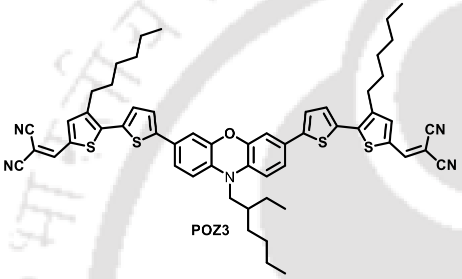	$\mu_h = 4.46\times 10^{-4}$	SCLC	69
9	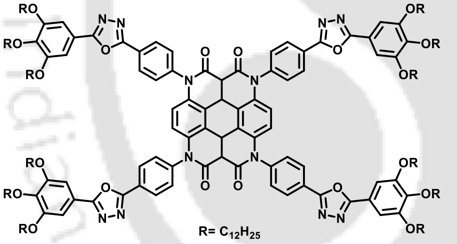	$\mu_h= 1.46\times 10^{-4}$ $\mu_e= 3.07\times 10^{-6}$	SCLC	70
9	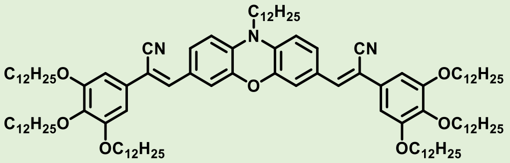	$\mu_h= 1.92\times 10^{-4}$ $\mu_e= 1.19\times 10^{-4}$	SCLC	Present work

μ_h (p-type) = Hole mobility

μ_e (n-type) = Electron mobility

SCLC = Space Charge Limiting Current

OFET = Organic Field Effect Transistor

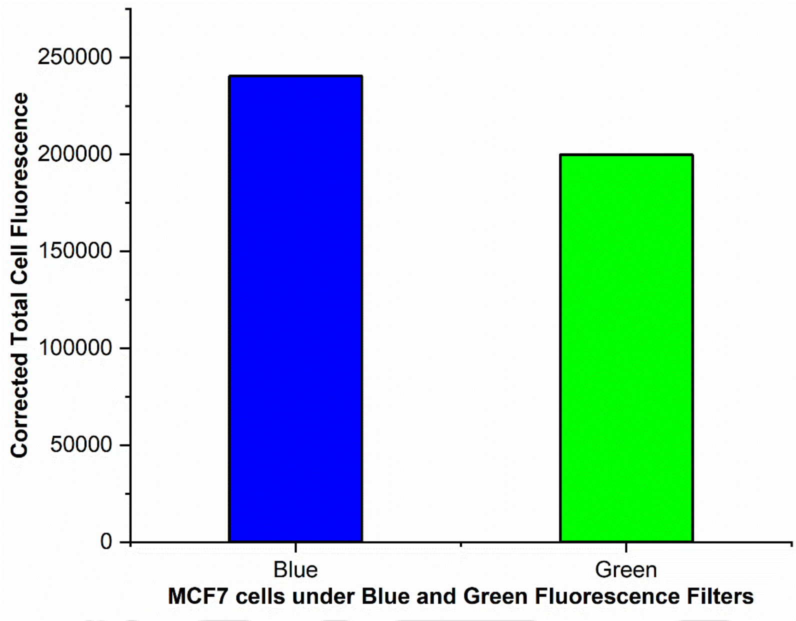

Figure A23. Fluorescence intensity of compound **PO4** under blue and green filters.

3.8. References

1. Y, Zhu, A. P. Kulkarni, P.T. Wu, and S.A. Jenekhe, New Ambipolar Organic Semiconductors. 2. Synthesis, Single-Crystal Structures, Redox Properties, and Photophysics of Phenoxazine-Based Donor-Acceptor Molecules, *Chem. Mater*. 2008, **20**, 4200–4211.

2. H. A. Sharji, · R. Ilmi, M. S. Khan, Recent Progress in Phenoxazine-Based Thermally Activated Delayed Fluorescent Compounds and Their Full-Color Organic Light-Emitting Diodes, *Top. Curr. Chem.*, 2024,**5**, 382.

3. A. N. Oleksy, J. Sołoducho, J. Cabaj, Phenoxazine Based Units- Synthesis, Photophysics and Electrochemistry, *J. Fluoresc.*, 2011, **21**,169–178.

4. M. Damaceanu, C. P. Constantin, L. Marin, Insights into the effect of donor-acceptor strength modulation on physical properties of phenoxazine-based imine dyes, *Dyes Pigm.*, 2016, **134**, 382-396.

5. A. P. Kulkarni, Y. Zhu, A. Babel, P. Tzu Wu, and S. A. Jenekhe, New Ambipolar Organic Semiconductors. 2. Effects of Electron Acceptor Strength on Intramolecular Charge Transfer Photophysics, Highly Efficient Electroluminescence, and Field-Effect Charge

Transport of Phenoxazine-Based Donor-Acceptor Materials, *Chem. Mater*, 2008, **20**, 4212–4223.

6. P. Ravichandirana, A. B. Czubarab, M. Masłykc, A. P. Bellad, P. M. Johnson, S.A. Subramaniyane, K. S. Shime, D. J. Yoon, a phenoxazine-based fluorescent chemosensor for dual channel detection of Cd^{2+} and CN^{-} ions and its application to bio-imaging in live cells and zebrafish, *Dyes Pigm.*, 2020, **172**, 107828.

7. W. Ma, X. Zhao, Q. Niu, T. Hu, J. Chen, A new phenoxazine-based turn-on fluorescent probe for monitoring hypochlorite in food/urine/water/beverage samples and bioimaging in zebrafish, *Microchem. J.*, 2023, **193**, 109107.

8. X. Wang, C. Ma, M. Xie, L. Chu, Y. Zhou, Q. Sun, W. Yang, S. Xue, Efficient and ultra-high luminance orange-red organic light emitting diode (OLED) based on a triphenylamine-benzothiadiazole-phenoxazine hybrid molecule with hybrid local and charge-transfer (HLCT) characteristic, *Dyes Pigm.*, 2024, **229**,112274.

9. L. Ai, S. Shen, L. Zhou, B. Li, and Y. Wang, Sulfone-Based HLCT Molecules with Efficient Orange and White Emission, *ACS Appl. Electron. Mater.*, 2024, **6**, 6688−6697.

10. M. Damaceanua, C. P. Constantina, A.E. Bejana, M. Mihailab, M. Kuskob, C. Diaconuc, I. Mihalacheb, R. Pascub, Heteroatom-mediated performance of dye-sensitized solar cells based on T-shaped molecules, *Dyes Pigm.*, 2019, **166**, 15–31.

11. F. Dumur, Recent advances on the phenoxazine-based hole transporting molecules for perovskite solar cells, *Chem. Phys., 2024,* **580**,112211.

12. M. Cheng, B. Xu, C. Chen, X. Yang, F. Zhang, Q. Tan, Y. Hua, L. Kloo, and L. Sun, Phenoxazine-Based Small Molecule Material for EfficientPerovskite Solar Cells and Bulk Heterojunction Organic Solar Cells, *Adv. Energy Mater*., 2015, **5**, 1401720.

13. M. Cheng, X. Yang, C. Chen, Q. Tana, and L. Sun, Molecular engineering of small molecules donor materials based on phenoxazine core unit for solution-processed organic solar cells, *J. Mater. Chem. A*, 2014, **2**, 10465–10469.

14. K. Narayanaswamy, B. Yadagiri, T. H. Chowdhury, T. Swetha, A. Islam, V. Gupta, and S. P. Singh, Impact of A–D–A-Structured Dithienosilole- and Phenoxazine- Based Small Molecular Material for Bulk Heterojunction and Dopant-Free Perovskite Solar Cells, *Chem. Eur. J.*, 2019, **25**, 16320 – 16327.

15. C. Chen, X. Ding, H. Li, M. Cheng, H. Li, Li Xu, F. Qiao, and H. Li, Highly Efficient Phenoxazine Core Unit Based Hole Transport Materials for Hysteresis-Free Perovskite Solar Cells, *ACS Appl. Mater. Interfaces*, 2018, **10**, 36608−36614.

16. Z. Li, Q. Tan, G. Chen, H. Gao, J. Wang, X. Zhang, J. Xiu, W. Chen and Z. He, Simple and robust phenoxazine phosphonic acid molecules as self-assembled hole selective contacts for high-performance inverted perovskite solar cells, *Nanoscale*, 2023, **15**, 1676.

17. M. A. Sridhar, M. Ramegowda, N. K. Lokanath, J. Shashidhara Prasad, G. B. Ere Gowda, K. N. Thimmaiah, Structural Studies of Some Phenoxazine Derivatives, *Mol. Cryst. Liq. Cryst.*, 1999, **326**, 189-214.

18. Z. Cheng, J. Liang, Z. Li, T. Yang, C. Lin, X. Mu, and Y. Wang, Photoluminescent manipulation of phenoxazinebased molecules via regulating conformational isomerization, and the corresponding electroluminescent properties, *J. Mater. Chem. C*, 2019, **7**, 14255.

19. H. F. Higginbotham, C. Yi, A. P. Monkman, and K. T. Wong, Effects of Ortho-Phenyl Substitution on the rISC Rate of D−A Type TADF Molecules, *J. Phys. Chem. C*, 2018, **122**, 7627−7634.

20. H. Tanaka, K. Shizu, H. Miyazaki and C. Adachi, Efficient green thermally activated delayed fluorescence (TADF) from a phenoxazine–triphenyl triazine (PXZ–TRZ) derivative, *Chem. Commun.*, 2012, **48**, 11392–11394.

21. L. X. Guo, Y.B. Xing, M. Wang, Y. Sun, X.Q. Zhang, B.P. Lin and H. Yang, Luminescent liquid crystals bearing an aggregation-induced emission active tetraphenylthiophene fluorophore, *J. Mater. Chem. C*, 2019, **7**, 4828-4837.

22. Y. Wang, J. Shi, J. Chen, W. Zhu, and E. Baranoff, Recent progress in luminescent liquid crystal materials: design, properties, and application for linearly polarised emission, *J. Mater. Chem. C*, 2015, **3**, 7993-8005.

23. Y. Iida, Y. Shimomura, M. Tokita, G.I. Konishi, Push-pull biphenyl and tolane derivatives as novel luminescent liquid crystals: synthesis and properties, *Liq. Cryst.*, 2024, **51**, 2032-2045.

24. Boyd, V., Cholewa, O. M., & Papas, K. K., Limitations in the Use of Fluorescein Diacetate/Propidium Iodide (FDA/PI) and Cell Permeable Nucleic Acid Stains for Viability

Measurements of Isolated Islets of Langerhans, *Curr. Trends Biotechnol. Pharm.*, 2008, ***2***, 66–84.

25. Shukla, S., Dwivedi, J., Yaduvanshi, N., & Jain, S., Medicinal and Biological Significance of Phenoxazine Derivatives., *Mini-Rev. Med. Chem.*, 2021, **21**, 1541–1555.

26. Y. Chen, Z. Peng, Y. Tao, Z. Wang, P. Lu, Y. Wang, Polymorphism-dependent emissions of two phenoxazine derivatives, *Dyes Pigm.*, 2019, **161**, 44–50.

27. X. Zhang, S. Jiang, G. Lin, H. Guo, F. Yang, Novel fluorescent columnar liquid crystal based on tetraphenylethylene- rufigallol-tetraphenylethylene triads, *J. Mol. Struct.*, 2022, **1252**, 132210.

28. C. Arivazhagan, P. Malakar, R. Jagan, E. Prasad and S. Ghosh, Dimesitylboryl-functionalised cyanostilbene derivatives of phenothiazine: distinctive polymorphism-dependent emission and mechanofluorochromism, *CrystEngComm*, 2018, **20**, 3162–3166.

29. L.X. Guo, Y.B. Xing, M. Wang, Y. Sun, X.Q. Zhang, B.P. Lin and H. Yang, Luminescent liquid crystals bearing an aggregation-induced emission active tetraphenylthiophene fluorophore, *J. Mater. Chem. C,* 2019, **7**, 4828-4837.

30. D. Verma, G. P. Maurya, S. Jawla, V. Haridas, and A. Sinha, Designing Luminescent Liquid Crystals Using an AIE-Active Pseudopeptide Chiral Dopant: Circular Dichroism, Circularly Polarized Luminescence, and Photoluminescence Studies, *ACS Appl. Opt. Mater.* 2024, **2**,11.

31. Q. Yang, J. Zhu, Z.Li, X.S. Chen, Y.X. Jiang, Z.W. Luo, P. Wang, and H. L. Xie, Luminescent Liquid Crystals Based on Carbonized Polymer Dots and Their Polarized Luminescence Application, *ACS Appl. Mater. Interfaces*, 2021, **13**, 26522−26532.

32. M. M. Abad, S. Varghese, B. Milian-Medina, J. Gierschner, R. Gimenez and M. B. Ros, Bent-core liquid crystalline cyanostilbenes: fluorescence switching and thermochromism, *Phys. Chem. Chem. Phys.*, 2015, **17**, 11715—11724.

33. A. M. Al-Soliemy, Novel asymmetrical phenothiazine for fluorescent detection of cyanide anions, *J. Mol. Struct.*, 2019, **1179**, 525-531.

34. Y. Wei, X. Zhang, L. Wang, Y. Liu, T. Bing, X. Liua and D. Shangguan, Interaction of bis-benzimidazole-substituted carbazole derivatives with G-quadruplexes and living cells, *RSC Adv*., 2015, **5**, 75911–75917.

35. J. W. Park, S. Nagano, S.J. Yoon, T. Dohi, J. Seo, T. Seki, and S. Y. Park, High Contrast Fluorescence Patterning in Cyanostilbene- Based Crystalline Thin Films: Crystallization-Induced Mass Flow Via a Photo-Triggered Phase Transition, *Adv. Mater.* 2014, **26**, 1354–1359.

36. S. Kumar, Chemistry of Discotic Liquid Crystals from Monomers to Polymers, *CRC Press*, 2011.

37. a) K. Ohta, Linear algebraic proof and examples of composite lattice-based liquid crystalline phases, *Mol. Cryst. Liq. Cryst.*, 2017, **658**, 13-31; (b) Kazuchika Ohta, Physics and Chemistry of Molecular Assemblies, *World Scientific*,2020.

38. J. H. Kim, T. Schembri, D. Bialas, M. Stolte and F. Würthner, F. Slip-stacked J-aggregate materials for organic solar cells and photodetectors. *Adv. Mater*., 2022, **34**, 2104678.

39. N. J. Hestand and F. C. Spano. Expanded H- and J-molecular aggregates theory: the effects of vibronic coupling and intermolecular charge transfer. *Chem. Rev*., 2018, **118**, 7069.

40. S. Mukherjee, P. Thilagar, Recent advances in purely organic phosphorescent materials, *Chem. Commun*., 2015, **51**, 10988-11003.

41. M. Baroncini, G. Bergamini and P. Ceroni, Rigidification or interaction-induced phosphorescence of organic molecules, *Chem. Commun*., 2017, **53**, 2081-2093.

42. J. Ren, Y. Tian, Y. Wang, J. Yang, M. Fang, and Z. Li, the influence of p–p stacking on the room temperature phosphorescence of phenothiazine 5,5-dioxide derivatives, *J. Mater. Chem. C*, 2022, **10**, 13741.

43. X. Tang, Q. Bai, Q. Peng, Y. Gao, J. Li, Y. Liu, L. Yao, P. Lu, B. Yang, and Y. Ma, Efficient Deep Blue Electroluminescence with an External QuantumEfficiency of 6.8% and CIEy < 0.08 Based on a Phenanthroimidazole−Sulfone Hybrid Donor−Acceptor Molecule, *Chem. Mater*., 2015, **27**, 7050−7057.

44. P. S. Singh, P. M. Badani, and R. M. Kamble, Impact of the donor substituent on the optoelectrochemical properties of 6H-indolo[2,3-b] quinoxaline amine derivatives, *New J. Chem.*, 2019, **43**, 19379-19396.

45. W.Li, Y. Pan, L. Yao, H. Liu, S. Zhang, C. Wang, F. Shen, P. Lu, B. Yang, and. Y. Ma, A Hybridized Local and Charge-Transfer Excited State for Highly Efficient Fluorescent OLEDs: Molecular Design, Spectral Character, and Full Exciton Utilization, *Adv. Optical Mater.*, 2014, **2**, 892–901.

46. M. Hou, H. Wang, Y. Miao, H. Xu, Z. Guo, Z. Chen, X. Liao, L. Li, J. Li, and K. Guo, Highly Efficient Deep-Blue Electroluminescence from an A−π−D−π−A Structure-Based Fluorescence Material with Exciton Utilizing Efficiency above 25%, *ACS Appl. Energy Mater.*, 2018, **1**, 3243−3254.

47. Y. Zhang, M. Qile, J. Sun, M. Xu, K. Wang, F. Cao, W. Li, Q. Song, B. Zou, and C. Zhang, Ratiometric pressure sensors based on cyano-substituted oligo(p-phenylene vinylene) derivatives in the hybridized local and charge-transfer excited state, *J. Mater. Chem. C*, 2016, **4**, 9954—9960.

48. L. Xianhao, M. Sun, L. Xu, R. Wang, H.i Zhou, Y. Pan, S. Zhang, Q. Sun, S. Xue and W. Yang, highly efficient non-doped blue fluorescent OLEDs with low-efficiency roll-off based on hybridized local and charge transfer excited state emitters, *Chem. Sci.*, 2020, **11**, 5058-5065.

49. X. Chen, D. Ma, T. Liu, Z. Chen, Z, Yang, J. Zhao, Z. Yang, Yi Zhang and Z. Ch, Hybridized Local, and Charge-Transfer Excited-State Fluorophores through the Regulation of the Donor-Acceptor Torsional Angle for Highly Efficient Organic Light-Emitting Diodes, *CCS Chem.* 2022, **4**, 1284–1294.

50. S. Xu, Y. Yuan, X. Cai, C. Zhang, F. Hu, J. Liang, G. Zhang, D. Zhang, and B. Liu, Tuning the singlet-triplet energy gap: a unique approach to efficient photosensitizers with aggregation-induced emission (AIE) characteristics, *Chem. Sci.*,2015, **6**, 5824.

51. Y. Pan, J. Huang, W. Li, Y. Gao, Z. Wang, D. Yu, Bing Yang, and Y. Ma, Theoretical investigation of high-efficiency organic electroluminescent material: HLCT state and hot exciton process, *RSC Adv.*,2017, **7**, 19576.

52. X. Wang, C. Ma, M. Xie, L. Chu, Y. Zhou, Q. Sun, W. Yang, S. Xue, Efficient and ultra-high luminance orange-red organic light emitting diode (OLED) based on a triphenylamine-benzothiadiazole-phenoxazine hybrid molecule with hybrid local and charge-transfer (HLCT) characteristic, *Dyes Pigm.*, 2024, **229**,112274.

53. Bala, I., Singh, N., Yadav, R.A.K., De, J., Gupta, S.P., Singh, D.P., Dubey, D.K., Jou, J.H., Douali, R. and Pal, S.K., Room temperature perylene-based columnar liquid crystals as solid-state fluorescent emitters in solution-processable organic light-emitting diodes. *J. Mater. Chem. C*, 2022, **8**, 12485-12494.

54. I. Bala, R.A.K. Yadav, M. Devi, J. De, N. Singh, K. Kailasam, J. Jayakumar, J.H. Jou, C.H. Cheng, and S.K. Pal, High-performing D–π–A–π–D benzothiadiazole-based hybrid local and charge-transfer emitters in solution-processed OLEDs, *J. Mater. Chem. C*, 2020, **8**, 17009-17015.

55. T. Jairam, and W.P. Hong, Recent progress in imidazole based efficient near ultraviolet/blue hybridized local charge transfer (HLCT) characteristic fluorophores for organic light-emitting diodes., *J. Mater. Chem. C*, **2022**, 10, 16173-16217.

56. H. Zhang, J. Zeng, W. Luo, H. Wu, C. Zeng, Synergistic tuning of the optical and electrical performance of AIEgens with a hybridized local and charge-transfer excited state. *J. Mater. Chem. C*, **2019**, 7, 6359–6368.

57. C. Wang, X. Li, Y. Pan, S. Zhang, Highly efficient non-doped green organic light-emitting diodes with combination of high photoluminescence and high exciton utilization. *ACS Appl. Mater. Interfaces*, 2016, **8**, 3041–3049.

58. S. Zhang, W. Li, L. Yao, Y. Pan, Shen, Enhanced proportion of radiative excitons in non-doped electro-fluorescence generated from an imidazole derivative with an orthogonal donor-acceptor structure. *Chem. Commun*., 2013, **49**, 11302–11304.

59. W.P. Hong, and J. Tagare, Recent Progress in Imidazole Based Efficient near Ultraviolet/Blue Hybridized Local Charge Transfer (HLCT) Characteristics Fluorophores for Organic Light-Emitting Diodes. *J. Mater. Chem. C*, 2022, **10**, 16173-16217.

60. Tang, X., Bai, Q., Peng, Q., Gao, Y., Li, J., Liu, Y., Yao, L., Lu, P., Yang, B. and Ma, Y., Efficient deep blue electroluminescence with an external quantum efficiency of 6.8% and CIE y< 0.08 based on a phenanthroimidazole–sulfone hybrid donor-acceptor molecule. *Chem. Mater*., 2015, **27**, 7050–7057.

61. P.K. Behera, S. Lenka, F.R. Chen, M. Roy, I. Mondal, D.S. Rao, S.P. Senanayak, J.H. Jou, and A.S. Achalkumar, Revelation of room temperature liquid crystallinity and yellow-

orange electroluminescence (EQE> 7%) in a columnar self-assembled N-annulated perylene bisimide, *Chem. Eng. J.*, 2024, **497**, 154719.

62. W. Lee, C.W. Chen, C. Chueh, C. Yag, and W.C. Chen, Synthesis of New Fluorene-Indolocarbazole Alternating Copolymers for Light-Emitting Diodes and Field Effect Transistors, *Polym. J.*, 2008, **40**, 249–255.

63. M. Cheng, B. Xu, C. Chen, X. Yang, F. Zhang, Q. Tan, Y. Hua, L. Kloo, and L. Sun, Phenoxazine-Based Small Molecule Material for Effi cient Perovskite Solar Cells and Bulk Heterojunction Organic Solar Cells, *Adv. Energy Mater.*, 2015, **5**, 1401720.

64. Y. Zhu, A. Babel, and S. A. Jenekhe, Phenoxazine-Based Conjugated Polymers: A New Class of Organic Semiconductors for Field-Effect Transistors, *Macromolecules*, 2005, **38**, 7983-7991.

65. X. Ding, C. Chen, L. Sun, H. Li, H. Chen, J. Su, H. Li, H. Li, L. Xu, and M. Cheng, highly efficient phenothiazine 5,5-dioxide-based hole transport materials for planar perovskite solar cells with a PCE exceeding 20%, *J. Mater. Chem. A*, 2019, 7, 9510.

66. S. Melis, S. Hung, C. Bagade, Y. Chung, E. Hughes, X. Zhang, P. Barbara, P. Han, T. Li, D. McCusker, R. Hartsmith, J. Bertke, P. Dev, I. Stone, J. Joshi, P. Vora, and Edward Van Keuren Charge Transport through Superexchange in Phenothiazine–7,7,8,8-Tetracyanoquinodimethane (PTZ–TCNQ) Cocrystal Microribbon FETs Grown Using Evaporative Alignment, *ACS Appl. Electron. Mater.*, 2022, **4**, 5973-5983.

67. H. Yoon, W. Lee, J. Lee, D. Lim, D. Hwang, and I. Kang, Solution-Processable Field-Effect Transistors Fabricated Using Aryl Phenoxazine Based Polymers as the Active Layer, *Bull. Korean Chem. Soc*. 2009, **30**, 102371.

68. D. Shinde, J. Salunke, N. Candeias, Crystallisation-enhanced bulk hole mobility in phenothiazine-based organic semiconductors., *Sci Rep*, 2017, **7**, 46268.

69. M. Cheng, C. Chen, X. Yang, J. Huang, F. Zhang, B. Xu, and L. Sun., Novel Small Molecular Materials Based on Phenoxazine Core Unit for Efficient Bulk Heterojunction Organic Solar Cells and Perovskite Solar Cells, *Chem. Mater.*,2015, **27**, 1808−1814.

70. R. De, J. De, S.P. Gupta, I. Bal, U. K. Pandey and S. K. Pal, Oxadiazole-integrated heterocoronene discotics as ambipolar organic semiconductors, *J. Mater. Chem. C*, 2023, **11**, 980.

71. Hägerbäumer, A., Höss, S., Heininger, P., & Traunspurger, W., Experimental studies with nematodes in ecotoxicology: an overview., *J. Nematol.*, 2015, **47**, 11.

72. Hunt, P. R., The C. elegans model in toxicity testing., *J. Appl. Toxicol.*, 2017, **37**, 50-59.

73. C. Zhang, Y.T. Sun, S. Gan, A. Ren, S. Milaneh, D.J. Xiang, and W.L. Wang, Recent progress of organic fluorescent molecules for bioimaging applications: cancer-relevant biomarkers, *J.Mater.Chem. C.*, 2023, **11**, 16859-16889.

74. A.S. Stender, K. Marchuk, C. Liu, S. Sander, M.W. Meyer, E.A. Smith, N. Fang, Single cell optical imaging and spectroscopy. *Chem.Rev*., 2013, **113**, 2469-2527.

75. A. Murschhauser, P.J.F. Röttgermann, D. Woschee, M.F. Ober, Y. Yan, K .A. Dawson, J.O.Radler, A high-throughput microscopy method for single-cell analysis of event-time correlations in nanoparticle-induced cell death. *Commun Bio*., 2019, **2**, 35.

76. A. Saini, V. Sharma, P. Mathur, M. M. Shaikh, the development of fluorescence turn-on probe for Al(III) sensing and live cell nucleus-nucleoli staining. *Sci. Rep*., 2016, **6**, 34807.

77. C. Sadhu, A.K. Mitra, Synthetic, biological and optoelectronic properties of phenoxazine and its derivatives: a state of the art review. *Mol. Divers*., 2024, **28**, 965-1007.

78. X.Y. Zhu, H.W. Yao, Y.J. Fu, X.F. Guo, H. Wang, Effect of substituents on Stokes shift of BODIPY and its application in designing bioimaging probes. *Anal. Chim. Acta*., 2019, **1048**, 194-203.

79. S. Valdez, M. Robertson, & Z. Qiang, Fluorescence resonance energy transfer measurements in polymer science: A review, *Macromol. Rapid Commun.*, 2022, **43**, 2200421.

80. P. P. Provenzano, K. W. Eliceiri, & P. J Keely, Multiphoton microscopy and fluorescence lifetime imaging microscopy (FLIM) to monitor metastasis and the tumour microenvironment, *Clin. Exp. Metastasis*, 2009, **26**, 357-370.

81. S. Oshimizu, S. Takeshi, T. Sato, R. Yamakado, Y. Tatewaki, and S. Okada, Synthesis and Solid-State Polymerization of 5-(Pyren-1-yl) penta-2,4- diyn-1-ol Derivatives with an N-Phenylurethane or N-Benzylurethane Group, *Cryst. Growth Des.*, 2020, **20**, 6356-6365.

82. R. K. Gupta, S. K. Pathak, J. De, S. K. Pal, and A. S. Achalkumar, Room temperature columnar liquid crystalline self-assembly of acid chromic, luminescent, star-shaped molecules with cyano vinylene chromophores, *J. Mater. Chem. C*, 2018, **6**, 1844

83. J. W. Park, S. Nagano, S.-J. Yoon, T. Dohi, J. Seo, T. Seki, S. Y. Park, High Contrast Fluorescence Patterning in Cyanostilbene-Based Crystalline Thin Films: Crystallization-Induced Mass Flow Via a Photo-Triggered Phase Transition, *Adv. Mater.* 2014, ***57***, 1354–1359.

Chapter 4

Indolo [2,3-b]quinoxaline, a core for the stabilization of room temperature liquid crystalline self-assembly, aggregation-induced emission bioimaging applications.

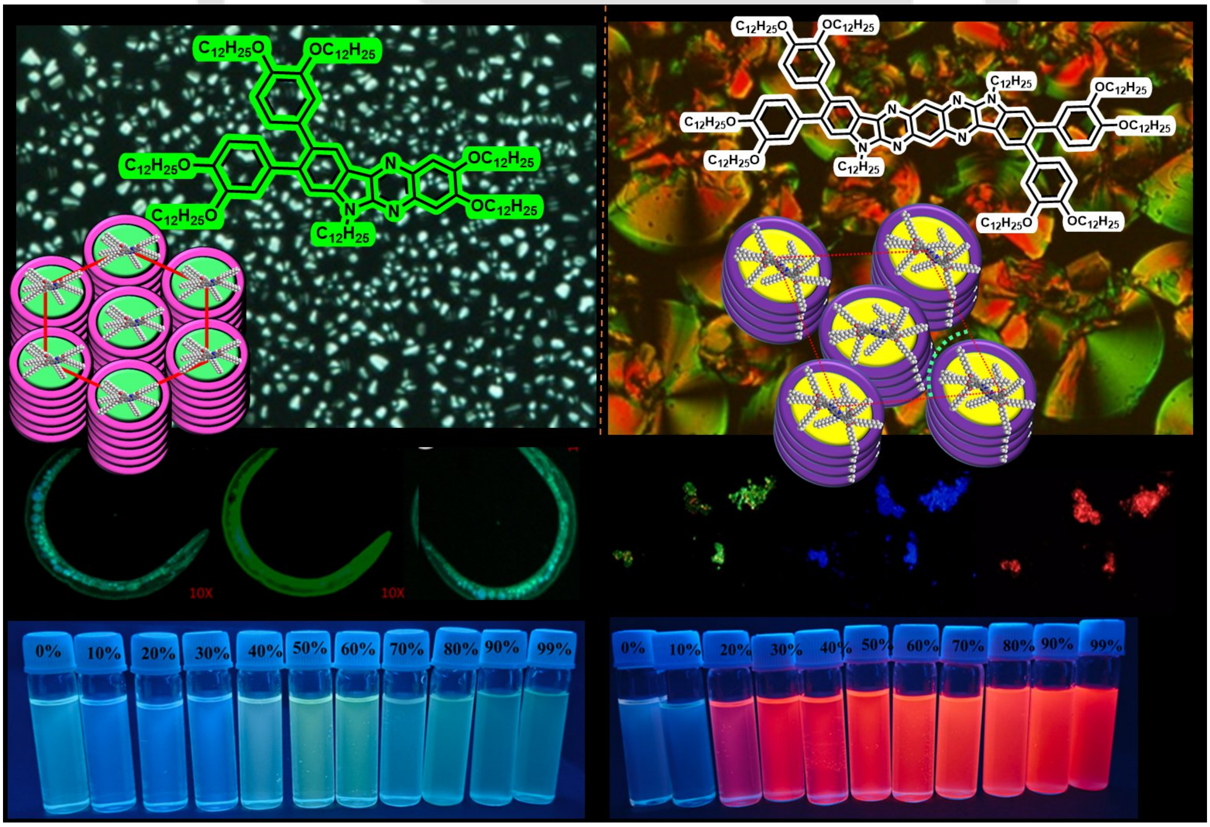

4.1. Introduction

Indolo[2,3-b]quinoxaline represents a novel class of heterocyclic compounds with an inherent donor-acceptor (D–A) system,[1,2] where the electron-rich indole unit is fused with the electron-deficient quinoxaline moiety.[3,4] This structure endows the compounds with exceptional thermal stability,[5] making them ideal candidates for applications in the pharmaceutical industry, optoelectronic devices (**4.2**),[6] and photo-initiators in dye-sensitized solar cells (**4.3**),[4-7] batteries,[8] organic transistor memory (**4.4**),[9] hole injection layer (HIL, **4.7**),[10] anion sensing (**4.5**), live cell imaging (**4.5**).[11] The first indolo [2,3-b] quinoxaline derivative was synthesized in 1895 by condensing 1,2-diaminobenzene with isatine, combining the structural features of indoles and quinoxalines.[12] The electronic properties of these indolo-quinoxaline derivatives can be fine-tuned by modifying the donor group within the D–A framework.[13] These compounds have been successfully incorporated into multilayer organic light-emitting diodes (OLEDs),[14] acting as electron-transporting and emitting layers in deep-red organic electrophosphorescent devices (**4.6**).[15] Quinoxaline derivatives are widely used in OLEDs[16] due to their favorable electron affinity, emission properties, and thermal stability. Their low-lying LUMO (Lowest Unoccupied Molecular Orbital) also makes them adequate hole-blocking layers in OLEDs.[17] The potential of quinoxaline-based compounds was first demonstrated by Park and co-worker,[18] who introduced them as organic sensitizers. Research has recently focused on quinoxaline-based conjugated polymers and small molecules for organic photovoltaic cells (OPVs).[7,17] The unique dipolar structure of indoloquinoxaline compounds promotes excellent intramolecular charge transfer, enhancing their optoelectronic performance.[3] Further studies have highlighted the biological properties of quinoxaline derivatives, including DNA intercalation (**4.8**), antitumor activity, potent antimalarial effects,[19] selective photo-induced DNA cleavage, cytotoxicity,[12] and anti-herpesvirus activity.[20,21]

Developing fused heterocyclic organic dyes with donor-acceptor (D-A) architectures in optoelectronic devices has garnered significant attention. These dyes offer advantages such as easy synthesis, low-cost processing, good solubility in organic solvents, excellent structure-property relationships, and tunable optoelectronic properties. They also exhibit unique characteristics such as positive solvatochromism, aggregation-induced emission (AIE, **4.1**),[22] thermally activated delayed fluorescence (TADF), and strong semiconducting properties. D-A-based organic dyes enhance charge transfer processes and can be engineered to exhibit either hole (p-type) or electron (n-type) transporting properties. While research has primarily focused on environmentally stable p-type charge transfer materials, ambipolar materials that can transport electrons and holes are increasingly recognized for their potential to improve power efficiency and reduce device costs. [13]

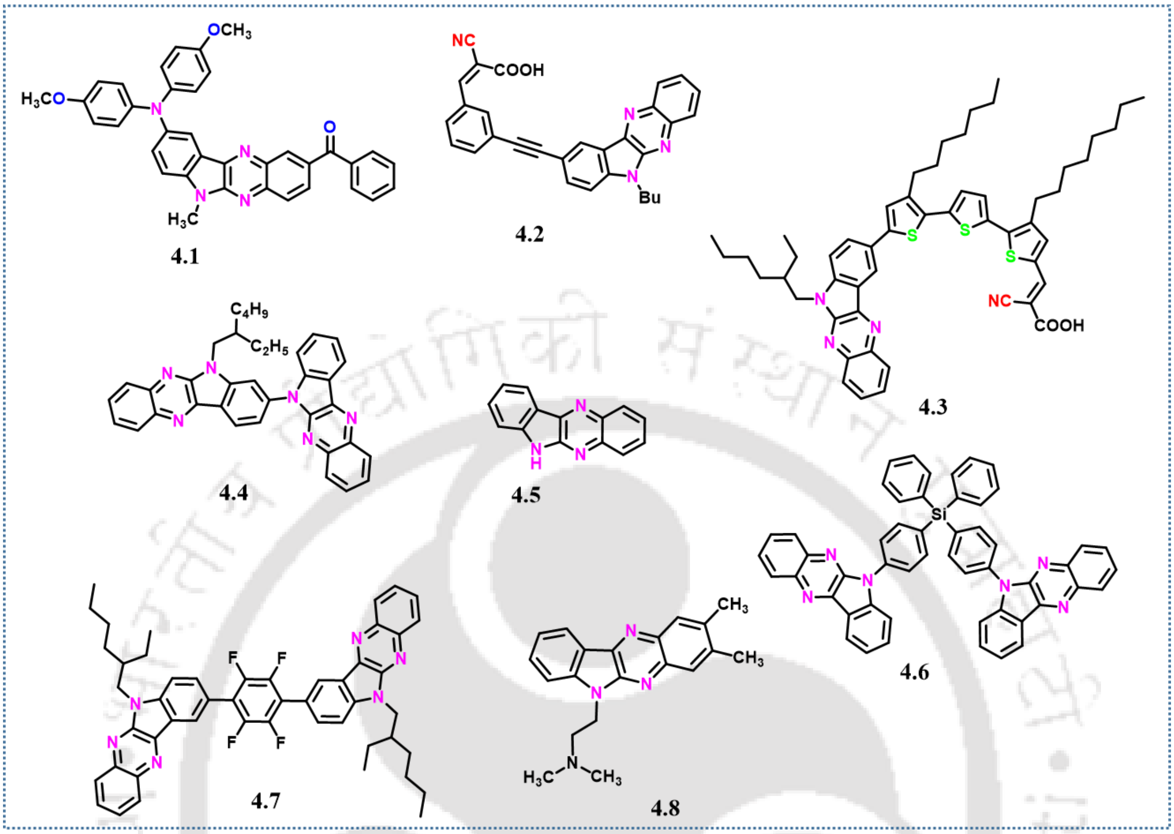

Figure 4.1. Structures of Indolo[2,3-b]quinoxaline-based compounds are used in various applications (**4.1-4.8**).

Researchers have pioneered the creation of advanced materials with tunable fluorescence properties by integrating AIE-active fluorophores into systems like liquid crystals (LCs).[23-34] These innovative luminescent liquid crystal (LLC) materials, which merge the unique properties of liquid crystals with luminescent molecules, have captured significant attention due to their remarkable light-emitting capabilities, self-organizing behavior, and responsiveness to external stimuli. These features make LLCs exceptionally well-suited for cutting-edge applications in advanced electronics, including OLEDs, lasers, LCDs, sensors, and semiconductors.[35-39] Moreover, the tunable emission properties of LLCs extend their potential to high-resolution, non-invasive biological imaging, enabling deeper insights into cellular processes.[40-45]

However, despite these exciting advantages, a persistent challenge in OLEDs and other optoelectronic devices is the aggregation-caused quenching (ACQ) effect, in which many donor-acceptor (D-A) molecules lose their emissive properties or are quenched upon aggregation in the solid state.[13,46] To overcome this limitation, Tang et al. (2001) introduced the groundbreaking aggregation-induced emission (AIE) phenomenon, which prevents ACQ by restricting intramolecular rotation and conformational changes within the molecules.[47] This innovation has paved the way for the development of solid-state emissive materials, mainly by blending AIE-active groups with traditional ACQ blocks, thus unlocking new possibilities for high-performance optoelectronic devices.

One of the critical hurdles in designing luminescent liquid crystals (LLCs) is the tendency of chromophoric mesogens to aggregate tightly, leading to fluorescence quenching. However, introducing AIE properties has effectively addressed this issue, ensuring enhanced emission efficiency even in the solid state. Several strategies, including modifying luminogens with flexible chains or incorporating AIE fluorophores into mesogenic structures, have successfully created materials that exhibit superior performance in devices such as liquid crystal displays (LCDs), benefiting from improved brightness, contrast, efficiency, and viewing angles.

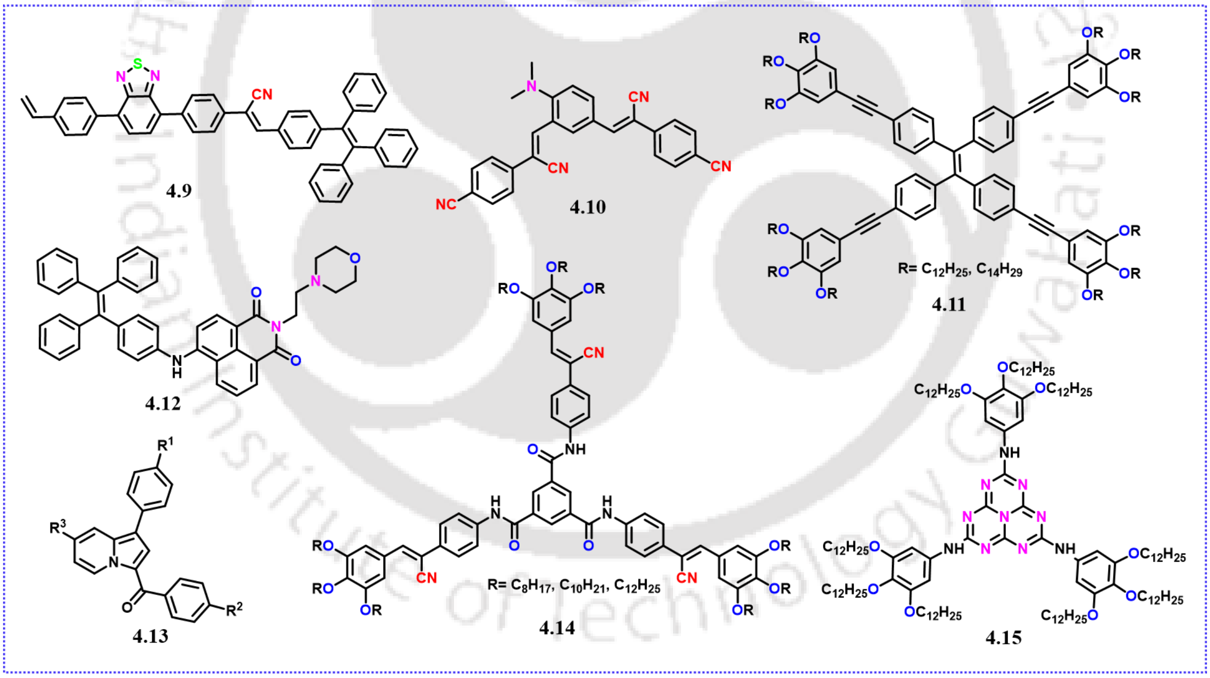

Figure 4.2. Structures of Aggregation-induced emission (AIE) based compounds are used in various applications (**4.9-4.15**).

Material scientists employ three primary strategies to further tackle these challenges in designing luminescent liquid crystalline materials: synthetic, doping, and supramolecular approaches.[26] The synthetic approach involves modifying luminogens to encourage liquid crystalline behavior or pairing AIE luminophores with mesogenic structures. The doping approach incorporates AIE emitters into liquid crystals or their mixtures, enhancing emission in the ordered mesophase. Meanwhile, the supramolecular approach utilizes non-covalent interactions to assemble structures that combine liquid crystallinity with AIE properties, ultimately developing highly efficient luminescent materials. In pursuing luminescent mesogens, researchers have advanced the field by introducing flexible terminal chains to functionalize emissive cores such as pyrene and anthracene, enhancing their luminescent properties within liquid crystalline environments.[48-50] This ongoing innovation continues to drive the evolution of materials that hold immense promise for various applications across optoelectronics, such as OLED (**4.10**, **4.15**),[35,37] charge transport (**4.14**),[39] mechnochromic (**4.11**),[38] bioimaging (**4.9**, **4.12**),[43,44] sensor [51-54] and beyond.

In the columnar phase of discotic liquid crystals (DLCs), molecules form stacked columns that act as 'molecular wires' for efficient charge and exciton transport. These versatile materials have energy, photovoltaics, drug delivery, and sensing applications, outperforming traditional conjugated polymers.[55-66]

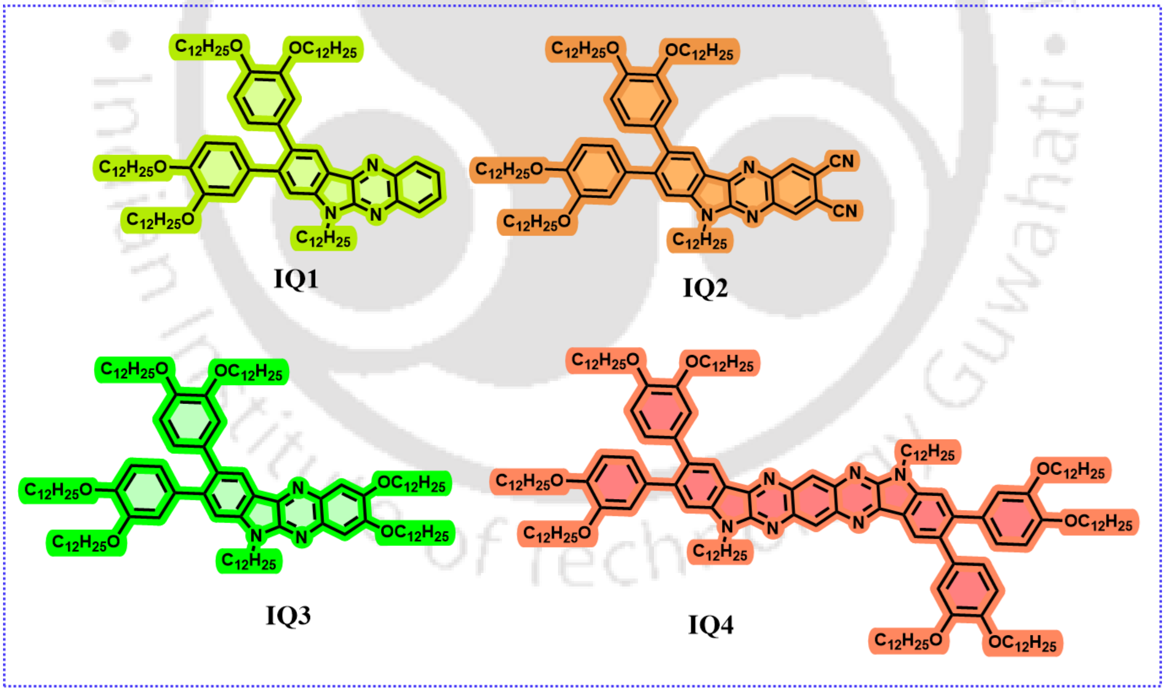

Figure 4.3. Structures of **IQ** are studied in this work.

To the best of our knowledge, indole[2,3-b]quinoxaline based room-temperature liquid crystals were not previously reported. Given the significance of indole[2,3-b]quinoxaline derivatives in solid-state emissive and liquid crystalline D–A materials, we have designed and synthesized four derivatives, **IQ1–IQ4**, based on indolo[2,3-b]quinoxaline. These compounds were then characterized using various spectroscopic techniques. Among these, **IQ3** and **IQ4** show the liquid crystalline behavior. Additionally, their photophysical properties, including aggregation-induced emission (AIE) and electrochemical characteristics, were thoroughly investigated. Among the four indolo[2,3-b]quinoxaline compounds, we have selected compound **IQ4** for staining toward nematodes and cancer cells due to its excellent fluorescence behavior and AIE-active nature. The study revealed high-contrast visualization in both solvent and aggregated state, enabling precise observation of cellular structures of nematode without interference from background fluorescence or crystallization issues. This unique attribute presents a valuable opportunity for targeted MCF7 human breast cancer cell imaging, facilitating improved visualization and deeper insights into cellular dynamics and behavior.

4.2. Result and Discussion

4.2.1. Synthesis and molecular structural characterization

The synthetic approach utilized to prepare target **IQ**s is outlined in schemes 4.1 and 4.2

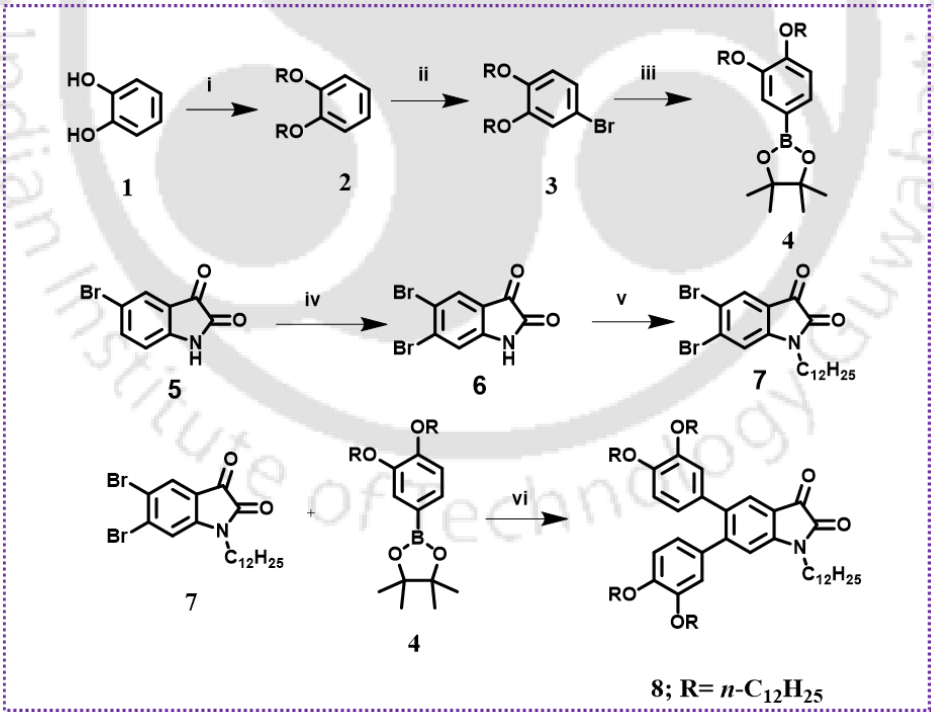

Scheme 4.1. Synthesis of *N*-alkylated isatin derivative **8**; Reagents and Conditions**:** (i) RBr, anhydrous K_2CO_3, DMF, 80 °C, N_2 atm, 24 h, 80%; (ii) NBS, SiO_2, DCM, rt, N_2 atm, 24 h, 76%; (iii) 1,3,5-Tris(4,4,5,5-tetramethyl-1,3,2-dioxaborolan-2-yl) benzene, $Pd(PPh_3)Cl_2$, KOAc, Toluene ,110 °C, N_2 atm, 24 h, 70-76%; (iv) NBS, DMF, N_2, 25 °C, 12 h, 40%; (v) RBr, anhydrous K_2CO_3, DMF, 80 °C, N_2 atm, 24 h, 66%; (vi) K_2CO_3, Toluene: water, $Pd(PPh_3)_4$, reflux, 18 h, 76-78%.

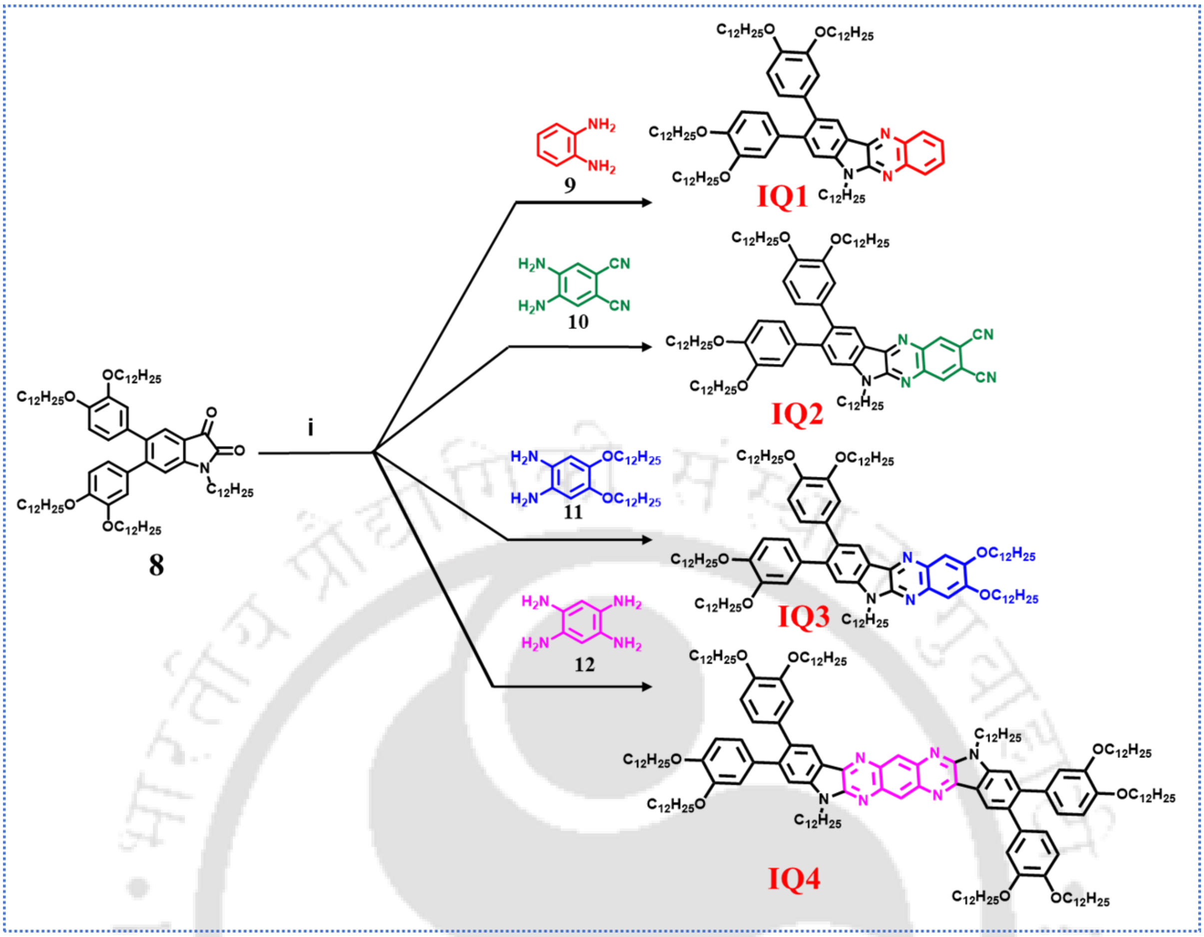

Scheme 4.2. Synthesis of target Indolo[2,3-b] quinoxaline derivatives (**IQ**s); Reagents and Conditions**:** (i) Glacial acetic acid, Et_3N, 110 °C, 24 h, 64-78%.

The target **IQ** derivatives (**IQ1**–**IQ4**) were synthesized using a straightforward synthetic pathway (Scheme 4.1 and 4.2). In the first step, catechol 1 was *N*-alkylated via a nucleophilic substitution reaction with *n*-$C_{12}H_{25}Br$ in anhydrous K_2CO_3. Compound **3** was then prepared using NBS and silica in dry DCM,[67] followed by the preparation of the dioxoborolane derivative **4** using dioxoborolane reagent, $Pd(PPh_3)_2Cl_2$, and KOAc in toluene.[67] The Suzuki coupling reaction of the dioxoborolane derivative with $Pd(PPh_3)_4$ as a catalyst and K_2CO_3 as a base led to the formation of compound **8.**[67] Finally, the **IQ** derivatives were synthesized through a condensation reaction between *N*-alkylated isatin derivative, **8** and various diamino-benzene derivatives in the presence of glacial acetic acid and a catalytic amount of triethyl amine.[11,16] The products were purified by column chromatography using an ethyl acetate-hexane mixture, yielding solid products in good yields. All compounds were characterized using standard analytical techniques, including MALDI-TOF mass spectrometry, ^{1}H NMR, ^{13}C NMR, and IR spectroscopy. Thermogravimetric analysis (TGA) was conducted to assess the thermal stability of the compounds, revealing decomposition onset temperatures ranging from 357 to 397 °C for 5 wt% decomposition. (Table 4.1, Figure 4.4).

4.2.2. Thermal behaviour

The determination of mesomorphism involved complementary techniques. Initially, polarized optical microscopy (POM) with a programmable hot stage was employed to observe optical textures. This method allowed the visualization of linear defects that emerged from the homeotropic domain on cooling from the isotropic state. These structures were then transformed into a mosaic pattern of the columnar hexagonal (Col_h) and pseudo-focal conic of the columnar oblique (Col_{ob}) phase (Figures 4.5a and 4.5b).[62] Differential scanning calorimetry (DSC) helped confirm transition temperatures and quantify associated enthalpy changes. These measurements confirmed the mesomorphic properties observed under POM.

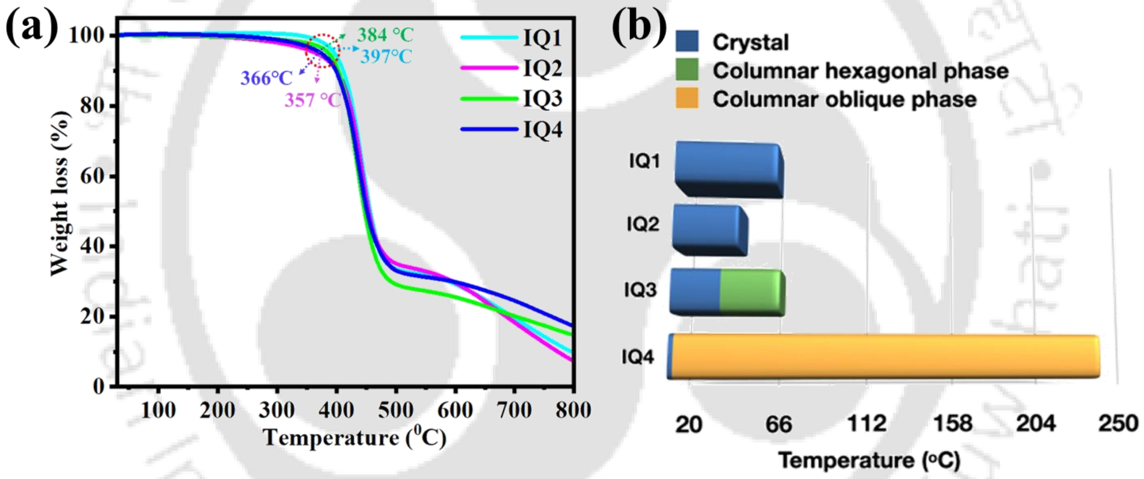

Figure 4.4. (a) TGA plots of compound (heating rate of 10 °C/min, Nitrogen atmosphere). (b) The bar graph represents **IQ** compounds' mesomorphic behaviors (Considered the second heating scan of DSC).

Further, differential scanning calorimetry (DSC) confirmed the transition temperatures and quantified the associated enthalpy changes (Figure 4.5 c and 4.5 d). Furthermore, powder X-ray diffraction (XRD) analyses were conducted to unequivocally assign the symmetry of the columnar phase observed at high and low temperatures. A summarized overview of phase transition temperatures and enthalpy values for all compounds investigated is provided in Table 4.1. The enhanced attractive interactions of the aromatic core complemented with the increased fluidity/nanophase segregation offered by the alkyl chains in compounds **IQ3** and **IQ4** were suggested as contributing factors that realized the liquid crystalline behavior compared to compounds **IQ1** and **IQ2**.

Table 4.1. Phase transition temperatures (°C), corresponding enthalpies (kJmol^{-1}), and decomposition temperatures were obtained from DSC^{a} and TGA^{b}

Entry	Phase sequence (kJ/mol)^{a}		T_5^{b} (°C)
	Second Heating	First Cooling	
IQ1	Cr_1 3.1 (18.2) Cr_2 25.6 (0.6) Cr_3 67.9 (1.7) I	I -8.0 (16.0) Cr	397
IQ2	Cr 50.4 (14.3) I	I 33.7 (15.9) Cr	357
IQ3	Cr_1 4.01 (1.57) Cr_2 42.64 (20.26) Col_h 70.0 I^{c}	I^{c} 69.0 Col_h 25.2 (0.24) Cr_2 -0.79 (13.79) Cr_1	384
IQ4	Cr 22.3 (8.7) Col_{ob} 222.8 (28.4) I	I 215.79 (27.7) Col_{ob} 14.9 (5.5) Cr	366

^{a}Peak temperatures in the DSC thermograms obtained during the second heating and first cooling cycles at 5 °C min^{-1} Col_h = Columnar hexagonal phase; Col_{ob} = Columnar oblique phase; I = Isotropic phase. b = Temperature at which 5 wt% decomposition occurred (°C). c = Isotopic is not detected, the value observed from polarise optical microscope.

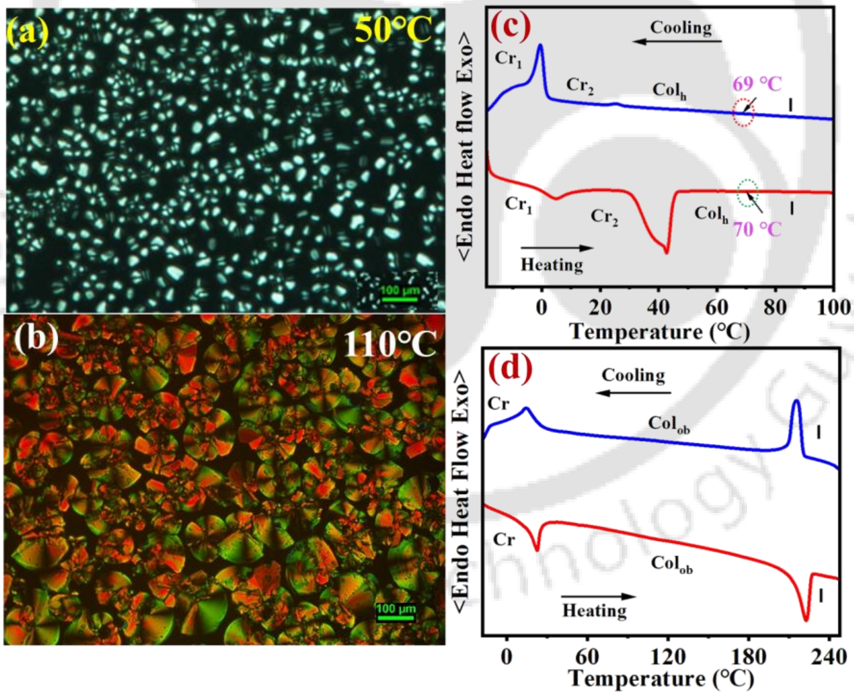

Figure 4.5. POM images were obtained for the (a) Col_h phase **IQ3** at 50 °C and (b) Col_{ob} phase **IQ4** at 110 °C (scale bar corresponds to 100 μm). DSC thermograms were obtained for (c) **IQ3**, and (d) **IQ4** (blue trace, first cooling scan; red trace, second heating scan).

Compared to earlier reports, the POM images observed for both compounds at different temperatures showed characteristic columnar phase textures, and fluidity was noted with the application of mechanical shear on the samples in the mesophase range. During heating and cooling cycles, the DSC thermogram profiles exhibited prominent peaks in **IQ4** corresponding to the phase transitions from crystal to columnar phase and columnar to isotropic phase. However, in **IQ3**, the phase transition from $\mathrm{Col_h}$ to isotropic is not observed in the DSC thermogram; the isotropic temperature is noted from a polarized optical microscope. For example, in the case of compound **IQ4**, there is an endothermal transition from one crystalline (Cr) phase to a mesophase $\mathrm{Col_{ob}}$ at ≈ 22 °C (ΔH = 8.7 kJ/mol), followed by another endothermal transition from mesophase ($\mathrm{Col_{ob}}$) to isotropic liquid was seen at ≈ 222 °C (ΔH = 28.4 kJ/mol) during the second heating cycle. Upon cooling, exothermic peaks are observed at ≈ 215 °C (ΔH = 27.7 kJ/mol) and ≈ 14.9 °C (ΔH = 5.5 kJ/mol), corresponding to transitions from isotropic liquid to mesophase ($\mathrm{Col_{ob}}$) and from mesophase ($\mathrm{Col_{ob}}$) to crystalline phase (Cr), respectively. Similar behavior was noticed in the case of **IQ3**, with a reduced clearing point due to a decrease in the aromatic core.

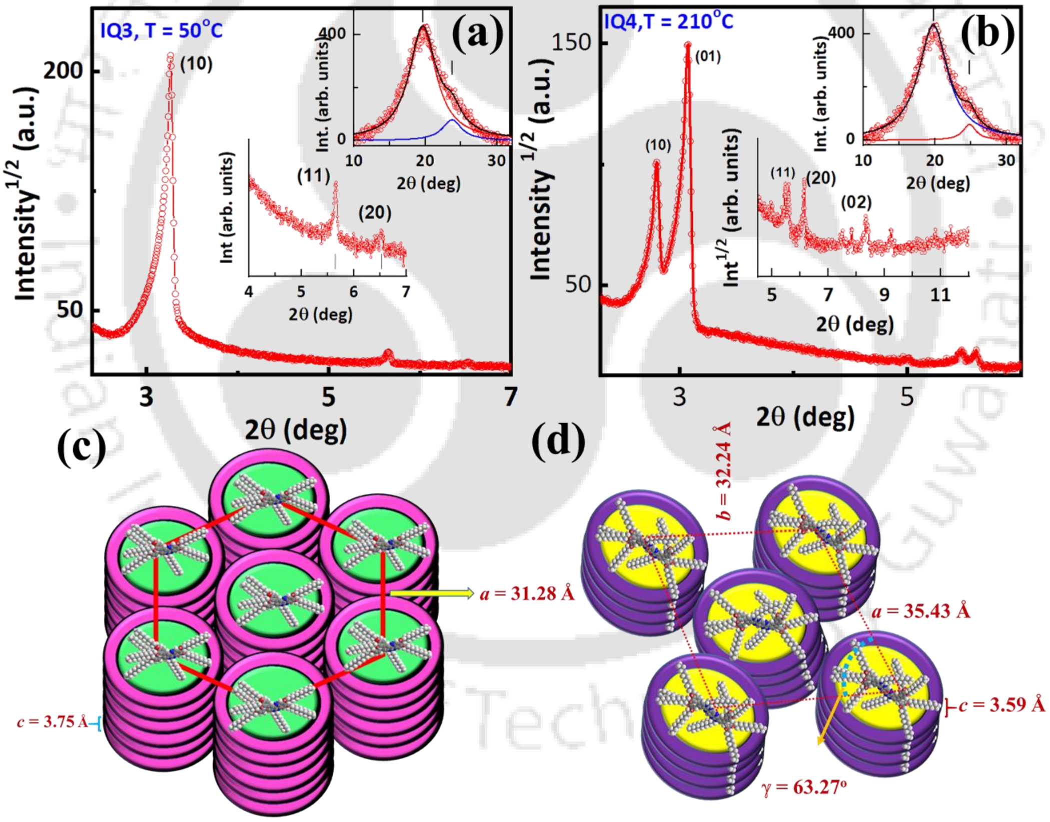

Figure 4.6. XRD profiles depicting the intensity against 2θ obtained for the (a) $\mathrm{Col_h}$ phase of **IQ3** at 50 °C and (b) the $\mathrm{Col_{ob}}$ phase of **IQ4** at 210 °C (insets show the expansion of the middle and wide-angle regions, The diffuse peaks-shown as red and blue lines- became more prominent after the deconvolution procedure, representing the contribution due to flexible hydrocarbon and the rigid core-core packing. The solid lines (dark, red, blue) are fitting to Lorentzian expression); (c) the schematic diagram depicting the self-assembly of **IQ3** into $\mathrm{Col_h}$ phase at 50 °C and (d) **IQ4** into $\mathrm{Col_{ob}}$ phase at 210 °C.

The structural organization of **IQ**-based DLCs was investigated using small-angle X-ray scattering (SAXS) and wide-angle X-ray scattering (WAXS) at various temperatures. Among the four compounds studied (**IQ1**, **IQ2**, **IQ3**, and **IQ4**), **IQ3** demonstrated a stable columnar hexagonal (Col$_h$) phase at 50 °C, and **IQ4** shows a Col$_{ob}$ phase at 210 °C, 110 °C and 30 °C (Table A2). The SAXS pattern of **IQ3** at 50 °C revealed three distinct Bragg peaks in the small-angle region at 27.09Å, 15.64 Å, and 13.54 Å, with a ratio of 1: 0.58: 0.5 corresponding to the hexagonal lattice with Miller indices (10), (11) and (20), respectively (Figure 4.6a; Table 4.2). Thus, the Col phase was confirmed as the Col$_h$ phase with the hexagonal lattice parameter a = 31.28 Å, effectively the distance between the two columns of a hexagonal lattice. In the wide-angle regime, a d-spacing of 4.53 Å was observed, indicative of the packing of the fluid-like alkyl chains. The SAXS pattern of **IQ4** at 210 °C revealed five distinct Bragg peaks in the small-angle region at 31.65 Å, 28.80 Å, 17.70 Å, 15.82 Å, and 14.40 Å, corresponding to the Miller indices (10), (01), (11), (20) and (02), respectively (Figure 4.6b; Table 4.2). These peaks were indexed to a columnar phase with oblique lattice, with lattice parameters of a = 35.43 Å, b = 32.24 Å, with an angle of γ = 63.27°. In the wide-angle regime, a d-spacing of 4.50 Å was observed, indicative of the packing of the fluid-like alkyl chains. The columnar oblique mesophase exists till 30 °C (Figure A11, Table A1). This stability is consistent with complementary data obtained from DSC and polarized optical microscopy (POM). The molecular organization within the mesophase was further examined, revealing an estimated one molecule per unit cell (Z ≈ 1). A schematic representation (Figure 4.6c ,d) illustrates the self-assembly of **IQ3** and **IQ4** molecules into columnar hexagonal and columnar oblique phases.

Table 4.2. Results of (*hkl*) indexation of XRD profiles of **IQ**s at a given temperature (T) of mesophase

Compounds (D/Å)	Phase (T/°C)	d-spacing		Miller Index (hk)	Lattice parameters (Å), Lattice area S (Å^2), Molecular volume (Å^3)
		d_{obs} (Å)	d_{cal}(Å)		
IQ3 (46.24) MW: 1645.70	$\mathrm{Col_h}$ (50 °C)	27.09 15.65 13.56 4.52(h_a) 3.75(h_c)	27.09 15.64 13.54	10 11 20	a =31.28 A = 847.1 V = 3175.9 $Z \approx 1$
IQ4 (54.12) MW: 2476.00	$\mathrm{Col_{ob}}$ (210 °C)	31.65 28.80 17.70 16.16 15.79 14.40 11.78 11.28 10.59 9.58 4.50 (h_a) 3.59 (h_c)	31.65 28.80 17.70 16.12 15.82 14.40 11.76 11.26 10.59 9.60	10 01 11 -12 20 02 -31 -32 -23 03	a = 35.43 b = 32.24 γ = 63.27° A = 1020.39 V = 3663.20 $Z \approx 1$
	$\mathrm{Col_{ob}}$ (110°C)	29.64 28.80 16.48 14.85 14.44 11.18 10.81 9.89 4.56(h_a) 3.55(h_c)	29.64 28.80 16.48 14.82 14.40 11.19 10.76 9.88	10 01 11 20 02 -13 12 30	a = 36.09 b = 35.06 γ= 55.22° A = 1039.43 V = 3688.19 $Z \approx 1$
	$\mathrm{Col_{ob}}$ (30 °C)	29.55 26.46 17.83 14.77 13.21 11.57 10.12 9.83 7.31 4.42(h_a) 3.50(h_c)	29.55 26.46 17.83 14.78 13.23 11.82 9.99 9.85 7.45	10 01 11 20 02 21 -31 30 -33	a = 30.32 b = 27.15 γ= 77.06° A = 802.32 V = 2806.65 $Z \approx 1$

[a] The diameter (D) of the disk (estimated from Chem 3D Pro 8.0 molecular model software from Cambridge Soft). d_{obs}: spacing observed; d_{cal}: spacing calculated (deduced from the lattice parameters; a,b for $\mathrm{Col_{ob}}$, and a for $\mathrm{Col_h}$ phase). The spacings marked h_a and h_c correspond to diffuse reflections in the wide-angle region arising from correlations between the alkyl chains and core regions, respectively. Z indicates the number of molecules per columnar slice of thickness h_c, estimated from the lattice area S and the volume V.

4.2.3. Photophysical properties

The photophysical properties of the four compounds (**IQ1**–**IQ4**) were investigated in both solution and thin film states, with the thin films spin-coated onto quartz substrates. The compounds were dissolved in various solvents at a concentration of 1 wt%/vol, exhibiting good solubility in polar aprotic solvents such as chloroform, THF, cyclohexane, and toluene. Photophysical measurements in solution were conducted using 20 µM chloroform solutions, while thin films were prepared from 1 wt%/vol- toluene solutions. The absorption spectra of the **IQ** derivatives in micromolar solutions displayed broad bands around 274–477 nm in the more extended wavelength region. The electronic spectra of the **IQ**s featured higher energy n–π* and π–π* transitions (λ_{max} = 274 to 394 nm), characteristic of vibrionic patterns, originating from the indole-quinoxaline unit. Additionally, lower energy intramolecular charge transfer (ICT) transitions (λ_{max} = 431 to 477 nm) were observed (Figure 4.7, A12, and A13).[13,17,33] These lower energy transitions indicate the inherent ICT character within the **IQ**s, arising from charge transfer between the electron-donating indole unit and the electron-accepting quinoxaline unit.[5,13,33] The detailed results are summarized in Table 4.3. Corresponding emission spectra revealed emission maxima in the 400–570 nm (Figure 4.7), accompanied by significant Stokes shifts ranging from 8700 to 16700 cm^{-1}. These compounds also exhibited high molar extinction coefficients, ranging from 19,000 to 20,425 L mol^{-1} cm^{-1} (Table 4.3). The optical energy gap, estimated from the absorption onset, was between 2.59 and 3.07 eV.

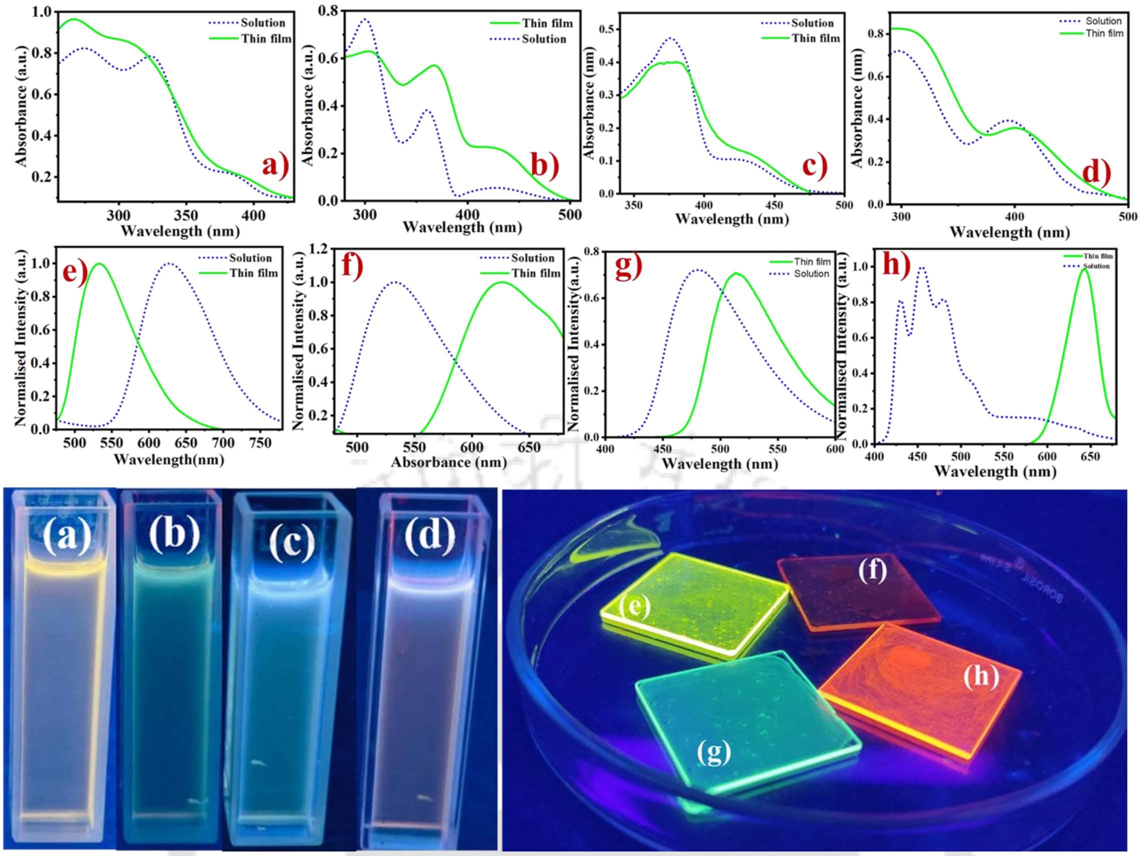

Figure 4.7. Absorption and emission spectra of compounds (a, e) **IQ1**, (b, f**) IQ2**, (c, g) **IQ3**, and (d, h) **IQ4** in solution and thin film. Photographs of micromolar solutions of compounds (a) **IQ1**, (b) **IQ2, (c) IQ3**, and (d) **IQ4** in chloroform and spin-coated thin films on quartz plates (e) **IQ1**, (f) **IQ2**, (g) **IQ3**, and (h) **IQ4** under UV light of long wavelength (λ = 365 nm).

Table 4.3. Photophysical properties of **IQ**s in solution and thin film state

Entry	Solution State[a]						Thin film State[b]			
	Absorption [nm]	Emission [nm]	Stokes Shift (cm^{-1})	ε (Lmol^{-1} cm^{-1})	ΔE_g, opt. [eV]	Abs. Q. Y.	Absorption [nm]	Emission [nm]	Stokes Shift (cm^{-1})	Abs. Q. Y.
IQ1	274, 323, 383	506	16733	20425	3.07	12.36	266, 306, 394	595	20787	60.09
IQ2	300, 360 ,431	553	15250	18425	2.62	1.21	304, 367, 433	532	14097	0.30
IQ3	298, 375, 432	413	9343	18652	2.64	17.05	367, 384, 436	515	7830	11.12
IQ4	300, 394 ,477	406, 431, 457	8702	19000	2.59	9.93	317, 398	643	15993	41.57

For the practical application of D–A molecule, it is crucial for the molecule to exhibit emission in the solid or aggregate state. UV-vis absorption and fluorescence studies were conducted on their neat solid films to explore the optical properties of **IQ**s in this state. In the solid state, the absorption maxima of the **IQ**s were slightly higher and broader compared to the solution, with bathochromic shifts in the ICT band, suggesting intermolecular aggregation. Similarly, the emission maxima in the solid films (ranging from 515 to 643 nm) were red-shifted relative to the solution state, further indicating aggregate formation (Figure A14). In the case of **IQ1**, the absorption spectra in the thin film state exhibited a slight blue shift compared to the solution, indicating the formation of *H*-type (head-to-head) aggregates. Although *H*-aggregates typically experience fluorescence quenching, some examples of emissive *H*-aggregates have been reported in the literature.[68.69] The broad absorption bands observed for other **IQ**s in thin films suggest the formation of excimers (Figure 4.7), with a slight bathochromic shift indicative of *J*-type (head-to-tail) aggregates. The red-shifted λ_{max} in the absorption spectra of **IQ**s in the thin film could be attributed to short-range charge transfer interactions, which enhance the overlap of wave functions among the π-conjugated aromatic cores.[70,71] Interestingly, most compounds exhibited more intense emissions in the solid state, except for **IQ2**; in the case of **IQ2**, which has two cyano groups, a significant red shift in both absorption and emission spectra suggests increased conformational planarity, structural rigidity, and electronic conjugation. This could lead the molecule to adopt a disc-like conformation, promoting intermolecular π-π interactions and the formation of detrimental species, such as excimers and exciplexes, which results in decreased or quenched emission intensity in the aggregate/solid state due to the Aggregation-Caused Quenching (ACQ) effect.[13] The absolute quantum yield and fluorescence lifetime are higher in the thin film state compared to the solution state for most **IQ** compounds, as shown in Figures 4.8, 4.9, Tables 4.3, and A2, except for **IQ2**.

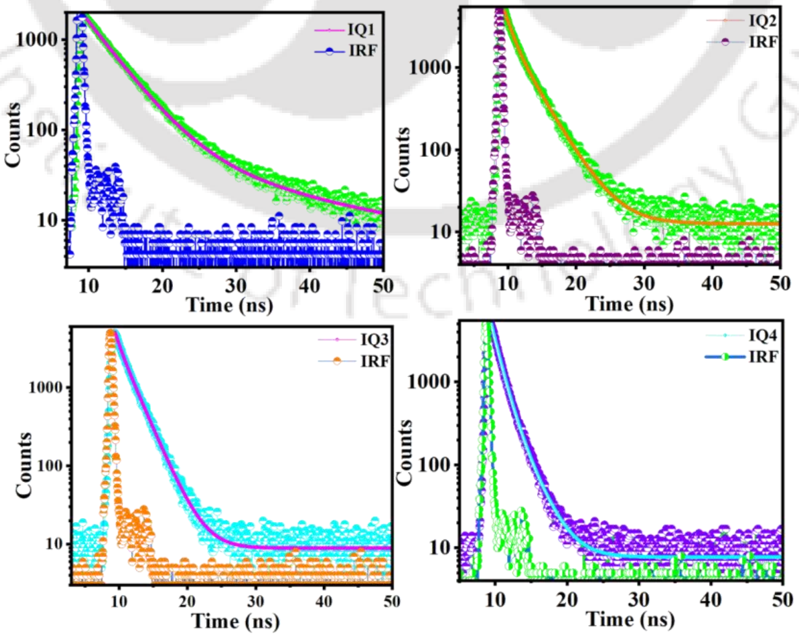

Figure 4.8. Time-resolved PL decay curves of **IQ** (**IQ1-IQ4**) in solutions state.

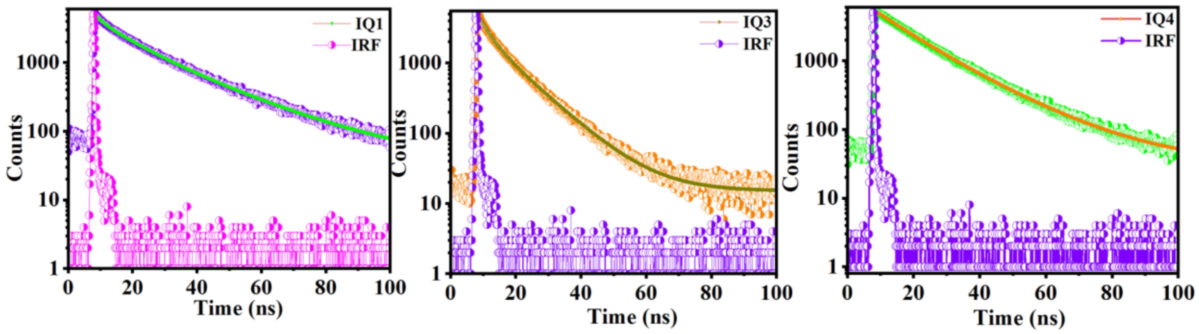

Figure 4.9. Time-resolved PL decay curves of **IQ** (**IQ1-IQ4**) in the solid state.

We hypothesize that the solid-state emissions of the D–A pairs in the fluorescent molecules **IQ3** and **IQ4** may exhibit Aggregation-Induced Emission (AIE) properties. To determine if this unusual behavior results from aggregation, we investigated their AIE characteristics, as described in the following section.

4.2.3.1. Aggregation-induced emission (AIE) property

The AIE activity of the dyes was investigated by forming nano aggregates or nanoparticles through a surfactant-free precipitation method. The molecules are highly soluble in THF but insoluble in water, leading to aggregation at higher water fractions. Solutions of THF with increasing water content (maintaining a constant concentration of 20 μM) were prepared to assess nanoparticle formation using UV-vis and emission spectra (Figure 4.10a-d, A17). Initially, the addition of water (10-50% *fw*) reduced the emission intensity compared to the neat THF solution (Figures 4.10 c and 4.10 f) due to the formation of a twisted intramolecular charge transfer (TICT) state, which is known to be a non-emissive, or "dark," state.[3,13] At higher water fractions, the immiscibility of the molecules in the THF/water mixture promotes aggregate formation. The absence of precipitates suggests nanoscale aggregates (Figure 4.10a).[33] UV-visible spectra showed increased absorption intensity and "level-off tail" features, indicating nanoparticle formation due to poor solubility in water.[33] At high water fractions, nanoparticle formation restricted intramolecular motion (RIM).[2] It limited the ICT effect, boosting emission intensity, a phenomenon known as the AIE effect.[3, 13] Remarkably, at a 70% THF/water fraction in **IQ3** and an 80% THF/water fraction in **IQ4**, the emission wavelengths closely resemble those observed in solid films (Figure 4.7). The absolute quantum yield of different aggregate states shows that with increasing water content, the absolute quantum yield increases, with the highest, i.e, 18.23 %, in 80 % THF/water (Table A2). DLS confirmed nanoparticle presence with low polydispersity indices, indicating uniform suspensions (Figure A18, Table A4).[33] Adding water enhanced emission intensity, indicating nanoparticle formation in the hydrophobic environment. Nanoparticle formation at high water content restricted intramolecular motions, blocked non-radiative decay, and prevented less emissive excimer species, promoting efficient fluorescence. This demonstrates that **IQ3** and **IQ4** are AIE-active fluorophores capable of overcoming the ACQ problem. DLS showed hydrodynamic sizes of 547.5 nm for **IQ3** and 906 nm for **IQ4**., while FESEM confirmed the aggregate formation (Figure 4.13).

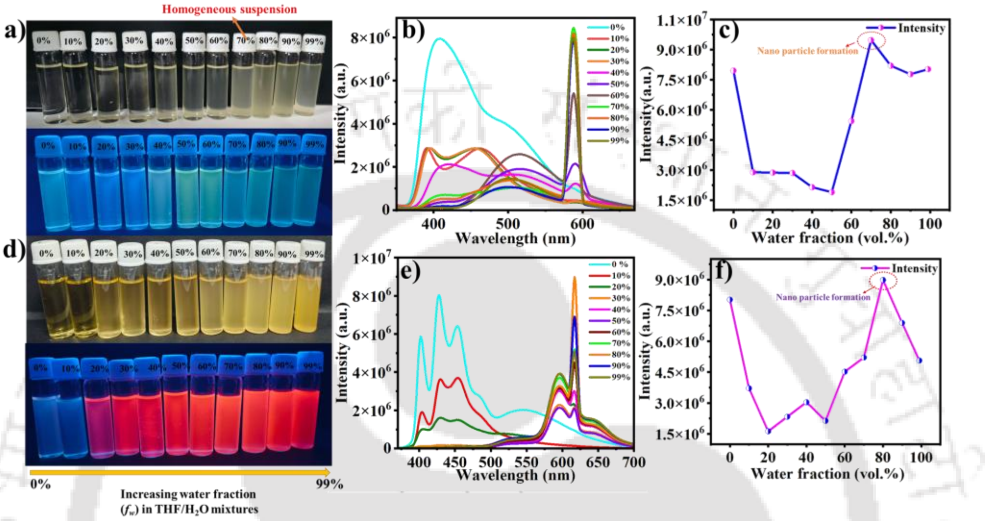

Figure 4.10. Emission images of (a) **IQ3** and (d) **IQ4** AIE effects in THF/water mixtures (20 µM) with different % water fractions (*f*w) in daylight and UV light. Emission spectra (b) **IQ3** and (e) **IQ4**. Plots of intensity versus % water fraction of (c) **IQ3** and (f) **IQ4** in THF/water mixtures.

4.2.4. Electrochemical properties

The energy and electron transfer processes, as well as the reversibility of redox reactions, are significantly influenced by the electronic energy levels, particularly the frontier molecular orbitals (HOMO and LUMO levels) of organic semiconductors. These characteristics were investigated through cyclic voltammetry (CV) in 0.5 mM solutions of **IQ**s in anhydrous dichloromethane, with 0.1 M tetrabutylammonium perchlorate (TBAP) as the supporting electrolyte and a scan rate of 100 mV/s. The electrochemical results, summarized in Table 4.4, Figure 4.11 & A19, show that compounds **IQ1**, **IQ2**, **IQ3**, and **IQ4** exhibited an irreversible first reduction at -1.25, -1.29, -1.23, and -1.28 V, respectively, corresponding to the reduction in quinoxaline unit.[13,17]

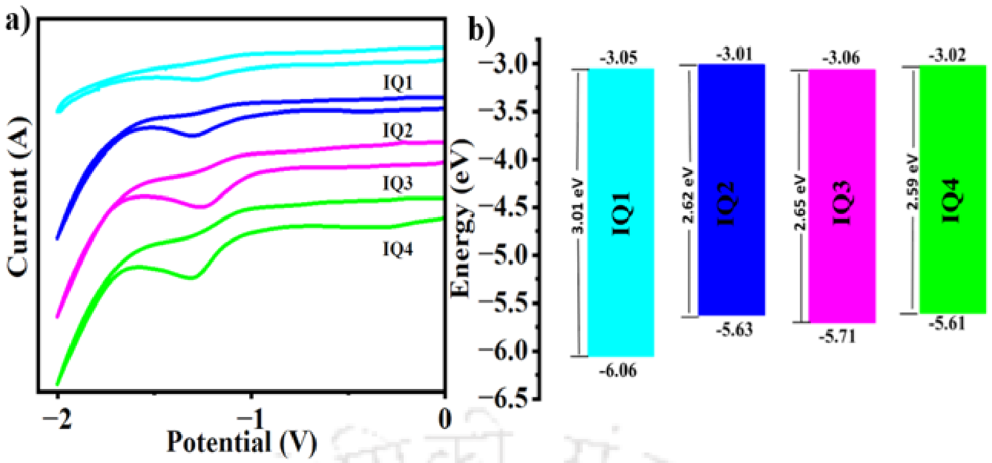

Figure 4.11. (a) Cyclic voltammogram of **IQ**s. (b) Energy band level diagram showing experimental HOMO and LUMO energy levels of **IQ**s.

Table 4.4. Electrochemical^{a,b} data, and the data obtained from DFT^{h} calculations for **IQ**s

Electrochemical data					Data from DFT calculation		
Entry	$E_{1st\ red}$[c]	E_{LUMO} [d,e]	E_{HOMO} [d,f]	$\Delta E_{g,(opt)}$ [d,g]	E_{LUMO} [dh]	E_{HOMO} [dh]	ΔE_g[d,h]
IQ1	-1.25	-3.05	-6.06	3.01	-1.85	-5.29	3.44
IQ2	-1.29	-3.01	-5.63	2.62	-2.73	-5.72	2.99
IQ3	-1.23	-3.06	-5.71	2.65	-1.68	-5.21	3.53
IQ4	-1.28	-3.02	-5.61	2.59	-2.02	-4.98	2.96

[a] 0.5mM Dichloromethane solutions; [b]experimental conditions: Ag/AgNO$_3$ as reference electrode, glassy carbon working electrode, platinum wire counter electrode, TBAP (0.1M) as a supporting electrolyte, room temperature; [c] in volts (V); [d] in eV; [e] estimated from the formula by using E_{LUMO}= -(4.8 - $E_{1/2}$, Fc/Fc^{+} + E $_{red}$, onset) eV; [f] estimated from the formula E_{HOMO} = E_{LUMO} – Eg, opt) eV; [g]calculated from the red edge of the absorption band of each compound.E1/2, $^{Fc/Fc+}$ = 0.50.[h] Obtained from DFT calculations by employing the combination of Becke3-Lee-Yang-Parr (B3LYP) hybrid functional and 6-31G (d, p) basis set using the Gaussian 09 package.

The lower oxidation waves in **IQ1** and **IQ2** observed in the range 0.99 to 0.91 V may be due to oxidation of the alkoxy group,[13] and the first oxidation (Table A5, Figure A19) wave observed within 1.29 to 1.24 V attributed to oxidation of indole moiety.[13,17] For compounds **IQ3** and **IQ4**, the first oxidation peak was 1.27 to 1.26 V due to the oxidation of indole moiety;[17] however, the prominent lower oxidation peak of the alkoxy group was not observed in **IQ3** and **IQ4**. From the first reduction potential values, the estimated lowest occupied molecular orbital (LUMO) levels of **IQ**s were found to be -3.05, -3.01, -3.06, and -3.02 eV, respectively.

The corresponding highest occupied molecular orbital (HOMO) levels, derived from their optical band gaps ($E_{g,\ opt}$) of 3.01, 2.62, 2.65, and 2.59 eV, were found to be around -6.06, -5.63, -5.71, and -5.61 eV, respectively (Table A5). Overall, these results indicate that the more conjugate the structures, the band gap decreases, as seen in the **IQ4** molecule, with a decrease of 0.42 compared to **IQ1**.

4.2.5. DFT studies

To explore the geometry, electronic structure, molecular conformation, and frontier molecular orbitals (FMOs: HOMO and LUMO) of **IQ**s, density functional theory (DFT) calculations were performed using the B3LYP/6-31G (d, p) method. The HOMO and LUMO distributions revealed that the energy levels are primarily localized around the core aromatic rings of the indole and quinoxaline units, as shown in Figures 4.12 and A21. For **IQ1**, the calculated HOMO and LUMO energy levels were -5.29 eV and -1.85 eV, respectively, resulting in a HOMO-LUMO gap of 3.44 eV. In comparison, introducing a -CN group on the phenyl moiety (**IQ2**) slightly reduced the HOMO-LUMO gap. The band gap for **IQ4** is even further reduced compared to **IQ2** and **IQ3**, which can be attributed to the increased conjugation in the core aromatic rings. These theoretical findings align with the experimental data, confirming the slight decrease in the band gap from **IQ1** to **IQ4** as the structure evolves. The optimized molecular diameters of the **IQ**s ranged from approximately 38.26 Å to 54.12 Å, as shown in Figure A22. The 3D molecular electrostatic potential (MEP) maps indicate a concentration of electron density around the oxygen atom of indole and the nitrogen atom of the quinoxaline units. At the same time, the central aromatic core remains electron-deficient (Figures A22 and A23). The theoretical band gaps for the **IQ**s ranged from 3.44 eV to 2.96 eV, slightly larger than the optical band gaps but following the same trend as shown in Table 4.4.

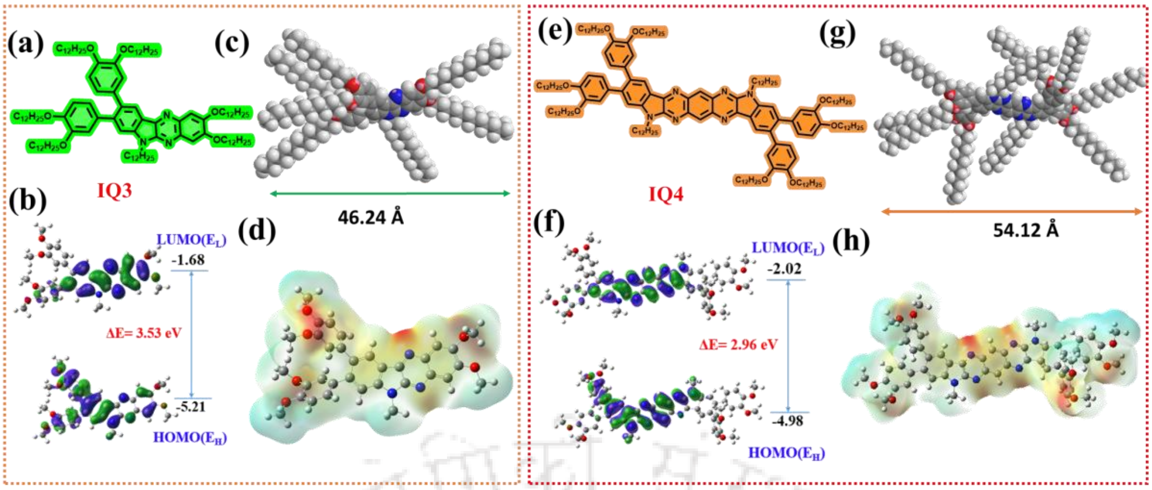

Figure 4.12. Molecular models and frontier molecular orbitals of **IQ3** and **IQ4** were obtained from DFT calculations at the B3LYP/ 6-31G(dp) level, and 3D molecular electrostatic potential contour maps (E_H and E_L denote energies of the HOMO and LUMO, respectively (chain length is limited to methyl for the sake of computational time)).

4.2.6. Morphology studies

The morphology of drop-cast homogeneous suspensions of **IQ3** and **IQ4**, using THF/ water mixtures, was analyzed through FESEM. The FESEM images of **IQ3** (70% THF/ water) and **IQ4** (80% THF/ water) revealed the formation of nano-aggregates, corresponding to the maximum aggregation-induced emission observed (Figure 4.13). These findings confirm that the enhanced emission in these specific THF/water mixtures results from nano-scale aggregation. Additionally, the AFM and FESEM images of the drop-cast samples of all **IQ**s, shown in Figure A20, demonstrate that they form a very smooth surface.

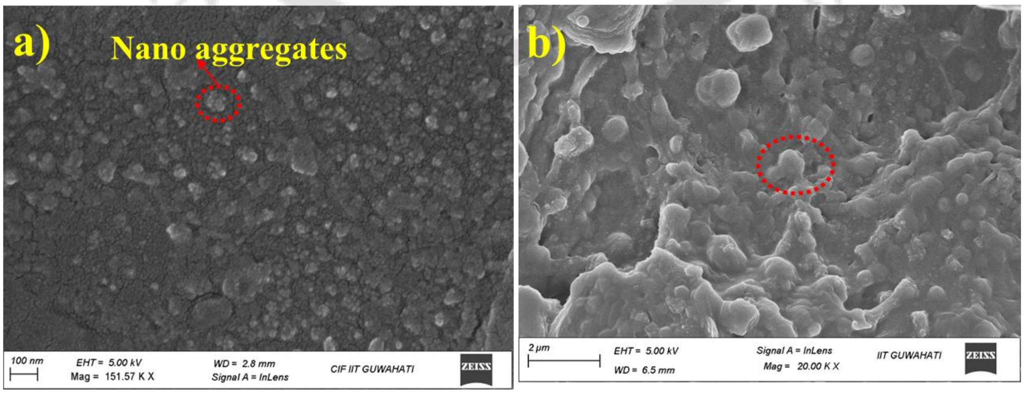

Figure 4.13. (a) The FESEM images of drop cast of homogenous suspension of **IQ3** in 70% THF/ water and (b) **IQ4** in 80% THF/water show nano-aggregates formation.

4.3. Bioimaging studies

Nematodes belonging to species like *Caenorhabditis elegans* are widely used model organisms in biomedical research due to their simple anatomy, transparent body, and well-characterized genetic makeup.[72] Their transparency throughout all life stages makes them ideal candidates for fluorescence-based bioimaging studies, enabling detailed visualization of cellular structures and dynamic biological processes.[73-75] Importantly, the fluorescent materials that successfully stain the nematode tissues, organelles, or cellular structures often demonstrate similar efficacy in cancer cells, as these compounds can target analogous biomolecules such as nucleic acids, proteins, or lipids.[76] Furthermore, literature reports indicate that nematodes are widely recognized as a robust model system for toxicological and imaging studies, offering valuable insights into the biological effects of various chemical probes and environmental toxins.[77] The present study selected indolo[2,3-b]quinoxaline core functionalized compound **IQ4** with periphery dodecyloxy side chain for its excellent fluorescent, photostability, and AIE-active nature for nematode cell imaging study. At the initial stage of the study, a solution of compound **IQ4** was prepared in THF solvent and subsequently introduced to a nematode cell tube for imaging purposes. The compound demonstrated effective penetration through the nematode cell tube, allowing interaction with internal structures under the fluorescent environment of the solution. This facilitated the evaluation of its fluorescent properties and staining efficiency within the nematode body (Figure 4.14).

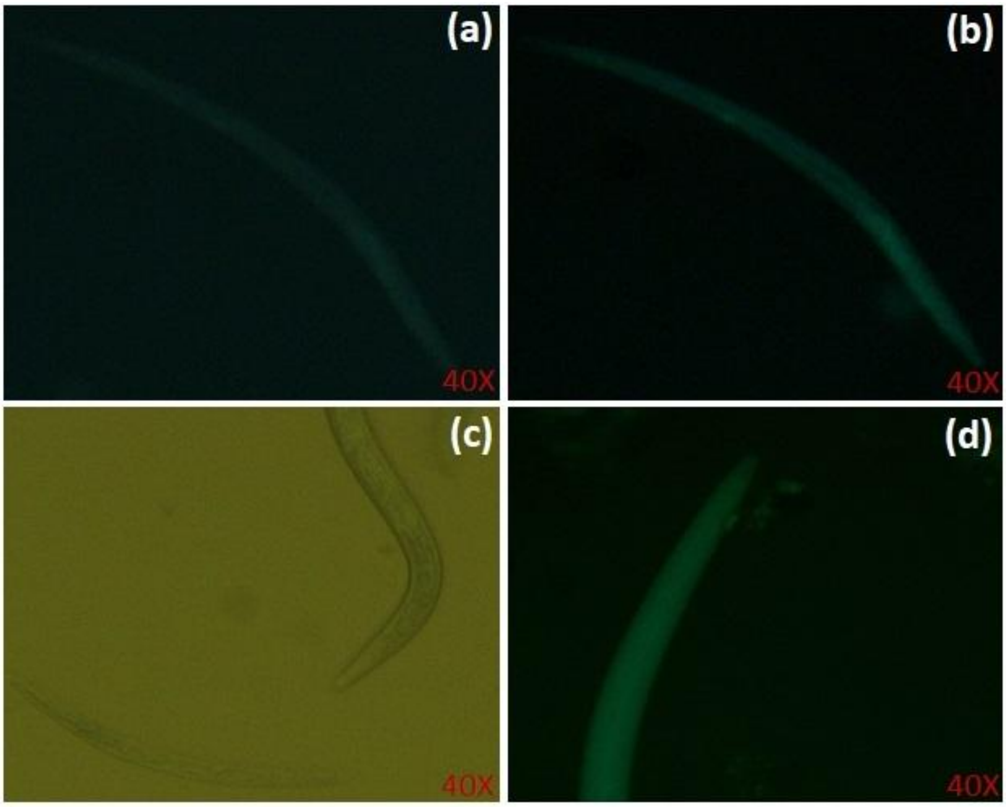

Figure 4.14. Nematode exposure with compound **IQ4** in THF (10 µM) under different filters. Panels (a), (b), and (d) show nematodes under blue filter; panel (c) displays the same exposure under white light (brightfield), Magnification 40x.

Further, the fluorescence microscopy images depict the staining of multiple nematodes using the exact solution of the compound **IQ4** in THF under different filters (Figure 4.15). Image 4.15a shows the bright-field microscopic view of the nematodes, confirming their structural integrity before fluorescence imaging. Under UV light excitation, images 4.15b and 4.15c reveal the selective uptake and binding of the fluorescent compound, emitting a strong green fluorescence along the nematode body, indicating successful staining without any noise background and solidification issues. The presence of red fluorescence in image 4.15d under the green filter suggests an alternative emission channel. The differential fluorescence response in multiple channels highlights the compound's versatility and potential applicability in multi-wavelength imaging and visualization. The uniform fluorescence distribution along the nematodes demonstrates the compound's staining efficiency and potential for bio-imaging applications.

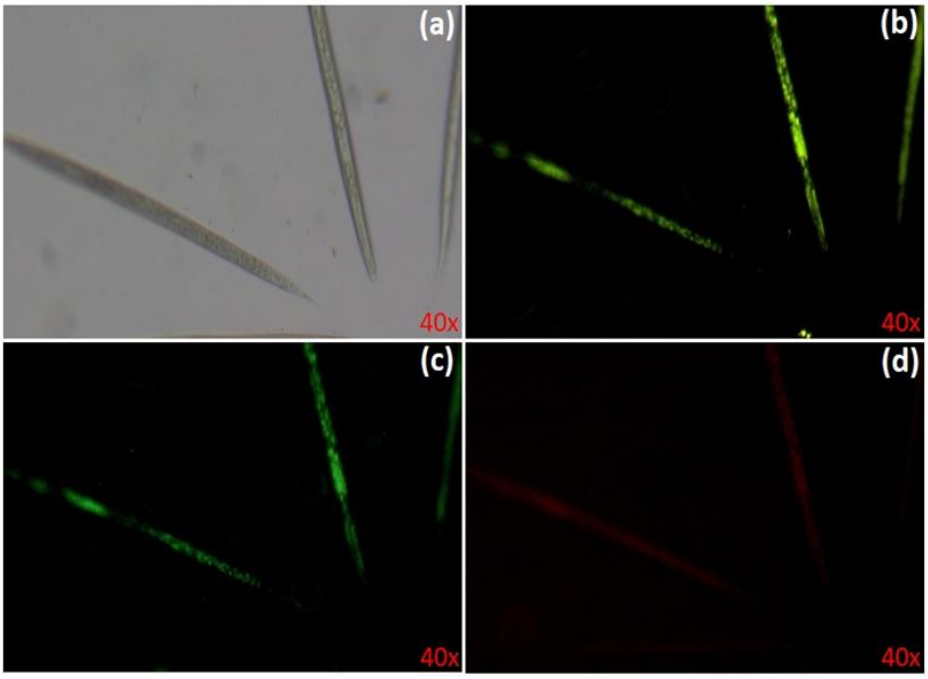

Figure 4.15. Multiple nematode exposure with compound **IQ4** in THF/water (10 µM) under different filters. Panel (a) shows exposure under white light; panels (b) show exposure under violet filter, and (c) show exposure under blue filter; panel (d) shows exposure under green filter. Magnification 40x.

However, this compound exhibits excellent fluorescence properties due to its aggregation-induced emission (AIE) nature, which limits molecular motions and further increases the emission intensity.[78] The fluorescence intensity significantly increased when water was added to the solution of the compound in THF with different proportions. It was observed that nematodes exhibited staining across their entire body with higher fluorescence intensity when exposed to the aggregate solution of compound **IQ4** with lower concentration (Figure 4.16). In the top row (4.16a-c) at 40X magnification, the images reveal a pronounced fluorescence signal distributed along the nematode body, with blue-green emission observed in 4.16a and 4.16c, indicating effective intracellular interaction, possibly localizing in lipid-rich or protein-rich areas. The green fluorescence in 4.16b further confirms the AIE-active nature of the compound, where molecular aggregation enhances emissive properties. The bottom row (4.16d-f) at 40X magnification highlights the nematodes with varying fluorescence intensities. The increased fluorescence in 4.16d and 4.16f suggests that the compound aggregates more efficiently on the nematode body as the water fraction increases, leading to a brighter fluorescence response. Image 4.16e shows a non-uniform fluorescence distribution, likely due to partial aggregation in different regions of the nematode cell body. This enhanced fluorescence provided a detailed visualization of their anatomical and cellular structures. It can be observed that AIE-based water fraction solutions of the compound with a minimal amount of THF solvent demonstrated significantly enhanced staining capability and fluorescence intensity compared to solutions prepared solely in THF solvent. This improvement can be attributed to an active AIE nature in the compound where molecular aggregation is promoted.[79] Additionally, water is a less toxic and more biocompatible medium for nematodes, minimizing the potential harmful effects of higher concentrations of organic solvents. The reduced toxicity of water-based systems enhances the nematode's ability to absorb the compound efficiently, ensuring uniform staining without adverse physiological impacts.[80] This makes water-rich media safer and more effective for imaging studies involving living organisms. Importantly, no solid crystallization and background noise were observed at room temperature, ensuring the compound's uniform dispersion within the nematodes. This consistent distribution enabled comprehensive and effective staining of the entire organism, facilitating detailed and reliable visualization of the nematode anatomy and specific internal structures. Furthermore, the indolo[2,3-b]quinoxaline core functionalized compounds' ability to display uniform staining underscores its potential as an effective tool for further advanced imaging in biological research. These results suggest that the synthesized compound exhibits superior bioimaging potential in aqueous environments, making it a promising candidate for nematode staining in biological and environmental research.

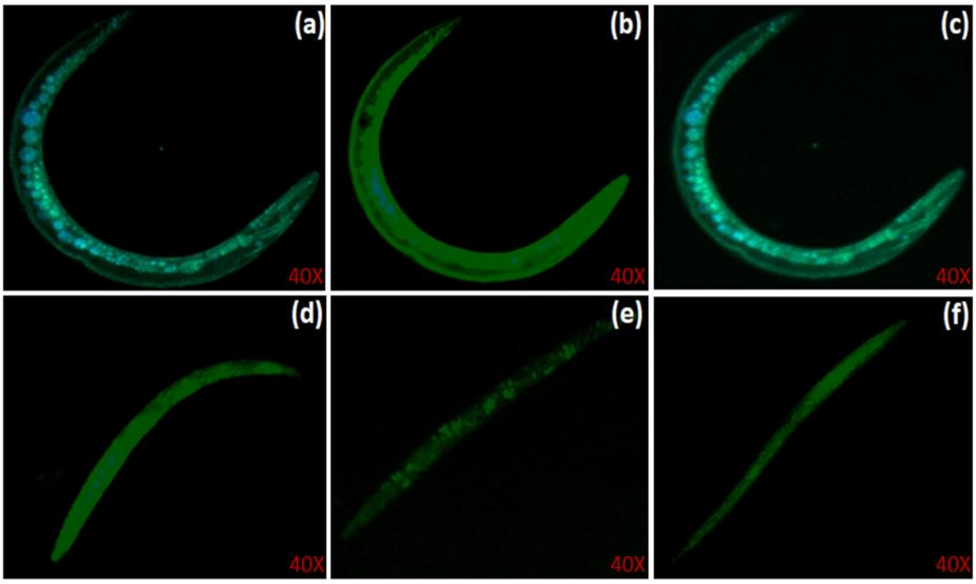

Figure 4.16. Nematode exposure with compound **IQ4** in THF/Water solution (5 µM) under different blue filters (a-f). Magnification 40x.

After successfully obtaining promising results in nematode cell imaging studies, we further extended our investigation to cancer cell imaging using the same compounds. The fluorescence microscopy images depict the staining of MCF7 breast cancer cells using the same compound

IQ4 in THF solvent, demonstrating its potential for bioimaging applications at the single-cell level. In a recent study, single-cell imaging has emerged as a powerful technique in cancer diagnostics, enabling the visualization of cellular processes at high spatial and temporal resolution.[81] Unlike bulk-cell analysis, this approach reveals subtle biochemical and morphological changes in individual cancer cells.[82-84] In this study, fluorescence microscopy investigated the indolo[2,3-b] quinoxaline functionalized compound for its bioimaging potential in MCF7 breast cancer cells. These findings demonstrate **IQ4**'s potential as a fluorescent probe for cancer cell imaging, aiding in real-time visualization and targeted diagnostics (Figure 4.17). Image 4.17a presents the bright-field microscopy of an individual MCF7 cell at 40X magnification, revealing its morphology and structural integrity. Images 4.17b and 4.17c show the fluorescence emission of **IQ4** in different channels, indicating successful cellular uptake and membrane localization. The green fluorescence observed in 4.17b and 4.17c suggests that **IQ4** interacts selectively with the cell membrane, likely due to hydrophobic interactions. The emission in the red channel 4.17d is relatively weak, implying that the fluorescence of **IQ4** is primarily in the green region, making it a suitable candidate for imaging applications in the visible spectrum. The well-defined membrane staining highlights **IQ4**'s affinity for lipid-rich regions, suggesting its potential for live-cell imaging and cancer cell differentiation. It can be observed that the compound maintains its functional state during the staining process, with no background noise or precipitation occurring in the solution. This stability is attributed to highly substituted dodecyloxy side chains, which reduce the crystallinity of the compound and enhance its stability at room temperature.

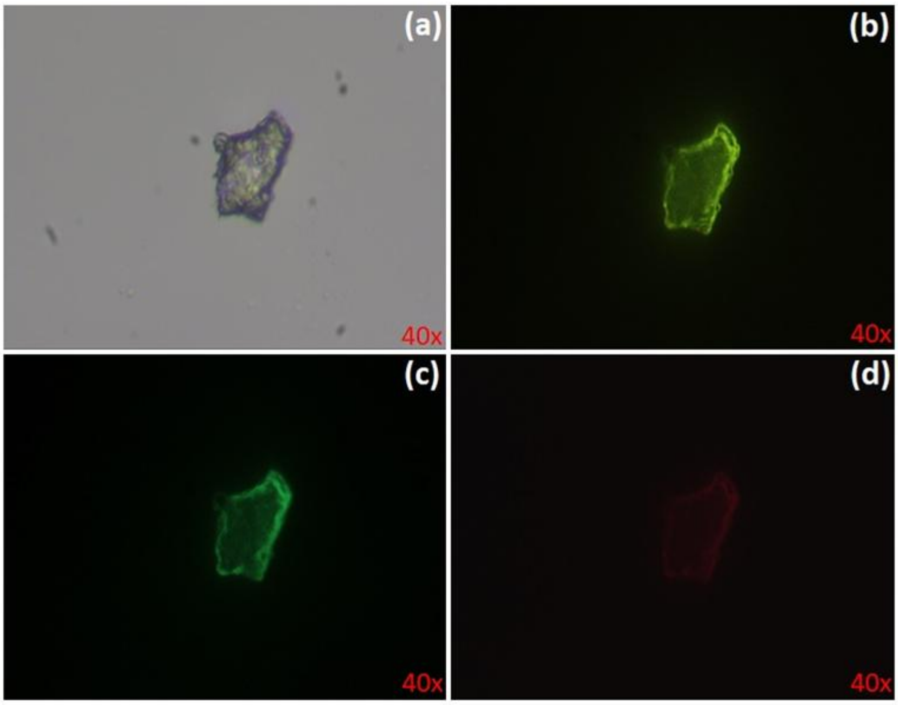

Figure 4.17. Fluorescent staining of MCF7 cancer cells with **IQ4** in THF (10 μM). Panel (a) shows unstained normal cells under white light (brightfield); panels (b) display stained cells under violet fluorescence filter and (c) display stained cells under blue fluorescence filter; panel (d) shows stained cells under green fluorescence filter. Magnification 40x.

Most importantly, AIE-active compounds offer significant advantages compared to conventional fluorescent materials in cell imaging studies.[85-87] Unlike traditional fluorescent materials, which often suffer from aggregation-caused quenching (ACQ) at high concentrations, AIE-active molecules exhibit enhanced fluorescence upon aggregation, improved brightness, photostability, and reduced background interference, making them highly suitable for biological imaging.[88,89] Further, we have investigated the aggregation-induced fluorescence enhancement of **IQ4** with MCF-7 breast cancer cells (Figure 4.18). It can be observed that the AIE uptake of **IQ4** induces molecular aggregation, resulting in a significant increase in fluorescence intensity. The brightfield image 4.18a suggested the morphology of the aggregates formed in the solution. In contrast, fluorescence images 4.18b-d captured under different filters highlight the enhanced emission properties with distinct clusters within the cellular environment. This fluorescence enhancement confirms the AIE effect, where restricted molecular motion in the aggregated state prevents non-radiative decay, and further increases the emission behavior of compounds with high fluorescence intensity.[90] The blue emission indicates that **IQ4** possesses a broad fluorescence response due to its high conjugation, rigid planar structure, and electron-rich nature of the indolo[2,3-b]quinoxaline core, which may further contribute to selective interactions with intracellular biomolecules. The strong fluorescence in MCF-7 cells suggests efficient cellular uptake and selective accumulation of

IQ4 aggregates within specific organelles, potentially the cytoplasm, membrane, and mitochondria localization, or lysosomes. This property enhances the contrast in cancer cell imaging, offering a high signal-to-noise ratio with minimal background interference. Importantly, a conjugated system with a highly substituted peripheral alkoxy chain environment enhances the solubility and promotes molecular aggregation in an aqueous medium. Additionally, it reduces the crystalline tendency of the molecular system and displays a columnar oblique phase at room temperature. On the other hand, the fluorescence intensity in the imaging results for both nematodes and cancer cells using **IQ4** was significantly enhanced in the uptake of AIE compared to the normal solvent-based study. This increase in intensity is attributed to molecular aggregation in the higher water fraction, promoting AIE behavior and improving imaging contrast. Such AIE-active fluorophores are advantageous in bioimaging applications as they enable real-time visualization of cancer cells without requiring extensive surface modifications or external quenchers. Further, we have calculated corrected total cell fluorescence (CTCF) to accurately quantify the fluorescence intensity using Image J 1.54f software, which further confirmed that the blue and red fluorescence background displayed the most potent signals as compared to the green fluorescence background (Figure A24).[91]

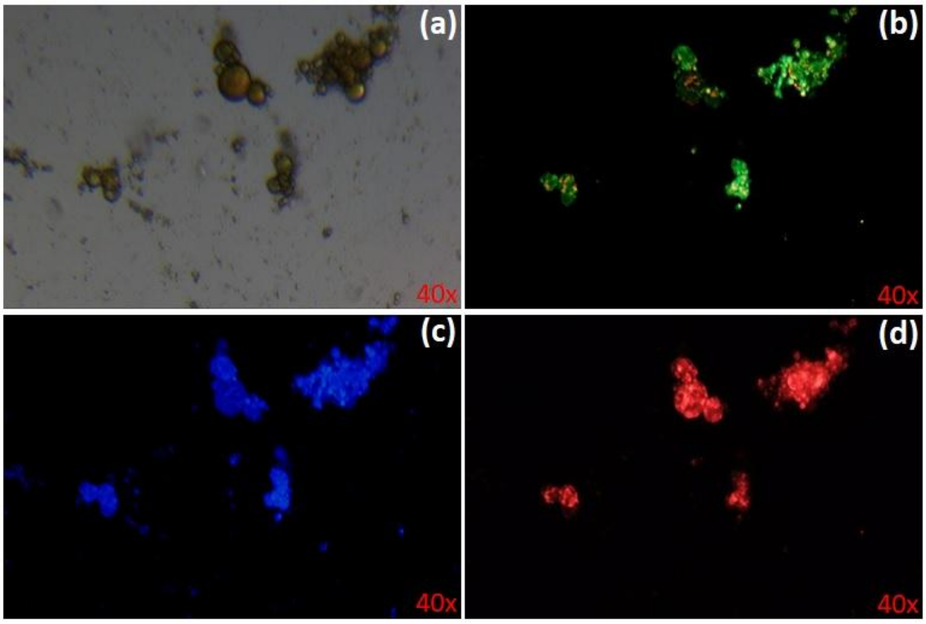

Figure 4.18. Fluorescent staining of MCF7 cancer cells incubated with AIE uptake of **IQ4** (5 µM). Panels (a) show unstained normal cells under white light. Panel (b) display stained cells under violet fluorescence filter and (c) display stained cells under blue fluorescence filter; panel (d) shows stained cells under green fluorescence filter. Magnification 40x.

4.4. Conclusions

We successfully synthesized four indole[2,3-b]quinoxaline-based D-A molecules. Among these, two compounds with more peripheral chains exhibited stabilized liquid crystalline behavior, marking the first examples in this class of molecules. Further structural analysis, including molecular orientation, frontier molecular orbitals, band gap, and electron density distribution, was performed using DFT calculations. All derivatives demonstrated high thermal stability and excellent solubility in common organic solvents. **IQ3** and **IQ4** stabilized columnar hexagonal and room-temperature columnar oblique liquid-crystalline phases, while the other compounds exhibited crystalline behavior. Photophysical studies revealed broad absorption spectra with band gap values ranging from approximately 3.00 to 2.59 eV, significant Stokes shifts, and high molar extinction coefficients. All derivatives showed enhanced emission in the solid state, except for **IQ2**, which exhibited quenching in the solid state. This behavior was further confirmed through AIE experiments in a THF-water mixture with compounds **IQ3** and **IQ4**. The compound **IQ4** exhibited strong permeability in nematodes, effectively crossing cellular membranes and dispersing uniformly throughout the cell body in solution and aggregate. This resulted in improved imaging contrast and higher fluorescence intensity, facilitating better visualization of the nematode cell body without interference from solidification and precipitation of the compound. Additionally, the AIE-active nature of compound **IQ4** enabled its successful application in staining MCF-7 breast cancer cells, where it exhibited efficient cellular uptake and strong fluorescence, allowing for high-clarity single-cell imaging. The compound stability, minimal background noise, and enhanced emission in aggregated states highlight its potential as a promising candidate for advanced bioimaging applications spanning model organisms and pathological cell studies.

4.5. Experimental section

This section presents the detailed synthesis procedure and the molecular structural characterization data for the intermediates and target compounds mentioned in the scheme. Compounds 2, 3, 6 & 11 have been synthesized using the literature-reported methods. [92-95]

Procedure for synthesis of 4 [67]

A mixture of compound 3 (1.06 mmol, 1 eq.), bis(pinacolato) diboran (2.12 mmol, 2 eq.), KOAc (12.77 mmol, 12 eq.) and Pd $(PPh_3)Cl_2$ (0.10 mmol, 1 eq.) in toluene (40 mL) was degassed by gently bubbling N_2 for 20 min. The mixture was heated at 110 °C for 36 h. After cooling, it was extracted with ethyl acetate (100 mL × 3). The combined organic layer was washed with water (100 mL) and brine solution (100 mL). The combined organic extracts were dried over anhydrous Na_2SO_4, and the obtained residue was then purified by column chromatography (silica gel, ethyl acetate-hexane 2:8).

4: R_f = 0.67 (10% EtOAc-Hexane); white solid, yield: 76%; IR: ν_{max} in cm^{-1}: 2919, 2850, 1608, 1515, 1350, 1156, 964, 688; ^1H NMR (600 MHz, $CDCl_3$, ppm): δ 7.39 (d, J = 7.8, 1H, H_{Ar}), 7.30 (s, 1H, H_{Ar}), 6.88 (d, J = 7.8 Hz,1H, H_{Ar}), 4.04 (m, 4H, 2×-OCH_2), 1.83 (m, 4H, 2×-CH_2), 1.47 (m, 4H, 2×-CH_2), 1.30 (bm, 44H, 16×-CH_2, 4×-CH_3), 0.90 (t, J = 6 Hz, 6H, 2×-CH_3).^{13}C NMR (150 MHz, $CDCl_3$, ppm): δ 152.16, 148.71, 128.85, 119.62, 112.89, 83.76, 69.07, 32.16, 29.88, 29.85, 29.68, 29.64, 29.60, 29.41, 26.29, 26.23, 25.06, 22.92, 14.34.MALDI-TOF mass calculated for $C_{36}H_{65}BO_4Na$ $(M+Na)^+$: 595.49, found: 595.742.

Procedure for synthesis of 6 [95]

To a solution of compound 11 (4.3 mmol,1 eq.) in *N, N*-dimethylformamide (10 mL) was added NBS (6.45 mmol, 1.5 eq.). The resulting reaction mixture was stirred at 25 °C for 12 h. After the reaction, the mixture was diluted with water (20 mL), the resultant precipitate was filtered, and the precipitate was dried in vacuo. The crude product was directly used for the next step.

Procedure for synthesis of 7 [95]

5,6-bromoindoline-2,3-dione (0.5 g, 1.64 mmol), 1-bromododecane (0.6 mL, 2.46 mmol), and anhydrous potassium carbonate (0.681 g, 4.92 mmol) were taken in 10 mL of *N, N*-dimethylformamide. This mixture was heated at 80 °C with stirring for 24 h. The reaction mixture was extracted with ethyl acetate (3×30 mL), and subsequently, the organic layer was washed with water (twice) and brine. Then, the organic extract was dried over anhydrous Na_2SO_4, and the obtained residue was purified by column chromatography (silica gel, ethyl acetate-hexane 1:9).

7: R_f = 0.65 (10% EtOAc-Hexane); red-orange solid, yield: 66%; IR: ν_{max} in cm^{-1}: 2925, 2859, 1734, 1608, 1545, 1468, 1441, 1320, 1259, 1120, 1057, 832, 708; ^1H NMR (600 MHz, $CDCl_3$, ppm): δ 7.85(s, 1H, H_{Ar}), 7.66 (s, 1H, H_{Ar}), 4.10 (t, J = 7.8 Hz, 2H, -NCH_2), 1.71 (m, 2H, -CH_2), 1.36 (bm, 18H, 9×-CH_2), 0.88 (t, J = 7.2 Hz, 3H, CH_3). ^{13}C NMR (150 MHz, $CDCl_3$, ppm): δ 180.4, 156.58, 145.62, 143.85, 126.13, 120.03, 115.42, 103.4, 40.27, 30.58, 28.29, 25.14, 21.37, 12.81. MALDI-TOF mass calculated for $C_{20}H_{27}Br_2NO_2$ (M^+): 471.04, found: 471.040.

Procedure for synthesis of 8 [92]

A mixture of compound **4** (0.34 mmol, 2 eq.), 5,6-dibromo-1-dodecylindoline-2,3-dione (0.158 mmol, 1 eq.), 2M K_2CO_3 (aq.) (10.5 ml, 6.33 mmol), and $Pd(PPh_3)_4$ (0.006 mmol, 0.042 eq.) in toluene (52.5 mL) was degassed by gently bubbling N_2 for 30 min. The mixture was heated at 110 °C for 24 h. The reaction mixture was extracted with ethyl acetate (3×30 mL), and subsequently, the organic layer was washed with water (twice) and brine. Then, the organic extract was dried over anhydrous Na_2SO_4, and the obtained residue was purified by column chromatography (silica gel, ethyl acetate-hexane 1:9).

8: $R_{f\,=}$ 0.66 (10% EtOAc-Hexane); reddish brown color solid, yield: 76 %; IR: ν_{max} in cm^{-1}: 2920, 2852, 1734, 1594, 1464, 1349, 1139, 1066, 796, 722, 457; ^1H NMR (600 MHz, $CDCl_3$, ppm): δ 7.79 (d, *J* = 2Hz, 1H, H_{Ar}), 7.57 (d, *J* = 2Hz, 1H, H_{Ar}), 7.04 (m, 2H, H_{Ar}), 6.90 (m, 4H, H_{Ar}), 4.04 (m, 8H, 4×-OCH_2) 3.45 (m, 2H, -NCH_2), 1.85 (m, 8H, 4×-CH_2) 1.49 (m, 8H, 4×-CH_2) 1.3 (bm, 84 H, 42×-CH_2), 0.88 (m, 15H, 5×-CH_3). ^{13}C NMR (150 MHz, $CDCl_3$, ppm): δ 184.3, 159.65, 149.55, 148.79, 146.04, 139.52, 136.43, 131.3, 129.8, 127.6, 122.3, 121.9, 119.5, 119.04, 115.0, 113.9, 113.19, 112.16, 111.91, 110.88, 68.02, 40.18, 30.68, 28.42, 28.12, 26.76, 25.29, 24.79, 21.44,12.87. MALDI-TOF mass calculated for $C_{80}H_{133}NO_6$ (M^+): 1204.21, found: 1204.651.

Procedure for the synthesis of IQs [11,16]

Compounds a, b, c, and d (1 equiv.) and compound 8 (1.2 equiv. for **IQ1**, **IQ2**, **IQ3**, and or 2.1 equiv. for **IQ4**) were transferred into a 50 mL two-neck round bottom flask and 10 mL acetic acid under N_2 atmosphere, which was heated to 100 °C. After adding 1.0 mL of triethylamine, it was refluxed at 110 °C for 24 h and concentrated in the reaction mixture. The crude product was purified by column chromatography on silica gel with 2-5% ethyl acetate-hexane to yield a solid compound.

IQ1*:* $R_{f\,=}$ 0.80 (10% EtOAc-hexanes), yellow solid, yield: 78%; IR: ν_{max} in cm^{-1} 2918, 2850,1579,1515, 1467,1246,1128,813,754,680. ^1H NMR (600 MHz, $CDCl_3$, ppm): δ 8.69 (s, 1H, H_{Ar}), 8.33 (d, *J* = 9.6 Hz, 1H, H_{Ar}), 8.14 (d, *J* = 10.2 Hz, 1H, H_{Ar}), 7.72 (m, 4H, H_{Ar}), 7.30 (s, 1H, H_{Ar}), 7.09 (d, *J* = 10.8 Hz, 2H, H_{Ar}), 7.02 (m, 2H, H_{Ar}), 4.12 (t, *J* = 7.8 Hz, 6H, 3×-OCH_2), 4.07 (t, *J* = 7.8 Hz, 2H, OCH_2) 4.03 (t, *J* = 7.8 Hz, 2H, -NCH_2), 1.89 (m, 6H, 3×-CH_2), 1.63 (m, 6H, 3×-CH_2), 1.39 (bm, 88H, 44×-CH_2), 0.89 (m, 15H, 5×-CH_3).^{13}C (150MHz, $CDCl_3$, 25 °C): δ 149.60, 149.01, 148.75, 147,07, 141.03, 140.59, 140.36, 139.47, 133.82, 133.54, 132.89, 131.90, 129.97, 129.23, 128.71, 127.95, 127.66, 126.03, 122.27, 121.44, 119.15, 119.20, 115.65, 114.26, 113.43, 113.05, 69.45, 43.06, 34.68, 31.95, 31.93, 31.60, 29.72, 29.69, 29.67, 29.63, 26.14, 26.12, 26.10, 26.08, 25.29, 22.71, 14.13, 11.93. MALDI-TOF mass calculated for $C_{86}H_{137}N_3O_4$ (M^+): 1276.0, found: 1276.068.

IQ2: R_f = 0.70 (10% EtOAc-hexanes); red solid; yield: 64%; IR: ν_{max} in cm^{-1}: 2920, 2852, 2234, 1511, 1465, 1375, 1244, 1139, 852, 721,604; ^{1}H NMR (600 MHz, $CDCl_3$, ppm): δ 8.74 (s, 1H, H$_{Ar}$), 8.67 (d, *J* = 2Hz, 1H, H$_{Ar}$), 8.56 (s, 1H, H$_{Ar}$), 7.83 (d, 1H, *J* = 2Hz, H$_{Ar}$), 7.55 (m, 1H, H$_{Ar}$), 7.27 (s, 1H, H$_{Ar}$), 7.05 (m, 4H, H$_{Ar}$), 4.11 (t, *J* = 6.6 Hz, 6H, 3×-OCH_2), 4.06 (t, *J* = 6.6 Hz, 2H, -OCH_2), 4.02 (t, *J*= 6.6 Hz, 2H, -NCH_2), 2.05 (m, 8H, 4×-CH_2), 1.88 (m, 8H, 4×-CH_2), 1.51 (m, 8H, 4×-CH_2), 1.39 (bm, 76H, 38×- CH_2), 0.88 (m, 15H, 5×-CH_3). ^{13}C (150MHz, $CDCl_3$, 25 °C) δ: 149.60, 149.01, 148.75, 147.07, 141.03, 140. 59, 140.36, 139. 47, 133.82, 133.54, 132.89, 131.90, 129.97, 129.23, 128.71, 127.95, 127.06, 126.03, 122.27, 121.44, 119.65, 119.20, 115.65, 114.26, 113.43, 113.05, 69.45, 43.06, 34.68, 31.95, 31.93, 31.60, 29.72, 29.69, 29.67, 26.63, 26.14, 26.12, 26.10, 26.08, 22.71, 14.13, 11.43. MALDI-TOF mass calculated for $C_{88}H_{135}N_5O_4$ (M^+): 1326.05, found: 1326.058.

IQ3: R_f = 0.67 (10% EtOAc-hexanes); greenish-yellow gummy solid; yield: 68%; IR: ν_{max} in cm^{-1} 2920, 2851, 1696, 1598, 1511, 1466, 1373, 1247, 1136, 1025, 805, 631; ^{1}H NMR (600 MHz, $CDCl_3$, ppm): δ 8.63 (d, *J* = 2Hz, 1H, H$_{Ar}$), 7.67 (d, *J* = 2Hz, 1H, H$_{Ar}$), 7.59 (s, 1H, H$_{Ar}$), 7.40 (s, 1H, H$_{Ar}$), 7.29 (d, *J* = 2Hz, 2H, H$_{Ar}$), 7.07 (m, 2H, H$_{Ar}$), 7.01 (m, 2H, H$_{Ar}$), 4.22 (t, *J* = 6.6 Hz, 4H, 2×-OCH_2), 4.10 (t, *J* = 6 Hz, 4H, 2×-OCH_2), 4.06 (t, *J* = 6.6 Hz, 4H, 2×-OCH_2), 4.01 (t, *J* = 6.6 Hz, 2H, 2×- NCH_2), 1.96 (m, 4H, 2×-CH_2), 1.89 (m, 10H, 5×-CH_2), 1.55 (m, 10H, 5×-CH_2), 1.36 (bm, 116H, 58×-CH_2), 0.87 (m, 21H, 7×-CH_3). ^{13}C(150MHz, $CDCl_3$, 25 °C) δ: 151.46, 149.21, 148.85, 148.15, 147.94, 147.87, 145.54, 138.49, 137.17, 135.15, 133.17, 132.68, 131.56, 126.20, 121.53, 120.97, 118. 89, 114.89, 113.48, 112.64, 1122.24, 106. 13, 68.83, 68.74, 68. 47, 42.32, 31.31, 29.08, 29.05, 29.03, 28.90, 28.85, 28.81, 28.76, 26.01, 25.46, 25.43, 22.07, 13.50. MALDI-TOF mass calculated for $C_{110}H_{185}N_3O_6$ (M^+): 1644.43, found: 1644.431.

IQ4: R_f = 0.66 (10% EtOAc-hexanes); reddish-orange gummy solid; yield: 66%; IR: ν_{max} in cm^{-1}:2920, 2851, 1696, 1598, 1511, 1466, 1373, 1247, 1136,1025, 805, 631; ^{1}H NMR (600 MHz, $CDCl_3$, ppm): 8.63 (d, *J* = 2Hz, 2H, H$_{Ar}$), 8.06 (m, 2H, H$_{Ar}$), 7. 87 (m, 2H, H$_{Ar}$)7.73 (d, *J* = 2Hz, 2H, H$_{Ar}$), 7.28 (m, 2H, H$_{Ar}$), 7.07 (m, 4H, H$_{Ar}$), 7.01 (m, 4H, H$_{Ar}$), 4.11 (t, *J* = 6.6 Hz, 8H, 4×-OCH_2), 4.06 (t, *J* = 6.6 Hz, 8H, 4×-OCH_2), 4.02 (t, *J* = 6.6 Hz, 4H, 2×-NCH_2), 1.90 (m, 16H, 8×-CH_2), 1.57 (m, 16H, 8×-CH_2), 1.35 (bm, 168H, 84×-CH_2), 0.89 (m, 30H, 10×-CH_3). ^{13}C (150MHz, $CDCl_3$, 25 °C) δ: 149.55, 149.04, 148. 80, 148. 68, 146.88, 140.31, 138.04, 135.97, 134.04, 133.28, 133.13, 131.57, 127.14, 122.19, 120.92, 119. 63, 119.12, 115.55, 114.18, 113.34, 113.02, 69.49, 43.05, 31.88, 29.66, 29.63, 29.621, 29.42, 29.33, 29.31, 22.64, 14.07, 14.06. MALDI-TOF mass calculated for $C_{166}H_{268}N_6O_8$ (M^+): 2474.07, found: 2474.071.

4.6. Appendix

4.6.1. NMR Spectra

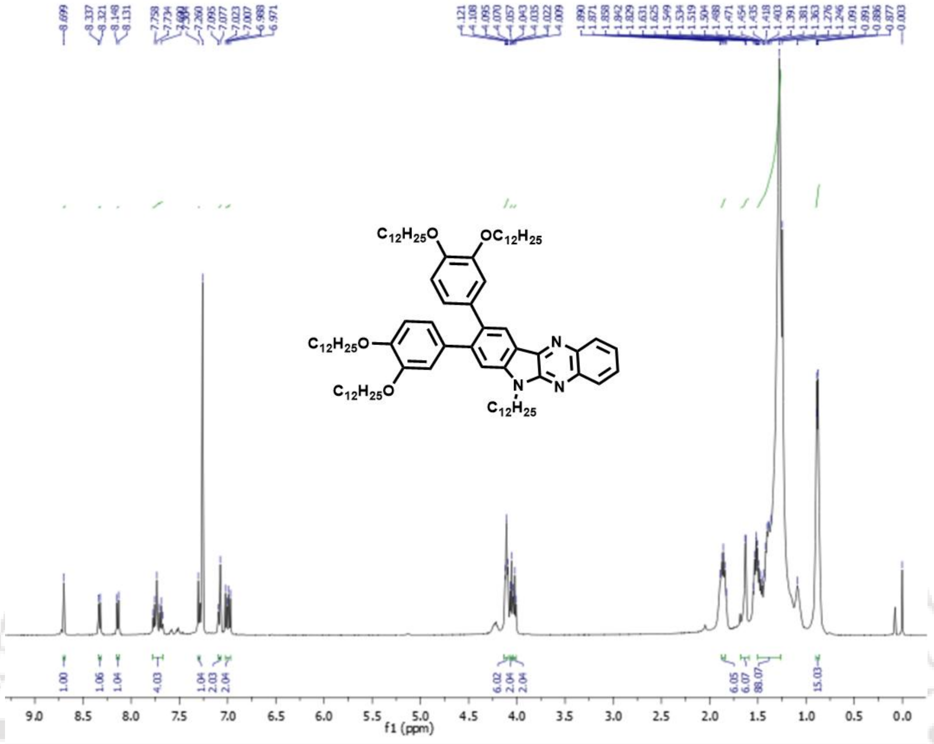

Figure A1. ^{1}H NMR (600 MHz) spectra of **IQ1** in $CDCl_3$.

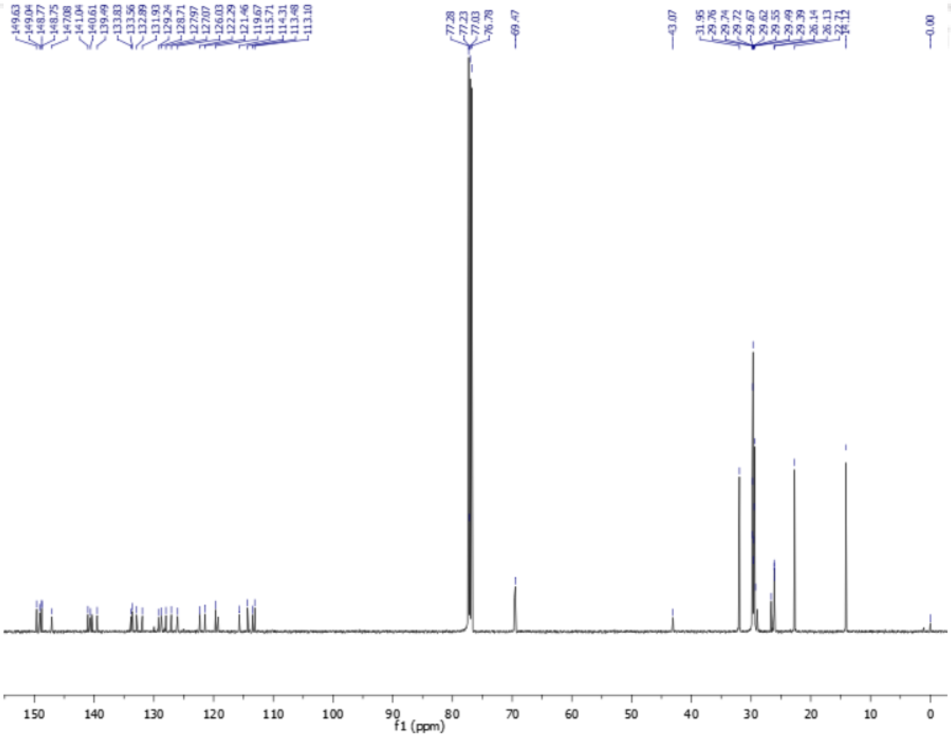

Figure A2. ^{13}C NMR (150 MHz) spectra of **IQ1** in $CDCl_3$.

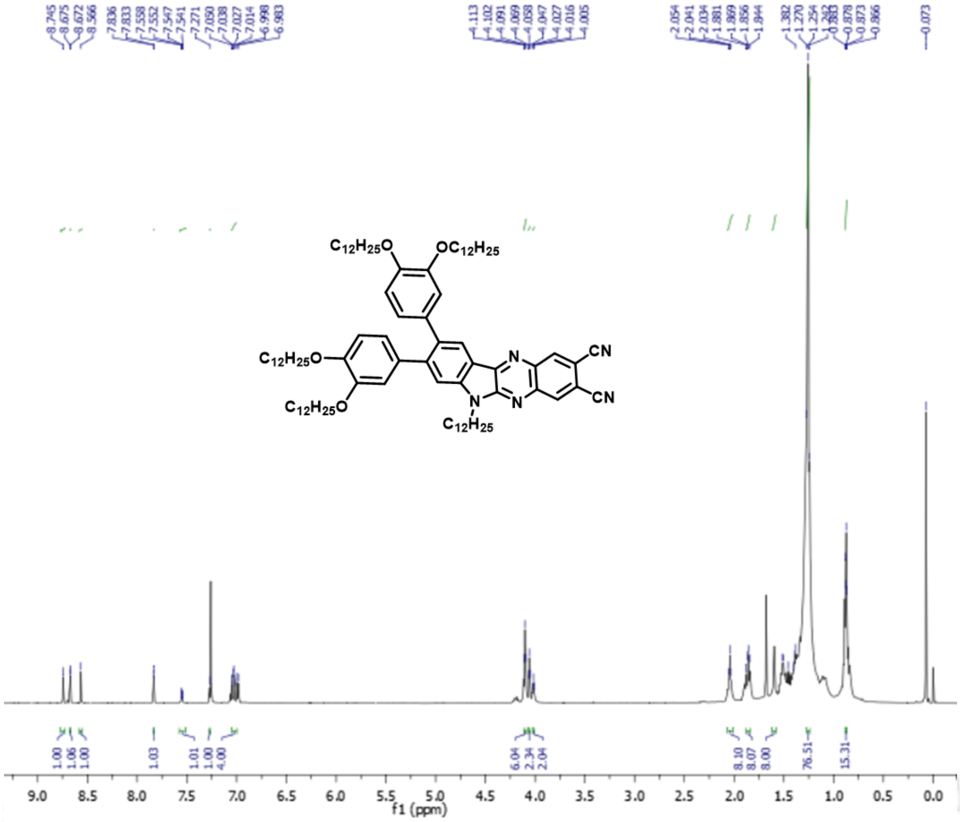

Figure A3. ^{1}H NMR (600 MHz) spectra of **IQ2** in $CDCl_3$.

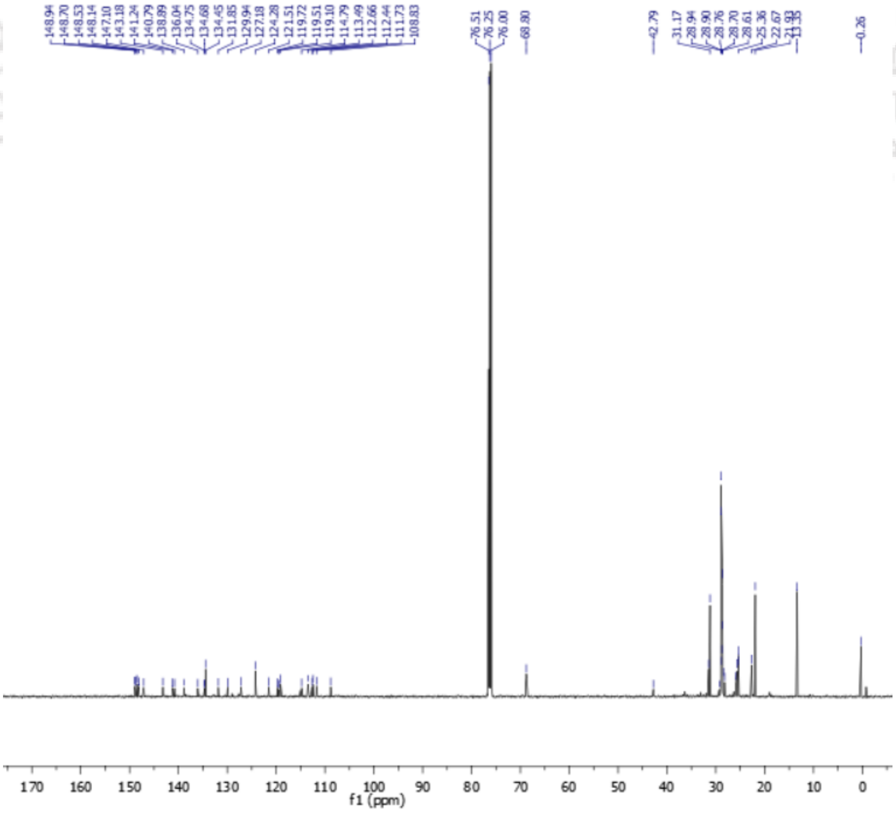

Figure A4. ^{13}C NMR (150 MHz) spectra of **IQ2** in $CDCl_3$.

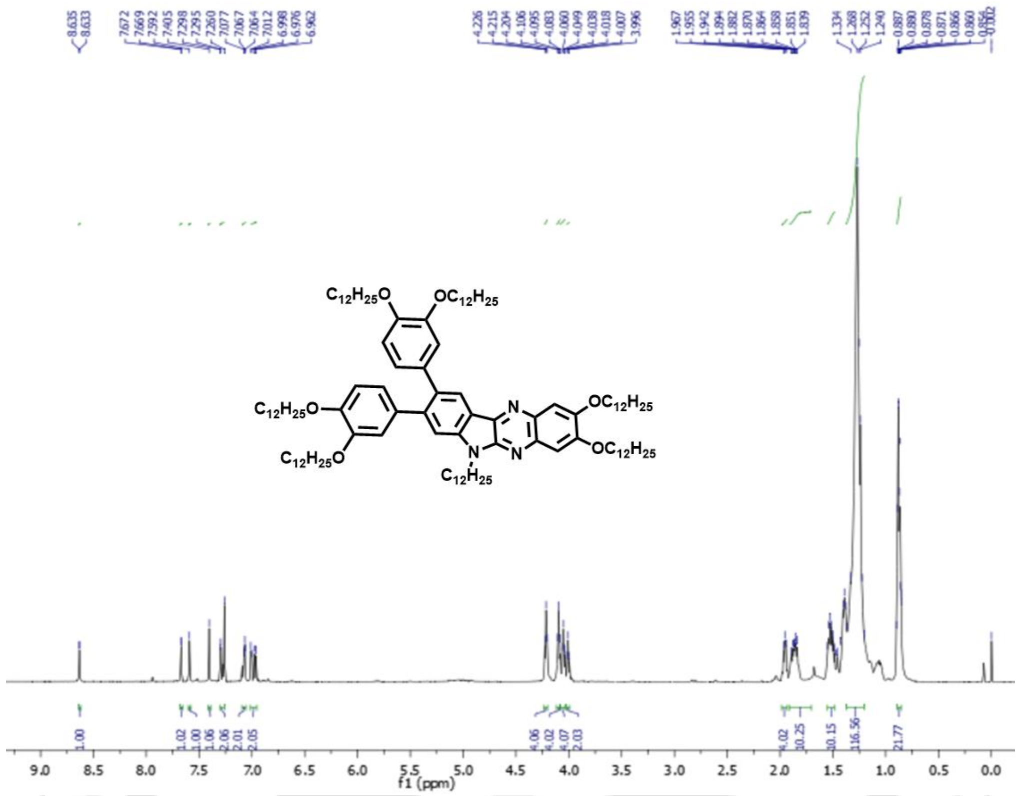

Figure A5. ^{1}H NMR (600 MHz) spectra of **IQ3** in $CDCl_3$.

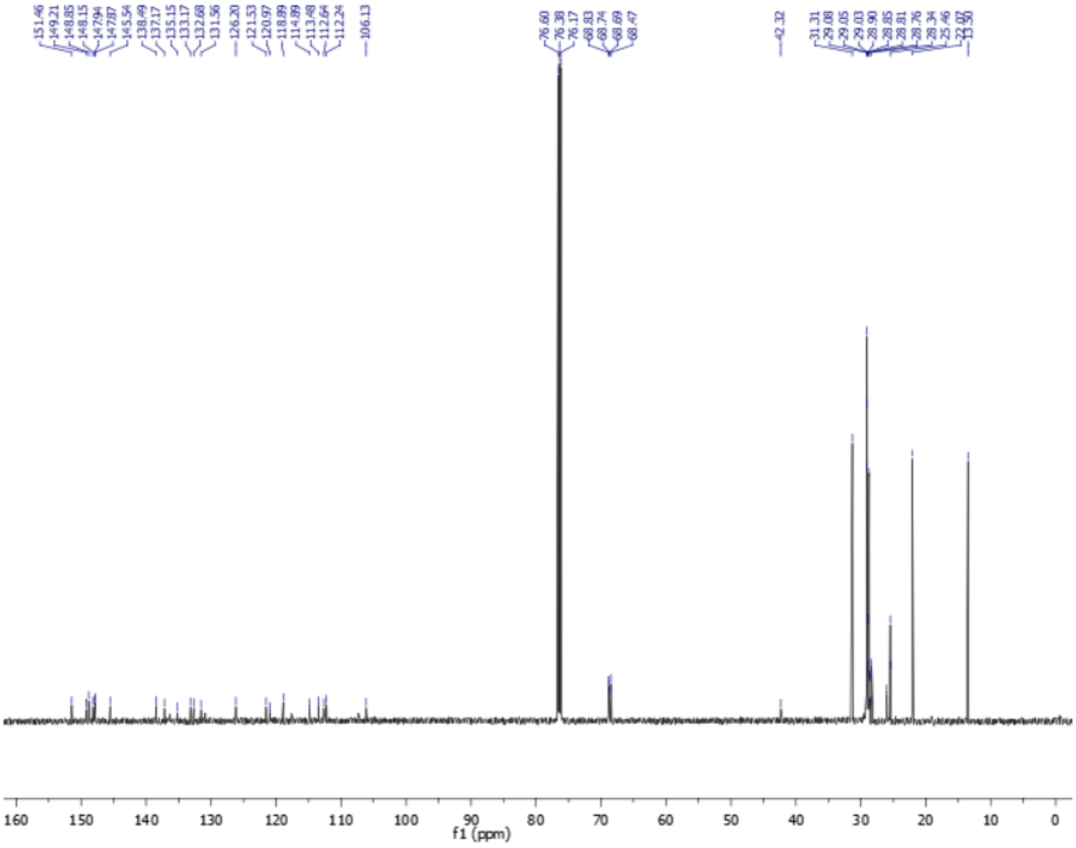

Figure A6. ^{13}C NMR (150 MHz) spectra of **IQ3** in $CDCl_3$.

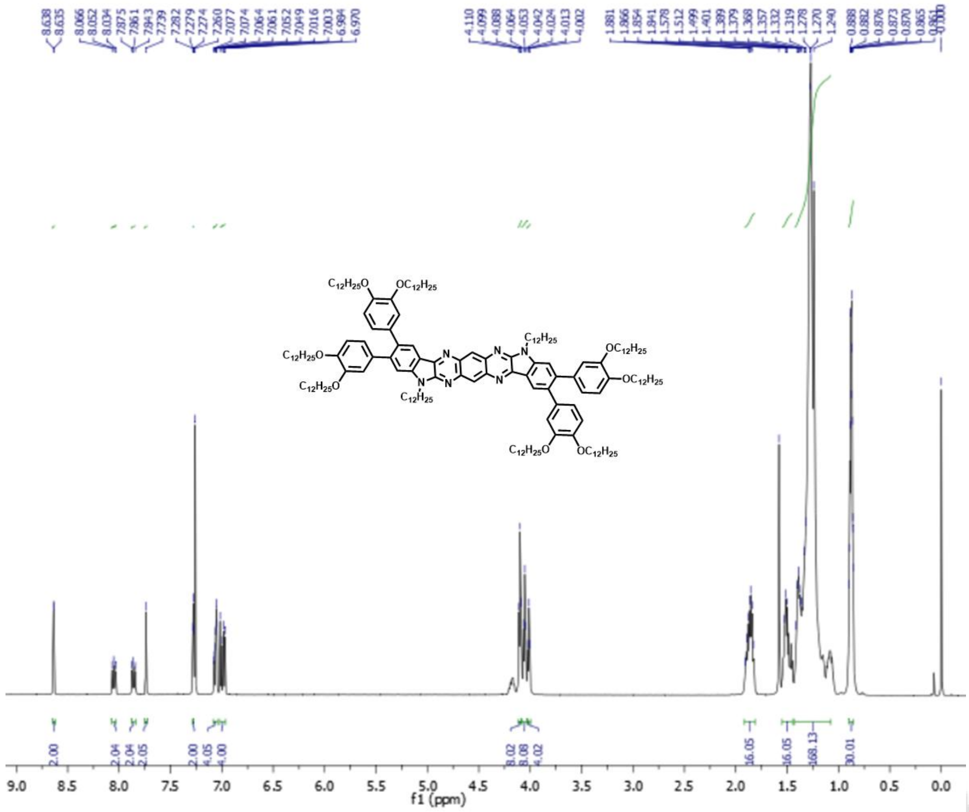

Figure A7. ^{1}H NMR (600 MHz) spectra of **IQ4** in $CDCl_3$.

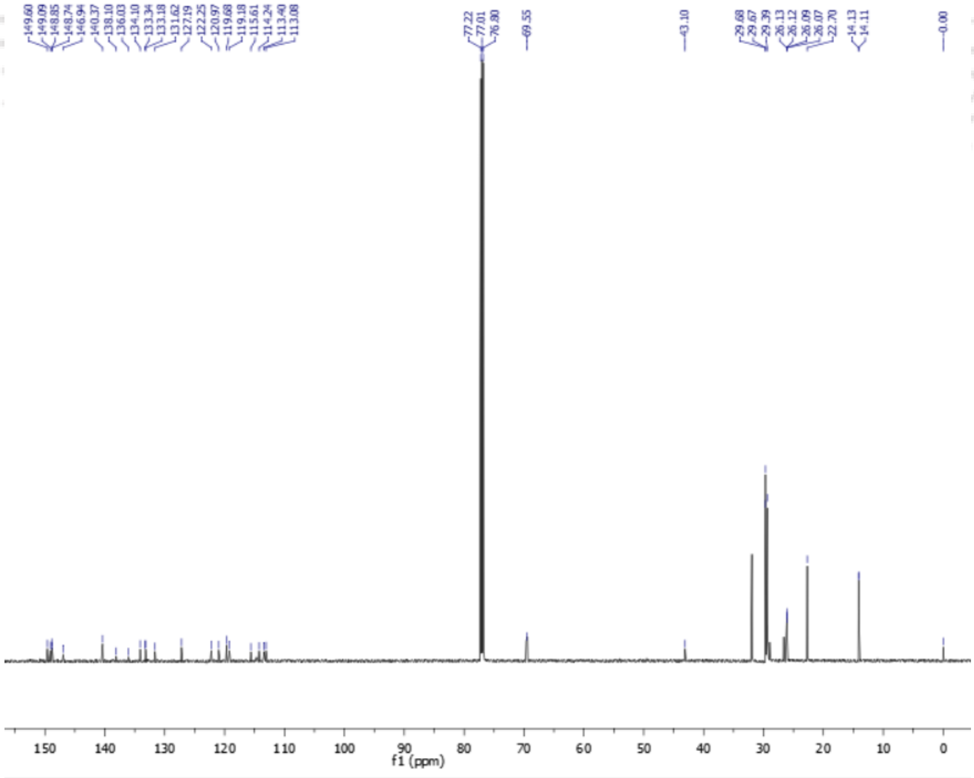

Figure A8. ^{13}C NMR (150 MHz) spectra of **IQ4** in $CDCl_3$.

4.6.2 Polarizing optical microscopy (POM)

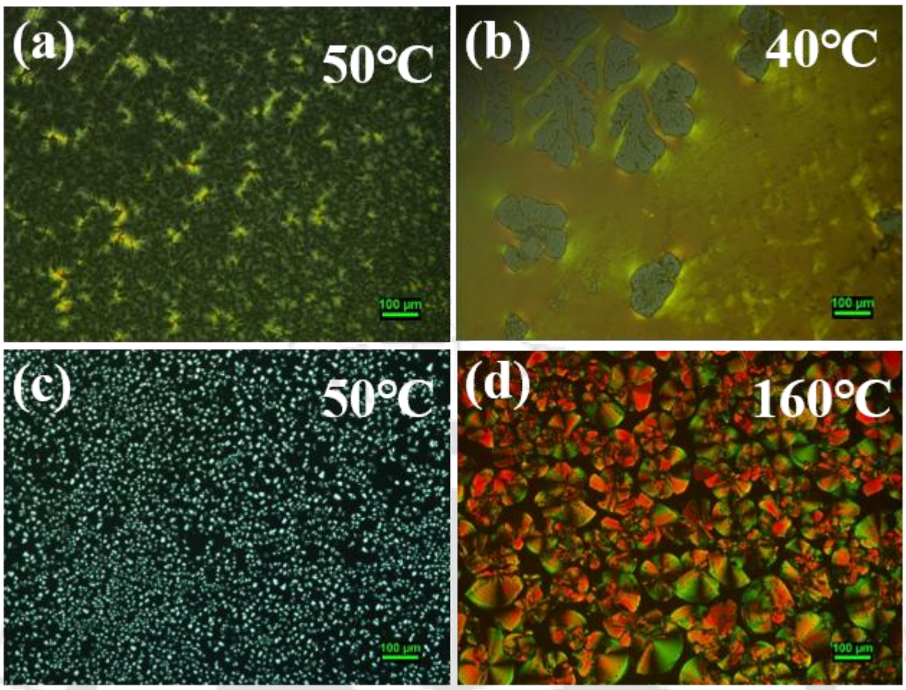

Figure A9. POM images of a) **IQ1**, b) **IQ2**, c) **IQ3**, and d) **IQ4** on a cooling process from isotropic melt.

4.6.3. Differential Scanning calorimetry (DSC)

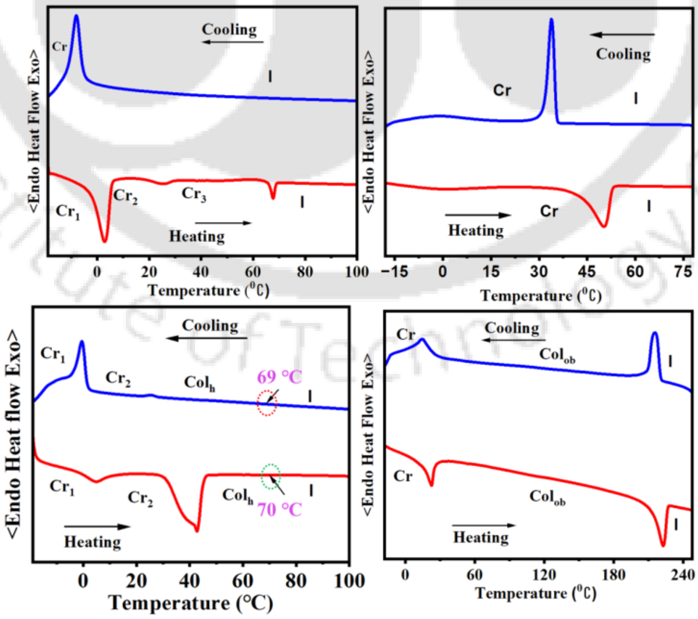

Figure A10. DSC thermograms were obtained for a) **IQ1**, b) **IQ2**, c) **IQ3**, and d) **IQ4** for the first cooling (blue trace) and second heating (red trace) taken at 5 C/min.

4.6.4. X-Ray Diffraction (XRD) Studies

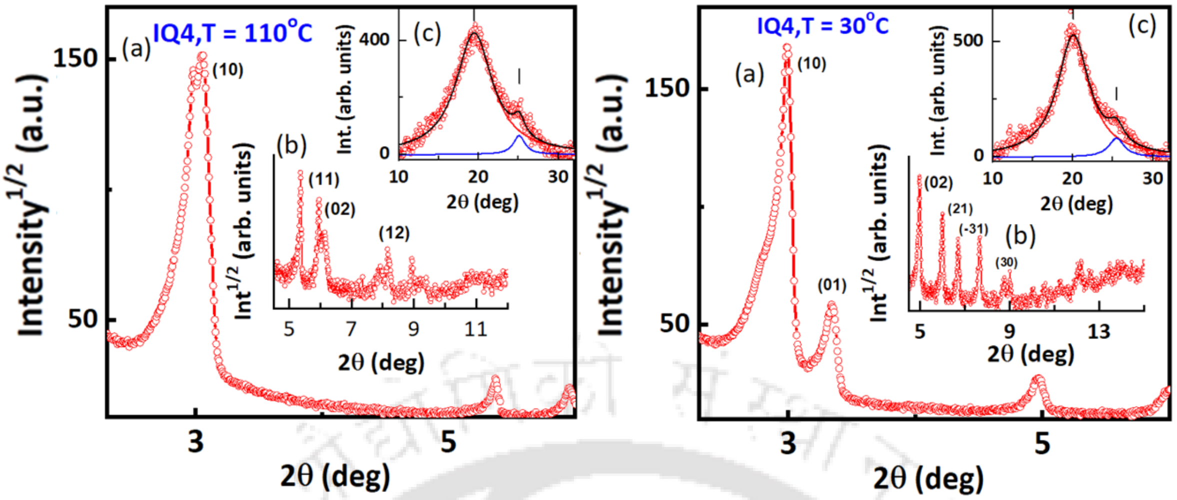

Figure A11. X-ray diffractograms for the Colob phases of IQ4 at 110 °C and at 30 °C in the (a) low, (b) middle (c) wide angle regions. The diffuse peaks-shown as red and blue lines- became more prominent after the deconvolution procedure, representing the contribution due to flexible hydrocarbon and the rigid core-core packing. The solid lines (dark, red,blue) are fitting to Lorentzian expression.

Table A1. Results of (*hkl*) indexation of XRD profiles of **IQ**s at a given temperature (T) of mesophase.

Compounds (D/Å)	Phase (T/°C)	d-spacing		Miller Index (*hk*)	Lattice parameters (Å), Lattice area S (Å^2), Molecular volume (Å^3)
		d_{obs} (Å)	d_{cal}(Å)		
IQ3 (46.24) MW: 1645.70	Col_h (50 °C)	27.09 15.65 13.56 4.52(h_a) 3.75(h_c)	27.09 15.64 13.54	10 11 20	*a =31.28* *A = 847.1* *V = 3175.9* *Z* ≈ 1
IQ4 (54.12) MW: 2476.00	Col_{ob} (210 °C)	31.65 28.80 17.70 16.16 15.79 14.40 11.78 11.28 10.59 9.58 4.50 (h_a) 3.59 (h_c)	31.65 28.80 17.70 16.12 15.82 14.40 11.76 11.26 10.59 9.60	10 01 11 -12 20 02 -31 -32 -23 03	*a* = 35.43 *b* = 32.24 γ = 63.27° *A* = 1020.39 *V* = 3663.20 *Z* ≈ 1
	Col_{ob} (110°C)	29.64 28.80 16.48 14.85 14.44	29.64 28.80 16.48 14.82 14.40	10 01 11 20 02	*a = 36.09* *b = 35.06* *γ= 55.22°* *A = 1039.43* *V = 3688.19*

		11.18 10.81 9.89 4.56(h_a) 3.55(h_c)	11.19 10.76 9.88	-13 12 30	$Z \approx 1$
	Col_{ob} (30 °C)	29.55 26.46 17.83 14.77 13.21 11.57 10.12 9.83 7.31 4.42(h_a) 3.50(h_c)	29.55 26.46 17.83 14.78 13.23 11.82 9.99 9.85 7.45	10 01 11 20 02 21 -31 30 -33	$a = 30.32$ $b = 27.15$ $\gamma = 77.06^o$ $A = 802.32$ $V = 2806.65$ $Z \approx 1$

[a]The diameter (D) of the disk (estimated from Chem 3D Pro 8.0 molecular model software from Cambridge Soft). d_{obs}: spacing observed; d_{cal}: spacing calculated (deduced from the lattice parameters; a,b for Col_{ob}, and a for Col_h phase). The spacings marked h_a and h_c correspond to diffuse reflections in the wide-angle region arising from correlations between the alkyl chains and core regions, respectively. Z indicates the number of molecules per columnar slice of thickness h_c, estimated from the lattice area S and the volume V.

4.6.5. Photophysical studies

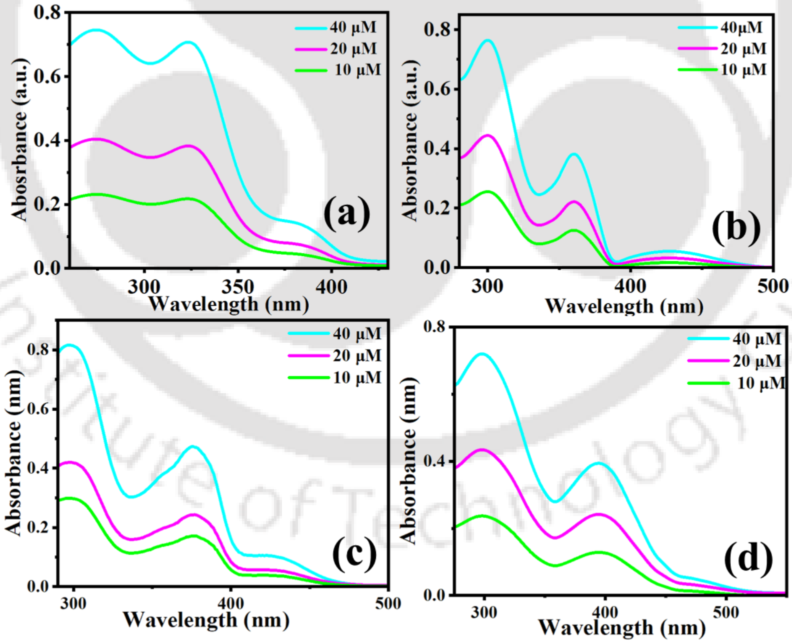

Figure A12. Absorption spectra of compounds a) **IQ1**, b) **IQ2**, c) **IQ3**, and d) **IQ4** in micromolar chloroform solutions.

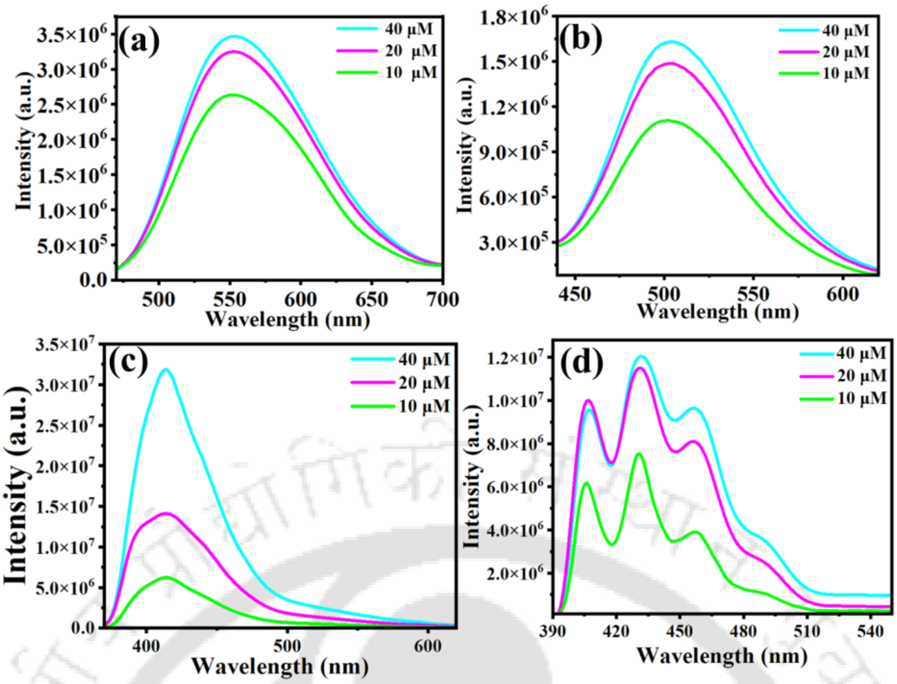

Figure A13. Emission spectra of compounds a) **IQ1**, b) **IQ2**, c) **IQ3**, and d) **IQ4** in micromolar chloroform solutions.

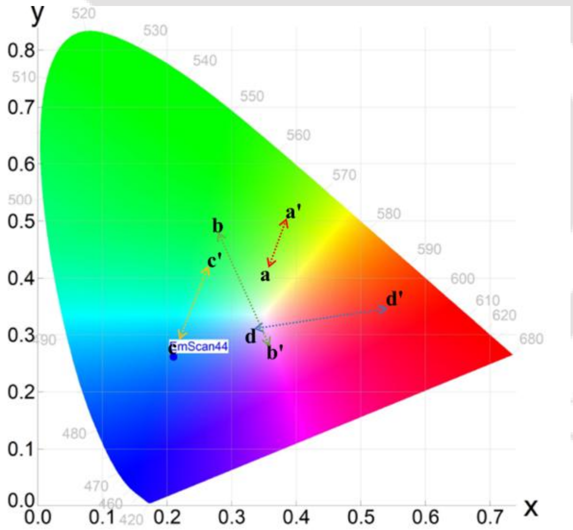

Figure A14: CIE coordinate of emission of **IQs** compound a, b, c, d (in solution state) and a', b', c,' d' (in solid state) **IQ1**, **IQ2**, **IQ3**, and **IQ4,** respectively.

Table A2. Absolute quantum yield of the IQ4 compound in different THF/water ratios.

Entry	THF/water (%)	Abs.QY
1	10	3.83
2	40	13.21
3	60	16.75
4	80	18.30

Table A3. Fluorescence lifetime of **IQs** in solution[a] and thin film state state[b]

Entry	Fluorescence Lifetime (ns)	
	Solution	Solid state
IQ1	6.05	19.32
IQ2	2.60	---
IQ3	2.01	8.88
IQ4	1.48	15.88

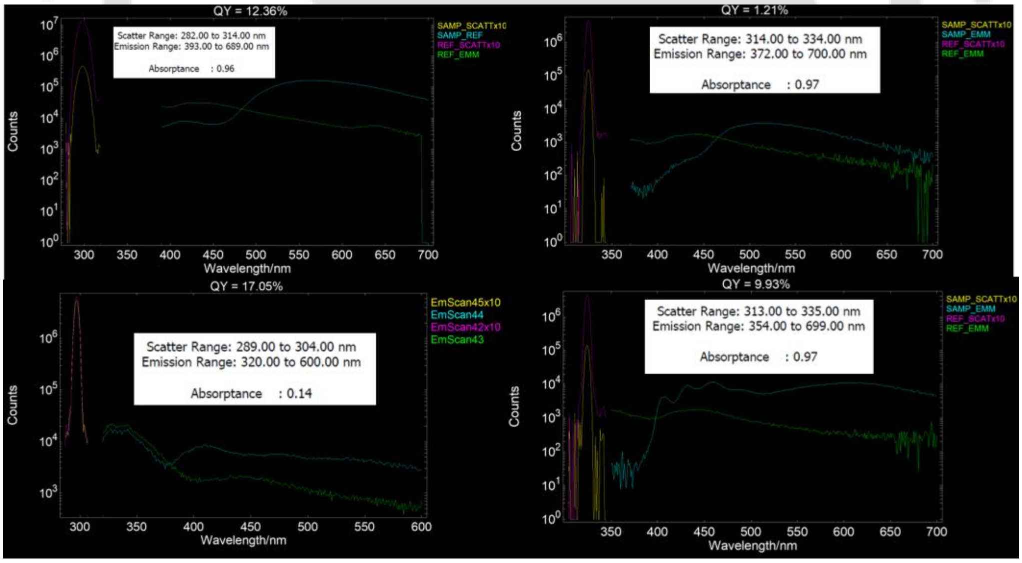

Figure A15. Graphical representations of quantum yield data were obtained using the FLS1000 Fluorescence Spectrometer for (a) **IQ1**, b) **IQ2**, (c) **IQ3**, and (d) **IQ4** in the solution.

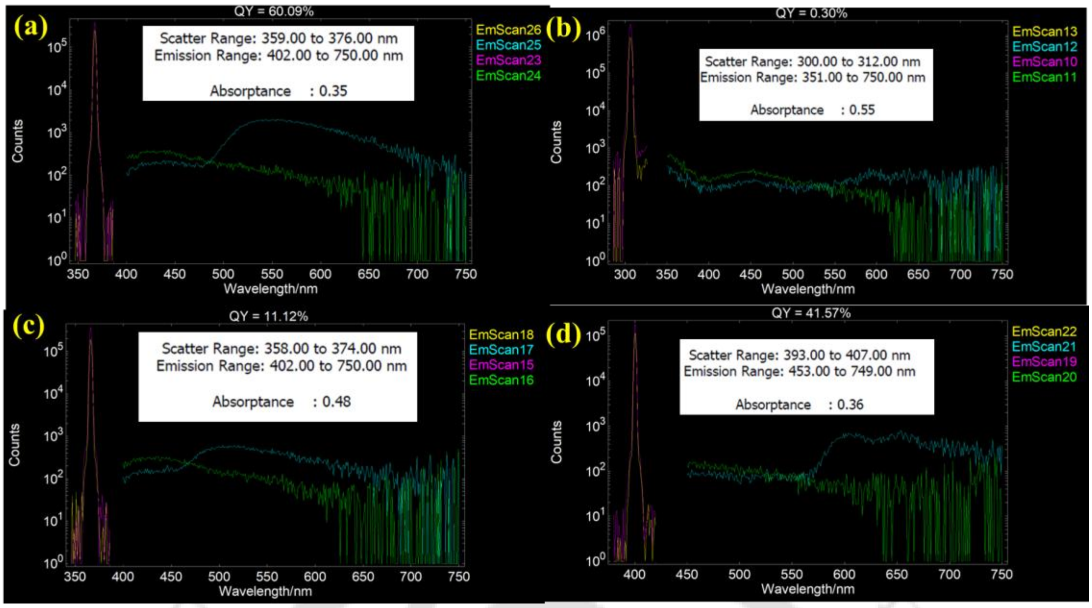

Figure A16. Graphical representations of quantum yield data were obtained using the FLS1000 Fluorescence Spectrometer for (a) **IQ1**, b) **IQ2**, (c) **IQ3**, and (d) **IQ4** in the solid.

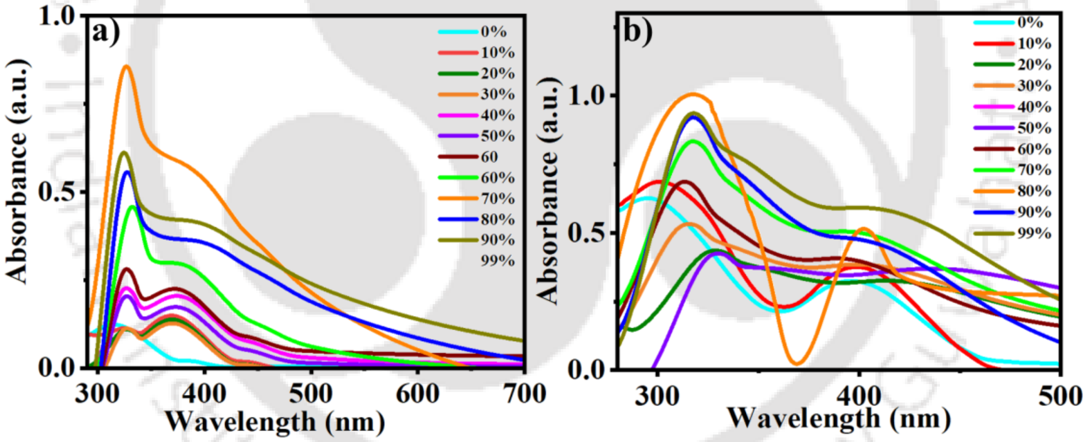

Figure A17. Absorption spectra (a) **IQ3** and (b) **IQ4** in THF/water mixtures.

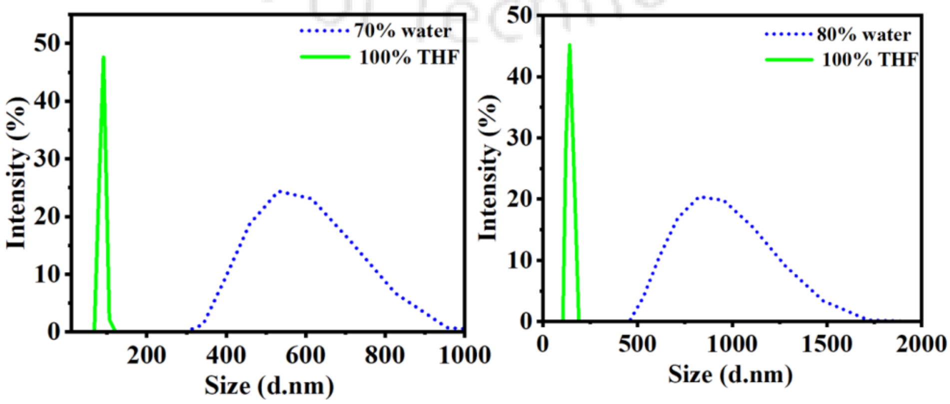

Figure A18. Plots of intensity (%) versus size (d. nm) of (a) **IQ3** and (b) **IQ4** in THF/water mixtures.

Table A4. Size and PDI of **IQ**s in THF/water mixtures

Compounds	Water fraction (vol.%)	Size (d.nm)	PDI
IQ3	0	87.78	1.00
	70	547.5	0.043
IQ4	0	141.7	1.00
	80	906.5	0.177

4.6.5. Electrochemical studies

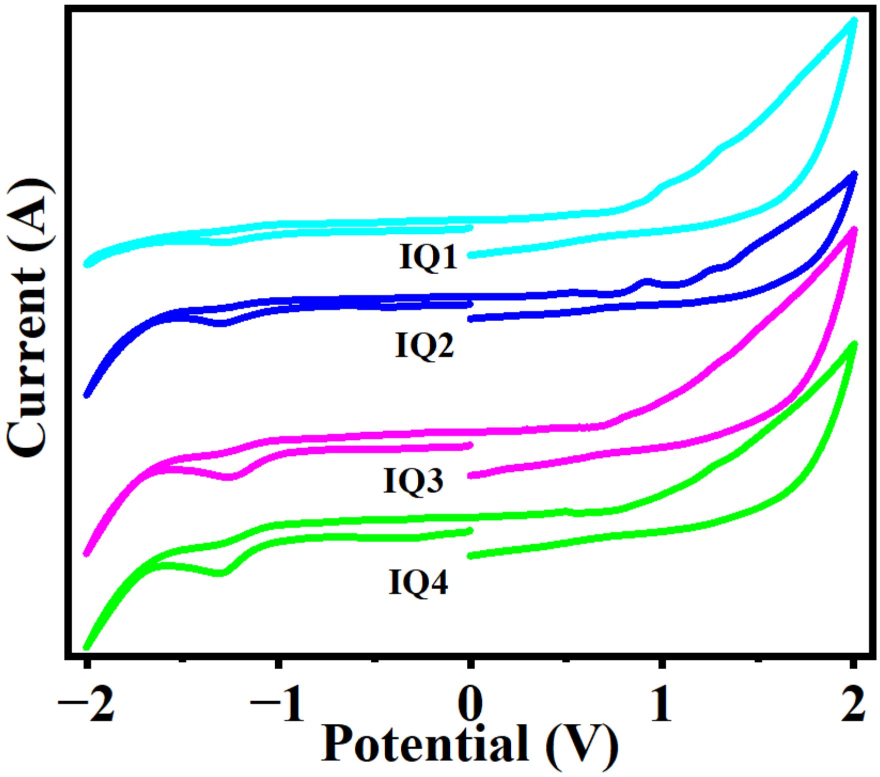

Figure A19. Cyclic voltammograms of **IQ**s in micromolar dichloromethane solutions in scan rate 100mv/s.

Table A5. Electrochemical[a,b] data and data obtained from DFT[h] calculations for **IQ**s

	Electrochemical data					Data from DFT calculation		
Entry	E^{peak}_{oxd} [c]	E^{peak}_{red} [c]	E_{LUMO} [d,e]	E_{HOMO} [d,f]	$\Delta E_{g},_{(opt)}$ [d,g]	E_{LUMO} [dh]	E_{HOMO} [dh]	ΔE_{σ} [d,h]
IQ1	1.29	-1.25	-3.05	-6.06	3.01	-1.85	-5.29	3.44
IQ2	1.24	-1.29	-3.01	-5.63	2.62	-2.73	-5.72	2.99
IQ3	1.27	-1.23	-3.06	-5.71	2.65	-1.68	-5.21	3.53
IQ4	1.26	-1.28	-3.02	-5.61	2.59	-2.02	-4.98	2.96

[a] 0.5mM Dichloromethane solutions; [b]experimental conditions: Ag/AgNO$_3$ as reference electrode, glassy carbon working electrode, platinum wire counter electrode, TBAP (0.1M) as a supporting electrolyte, room temperature; [c] in volts (V); [d] in eV; [e] estimated from the formula by using E_{LUMO}= -(4.8 - $E_{1/2}$, Fc/Fc$^+$ + $E_{red, onset}$) eV; [f] estimated from the formula $E_{HOMO} = E_{LUMO} - E_{g, opt}$) eV; [g]calculated from the red edge of the absorption band of each compound. $E_{1/2}$, $^{Fc/Fc+}$ = 0.50.[h] Obtained from DFT calculations by employing the combination of Becke3-Lee-Yang-Parr (B3LYP) hybrid functional and 6-31G (d, p) basis set using the Gaussian 09 package.

4.6.6. Morphology studies

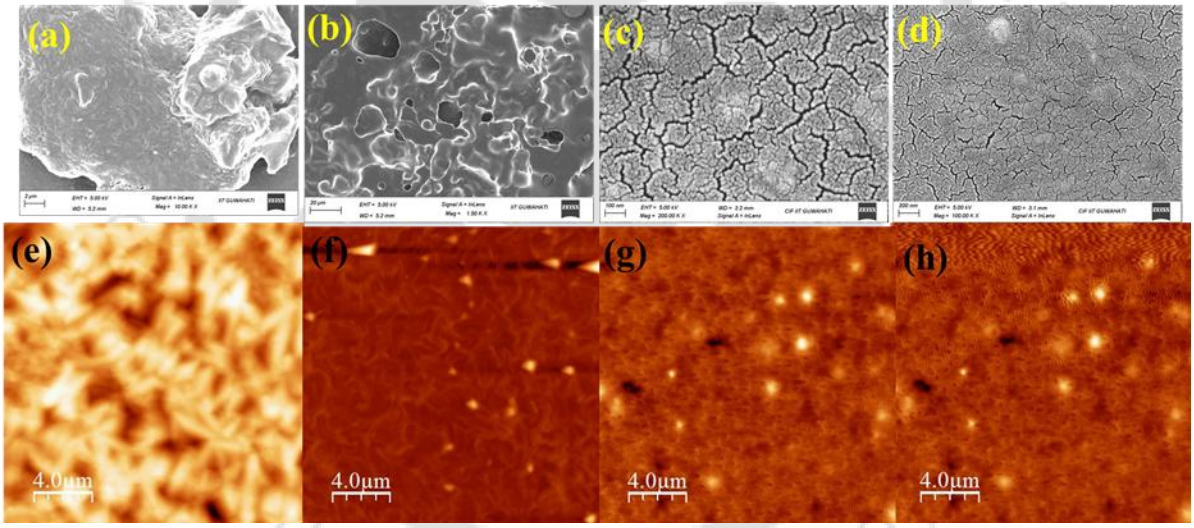

Figure A20. The SEM images (a, b, c, & d) and AFM images (d, e, f, & g) of **IQ1**, **IQ2**, **IQ3**, and **IQ4** compounds, respectively.

4.6.7. DFT Studies

Computational studies were conducted in the B3LYP/6-31g (d, p) method using the Gaussian 09 program package to understand compound **IQ**s' electronic properties and frontier molecular orbital energy level. The absence of imaginary frequency ensured the energy-minimized structure of all the compounds.

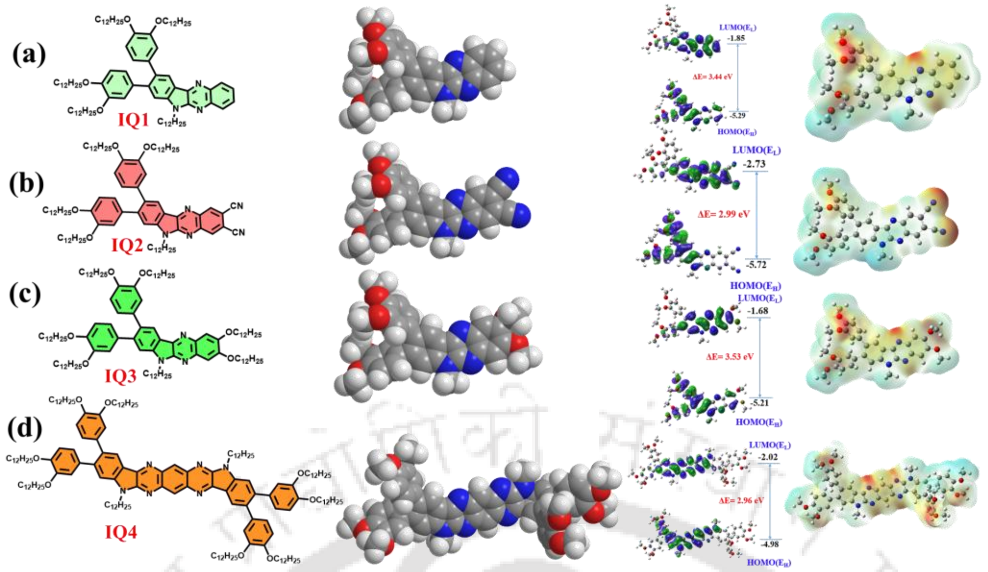

Figure A21. Molecular models and frontier molecular orbitals of **IQ**s obtained from DFT calculations at the B3LYP/ 6-31G (d, p) level and 3D molecular electrostatic potential contour maps. (E_H and E_L denote energies of the HOMO and LUMO, respectively (chain length is limited to methyl for the sake of computational time)).

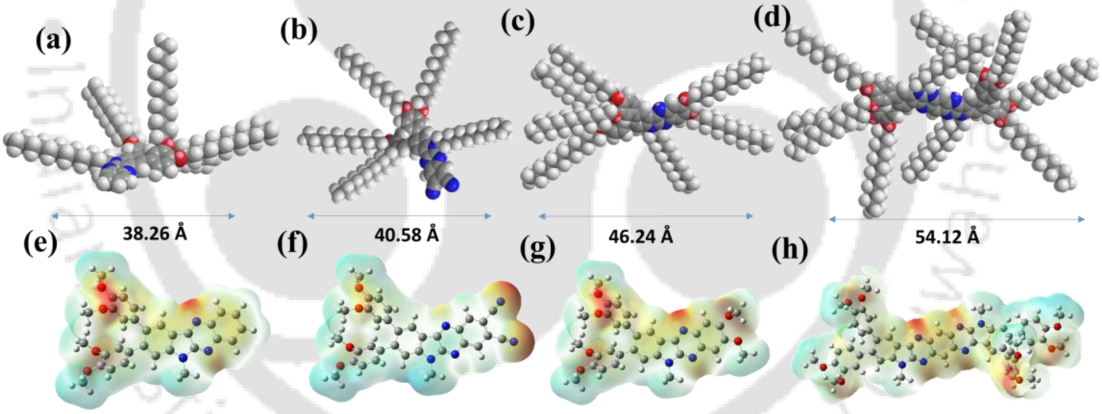

Figure A22. Energy minimized molecular model of (a) **IQ1**, (b) **IQ2**, (c) **IQ3**, and (d) **IQ4** (obtained from Chem3D Ultra); The 3D molecular electrostatic potential (MEP) contour maps (e) **IQ1**, (f) **IQ2**, (g) **IQ3**, and (h) **IQ4** chain length is limited to methyl for the sake of computational time).

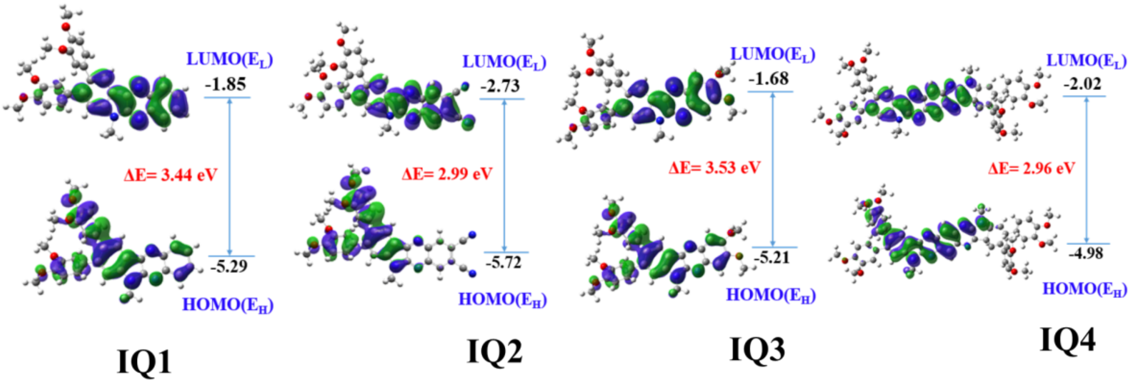

Figure A23. Frontier molecular orbitals of **IQ**s obtained from DFT calculations at the B3LYP/6-31G (d, p) level; E_H and E_L denote energies of the highest occupied molecular orbital (HOMO) and the lowest unoccupied molecular orbital (LUMO), respectively (Chain length is limited to methyl for the sake of computational time).

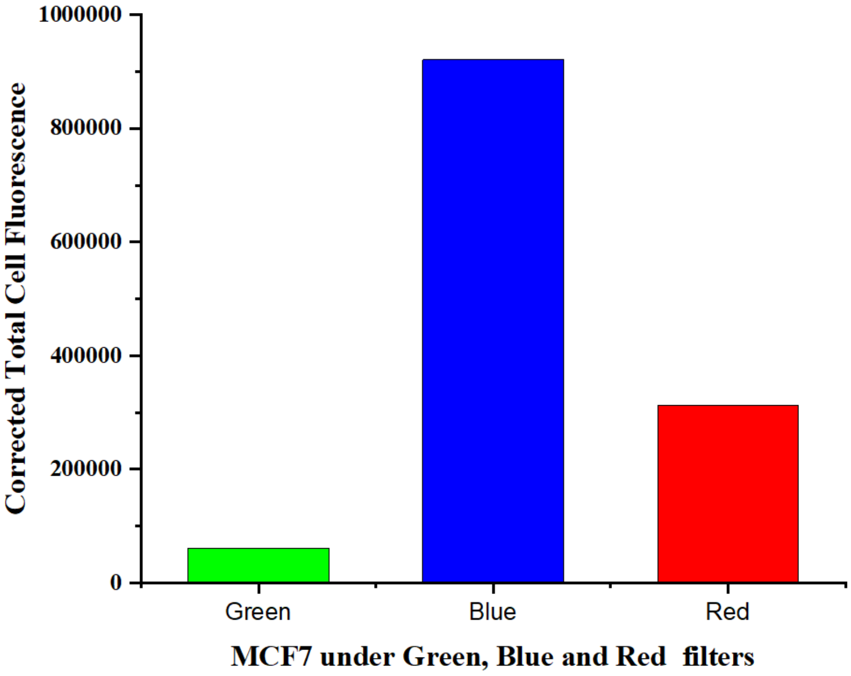

Figure A24. Fluorescence intensity of compound **IQ4** under green, blue, and red filters

4.7. References

1. B.K. Sharma, A.M. Shaikh, S. Chacko, R.M. Kamble., Synthesis, Spectral, Electrochemical and Theoretical Investigation of indolo[2,3-b]quinoxaline Dyes Derived from Anthraquinone for n-type Materials., *J. Chem. Sci.*, 2017, **129**, 483–494.

2. D.N. Kanekar, S.S. Dhanawade, A.B. Jadhav, M. Ghadiyali, S. Chacko, R.M. Kamble. Fluorescent Indolo[2,3-b]quinoxalin-2-yl(phenyl)methanone Dyes: Photophysical, AIE Activity, Electrochemical, and Theoretical Studies., *Monatsh. Chem.*, 2022, **153**, 895–906.

3. R. J. Pandhare, P. M. Badani, R. M. Kamble., Synthesis of D−A-Based Violet−Red Light-Emitting Indolo[2,3-b]quinoxalin-2-yl (Phenyl) Methanone Amine Dyes: Opto-Electrochemical, AIE, and Theoretical Properties., *J. Mol. Struct.*, 2024, **1298**, 137080.

4. X. Qian, H.H. Gao, Y.Z. Zhu, L. Lu, J.Y. Zheng., 6H-Indolo[2,3-b]quinoxaline-Based Organic Dyes Containing Different Electron-Rich Conjugated Linkers for Highly Efficient Dye-Sensitized Solar Cells., *J. Power Sources*, 2015, **280**, 573–580.

5. K. J. Thomas, P. Tyagi. Synthesis, Spectra, and Theoretical Investigations of the Triarylamines Based on 6H-Indolo[2,3-b]quinoxaline., *J. Org. Chem.*, 2010, **75**, 8100–8111.

6. A.M. Shaikh, B.K. Sharma, R.M. Kamble. Photophysical, Electrochemical, and Thermal Studies of 5-Methyl-5H-Benz[g]indolo[2,3-b]quinoxaline Derivatives: Green and Yellow Fluorescent Materials., *Can. Chem. Trans.*, 2015, **3**, 158.

7. X. Qian, H.H. Gao, Y.Z. Zhu, L. Lu, J.Y. Zheng., 6H-Indolo[2,3-b]quinoxaline-Based Organic Dyes Containing Different Electron-Rich Conjugated Linkers for Highly Efficient Dye-Sensitized Solar Cells, *J. Power Sources*, 2015, **280**, 573–580.

8. W. Zhang, R. Walser-Kuntz, J.S. Tracy, T.K. Schramm, J. Shee, M. Head-Gordon, G. Chen, B.A. Helms, M.S. Sanford, F.D. Toste., Indolo[2,3-b]quinoxaline as a Low Reduction Potential and High Stability Anolyte Scaffold for Nonaqueous Redox Flow Batteries., *J. Am. Chem. Soc.*, 2023, **145**, 18877–18887.

9. J. Zhao, H. Li, H. Li, Q. Zhao, H. Ling, J. Li, J. Lin, L. Xie, Z. Lin, M. Yi, W. Huang., Synthesis, Characterization, and Charge Storage Properties of π-Biindolo[2,3-b]quinoxaline for Solution-Processing Organic Transistor Memory., *Dyes Pigm.*, 2019, **167**, 255–261.

10. D. Dong, D. Fang, H. Li, C. Zhu, X. Zhao, J. Li, L. Jin, L. Xie, L. Chen, J. Zhao, H. Zhang, and W. Huang, C-H Direct Arylated 6H-Indolo[2,3-b] quinoxaline Derivative as a Thickness-Dependent Hole-Injection Layer, *Chem. Asian J.*, 2017, **12**, 920 – 926.

11. M. Basak, B. Bhattacharjee, A. Ramesh, G. Das., Self-assembled quinoxaline derivative: Insight into disaggregation induced selective detection of nitro-aromatics in aqueous medium and live cell imaging., *Dyes Pigm.*, 2021, **196**, 109779.

12. K. M. Driller, S. Libnow, M. Hein, M. Harms, K. Wende, M. Lalk, D. Michalik, H. Reinke, P. Langer, Synthesis of 6H-indolo[2,3-b]quinoxaline-N-glycosides and their cytotoxic activity against human keratinocytes (HaCaT*), Org. Biomol. Chem.*, 2008, **6**, 4218–4223.

13. P. Singh, M. Ghadiyali, S. Chacko, R.M. Kamble, D-A- D based pyrido-pyrazino[2,3-b]indole amines as blue-red fluorescent dyes: Photophysical, aggregation-induced emission, electrochemical and theoretical studies, *J. Lumin.*, 2022, **242**,118568.

14. P. Tyagi, A. Venkateswara Rao, K. J. Thomas., Solution Processable Indoloquinoxaline Derivatives Containing Bulky Polyaromatic Hydrocarbons: Synthesis, Optical Spectra, and Electroluminescence., *J. Org. Chem.*, 2011, **76**, 4571-4581.

15. T. H. Su, C. H. Fan, Y. H. Ou-Yang, L. C. Hsu, C. H. Cheng, highly efficient deep-red organic electrophosphorescent devices with excellent operational stability using bis(indoloquinoxalinyl) derivatives as the host materials, *J. Mater. Chem. C*, 2013, **1**, 5084–5092.

16. V. K. Vishwakarma, S. Nath, M. Gupta, D. K. Dubey, S. S. Swayamprabha, J. H. Jou, S. K. Pal, A. A. Sudhakar. Room-Temperature Columnar Liquid Crystalline Materials Based on Pyrazino[2,3-g] quinoxaline for Bright Green Organic Light-Emitting Diodes., *ACS Appl. Electron. Mater.*, 2019, **1**, 1959–1969.

17. A. Venkateswara Rao, P. Tyagi, K. J. Thomas, P. W. Chen, K. C. Ho., Organic Dyes Containing Indolo[2,3-b] quinoxaline as a Donor: Synthesis, Optical, and Photovoltaic Properties., tetrahedron, 2014, **70**, 6318–6327.

18. D.W. Chang, H.J. Lee, J.H. Kim, S.Y. Park, S. M. Park, L. Dai, J.B. Baek, *Org. Lett.* 2011, **13**, 3880.

19. S. Karki, R. Hazare, S. Kumar, V. Bhadauria, J. Balzarini, E. DeClercq. Synthesis, Anticancer, and Cytostatic Activity of Some 6H-Indolo[2,3-b] quinoxalines., *Acta Pharm.*, 2009, **59**, 4, 431.

20. J. Harmenberg, B. Wahren, J. Bergman, S. Akerfeldt, L. Lundblad., Antiherpesvirus Activity and Mechanism of Action of Indolo[2,3-b]quinoxaline and Analogs., *Antimicrob. Agents Chemother.*, 1988, **32**, 1720–1724.

21. L. M. Wilhelmsson, N. Kingi, and J. Bergman, Interactions of Antiviral Indolo[2,3-b]quinoxaline Derivatives with DNA, *J. Med. Chem.*, 2008, **51**, 7744–7750.

22. P.S. Singh, M. Ghadiyali, S. Chacko, R.M. Kamble. D−A−D Based Pyrido-pyrazino[2,3-b]indole Amines as Blue-Red Fluorescent Dyes: Photophysical, Aggregation-Induced Emission, Electrochemical, and Theoretical Studies., *J. Lumin.*, 2021, **242**, 118568.

23. Y. Liang, X. Liu, Y. Pu, R. Zhang, L. Zhou, Y. Xiao, Synthesis, LC self-assembly and photophysical behavior of stimuli-responsive cyanostilbene-based hexacatenar mesogens with multicolor switching, *J. Lumin.*, 2023, **262**, 119977.

24. X. Zhang, W. Qina, B. Cheng, H. Guoa, F. Yanga, First columnar rufigallol liquid crystals with high fluorescence at aggregated states, *J. Mol. Liq.*, 2020, **298**, 112074.

25. M. M. Abadía, R. Giménez, and M. B. Ros, Self-Assembled α-Cyanostilbenes for Advanced Functional Materials, *Adv. Mater.*, 2018, **30**, 1704161.

26. J. Voskuhl, M. Giese, Mesogens with aggregation-induced emission properties: Materials with a bright future, *Aggregate.* 2022, **3**,124.

27. H. Bui, J. Kim, H. Kim, B. Ki Cho, and S. Cho, Advantages of Mobile Liquid-Crystal Phase of AIE Luminogens for Effective Solid-State Emission, *J. Phys. Chem. C*, 2016, **120**, 26695−26702.

28. W. Z. Yuan, Z. Yu, P. Lu, C. Deng, J. W. Y. Lam, Z. Wang, E. Q. Chen, Y. Mad and Ben Z. Tang, High-efficiency luminescent liquid crystal: aggregation-induced emission strategy and biaxially oriented mesomorphic structure, *J. Mater. Chem.*, 2012, **22**, 3323–3326.

29. S. Dai, Z. Cai, Z. Peng, Z. Wang, B. Tong, J. Shi, S. Gan, Q. He, W. Chen and Y. Dong, A stabilized lamellar liquid crystalline phase with aggregation-induced emission features based on pyrrolopyrrole derivatives, *Mater. Chem. Front.*, 2019, **3**, 1105.

30. X. Kong, R. Luo, H. Gong, D. Chen, S. Yang, S. Li, G. Wang & Z. He, Discotic liquid crystals with aggregation-induced emission properties based on tetraphenylethylene and triphenylene derivatives, *Mol. Cryst. Liq. Cryst.*, 2021,**724**, 26-37.

31. Y. Guo, D. Shi, Z. W. Luo, J. Xu, M. Li, L. Hu Yang, Z. Q. Yu, E. Chen, and H. Lou Xie, High-Efficiency Luminescent Liquid Crystalline Polymers Based on Aggregation Induced Emission and "Jacketing" Effect: Design, Synthesis, Photophysical Property, and Phase Structure, *Macromolecules*, 2017, **50**, 9607−9616.

32. L. Liu, M. Wang, L. X. Guo, Y. Sun, X. Q. Zhang, B. P. Lin, and H. Yang, Aggregation-Induced Emission Luminogen-Functionalized Liquid Crystal Elastomer Soft Actuators, *Macromolecules*, 2018, **51**, 4516−4524.

33. Yi Liu, Li Hong You, Fa Xu Lin, Kuo Fu, Wang Zhang Yuan, Er-Qiang Chen, Zhen-Qiang Yu, and Ben Zhong Tang, Highly Efficient Luminescent Liquid Crystal with Aggregation-Induced Energy Transfer, *ACS Appl. Mater. Interfaces*, 2019, **11**, 3516−3523.

34. B. Li, J. Zhang, J. Wang and X. Chen, Aggregation-Induced Emission-Active Cyanostilbene-Based Liquid Crystals: Self-Assembly, Photophysical Property, and Multiresponsive Behavior, *Molecules*, 2024, **29**, 5811.

35. C. Zeng, J. Dai, T. Yang, Z. Wang, Y. Gao, J. Xia, Y. Chen, M. Sun, Multi-stimuli fluorescence responsiveness of *α*-cyanostilbene derivative: AIEE, stimuli response to polarity, acid, force, and light, applications in anti-counterfeiting and single phosphor w-OLED, *Dyes Pigm.*, 2024, **222**, 111906.

36. Y. Wang, Y. Liao, C. P. Cabry, D. Zhou, G. Xie, Z. Qu, D. W. Bruce, and W. Zhu, Highly efficient blueish-green fluorescent OLED based on AIE liquid crystal molecules: from ingenious molecular design to multifunction materials, *J. Mater. Chem. C*, 2017, **5**, 3999.

37. I. Bala, L. Ming, R. Yadav, J. De, D. Dubey, S. Kumar, H. Singh, J. Jou, K. Kailasam, and S. Pal, Deep-Blue OLED Fabrication from Heptazine Columnar Liquid Crystal Based AIE-Active Sky-Blue Emitter, *Chemistry Select*, 2018, **3**, 7771 – 7777.

38. J. De, A. Haseeb, R. Yadav, S. P. Gupta, I. Bala, P. Chawla, K. K. Kesavan, J. Jou, and S. Pal, AIE-active mechanoluminescent discotic liquid crystals for applications in OLEDs and bio-imaging, *Chem. Commun.*, 2020, **56**, 14279-14282.

39. I. Bala, H. Kaur, M. Maity, R. Yadav, J. De, S. Gupta, J. Jou, U. Pandey, and S. Pal, Electroluminescent Aggregation-Induced Emission-Active Discotic Liquid Crystals Based on Alkoxy Cyanostilbene-Functionalized Benzenetricarboxamide with Ambipolar Charge Transport, *ACS Appl. Electron. Mater.*, 2022, **4**, 1163−1174.

40. Z. Huang, C. Zhou, Y. Yu, S. 7Wang, R. Fu, X. Liu, L. Mao, J. Yuan, L. Tao, Y. Wei, Synthesis of a polymerizable aggregation-induced emission (AIE) dye with A-D structure based on benzothiadiazole for fluorescent nanoparticles and its application in bioimaging, *Eur. Polym. J.*, 2022, **181**,111705.

41. V. S. Sharma, H. Mali, A. S. Sharma, S. P. Thakar, U. P. Patel, P. S. Shrivastav, Resorcinarene appended benzothiazole-based light-emitting macrocyclic compounds with nematic liquid crystalline phase and bio-imaging applications, *J. Mol. Liq.*, 2024, **397**,124110.

42. S. L. Rathod, V. S. Sharma, A. S. Sharma, M. Athar, P. S. Shrivastav, H. M. Parekh, Blue light-emitting Quinoline armed Thiacalix [4]arene 3D-scaffold: A systematic platform to construct fluorescent liquid crystals with bio-imaging applications, *J. Mol. Struct.*, 2022, **1270**, 133830.

43. W. Chen, C. Zhang, X. Han, S. Hua Liu, Y. Tan, and J. Yin, Fluorophore-Labeling Tetraphenylethene Dyes Ranging from Visible to Near-Infrared Region: AIE Behavior, Performance in Solid State, and Bioimaging in Living Cells, Key Laboratory of Pesticide and Chemical Biology, Ministry of Education, Hubei International Scientific and Technological, *J. Org. Chem.*, 2019, **84**, 14498−14507.

44. S. Choi, J. Rho, S. E. Yoon, J. Seok, H. Kim, J. Min, W. Yoon, S. Lee, H. Yun, O. Kwon, J. H. Kim, W. Kim, and E. Kim, Full Color Tunable Aggregation-Induced Emission Luminogen for Bioimaging Based on an Indolizine Molecular Framework., *Bioconjugate Chem.*, 2020, **31**, 2522−2532.

45. M. Hui Chua, K. Chin, X. Loh, Q. Zhu, and J. Xu., Aggregation-Induced Emission-Active Nanostructures: Beyond Biomedical Applications, *ACS Nano*, 2023, **17**, 1845−1878.

46. P. S. Singh, P. M. Badani, and R. M. Kamble, Impact of the donor substituent on the optoelectrochemical properties of 6H-indolo[2,3-b] quinoxaline amine derivatives, *New J. Chem.*, 2019, **43**, 19379-19396.

47. J. Luo, Z. Xie, Z. Xie, J.W.Y. Lam, L. Cheng, H. Chen, C. Qiu, H.S. Kwok, X. Zhan, Y. Liu, D. Zhu, B.Z. Tang, Aggregation-induced emission of 1-methyl-1,2,3,4,5 pentaphenylsilole, *Chem. Commun.*, 2001, **2001**, 1740–1741.

48. Y. Sagara and T. Kato, Stimuli-Responsive Luminescent Liquid Crystals: Change of Photoluminescent Colors Triggered by a Shear-Induced PhaseTransition, *Angew. Chem., Int. Ed.*, 2008, **47**, 5175–5178.

49. S. Yamane, Y. Saqara, T. Mutai, K. Araki and T. Kato, Mechanochromic luminescent liquid crystals based on a bianthryl moiety, *J. Mater. Chem. C*, 2013, **1,** 2648 2656.

50. S. Yamane, Y. Saqara and T. Kato, Steric effects on excimer formation for photoluminescent smectic liquid-crystalline materials, *Chem. Commun.*, 2013, **49**, 3839–3841.

51. D. Liu, C. H. Jang, a new strategy for imaging urease activity using liquid crystal droplet patterns formed on solid surfaces, *Sens. Actuators B*, 2014, **193**, 770– 773.

52. X. Zhan, Y. Liu, F. Wang, D. Zhao, K. Yang and D. Luo, A highly sensitive fluorescent sensor for ammonia detection based on aggregation-induced emission luminogen-doped liquid crystals, *Soft Matter*, 2022, **18**, 7662

53. X. Du, Y. Liu, D. Zhao, H. F. Gleeson, and D. Luo, A wireless fluorescent flexible force sensor based on aggregation-induced emission doped liquid crystal elastomers, *Soft Matter*, 2024, **20**, 2562.

54. X. Du, Y. Liu, F. Wang, D. Zhao, H. F. Gleeson, and D. Luo, A Fluorescence Sensor for Pb^{2+} Detection Based on Liquid Crystals and Aggregation-Induced Emission Luminogens, *ACS Appl. Mater. Interfaces*, 2021, **13**, 22361−22367.

55. T. Wöhrle, I. Wurzbach, J. Kirres, A. Kostidou, N. Kapernaum, J. Litterscheidt, J. C. Haenle, P. Staffeld, A. Baro, F. Giesselmann and S. Laschat, *Chem Rev.*, 2016, **116**, 1139–1241.

56. H. K. Bisoyi, Q. Li, Stimuli directed alignment of self-organized one-dimensional semiconducting columnar liquid crystal nanostructures for organic electronics, *Prog. Mater. Sci.*, 2019, **104**, 1.

57. H. K. Bisoyi, Q. Li, Liquid Crystals: Versatile Self-Organized Smart Soft Materials, *Chem. Rev.*, 2022, **122**, 4887−4926.

58. R. Termine and A. Golemme, Charge Mobility in Discotic Liquid Crystals, *Int. J. Mol. Sci.* 2021, **22**, 877.

59. A.E. Murschell, T. C. Sutherland, Anthraquinone-Based Discotic Liquid Crystals, *Langmuir*, 2010, **26**, 12859–12866.

60. X. Zhou, S.W. Kang, S. Kumar, R. R. Kulkarni, S. Z. D. Cheng, and Q. Li, Self-Assembly of Porphyrin and Fullerene Supramolecular Complex into Highly Ordered Nanostructure by Simple Thermal Annealing, *Chem. Mater.* 2008, **20**, 3551–3553.

61. R. De, S. K. Pal, Self-assembled discotics as molecular semiconductors, *Chem. Commun.*, 2023, **59**, 3050–3066.

62. S. Kumar, The Liquid Crystals book series Chemistry of Discotic Liquid Crystals from Monomers to Polymers, *CRC Press, Taylor & Francis Group*, 2011.

63. J. De, I. Bala, S. P. Gupta, U. K. Pandey, and S.K. Pal, High Hole Mobility and Efficient Ambipolar Charge Transport in Heterocoronene-Based Ordered Columnar Discotics, *J. Am. Chem. Soc.*, 2019, **141**, 18799−18805.

64. J. Xu, Room-Temperature Columnar Liquid Crystals from Twisted and Macrocyclic 9,9′-Bifluorenylidene Mesogen with Ambipolar Carrier Transport Properties, *ACS Mater. Au*, 2023, **3**, 450−455.

65. D. D. Nguyen, J. Labella, J. L. Martın, C. L. Folcia, J. Ortega, T. Torres, T. Sierra and J. L. Sessler, Columnar liquid crystals based on antiaromatic expanded porphyrins, *Chem. Commun.*, 2024, **60**, 3401–3404.

66. P. K. Behera, K. Yadav, D. S. S. Rao, U. K. Pandey and A. S. Achalkumar, Self-assembled anti-napthalene-3,4:9,10-bis(benzimidazole)s: stabilizing room temperature columnar phase with ambipolar conductivity., *ACS Appl. Electron. Mater.*, 2023, **5**, 5417–5421.

67. Q. Zhang, H. Peng, G. Zhang, Q. Lu, J. Chang, Y. Dong, X. Shi, and J. Wei, Facile Bottom-Up Synthesis of Coronene-based 3-Fold Symmetrical and Highly Substituted Nanographenes from Simple Aromatics., *J. Am. Chem. Soc.*, 2014, **136**, 5057–5064.

68. P. K. Behera, F. R. Chen, I. Mondal, S. Lenka, P. Gautam, N. Khatiwoda, I. Siddiqui, V. E. Krishnaprasad, R. Ahmed, D. S. Shankar Rao, S. P. Senanayake, J. H. Jou and A. S. Achalkumar, Superior electron mobility, red electroluminescence with high quantum efficiency from printable room temperature columnar liquid crystalline perylene bisimide. *Chem. Eng. J.*, 2024, **488**, 150762.

69. J. Gierschner, L. Lüer, B. Mili'an-Medina, D. Oelkrug, H.J. Egelhaaf, Highly emissive H-aggregates or aggregation-induced emission quenching? The photophysics of all-trans para-distyrylbenzene, *J. Phys. Chem. Lett.*,2013, **4**, 2686–2697.

70. J. H. Kim, T. Schembri, D. Bialas, M. Stolte and F. Würthner, F. Slip-stacked J-aggregate materials for organic solar cells and photodetectors., *Adv. Mater.*, 2022, **34**, 2104678.

71. N. J. Hestand and F. C. Spano. Expanded H- and J-molecular aggregates theory: the effects of vibronic coupling and intermolecular charge transfer., *Chem. Rev.*, 2018, **118**, 7069.

72. R. Mahesh, & K. Suchiang, Caenorhabditis elegans: A Model Organism to Decipher Biological Activities of Nanoparticles, *Model Org. Stud. Biol. Act. Toxic. Nanoparticles*, 2020, 139-175.

73. C. L. Ruark-Seward, E.L. Davis, & T. L. Sit, Electropermeabilization-based fluorescence in situ hybridization of whole-mount plant parasitic nematode specimens. *MethodsX*, 2019, **6**, 2720-2728.

74. X. Jiang, Y. Yang, H. Li, X. Qi, X. Zhou, M. Deng & S. A. Liang, a water-soluble fluorescent probe for the selective sensing of Ag^+ and its application in imaging living cells and nematodes, *J. Fluoresc.*, 2020, **30**, 121-129.

75. Y. Y. Hui, W. Hsiao, S. Haziza, M. Simonneau, F. Treussart, & H. C. Chang, Single particle tracking of fluorescent nanodiamonds in cells and organisms, *Curr. Opin. Solid State Mater. Sci.*, 2017, **21**, 35-42.

76. S. Liang, Y. Liu, T. Fu, F. Yang, X. Chen, & G. Yan, A water-soluble and biocompatible polymeric nanolabel based on naphthalimide grafted poly (acrylic acid) for the two-photon fluorescence imaging of living cells and C. elegans. *Colloids Surf. B Biointerfaces*, 2016, **148**, 293-298.

77. D. Sepúlveda-Crespo, R. M. Reguera, F. Rojo-Vázquez, R. Balaña-Fouce, & M. Martínez-Valladares, Drug discovery technologies: Caenorhabditis elegans as a model for anthelmintic therapeutics, *Med. Res. Rev.*, 2020, **40**, 1715-1753.

78. N. L. Leung, N. Xie, W. Yuan, Y. Liu, Q. Wu, Q. Peng, Q. Miao, J.W. Lam, B. Z. Tang, Restriction of intramolecular motions: the general mechanism behind aggregation-induced emission, *Chem. Eur. J.*, 2014, **20**, 15349-15353.

79. F. Würthner, Aggregation-induced emission (AIE): a historical perspective, *Angew. Chem. Int. Ed.*, 2020, **59**, 14192-14196.

80. R. Nass, & I. Hamza The Nematode C. elegans as an animal model to explore toxicology in vivo: solid and axenic growth culture conditions and compound exposure parameters. *Curr. Protoc. Toxicol.*, 2007, **31**, 1-9.

81. A. Murschhauser, P.J.F. Röttgermann, D. Woschee, M.F. Ober, Y. Yan, K.A. Dawson, J.O. Radler, A high-throughput microscopy method for single-cell analysis of event-time correlations in nanoparticle-induced cell death. *Commun Bio*., 2019, **2**, 35.

82. Saini, V. Sharma, P. Mathur, M. M. Shaikh, the development of fluorescence turn-on probe for Al(III) sensing and live cell nucleus-nucleoli staining. *Sci. Rep*., 2016, **6**, 34807.

83. A. S. Stender, K. Marchuk, C. Liu, S. Sander, M. W. Meyer, E. A. Smith, B. Neupane, G. Wang, J. Li, J. X. Cheng, B. Huang& N. Fang, Single-cell optical imaging and spectroscopy, *Chemical Rev.*, 2013, **113**, 2469-2527.

84. T. Ren, M. Z. Yang, W. M. Zhang, L. J. Qin, S. C. Zhou, N. N. Cheng, Y. J. Huang, J. Sun, N. Xu, H. B. Sun, B. B. Zhang, a novel fluorescent dye selectively images and kills cancer stem cells by targeting mitochondria: Evidence from a cell line based zebrafish xenograft model, *Oncol. Lett.*, 2023, **26**, 472.

85. G. Niu, R. Zhang, X. Shi, H. Park, S. Xie, R. Kwok, J.W. Lam, B. Z. Tang, AIE luminogens as fluorescent bioprobes, *TrAC, Trends Anal. Chem*., 2020, **123**, 115769.

86. J. Li, J. Wang, H. Li, N. Song, D. Wang, & B. Z. Tang, Supramolecular materials based on AIE luminogens (AIEgens): construction and applications. *Chem. Soc. Rev.*, 2020, **49**, 1144-1172.

87. R. Dave, K. Pandey, V. Khatri, R. Patel, N. Gour, & D. Bhatia, Biological AIE Molecules: Innovations in Synthetic Design and AI-Driven Discovery. *Adv. Biol.*, 2400792.

88. X. Wang, J. Huang, M. Guo, Y. Zhong, & Z. Huang, Aggregation-Caused Quenching Dyes as Potent Tools to Track the Integrity of Antitumor Nanocarriers: *A Mini-Rev. Pharm*., 2025, **18**, 176.

89. H. Wang, & G. Liu, Advances in luminescent materials with aggregation-induced emission (AIE) properties for biomedical applications. *J. Mater. Chem. B*, 2018, **6**, 4029-4042.

90. N. L. Leung, N. Xie, W. Yuan, Y. Liu, Q. Wu, Q. Peng, Q. Miao, J.W. Lam, B. Z. Tang, Restriction of intramolecular motions: the general mechanism behind aggregation-induced emission. *Chem. Eur. J.*, 2014, **20**, 15349-15353.

91. D. K. Patel, S. L. Rathod, V. S. Sharma, A. S. Sharma, S. P. Thakar, U. P. Patel, H. Mali, P. S. Shrivastav, Pillar [5] arene-based cyclophanes with cinnamate modifications, *J. Mol. Liq.*, 2024, **399**, 124376.

92. S. Boonnab, C. Chaiwai, P. Nalaoh, T. Manyum, S. Namuangruk, C. Chitpakdee, T. Sudyoadsuk and V. Promarak, Synthesis, characterization, and physical properties of pyrene-naphthalimide derivatives as emissive materials for electroluminescent devices. *Eur. J. Org. Chem.*, 2021, 2402-2410.

93. P. K. Behera, K. Yadav, D. S. Shankar Rao, U. K. Pandey, and A. S. Achalkumar, Self-Assembled anti-Napthalene-3,4:9,10-bis(benzimidazole)s: Stabilizing Room Temperature Columnar Phase with Ambipolar Conductivity., *ACS Appl. Electron. Mater.* 2023, **5**, 5417−5421.

94. A. Wicklein, M.A. Muth, and M. Thelakkat, Room temperature liquid crystalline perylene diester benzimidazoles with extended absorption, *J. Mater. Chem.*, 2010, **20**, 8646-8652.

95. Y. Ding, L. Zhao, Y. Fu, L. Hao, Y. Fu, Y. Yuan, P. Yu, Y. Teng, Synthesis and Antiproliferative Activities Evaluation of Multi-Substituted Isatin Derivatives. *Molecules.* 2021, **26**, 176.